

**Biomolecule-assisted synthesis of nanoparticles
and their characterization for potential
application in biophysical studies**

**THESIS
SUBMITTED FOR THE DEGREE OF
DOCTOR OF PHILOSOPHY (SCIENCE)
OF
JADAVPUR UNIVERSITY
2013**

**BY
NIRMAL GOSWAMI**



**DEPARTMENT OF CHEMICAL, BIOLOGICAL AND
MACROMOLECULAR SCIENCES,
S. N. BOSE NATIONAL CENTRE FOR BASIC SCIENCES,
BLOCK JD, SECTOR III, SALT LAKE,
KOLKATA 700 098, INDIA**



सत्येन्द्र नाथ बसु राष्ट्रीय मौलिक विज्ञान केन्द्र SATYENDRA NATH BOSE NATIONAL CENTRE FOR BASIC SCIENCES

CERTIFICATE FROM THE SUPERVISOR

This is to certify that the thesis entitled "Biomolecule-assisted synthesis of nanoparticles and their characterization for potential application in biophysical studies" submitted by Mr. Nirmal Goswami, who got his name registered on June 24, 2010 for the award of **Ph.D. (Science)** degree of **Jadavpur University**, is absolutely based upon his own work under the supervision of Dr. Samir Kumar Pal and that neither this thesis nor any part of it has been submitted for any degree/diploma or any other academic award anywhere before.



1st October 2013
(Signature of Supervisor/date with official seal)

Dr. SAMIR KUMAR PAL
Associate Professor,
S. N. Bose National Centre,
For Basic Sciences
Government of India
Block-JD, Sector-III, Salt Lake
Kolkata-700098

ब्लाक नं ० डी०, सेक्टर-३, साल्ट लेक, कोलकाता ७०००९८, BLOCK-JD, SECTOR III, SALT LAKE, KOKATA - 700 098
दूरभाष/ Phones : 0091-(0)33-2335 5705-8, 2335 3057/61, 2335 0312/1313

इ-मेल/ E-mail : root@bose.res.in

Webpage : <http://www.bose.res.in>

Fax : 0091-(0)33-2335 3477

FUNDED BY THE DEPARTMENT OF SCIENCE & TECHNOLOGY, GOVT. OF INDIA

निषिवद्व विज्ञान और प्रौद्योगिकी विभाग भारत सरकार द्वारा

To My Family

Acknowledgements

Because this may be my only opportunity to thank these individuals in writing, I may be a bit more verbose in my thanks than necessary.

First and foremost I would like to express my gratitude to Dr. Samir Kumar Pal for creating the research environment in which I have performed my Ph.D. work, for his constant availability and myriad helpful discussions. He has provided guidance at key moments in my work while also allowing me to work independently. He has taught me, both consciously and unconsciously, how good experimental work is done. I appreciate all his contributions of time, ideas, and support to make my Ph.D. experience productive and stimulating. The joy and enthusiasm he has for his research was contagious and motivational for me, even during tough times in the Ph.D. pursuit. I am also thankful for the excellent example he has provided as a successful experimental scientist and professor.

I would also like to thank Prof. Thalappil Pradeep of Department of Chemistry, IIT Madras, India and Prof. Gautam Basu of Bose Institute, India; Prof. Peter Lemmens of Braunschweig University of Technology, Germany; Prof. Jaydeep Dutta of Water Research Center, Sultan Qaboos University; Dr. Barnali Ghosh of S. N. Bose Centre, India; Dr. Achintya Singha of Bose Institute, India and Dr. N. T. K. Thanh of Physics and Astronomy Department, University College London, U.K. for fruitful collaboration.

Special recognition is given to Prof. Thalappil Pradeep for his valuable advices and for reviewing my works. For support and discussions, I am gratified to the lab members of the Pradeep research group: P. Lourdu Xavier, M. S. Bootharaju, T. Uday Baskar Rao and Ananya Bakshi. I am also very much thankful to them for their hospitality and the great efforts they made during my visit in IITM.

I owe a special thanks to Prof. Gautam Basu for his help and advice. We co-designed the NMR experiments and interpreted the data together, and I appreciate his enthusiasm, intensity, and willingness to do frequent discussion. I would also like to acknowledge Mr. Barun Majumder for his assistance in NMR experiments.

I am also obliged to the director of S. N. Bose National Centre for Basic Sciences, Prof. Arup Kumar Raychaudhuri for his great effort in increasing the experimental facility at the centre, which has proved to be a boon for our research work. I am also thankful to all those faculty members of the centre whose activities at several instances have promoted our progress. I thank all the staff members of this institute for their sincere cooperation and help.

Because of the research environment sustained by Dr. Pal, I have crossed paths with a number of Ph.D. students (Dr. Pramod Kumar Verma, Dr. Abhinandan Makital) who have influenced and enriched my research. The members of the Pal group have contributed immensely to my personal and professional time at S. N. Bose Centre. The direction of my Ph.D. work has been strongly influenced by the members of the Pal group, notably Anupam, Surajit, and Ranajay. I would like to acknowledge my other colleagues (Subrata, Tanumoy, Soumik, Soma, Siddhi, Susobhan, Samim and Nabarun) for providing me a homely and cheerful environment. I am, especially, thankful to

Anupam, Surajit and Subrata who shared glorious moments over a long period of time, supported my work annoyances, and also for the good moments of fun!

My time at S. N. Bose Centre was made enjoyable in large part due to the many friends and groups that became a part of my life. I am also thankful to all my friends at this centre for providing company at several instances. I gratefully acknowledge the Council of Scientific & Industrial Research of India for providing me a fellowship. My work was also supported by the DST.

Lastly, I would like to thank my family for all their love and encouragement. To my parents who raised me with a love of science and supported me in all my pursuits. To my brother Monoj for all the sweet memories I share with him. And most of all to my wife Krishna whose faithful support during the final stages of my Ph.D. is very much appreciated. Without their sacrifices, moral supports and blessings the thesis would not have taken its shape. Thank you.

Dated:

*Department of Chemical, Biological
and Macromolecular Sciences,
S. N. Bose National Centre for Basic Sciences,
Salt Lake, Kolkata 700098,
India.*

(Nirmal Goswami)

CONTENTS

| | Page |
|--|-------------|
| Chapter 1: Introduction | |
| 1.1. Background | 1 |
| 1.2. Fundamental Concepts of Nanotechnology | 1 |
| 1.3. Classification of Nanomaterials | 2 |
| 1.4. Synthesis of Nanomaterials | 5 |
| 1.5. Scope and Objective | 6 |
| 1.6. Summary of the Work Done | 11 |
| 1.6.1. Exploration of Key Pathways in the Biomolecule-assisted Metal Ion Reduction for Nanoparticle Synthesis | 11 |
| 1.6.1.1. Protein-assisted Synthesis Route of Metal Nanoparticles: Exploration of Key Chemistry of the Biomolecule | 11 |
| 1.6.2. Studies on the Oxidation of Host Biological Macromolecules Relevant to Biomolecule-assisted Metal Ion Reduction | 12 |
| 1.6.2.1. Toward an Alternative Intrinsic Probe for Spectroscopic Characterization of a Protein | 12 |
| 1.6.3. Biomineralization and Sensing Mechanisms of Toxic Metal Ion in a Biological Matrix | 13 |
| 1.6.3.1. Protein Directed Synthesis of NIR-Emitting, Tunable HgS Quantum Dots and their Applications in Metal Ion Sensing | 13 |
| 1.6.4. Synthesis and Promising Application of a Potential Nanobiocomposite | 13 |
| 1.6.4.1. MoS ₂ Nanocrystals Confined in DNA Matrix Exhibiting Energy Transfer | 13 |
| 1.6.5. Reduction of a Trace Element in Biological Matrix and its Potential Application in Toxic Metal Ion Sensing | 14 |

| | | |
|----------|--|----|
| 1.6.5.1. | Copper Quantum Clusters in Protein Matrix: Potential Sensor of Pb ²⁺ ion | 14 |
| 1.7. | Plan of Thesis | 14 |
| | References | 16 |

Chapter 2: An Overview of Steady-State and Dynamical Tools and Systems

| | | |
|----------|---|----|
| 2.1. | Steady-State and Dynamical Tools | 20 |
| 2.1.1. | Fluorescence Anisotropy | 20 |
| (i) | Theory | 21 |
| (ii) | Experimental Methods | 24 |
| 2.1.2 | Förster Resonance Energy Transfer (FRET) | 25 |
| 2.1.3 | Dexter Energy Transfer | 28 |
| 2.1.4 | Autocatalysis | 30 |
| 2.1.5 | Langmuir-Hinshelwood Mechanism | 32 |
| 2.1.6 | Tachiya Model | 33 |
| 2.1.7 | Distance Distribution in Donor-Acceptor Systems | 35 |
| 2.2. | Systems | 36 |
| 2.2.1. | Molecular Probes | 36 |
| 2.2.1.1. | 2,5-Cyclohexadiene-1,4-Dione (p-Benzoquinone, BQ) | 36 |
| 2.2.1.2 | Crystal Violet (CV) | 36 |
| 2.2.1.3. | Ala-Ala-Phe 7-Amido-4-Methyl Coumarin (AAF-AMC) | 36 |
| 2.2.1.4. | N-CBZ-Gly-Gly-Leu <i>p</i> -Nitroanilide (CBZGGL-pNA) | 36 |
| 2.2.1.5. | 2'-(4-Hydroxyphenyl)-5-[5-(4-Methylpiperazine -1-yl)-Benzimidazo-2-yl-Benzimida-zole, Hoechst 33258 | 36 |
| 2.2.1.6. | Kynurenone (KN) | 38 |

| | | |
|----------|--|----|
| 2.2.1.7. | 4-(Dicyanomethylene)-2-Methyl-6-(p-Dimethylaminostyryl) 4H-Pyran (DCM) | 38 |
| 2.2.2. | Proteins | 38 |
| 2.2.2.1. | Human Serum Albumin (HSA) | 38 |
| 2.2.2.2. | Bovine Serum Albumin (BSA) | 40 |
| 2.2.2.3. | α -Chymotrypsin (CHT) | 40 |
| 2.2.2.4. | Subtilisin <i>Carlsberg</i> (SC) | 41 |
| 2.2.3. | Deoxyribonucleic Acid (DNA) | 42 |
| | References | 44 |

Chapter 3: Instrumentation and Sample Preparation

| | | |
|---------|---|----|
| 3.1. | Instrumental Setup | 50 |
| 3.1.1 | Steady-State Absorption and Fluorescence Spectroscopy | 50 |
| 3.1.2. | Circular Dichroism Spectroscopy | 51 |
| 3.1.3. | Time Correlated Single Photon Counting | 53 |
| 3.1.4. | Dynamic Light Scattering | 54 |
| 3.1.5. | X-Ray Diffractometer | 56 |
| 3.1.6. | Fourier Transform Infrared Spectroscopy | 57 |
| 3.1.7. | Matrix-Assisted Laser Desorption/Ionization-Time of Flight (MALDI-TOF) Mass Spectrometry | 59 |
| 3.1.8. | Transmission Electron Microscopy | 60 |
| 3.1.9. | Scanning Electron Microscopy | 61 |
| 3.1.10. | X-Ray Photoelectron Spectroscopy | 62 |
| 3.1.11. | Femtosecond Time-Resolved Fluorescence Up-Conversion | 64 |
| 3.1.12. | Differential Scanning Calorimetry | 65 |
| 3.1.13. | Refractive Indices Measurement | 66 |
| 3.1.14. | Thermogravimetric-Differential Thermal Analyzer | 66 |
| 3.1.15. | Laser Raman Spectroscopy | 67 |
| 3.2. | Sample Preparation | 69 |
| 3.2.1. | Measurement of Enzymatic Activity | 69 |

| | |
|---|----|
| 3.2.2. Preparation of Genomic DNA Solutions | 70 |
| 3.2.3. Preparation of CV–HSA Complex | 70 |
| 3.2.4. Synthesis of Au@Protein Nanobioconjugates | 70 |
| 3.2.5. Extraction of Protein Mixture from E. Coli | 71 |
| 3.2.6. Synthesis of Au@E. Coli Protein Extracts Nanobioconjugates | 71 |
| 3.2.7. Synthesis of Protein Stabilized HgS Quantum Dots | 71 |
| 3.2.8. Synthesis of Bulk HgO | 72 |
| 3.2.9. Synthesis of Bulk HgS | 72 |
| 3.2.10. Synthesis of MoS ₂ Nanocrystals | 72 |
| 3.2.11. Preparation of MoS ₂ @DNA-CTAC Thin Film | 72 |
| 3.2.12. Preparation of Hoechst 33258 (H258)–DNA Complex | 73 |
| 3.2.13. Synthesis of CuQC@BSA | 73 |
| 3.2.14. Quantum Yield Calculation | 73 |
| References | 74 |

Chapter 4: Exploration of Key Pathways in the Biomolecule-assisted Metal Ion Reduction for Nanoparticle Synthesis

| | |
|---|----|
| 4.1. Introduction | 76 |
| 4.2. Results and Discussion | 77 |
| 4.2.1. Protein-assisted Synthesis Route of Metal Nanoparticles: Exploration of Key Chemistry of the Biomolecule | 77 |
| 4.3. Conclusion | 87 |
| References | 88 |

Chapter 5: Studies on the Oxidation of Host Biological Macromolecules Relevant to Biomolecule-assisted Metal Ion Reduction

| | | |
|--------|---|-----|
| 5.1. | Introduction | 92 |
| 5.2. | Results and Discussion | 93 |
| 5.2.1. | Protein-assisted Synthesis Route of Metal Nanoparticles: Exploration of Key Chemistry of the Biomolecule | 93 |
| 5.3. | Conclusion | 105 |
| | References | 106 |

Chapter 6: Biomineralization and Sensing Mechanisms of Toxic Metal Ion in a Biological Matrix

| | | |
|--------|---|-----|
| 6.1. | Introduction | 109 |
| 6.2. | Results and Discussion | 111 |
| 6.2.1. | Protein Directed Synthesis of NIR-Emitting, Tunable HgS Quantum Dots and Their Applications in Metal Ion Sensing | 111 |
| 6.3. | Conclusion | 126 |
| | References | 127 |

Chapter 7: Synthesis and Promising Application of a Potential Nanobiocomposite

| | | |
|--------|--|-----|
| 7.1. | Introduction | 131 |
| 7.2. | Results and Discussion | 133 |
| 7.2.1. | MoS ₂ Nanocrystals Confined in DNA Matrix Exhibiting Energy Transfer | 133 |
| 7.3. | Conclusion | 145 |
| | References | 146 |

Chapter 8: Reduction of a Trace Element in Biological Matrix and its Potential Application in Toxic Metal Ion Sensing

| | | |
|--------|--|-----|
| 8.1. | Introduction | 151 |
| 8.2. | Results and Discussion | 152 |
| 8.2.1. | Copper Quantum Clusters in Protein Matrix: Potential Sensor of Pb ²⁺ ion | 152 |
| 8.3. | Conclusion | 161 |
| | References | 162 |
| | LIST OF PUBLICATIONS | 165 |

Chapter 1

Introduction

1.1. Background

The term “colloid”, which was coined by Thomas Graham in 1861, is described as the distinctive behaviour of any form of matter, soft to hard, with a physical size in the 1–1000 nm range and with properties intermediate between that of a solution and a suspension. A lot has happened since then and the field has been propagated from colloidal science to nanoscience and nanotechnology. Over the past few decades, we have been fascinated by nanomaterial properties and the ground-breaking works of many brilliant scientists. By 1959, Richard Feynman delivered his remarkable speech on the future of miniaturization, *“Plenty of Room at the Bottom”*. He opened up a new field of Physics and inspired by his speech the term “Nanotechnology” was first used by Norio Taniguchi in 1974. Step by step, we gain more understanding about nanomaterials and especially their properties, which is a treasure trove for technological applications and a demanding criterion for the underlying physical theories.

1.2. Fundamental Concepts of Nanotechnology

Nanotechnology, a research field with high interest nowadays, is considered to be an area that is able to use materials for various purposes like optics, electronics, biology and medicine. As defined by the Royal Society: *Nanotechnology is the design, characterisation, production and application of structures, devices and systems by controlling shape and size at nanometer scale* (The Royal Society & The Royal Academy of Engineering, 2004a). It is the area of science and technology where extremely small size plays critical role. By convention, nanotechnology is taken as the scale range of 0.1 to 100 nanometer (nm). One nanometer (nm) is one billionth, or 10^{-9} of a meter. By comparison, one may think about typical carbon-carbon bond lengths, or the spacing between the atoms in a molecule, and as wide as DNA double-helix. In the nanoscale regime, the materials have properties that can be very different from those at a larger scale as well as distinct from molecules. A number of physical phenomena become pronounced as the size of the material decreases to nanometer regime. For example, the “quantum size effect”, where the electronic properties of solids are altered with reductions in particle size, become significant when

the nanometer size range is reached, typically at the size of 100 nm or less. Furthermore, surface to volume ratio, thermal, electronic, catalytic properties have also been altered significantly compare to microscopic materials. Apart from the size effect, materials chemistry has become expanded and enriched with shape, surface, defect, self-assembly properties that are designed to evoke a specific function and orchestrated to target a particular end use.

1.3. Classification of Nanomaterials

"Nanomaterials" exhibit novel properties generally fall into various categories. Here, we briefly introduce three kinds of nanomaterial.

Metal Nanoparticles: In recent years, researchers in the field of nanotechnology are finding that metal nanoparticles have all kinds of previously-unexpected benefits because of their unique properties, including large optical field enhancements resulting in the strong scattering and absorption of light. The interesting optical properties of metal nanoparticles are due to their unique interaction with light. In the presence of oscillating electromagnetic field of the light, the free electrons of the metal nanoparticle undergo a collective coherent oscillation with respect to the positive metallic lattice. This process is resonant at a particular frequency of the light and is termed the surface plasmon resonance (SPR) absorption which can be simply visualized as a photon confined to the small size of the nanostructure, constituting an intense electric field around the particle. The surface plasmon oscillation decays by radiating its energy resulting in light scattering or by nonradiatively as a result of conversion of absorbed light to heat [1]. The electric field intensity and the scattering and absorption cross-sections are all strongly enhanced at the SPR frequency. For gold (Au), silver (Ag), and copper (Cu), the resonance condition is fulfilled at visible frequencies. Since Cu is easily oxidized, Au and Ag nanostructures are most attractive for optical applications.

The spectral position and shape of the plasmon band for a given particle has been determined by Gustav and Mie [2] and can be represented in the following way,

$$E(\lambda) = \frac{24\pi^2 N a^3 \varepsilon_{ex}^{3/2}}{\lambda \ln(10)} \left[\frac{\varepsilon_i(\lambda)}{(\varepsilon_r(\lambda) + \chi \varepsilon_{ex})^2 + \varepsilon_i(\lambda)^2} \right] \quad (1.1)$$

where ε_r and ε_i are respectively, the real and imaginary components of the dielectric function of the metal, ε_{ex} is the external environment dielectric function, r is the radius of the particle, χ is factor related to the eccentricity of the particle, and N is the number of atoms present in the particle. Using equation (1.1), one can reasonably predict the position and shape of plasmon absorption for spherical and spheroidal metal nanoparticles which have sizes comparable to the wavelength of the incident light (i.e. $R \approx \lambda$) [3]. The average radius of metallic NPs, can be approximately estimated from the resonance optical absorption spectrum as per the Mie scattering formula [2],

$$r_{metal} = \frac{v_F}{\Delta\omega_{1/2}} = \frac{v_F}{2\pi c_0 \left(\frac{\Delta\lambda}{\lambda_p^2} \right)} \quad (1.2)$$

where v_F = Fermi velocity and $\Delta\omega_{1/2}$ is the full width at half-maximum (FWHM) of the SPR absorption when plotted as a function of angular frequency ω , c_0 is the speed of light in vacuum, λ_p is the wavelength where absorption peak appears, and $\Delta\lambda$ gives the FWHM of the band.

For metal NPs localized surface plasmon oscillations can give rise to the vivid characteristic colour, which makes them valuable candidate for optical detection of chemical and biological species, surface-enhanced Raman scattering (SERS) as well as in biomedical applications. Moreover, the decrease in the particle size to the nanometer length scale increases the surface-to-volume ratio which makes the NPs to be potentially useful in the field of catalysis. In most of their potential applications, surface plays an important role, however, being so small, high surface energy and the large surface curvature could make the NPs unstable. Hence, a number of strategies have been employed to stabilize the NPs in solution where the use of “capping ligand” is perhaps the best recognised.

Metal Nanoclusters: Similar to metal NPs, study of metal nanoclusters (NCs) has also received considerable attention in recent years because they bridge the evolution of properties from isolated atoms to nanoparticles and even to the bulk [4, 5]. Providing the “missing link” between atomic and nanoparticles behaviour in noble metals, the fluorescent, water-soluble metal nanoclusters offer complementary transition energy size scalings at smaller dimensions. Their robust, discrete, size-dependent emission makes

them ideal fluorophores for single-molecule spectroscopic studies. Their transition energies have been found to scale with the inverse of the cluster radius based on the spherical jellium model [6], valid for metals with free electrons such as gold and silver. Due to the similarity in electronic structure of metal clusters and single atoms, the metal clusters are also called “multi-electron artificial atoms” [7, 8].

According to the spherical jellium model, a metal cluster is represented as uniform, positively charged sphere with electronic shells filled with free electrons. These free electrons are provided by the valence electrons of metal atoms, and they delocalize and form spherical electron shells surrounding the positively charged core. Due to a strong electron screening effect, valence electrons of noble metal atoms are considered free after neglecting electron-electron and electron-ion interactions [9]. Distinct from the electronic structure of single atoms, cluster electron density is independent of the number of free electrons in the metal clusters. However, analogous to single atoms, free electrons in metal clusters are also delocalized for electronic shells surrounding the atoms and subject to the Pauli Exclusion Principle. The jellium model predicts that the emission energy of metallic NCs follow a power law of the number of atoms in the NC with no adjustable parameters by the simple scaling relation of $E_{\text{fermi}}/N^{1/3}$ in which E_{fermi} is the Fermi energy of bulk metal and N is the number of atoms in the NC. It has been successfully applied to small gold NCs [10], describing accurately the size-dependent electronic structure and relative electronic transitions of the small clusters [6].

Quantum Dots: A quantum dot (QD) is a semiconductor whose excitons are confined in all three spatial dimensions. Amongst the various types of nanomaterials, QDs have been widely investigated and are quite understandable [11, 12]. They exhibit size-tunable band gaps and luminescence energies owing to the “quantum-size effect”. In order to understand that effect, first consider an electron excited from the valence band by the absorption of a quantum of light moves to the conduction band, leaving behind a hole in the valence band. Together, the bound state of the electron and the electron hole which are attracted by coulombic force is called exciton. Taking a simple Bohr model picture of the exciton, the electron and hole orbit each other at a distance known as the Bohr radius, which varies depending on the material, ranging from a few to tens of nanometers. In a semiconductor crystallite whose diameter is smaller than the size of its excitons Bohr radius, the excitons are squeezed, leading to quantum confinement [11].

Compared with the organic fluorophores that were previously used for biological labelling, quantum dots are much brighter and do not photobleach. They also provide a readily accessible range of colours. As fluorophores, high quality QDs are extremely bright, with quantum yields (QYs) approaching unity. QDs have been used for a wide variety of applications, such as light emitting diodes, lasers and solar cells, staining and lighting up cells for visualization, photocatalysis etc. However, with regard to biological applications toxicity remains a complicated question. Additionally, cellular uptake of QDs is extremely complex, varying not only with size but with QD surface properties as well as cell type [13].

1.4. Synthesis of Nanomaterials

The fact is without chemical synthesis there would be no new material, and therefore in the early days, the great appeal of a synthetic approach to nanomaterials was the ability to create nanoscale building blocks of any composition. The synthetic routes to nanomaterials can mainly be divided into two categories:

Top-Down Approach: It starts with a large structure and proceeds to make it smaller through successive cuttings (Figure 1.1). Different kinds of lithographic techniques, cutting (such as electron beam, photo ion beam or X-ray lithography cutting), etching, grinding, ball milling and sol gel technique are the example of top-down approach. The top-down method is currently in use to manufacture computer chips as well as other products that we use every day. However, the techniques suffer from the need to remove large amounts of material. Physical limits of the technique is also a problem.

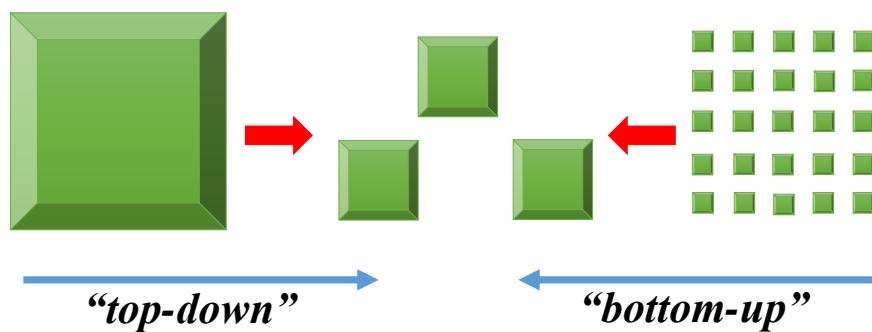


Figure 1.1. Approaches for the synthesis of nanomaterials.

Bottom-Up Approach: It can be accessed from a molecularly dispersed system whereby the size of a dissolved species is increased continuously until the nanometer regime is reached. In general, it refers to the build-up of a material from the bottom (Figure 1.1): atom-by-atom, molecule-by-molecule, or cluster-by-cluster. Colloidal dispersion is a good example of bottom-up approach in the synthesis of nanoparticles. This approach allows smaller geometries of the nanomaterials compare to top-down approach. It is more economical than top-down approach as it does not waste material to etching. However, getting control over the methods is difficult.

1.5. Scope and Objective

Nanomaterials are extremely important because of their potential application in optoelectronics, catalysis, sensing, biology and medicine [14-17]. The well-established fact is that, unusual chemical and physical properties originate when the particle size reduces significantly from their bulk counterpart. So, the development of synthetic techniques down to the size of nanometer regime for inorganic nanoparticles is continuous to be the topic of ongoing research. During last few years, different kinds of nanostructures have been developed such as sphere, rod, wire, chain, disc, and others [18-20]. Numerous methods have been described to synthesize inorganic nanoparticles such as sol-gel synthesis, hydrothermal, sonochemical, co-precipitation, hydrolysis and thermolysis of precursors [21-24]. While these synthetic routes are quite straightforward and relatively well understood, the use of a biomolecule as template or scaffold for the synthesis of nanomaterials through biomineralization has not been realized in detail. Biomineralization is a natural process in which living organisms adapt to form hard structures by mineralizing metal ions through mineralizing peptides, vesicles, etc. It is regarded as a paradigm for the development of novel routes for the synthesis of functional materials with nanometer precision in all three dimension.

Among many biological systems that could participate in biomineralization and be incorporated into bio-nanomaterials, proteins and DNA have been the subject of particular attention due to their nanoscale dimensions, distinctive molecular structures and functionalities, and their capability to control the size of inorganic crystals during nucleation and growth to a remarkable degree due to their bulky nature [25]. In some

cases, electron transfer is associated with the formation of nanoparticles. For example, during the synthesis of Au nanoparticles using protein as biomolecule, some of the amino acids transfer its electron to reduce the Au ion [26]. Therefore the protein may undergoes chemical modification as a consequence of nanoparticle formation (metal ion reduction). The consequence of biomineralization process may alter the structure and function of the biomolecules. Thus, the investigation of structural and functional properties of the biomolecules under the influence of strong oxidising agent is very crucial and important. Optical spectroscopy is an ideal tool to monitor the structure and dynamics of the biomolecules. Several ultrafast spectroscopic techniques such as picosecond-resolved fluorescence spectroscopy, femtosecond transient absorption, and femtosecond-resolved fluorescence upconversion have been employed to investigate the structure and dynamics of the biomolecules. In one of our studies, we have explored the role of an oxidising agent for the modification of proteins/enzymes [27]. By using steady-state and time-resolved fluorescence spectroscopy we have established that the chemical modification results an alternative intrinsic probe (kynurenine) within structural and functional integrity.

The key focus of this thesis is to develop various kinds of inorganic nanomaterials in different biological matrix. Although there have been attempts to interface proteins with nanomaterials, many of these studies have focused on the modification and/or enhancement of nanomaterial properties to confer a specific biological function. It is, however, also important to understand how the self-sustained biomineralization process can be utilized for the synthesis of various nanomaterials under environmentally benign condition. How nanomaterial properties such as curvature and surface chemistry influence the structure and function of conjugated proteins/enzymes is also crucial. Metal nanoparticles are found to serve as effective catalyst to activate the reduction of 4-nitrophenol in the presence of NaBH₄ [28, 29]. However, the mechanism of that catalytic reaction is still fuzzy in the existing literature. Therefore, a detailed study highlighting every step involved in catalytic process using metal NPs is essential from the viewpoint of industrial application.

Semiconductor QDs have attracted considerable attention because of their unique tunable physical and chemical properties suitable for multifunctional applications [11, 30,

31]. Luminescent mercury sulphide (HgS) QDs are highly attractive for infrared sensing, optoelectronics, as well as for the more fundamental studies of their optical properties [32, 33]. Although advanced studies have been performed on zinc and cadmium based chalcogenides, however, the potential development of tunable NIR luminescent HgS quantum dots (QDs) through biomimetic process is yet to be fully understood. Moreover, like other QDs, bioconjugated HgS QDs can be utilized in toxic metal ion sensing by exploiting their luminescence properties. However, the sensing mechanism addressing the specific interaction of detected ions with the sensor QDs is crucial and therefore studies on this direction seem to be very exciting.

Transition metal chalcogenide semiconductors display interesting properties that are important for sensing, catalysis, photovoltaics, and even biology [31, 34-40]. In particular, molybdenum disulphide (MoS_2) is a prototypical transition metal dichalcogenide material, which is one of the most studied 2D materials after graphene. A number of intrinsic properties starting from catalysis, photovoltaics to optics imply that MoS_2 could also be one of the most valuable materials in nanotechnology. Recently, advanced studies have been performed on 2D MoS_2 nanosheets; however, the potential development of quantum confined MoS_2 nanocrystals (NCs) through biomimetic process has remained largely unexplored. In this regard, biomolecules like DNA offers a great potentiality as a building block to create nanostructures. But before use, proper engineering with such system and their extensive studies are necessary. Hence, the synthesis and study of MoS_2 NCs conjugated with DNA having interesting properties are very important for their multifunctional applications.

Noble metal quantum clusters (QCs) are the missing link between isolated noble metal atoms and nanoparticles [41]. Dramatic growth has been witnessed in the field of atomic clusters during the last few decades, due to their fascinating properties [42]. While naturally formed metal NPs are reported, unfortunately, QCs are not observed so far to occur naturally, may be because of their high reactivity. The biomimetic process has been mimicked to synthesize QCs too by carefully adjusting the concentration of metal ions and modifying the environment suitably. Unlike semiconductor QDs, quantum confinement effects starts only below 2 nm in QCs, hence, controlling the size becomes a tedious but crucial process. In recent years, extensive

studies have been focused on luminescent Au and Ag QCs, however, studies focusing on the synthesis and optical properties of other QCs such as Cu are still scarce primarily because of the difficulty in preparing highly stable and extremely tiny particles. So, synthesis of atomically precise, luminescent Cu QCs through biomineralization process and application of their properties will be very interesting for the basic understanding of material science as well as for their technological applications.

The experimental tools used for studying the dynamical processes involve picosecond and femtosecond time-resolved carrier relaxation dynamics, fluorescence anisotropy, Förster resonance energy transfer (FRET), Dexter energy transfer, and photoinduced electron transfer (PET). The different experimental techniques employed for the characterization of the bionanoconjugates include steady-state UV-vis absorption and fluorescence, enzyme kinetics, thermogravimetric analysis (TGA), Fourier transform infrared spectroscopy (FTIR), Raman spectroscopy, matrix-assisted laser desorption ionization (MALDI) mass spectrometry, X-ray diffraction (XRD), circular dichroism (CD), dynamic light scattering (DLS), scanning electron microscopy (SEM), high-resolution transmission electron microscopy (HRTEM) and X-ray photoelectron spectroscopy (XPS).

In this backdrop the main objectives of the thesis are summarized as follows:

- ✓ As the level of understanding in the protein protected nanomaterials at the nano-biointerface increases, it is necessary to understand how the nanoparticles are being formed using protein at the cost of their native structural integrity. Using Au as model nanoparticle, we will explore the details of the associated biochemistry of the proteins dictating kinetics, size, and crystallinity of the nanoparticles. The kinetics of nanoparticles formation in this route, which involves nucleation (induction period) and subsequent growth (acceleration period), has been modelled in a simple scheme of autocatalytic process. As-synthesised nanoparticle can be utilized as an efficient catalyst for 4-nitrophenol reduction. The kinetic data obtained from UV-vis spectroscopy which reveals the efficient catalytic activity of the nanoparticles, have been explained in terms of the Langmuir–Hinshelwood model.

- ✓ Protein consists of several amino acids like tryptophan, tyrosine, arginine, lysine etc., which has the capability of reducing several metal ions. The reduction process involves electron transfer from the amino acid to the metal ion and as a consequence the corresponding amino acid becomes oxidized. As a mimic study, we will present an electron transfer reaction in protein cavity which causes the tryptophan residue to undergo chemical modification to form one of its metabolite kynurenone. Structural and functional integrity upon modification of the native protein have been confirmed by using different spectroscopic techniques. The study is an attempt to explore an alternative intrinsic fluorescence probe for the spectroscopic investigation of a protein.
- ✓ Akin to metal nanoparticles, semiconductor quantum dots (QDs) have also shown great promise for a range of applications due to their high versatility, and size tunable optical properties. In one of our studies, we will describe a new methodology to synthesize protein functionalized, size-tunable luminescent HgS QDs through biomineralization process. Basically the synthesis has been carried out in a protein matrix, and the QDs are formed through an intermediate. We have demonstrated that the as-prepared QDs can serve as selective sensor material for Hg(II) and Cu(II) ions, based on the specific luminescence quenching. From picosecond time-resolved studies, we have shown that for Hg(II), quenching proceeds by Dexter-type energy transfer process whereas in case of Cu(II), quenching takes place through a photoinduced electron transfer mechanism.
- ✓ Molybdenum disulfide (MoS_2) nanostructures are receiving considerable attention as 2D material, however, the colloidal synthesis of MoS_2 nanocrystals (NCs) is quite delicate, and as a result, there is less development compared to other synthetic routes. In one of our studies, we will demonstrate the synthesis and characterization of MoS_2 NCs using DNA as a host matrix. We have also observed negligible perturbation in the native structure of DNA upon interaction with MoS_2 NCs. To check whether MoS_2 NCs adequately quench the fluorescence of the dye/donor molecules we have introduced a well-known DNA minor groove binding probe, Hoechst 33258. This study is based on Förster resonance energy transfer (FRET), which has recently experienced a significant interest of several

groups. Furthermore, employing a statistical method we have estimated the probability of distance distribution between donor and acceptor.

- ✓ Quantum clusters (QCs) are sub-nanometer core sized clusters composed of a group of atoms, most often luminescent in the visible region, and possess intriguing photo-physical and chemical properties. A trend is observed in the use of ligands, ranging from phosphines to functional proteins, for the synthesis of QCs in the liquid phase. We will describe a method to prepare highly stable blue luminescent Cu QCs (<2 nm) using bovine serum albumin as a model protein. Using MALDI-MS, we have tentatively assigned that the clusters consist of 5 and 13 number of Cu atoms. The quantum clusters serve as sensor material for hydrogen peroxide and lead ion. We have proposed that the mechanism of luminescence quenching is due to aggregation of the QCs in presence of lead ion.

1.6. Summary of the Work Done:

1.6.1. Exploration of Key Pathways in the Biomolecule-assisted Metal Ion Reduction for Nanoparticle Synthesis:

1.6.1.1. Protein-assisted Synthesis Route of Metal Nanoparticles: Exploration of Key Chemistry of the Biomolecule [43]:

Essentially, biomolecule-assisted synthesis of inorganic nanoparticles can be divided into two categories. One uses multi-domain protein cages (template) and other relies on the self-assembly of the biomolecules including small peptides, DNA and denatured protein. Protein templated synthesis of various nanomaterials is relatively well understood as the cages of the biological macromolecules and their specific interaction with inorganic ions ultimately dictate the size and crystallinity of the nanomaterials. On the other hand formation of nanoparticles using protein in the cost of the native structural integrity for the self-assembly is not well understood till date. In the present work we report a protein-assisted synthesis route to prepare highly crystalline 3-5 nm gold nanoparticles, which relies systematic thermal denaturation of a number of proteins and protein mixture from *E. coli* in absence of any reducing agent. By using UV-vis, circular dichroism (CD) spectroscopy and high resolution transmission electron microscopy (HRTEM) we have explored details of the associated biochemistry of the

proteins dictating kinetics, size and crystallinity of the nanoparticles. The kinetics of nanoparticles formation in this route, which is sigmoidal in nature, has been modelled in a simple scheme of autocatalytic process. Interestingly, the protein-capped as-prepared Au nanoparticles are found to serve as effective catalyst to activate the reduction of 4-nitrophenol in the presence of NaBH₄. The kinetic data obtained by monitoring the reduction of 4-nitrophenol by UV-vis spectroscopy, revealing the efficient catalytic activity of the nanoparticles, have been explained in terms of the Langmuir-Hinshelwood model. The methodology and the details of the protein-chemistry presented here may find relevance in the protein-assisted synthesis of inorganic nanostructures in general.

1.6.2. Consequence of Metal Ion Reduction for the Nanoparticle Synthesis in Biological Macromolecules:

1.6.2.1. Toward an Alternative Intrinsic Probe for Spectroscopic Characterization of a Protein [27]:

The intrinsic fluorescent amino acid tryptophan is the unanimous choice for the spectroscopic investigation of proteins. However, several complicacies in the interpretation of tryptophan fluorescence in a protein are inevitable and an alternative intrinsic protein probe is a longstanding demand. In this work, we report an electron transfer reaction in a protein cavity which causes the tryptophan residue (Trp214) to undergo chemical modification to form one of its metabolite kynurenine (Kyn214). Structural integrity upon modification of the native protein, is confirmed by steady-state and time-resolved fluorescence spectroscopy. Femtosecond resolved fluorescence transients of the modified protein describe the dynamics of solvent molecules in the protein cavity in both the native and denatured states. In order to establish general use of the probe, we have studied the dipolar interaction of Kyn214 with a surface bound ligand (crystal violet; CV) of the protein. By using the sensitivity of FRET, we have determined the distance between Kyn214 (donor) and CV (acceptor). Our study is an attempt to explore an alternative intrinsic fluorescence probe for the spectroscopic investigation of a protein.

1.6.3. Biomineralization and Sensing Mechanisms of Toxic Metal Ion in a Biological Matrix:

1.6.3.1. Protein Directed Synthesis of NIR-emitting, Tunable HgS Quantum Dots and their Applications in Metal Ion Sensing [35]:

The development of luminescent mercury sulfide quantum dots (HgS QDs) through biomineralization process has remained unexplored. Herein, we report a simple, two step route for the synthesis of HgS quantum dots in bovine serum albumin (BSA). The QDs were characterized by UV-vis, Fourier transform infrared spectroscopy (FTIR), luminescence, Raman spectroscopy, transmission electron microscopy (TEM), X-ray photoelectron spectroscopy (XPS), circular dichroism (CD), energy dispersive analysis of X-rays (EDAX), and picosecond time-resolved optical spectroscopy. Formation of various sized QDs was observed by modifying the conditions suitably. The QDs also showed tunable luminescence over the 680-800 nm spectral regions, with a quantum yield of 4-5%. We have demonstrated that the as-prepared QDs can serve as selective sensor materials for Hg(II) and Cu(II) ions, based on selective luminescence quenching. The quenching mechanism was found to be Dexter energy transfer and photoinduced electron transfer for Hg(II) and Cu(II) ions, respectively. The simple synthesis route of protein capped HgS QDs would provide additional impetus to explore applications for these materials.

1.6.4. Synthesis and Promising Application of a Potential Nanobiocomposite:

1.6.4.1. MoS₂ Nanocrystals Confined in DNA Matrix Exhibiting Energy Transfer [44]:

We describe the wet chemical synthesis of MoS₂ nanocrystals (NCs), a transition metal dichalcogenide, using DNA as a host matrix. As evidenced from transmission electron microscopy (TEM), the NCs are highly crystalline with an average size of 5.1 ± 0.2 nm. UV-vis absorption studies along with band gap calculations confirm that NCs are in quantum confinement. A prominent red shift of the optical absorption bands has been observed upon formation of thin film using CTAC (hexadecyltrimethylammonium chloride) i.e., in case of MoS₂@DNA-CTAC. In the thin

film, strong electron-phonon coupling arises due to the resonance effect which is reflected from the emergence of intense 1st, 2nd and 3rd order Raman peaks whenever excited with 488 nm line. We have established that our as-synthesised MoS₂ NCs quench the fluorescence of a well-known DNA minor groove binding probe, Hoechst 33258. Unprecedented fluorescence quenching (94%) of donor (Hoechst 33258) emission and efficient energy transfer (89%) between Hoechst 33258 and MoS₂ NCs (acceptor) are obtained. The donor-acceptor distance of these conjugates has been described by Förster resonance energy transfer (FRET) based model. Furthermore, employing a statistical method we have estimated the probability of distance distribution between donor and acceptor. We believe that the study described herein may enable substantial advances in the field of optoelectronics, photovoltaics, catalysis and many others.

1.6.5. Reduction of a Trace Element in Biological Matrix and its Potential Application in Toxic Metal Ion Sensing:

1.6.5.1. Copper Quantum Clusters in Protein Matrix: Potential Sensor of Pb²⁺ ion [45]:

A one-pot synthesis of extremely stable, water-soluble Cu quantum clusters (QCs) capped with a model protein, BSA is demonstrated. From matrix-assisted laser desorption-ionization time of flight (MALDI-TOF) mass spectrometry, we assign the clusters to be composed of Cu₅ and Cu₁₃ cores. The QCs also show luminescence properties having an excitation and emission maxima at 325 and 410 nm respectively, with a quantum yield of 15% which are found to be different from that of protein alone in similar experimental condition. The quenching of luminescence of the protein capped Cu QCs in presence of very low hydrogen peroxide concentration (~nM or less than ppb) reflects the efficacy of the QCs as potential sensing material in biological environments. Moreover, as-prepared Cu QCs can detect highly toxic Pb²⁺ ions in water, even at ppm level without suffering any interference from other metal ions.

1.7. Plan of Thesis:

The plan of the thesis is as follows:

Chapter 1: This chapter gives a brief introduction to the metal nanoparticles, quantum clusters, quantum dots, as well as scope and motivation behind the thesis work. A brief summary of the work done is also included in this chapter.

Chapter 2: This chapter provides an overview of the dynamical and steady-state tools, the structural aspects of biologically important systems (proteins, DNAs) and probes used in the research.

Chapter 3: Details of instrumentation, data analysis and experimental procedures have been discussed in this chapter.

Chapter 4: Autocatalytic mechanism of the biomolecule-assisted synthesis of metal nanoparticles and their application in surface catalysis have been discussed in this chapter.

Chapter 5: This chapter deals with the spectroscopic characterization of biomolecules upon oxidation, a mimic study of which is the formation of nanoparticles by the reduction of amino acids in protein.

Chapter 6: A new methodology to synthesize protein-functionalized, size-tunable NIR luminescent HgS quantum dots has been discussed in this chapter. Application in dual metal ion sensing with mechanism in details has also been described.

Chapter 7: Formation of transition metal dichalcogenide using DNA as a host matrix has been presented.

Chapter 8: This chapter offers a protein directed synthesis of atomically precise quantum clusters and their application in toxic metal ion sensing.

References

- [1] C. Burda, X. Chen, R. Narayanan, M.A. El-Sayed, Chemistry and Properties of Nanocrystals of Different Shapes, *Chem. Rev.* 105 (2005) 1025.
- [2] G. Mie, Contributions to the Optics of Turbid Media, Particularly of Colloidal Metal Solutions, *Ann. Phys.* 25 (1908) 377.
- [3] J.A. Creighton, D.G. Eadon, Ultraviolet-Visible Absorption Spectra of the Colloidal Metallic Elements, *J. Chem. Soc., Faraday Trans.* 87 (1991) 3881.
- [4] G.A. Ozin, H. Huber, Cryophotoclustering Techniques for Synthesizing Very Small, Naked Silver Clusters Agn of Known Size (where n = 2-5). The Molecular Metal Cluster-Bulk Metal Particle Interface, *Inorg. Chem.* 17 (1978) 155.
- [5] L.A. Peyser, A.E. Vinson, A.P. Bartko, R.M. Dickson, Photoactivated Fluorescence From Individual Silver Nanoclusters, *Science* 291 (2001) 103.
- [6] J. Zheng, P.R. Nicovich, R.M. Dickson, Highly Fluorescent Noble-Metal Quantum Dots, *Ann. Rev. Phys. Chem.* 58 (2007) 409.
- [7] W.D. Knight, K. Clemenger, W.A.d. Heer, W.A. Saunders, M.Y. Chou, M.L. Cohen, Electronic Shell Structure and Abundances of Sodium Clusters, *Phys. Rev. Lett.* 52 (1984) 2141.
- [8] W.A. Deheer, The Physics of Simple Metal-Clusters -Experimental Aspects and Simple-Models, *Rev. Mod. Phys.* 65 (1993) 611.
- [9] A. Henglein, Physicochemical Properties of Small Metal Particles in Solution: "Microelectrode" Reactions, Chemisorption, Composite Metal particles, and The Atom-to-metal Transition, *J. Phys. Chem.* 97 (1993) 5457.
- [10] J. Zheng, C. Zhang, R.M. Dickson, Highly Fluorescent, Water-Soluble, Size-Tunable Gold Quantum Dots, *Phys. Rev. Lett.* 93 (2004) 077402.
- [11] J.A. Smyder, T.D. Krauss, Coming Attractions for Semiconductor Quantum Dots, *Mater. Today* 14 (2011) 382.
- [12] Y. Yin, A.P. Alivisatos, Colloidal Nanocrystal Synthesis and the Organic-Inorganic Interface, *Nature* 437 (2005) 664.
- [13] T.-G. Iversen, T. Skotland, K. Sandvig, Endocytosis and Intracellular Transport of Nanoparticles: Present Knowledge and Need for Future Studies, *Nano Today* 6 (2011) 176.
- [14] P.C. Ray, Size and Shape Dependent Second Order Nonlinear Optical Properties of Nanomaterials and Their Application in Biological and Chemical Sensing, *Chem. Rev.* 110 (2010) 5332.
- [15] X. Lu, C. Wang, Y. Wei, One-Dimensional Composite Nanomaterials: Synthesis by Electrospinning and Their Applications, *Small* 5 (2009) 2349.

- [16] V.L. Colvin, The Potential Environmental Impact of Engineered Nanomaterials, *Nat. Biotech.* 22 (2004) 760.
- [17] P.K. Jain, X. Huang, I.H. El-Sayed, M.A. El-Sayed, Noble Metals on the Nanoscale: Optical and Photothermal Properties and Some Applications in Imaging, Sensing, Biology, and Medicine, *Acc. Chem. Res.* 41 (2008) 1578.
- [18] C. Burda, X.B. Chen, R. Narayanan, M.A. El-Sayed, Chemistry and Properties of Nanocrystals of Different Shapes, *Chem. Rev.* 105 (2005) 1025.
- [19] Y. Xiong, Y. Xia, Shape-Controlled Synthesis of Metal Nanostructures: The Case of Palladium, *Adv. Mater.* 19 (2007) 3385.
- [20] B. Wiley, Y. Sun, B. Mayers, Y. Xia, Shape-Controlled Synthesis of Metal Nanostructures: The Case of Silver, *Chem. Eur. J.* 11 (2005) 454.
- [21] Y. Lu, Y. Yin, B.T. Mayers, Y. Xia, Modifying the Surface Properties of Superparamagnetic Iron Oxide Nanoparticles through A Sol–Gel Approach, *Nano Lett.* 2 (2002) 183.
- [22] T.J. Daou, G. Pourroy, S. Bégin-Colin, J.M. Grenèche, C. Ulhaq-Bouillet, P. Legaré, P. Bernhardt, C. Leuvrey, G. Rogez, Hydrothermal Synthesis of Monodisperse Magnetite Nanoparticles, *Chem. Mater.* 18 (2006) 4399.
- [23] K.V.P.M. Shafi, A. Ulman, X. Yan, N.-L. Yang, C. Estournès, H. White, M. Rafailovich, Sonochemical Synthesis of Functionalized Amorphous Iron Oxide Nanoparticles, *Langmuir* 17 (2001) 5093.
- [24] S.H. Sun, H. Zeng, Size-Controlled Synthesis of Magnetite Nanoparticles, *J. Am. Chem. Soc.* 124 (2002) 8204.
- [25] H. Wei, Z.D. Wang, J. Zhang, S. House, Y.G. Gao, L.M. Yang, H. Robinson, L.H. Tan, H. Xing, C.J. Hou, I.M. Robertson, J.M. Zuo, Y. Lu, Time-Dependent, Protein-Directed Growth of Gold Nanoparticles within a Single Crystal of Lysozyme, *Nat. Nanotechnol.* 6 (2011) 93.
- [26] S. Si, T.K. Mandal, Tryptophan-Based Peptides to Synthesize Gold and Silver Nanoparticles: A Mechanistic and Kinetic Study, *Chem. Eur. J.* 13 (2007) 3160.
- [27] N. Goswami, A. Makhral, S.K. Pal, Toward an Alternative Intrinsic Probe for Spectroscopic Characterization of a Protein, *J. Phys. Chem. B* 114 (2010) 15236.
- [28] S. Wunder, F. Polzer, Y. Lu, Y. Mei, M. Ballauff, Kinetic Analysis of Catalytic Reduction of 4-Nitrophenol by Metallic Nanoparticles Immobilized in Spherical Polyelectrolyte Brushes, *J. Phys. Chem. C* 114 (2010) 8814.
- [29] K. Esumi, R. Isono, T. Yoshimura, Preparation of PAMAM– and PPI–Metal (Silver, Platinum, and Palladium) Nanocomposites and Their Catalytic Activities for Reduction of 4-Nitrophenol, *Langmuir* 20 (2004) 237.

- [30] P. Yang, Y. Zhao, Y. Lu, Q.Z. Xu, X.W. Xu, L. Dong, S.H. Yu, Phenol Formaldehyde Resin Nanoparticles Loaded with CdTe Quantum Dots: A Fluorescence Resonance Energy Transfer Probe for Optical Visual Detection of Copper(II) Ions, *ACS Nano* 5 (2011) 2147.
- [31] R. Shen, X. Shen, Z. Zhang, Y. Li, S. Liu, H. Liu, Multifunctional Conjugates to Prepare Nucleolar-Targeting CdS Quantum Dots, *J. Am. Chem. Soc.* 132 (2010) 8627.
- [32] L. Wu, B. Quan, Y. Liu, R. Song, Z. Tang, One-Pot Synthesis of Liquid Hg/Solid β -HgS Metal–Semiconductor Heterostructures with Unique Electrical Properties, *ACS Nano* 5 (2011) 2224.
- [33] M.K. So, C.J. Xu, A.M. Loening, S.S. Gambhir, J.H. Rao, Self-Illuminating Quantum Dot Conjugates for In Vivo Imaging, *Nat. Biotechnol.* 24 (2006) 339.
- [34] I.L. Medintz, M.H. Stewart, S.A. Trammell, K. Susumu, J.B. Delehanty, B.C. Mei, J.S. Melinger, J.B. Blanco-Canosa, P.E. Dawson, H. Mattossi, Quantum-Dot/Dopamine Bioconjugates Function as Redox Coupled Assemblies for In Vitro and Intracellular pH Sensing, *Nat. Mater.* 9 (2010) 676.
- [35] N. Goswami, A. Giri, S. Kar, M.S. Bootharaju, R. John, P.L. Xavier, T. Pradeep, S.K. Pal, Protein-Directed Synthesis of NIR-Emitting, Tunable HgS Quantum Dots and their Applications in Metal-Ion Sensing, *Small* 8 (2012) 3175.
- [36] Q.H. Wang, K. Kalantar-Zadeh, A. Kis, J.N. Coleman, M.S. Strano, Electronics and Optoelectronics of Two-Dimensional Transition Metal Dichalcogenides, *Nat. Nanotechnol.* 7 (2012) 699.
- [37] Q. Xiang, J. Yu, M. Jaroniec, Synergetic Effect of MoS₂ and Graphene as Cocatalysts for Enhanced Photocatalytic H₂ Production Activity of TiO₂ Nanoparticles, *J. Am. Chem. Soc.* 134 (2012) 6575.
- [38] W. Ho, J.C. Yu, J. Lin, J. Yu, P. Li, Preparation and Photocatalytic Behavior of MoS₂ and WS₂ Nanocluster Sensitized TiO₂, *Langmuir* 20 (2004) 5865.
- [39] B. Radisavljevic, A. Radenovic, J. Brivio, V. Giacometti, A. Kis, Single-Layer MoS₂ Transistors, *Nat. Nanotechnol.* 6 (2011) 147.
- [40] X. Michalet, F.F. Pinaud, L.A. Bentolila, J.M. Tsay, S. Doose, J.J. Li, G. Sundaresan, A.M. Wu, S.S. Gambhir, W. S., Quantum Dots for Live Cells, in Vivo Imaging, and Diagnostics *Science* 307 (2005) 538.
- [41] P.L. Xavier, K. Chaudhari, A. Baksi, T. Pradeep, Protein-Protected Luminescent Noble Metal Quantum Clusters: An Emerging Trend in Atomic Cluster Nanoscience, *Nano Rev.* 3 (2012) 14767.
- [42] T. Udayabhaskararao, T. Pradeep, New Protocols for the Synthesis of Stable Ag and Au Nanocluster Molecules, *J. Phys. Chem. Lett.* 4 (2013) 1553.

- [43] N. Goswami, R. Saha, S. Pal, Protein-Assisted Synthesis Route of Metal Nanoparticles: Exploration of Key Chemistry of the Biomolecule, *J. Nanopart. Res.* 13 (2011) 5485.
- [44] N. Goswami, A. Giri, S.K. Pal, MoS₂ Nanocrystals Confined in a DNA Matrix Exhibiting Energy Transfer, *Langmuir* 29 (2013) 11471.
- [45] N. Goswami, A. Giri, M.S. Bootharaju, P.L. Xavier, T. Pradeep, S.K. Pal, Copper Quantum Clusters in Protein Matrix: Potential Sensor of Pb²⁺ Ion, *Anal. Chem.* 83 (2011) 9676.

Chapter 2

Overview of Spectroscopic Tools and Systems

In order to investigate the various processes involved in course of study on ultrafast spectroscopy, synthesis and potential application of the nanocrystals, the different steady-state and dynamical tools that have been used are fluorescence anisotropy, Förster Resonance Energy Transfer (FRET) theory, Dexter Energy Transfer, autocatalysis, Langmuir-Hinshelwood (L-H) mechanism, enzyme kinetics, Tachiya model and distance distribution in donor-acceptor systems. In this chapter, a brief discussion about these tools has been provided. A brief overview of the various systems used has also been provided.

2.1. Steady-State and Dynamical Tools

2.1.1. Fluorescence Anisotropy: Anisotropy is defined as the extent of polarization of the emission from a fluorophore. Anisotropy measurements are commonly used in biochemical applications of fluorescence. It provides information about the size and shape of proteins or the rigidity of various molecular environments. Anisotropy measurements have also been used to measure protein-protein associations, fluidity of membranes and for immunoassays of numerous substances. These measurements are based on the principle of photoselective excitation of those fluorophore molecules whose absorption transition dipoles are parallel to the electric vector of polarized excitation light. In an isotropic solution, fluorophores are oriented randomly. However, upon selective excitation, partially oriented population of fluorophores with polarized fluorescence emission results. The relative angle between the absorption and emission transition dipole moments determines the maximum measured anisotropy (r_0). The fluorescence anisotropy (r) and polarization (P) are defined by,

$$r = \frac{I_{\parallel} - I_{\perp}}{I_{\parallel} + 2I_{\perp}} \quad (2.1)$$

$$P = \frac{I_{\parallel} - I_{\perp}}{I_{\parallel} + I_{\perp}}, \quad (2.2)$$

where I_{\parallel} and I_{\perp} are the fluorescence intensities of vertically and horizontally polarized emission when the fluorophore is excited with vertically polarized light. Polarization and anisotropy are interrelated as,

$$r = \frac{2P}{3-P} \quad (2.3)$$

$$\text{and} \quad P = \frac{3r}{2+r}. \quad (2.4)$$

Although polarization and anisotropy provides the same information, anisotropy is preferred since the latter is normalized by total fluorescence intensity ($I_T = I_{\parallel} + 2I_{\perp}$) and in case of multiple emissive species anisotropy is additive while polarization is not. Several phenomena, including rotational diffusion and energy transfer, can decrease the measured anisotropy to values lower than maximum theoretical values. Following a pulsed excitation the fluorescence anisotropy, $r(t)$ of a sphere is given by,

$$r(t) = r_0 \exp(-t/\phi) \quad (2.5)$$

where r_0 is the anisotropy at time $t = 0$ and ϕ is the rotational correlation time of the sphere.

(i) Theory: For a radiating dipole, the intensity of light emitted is proportional to the square of the projection of the electric field of the radiating dipole onto the transmission axis of the polarizer. The intensity of parallel and perpendicular projections are given by,

$$I_{\parallel}(\theta, \psi) = \cos^2 \theta \quad (2.6)$$

$$I_{\perp}(\theta, \psi) = \sin^2 \theta \sin^2 \psi \quad (2.7)$$

where θ and ψ are the orientational angles of a single fluorophore relative to the z and y-axis, respectively (Figure 2.1a). In solution, fluorophores remain in random distribution and the anisotropy is calculated by excitation photoselection. Upon photoexcitation by polarized light, the molecules having absorption transition moments aligned parallel to the electric vector of the polarized light have the highest probability of absorption. For the excitation polarization along z-axis, all molecules having an angle ψ with respect to the y-axis will be excited. The population will be symmetrically distributed about the z-axis. For experimentally accessible molecules, the value of ψ will be in the range from 0 to 2π with equal probability. Thus, the ψ dependency can be eliminated.

$$\langle \sin^2 \psi \rangle = \frac{\int_0^{2\pi} \sin^2 \psi d\psi}{\int_0^{2\pi} d\psi} = \frac{1}{2} \quad (2.8)$$

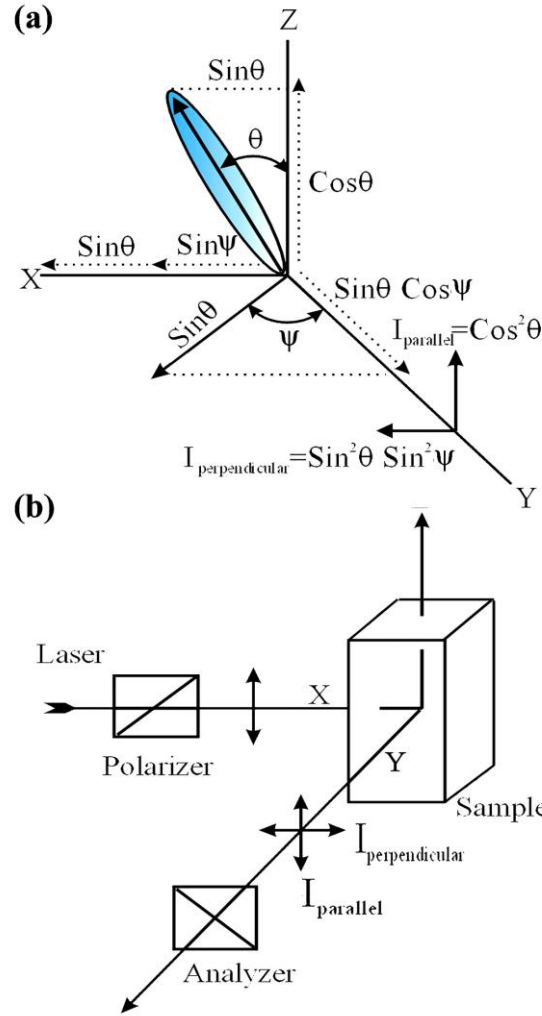


Figure 2.1. (a) Emission intensity of a single fluorophore (blue ellipsoid) in a coordinate system.
(b) Schematic representation of the measurement of fluorescence anisotropy.

$$\text{and } I_{\parallel}(\theta) = \cos^2 \theta \quad (2.9)$$

$$I_{\perp}(\theta) = \frac{1}{2} \sin^2 \theta \quad (2.10)$$

Consider a collection of molecules oriented relative to the z-axis with probability $f(\theta)$. Then, measured fluorescence intensities for this collection after photoexcitation are,

$$I_{\text{II}} = \int_0^{\pi/2} f(\theta) \cos^2 \theta d\theta = k \langle \cos^2 \theta \rangle \quad (2.11)$$

$$I_{\perp} = \int_0^{\pi/2} f(\theta) \sin^2 \theta d\theta = \frac{k}{2} \langle \sin^2 \theta \rangle \quad (2.12)$$

where $f(\theta)d\theta$ is the probability that a fluorophore is oriented between θ and $\theta+d\theta$ and is given by,

$$f(\theta)d\theta = \cos^2 \theta \sin \theta d\theta \quad (2.13)$$

k is the instrumental constant. Thus, the anisotropy (r) is defined as,

$$r = \frac{3\langle \cos^2 \theta \rangle - 1}{2} \quad (2.14)$$

when $\theta = 54.7^\circ$ i.e. when $\cos^2 \theta = 1/3$, the complete loss of anisotropy occurs. Thus, the fluorescence taken at $\theta = 54.7^\circ$ with respect to the excitation polarization is expected to be free from the effect of anisotropy and is known as magic angle emission. For collinear absorption and emission dipoles, the value of $\langle \cos^2 \theta \rangle$ is given by the following equation,

$$\langle \cos^2 \theta \rangle = \frac{\int_0^{\pi/2} \cos^2 \theta f(\theta) d\theta}{\int_0^{\pi/2} f(\theta) d\theta} \quad (2.15)$$

Substituting equation (2.13) in equation (2.15) one can get the value of $\langle \cos^2 \theta \rangle = 3/5$ and anisotropy value to be 0.4 (from equation (2.14)). This is the maximum value of anisotropy obtained when the absorption and emission dipoles are collinear and when no other depolarization process takes place. However, for most fluorophore, the value of anisotropy is less than 0.4 and it is dependent on the excitation wavelength. It is demonstrated that as the displacement of the absorption and emission dipole occurs by an angle γ relative to each other, it causes further loss of anisotropy (reduction by a factor $2/5$) [1] from the value obtained from equation (2.14). Thus, the value of fundamental anisotropy, r_0 is given by,

$$r_0 = \frac{2}{5} \left(\frac{3 \cos^2 \gamma - 1}{2} \right) \quad (2.16)$$

For any fluorophore randomly distributed in solution, with one-photon excitation, the value of r_0 varies from -0.2 to 0.4 for γ values varying from 90° to 0° .

(ii) Experimental Methods: For time-resolved anisotropy ($r(t)$) measurements (Figure 2.1b), emission polarization is adjusted to be parallel and perpendicular to that of the excitation polarization. Spencer and Weber [2] have derived the relevant equations for the time dependence of $I_{\parallel}(t)$ (equation (2.17)) and $I_{\perp}(t)$ (equation (2.18)) for single rotational and fluorescence relaxation times, ϕ and τ_f , respectively,

$$I_{\parallel}(t) = \exp(-t/\tau_f)(1 + 2r_0 \exp(-t/\phi)) \quad (2.17)$$

$$I_{\perp}(t) = \exp(-t/\tau_f)(1 - r_0 \exp(-t/\phi)) \quad (2.18)$$

The total fluorescence is given by,

$$F(t) = I_{\parallel}(t) + 2I_{\perp}(t) = 3\exp(-t/\tau_f) = F_0 \exp(-t/\tau_f) \quad (2.19)$$

The time dependent anisotropy, $r(t)$ is given by,

$$r(t) = \frac{I_{\parallel}(t) - I_{\perp}(t)}{I_{\parallel}(t) + 2I_{\perp}(t)} = r_0 \exp(-t/\phi) \quad (2.20)$$

$F(t)$ depends upon τ_f and $r(t)$ only upon ϕ so that these two lifetimes can be separated. This separation is not possible in steady state measurements. It should be noted that the degree of polarization (P) is not independent of τ_f and is therefore not as useful a quantity as r . For reliable measurement of $r(t)$, three limiting cases can be considered.

- (a) If $\tau_f < \phi$, the fluorescence decays before the anisotropy decays, and hence only r_0 can be measured.
- (b) If $\phi < \tau_f$, in contrast to steady-state measurements, ϕ can be measured in principle. The equations (2.17) and (2.18) show that the decay of the parallel and perpendicular components depends only upon ϕ . The only experimental disadvantage of this case is that those photons emitted after the period of a few times ϕ can not contribute to the determination of ϕ , but provided the signal-to-noise ratio is favorable, this need not be of great concern.
- (c) If $\phi \approx \tau_f$, then it becomes the ideal situation since almost all photons are counted within the time (equal to several rotational relaxation times) in which $r(t)$ shows measurable changes.

For systems with multiple rotational correlation times, $r(t)$ is given by,

$$r(t) = r_0 \sum_i \beta_i e^{-t/\phi_i} \quad (2.21)$$

where, $\sum_i \beta_i = 1$. It should be noted that the instrument monitoring the fluorescence, particularly the spectral dispersion element, responds differently to different polarizations of light, thus emerging the need for a correction factor. For example, the use of diffraction gratings can yield intensities of emission, which depend strongly upon orientation with respect to the plane of the grating. It is inevitably necessary when using such instruments to correct for the anisotropy in response. This instrumental anisotropy is usually termed as G-factor (grating factor) and is defined as the ratio of the transmission efficiency for vertically polarized light to that for horizontally polarized light ($G = I_{\parallel}/I_{\perp}$). Hence, values of fluorescence anisotropy, $r(t)$ corrected for instrumental response, would be given by [3],

$$r(t) = \frac{I_{\parallel}(t) - GI_{\perp}(t)}{I_{\parallel}(t) + 2GI_{\perp}(t)} \quad (2.22)$$

The G-factor at a given wavelength can be determined by exciting the sample with horizontally polarized excitation beam and collecting the two polarized fluorescence decays, one parallel and other perpendicular to the horizontally polarized excitation beam. G-factor can also be determined following longtime tail matching technique [3]. If $\phi < \tau_f$, it can be seen that the curves for $I_{\parallel}(t)$ and $I_{\perp}(t)$ should become identical. If in any experiment they are not, it can usually be assumed that this is due to a non-unitary G-factor. Hence normalizing the two decay curves on the tail of the decay eliminates the G-factor in the anisotropy measurement.

2.1.2. Förster Resonance Energy Transfer (FRET): Förster Resonance Energy Transfer [4] is an electrodynamic phenomenon involving the non-radiative transfer of the excited state energy from the donor dipole (D) to an acceptor dipole (A) (Figure 2.2a). FRET has got wide uses in all fluorescence applications including medical diagnostics, DNA analysis and optical imaging. Since FRET can measure the size of a protein molecule or the thickness of a membrane, it is also known as “spectroscopic ruler” [5]. FRET is very often used to measure the distance between two sites on a macromolecule. Basically, FRET is of two types: (a) Homo-molecular FRET and (b) Hetero-molecular

FRET. In the former case the same fluorophore acts both as energy donor and acceptor, while in the latter case two different molecules act as donor and acceptor.

Each donor-acceptor (D-A) pair participating in FRET is characterized by a distance known as Förster distance (R_0) i.e., the D-A separation at which energy transfer is 50% efficient. The R_0 value ranges from 20 to 60 Å. The rate of resonance energy transfer (k_T) from donor to an acceptor is given by [1],

$$k_T = \frac{1}{\tau_D} \left(\frac{R_0}{r} \right)^6 \quad (2.23)$$

where τ_D is the lifetime of the donor in the absence of acceptor, R_0 is the Förster distance and r is the donor to acceptor (D-A) distance. The rate of transfer of donor energy depends upon the extent of overlap of the emission spectrum of the donor with the absorption spectrum of the acceptor ($J(\lambda)$), the quantum yield of the donor (Q_D), the relative orientation of the donor and acceptor transition dipoles (κ^2) and the distance between the donor and acceptor molecules (r) (Figure 2.2b). In order to estimate FRET efficiency of the donor and hence to determine distances of donor-acceptor pairs, the methodology described below is followed [1]. The Förster distance (R_0) is given by,

$$R_0 = 0.211 [\kappa^2 n^{-4} Q_D J(\lambda)]^{1/6} \text{ (in } \text{\AA}) \quad (2.24)$$

where n is the refractive index of the medium, Q_D is the quantum yield of the donor and $J(\lambda)$ is the overlap integral. κ^2 is defined as,

$$\kappa^2 = (\cos\theta_T - 3\cos\theta_D \cos\theta_A)^2 = (\sin\theta_D \sin\theta_A \cos\varphi - 2\cos\theta_D \cos\theta_A)^2 \quad (2.25)$$

where θ_T is the angle between the emission transition dipole of the donor and the absorption transition dipole of the acceptor, θ_D and θ_A are the angles between these dipoles and the vector joining the donor and acceptor and φ is angle between the planes of the donor and acceptor (Figure 2.2b). κ^2 value can vary from 0 to 4. For collinear and parallel transition dipoles, $\kappa^2 = 4$; for parallel dipoles, $\kappa^2 = 1$; and for perpendicularly oriented dipoles, $\kappa^2 = 0$. For donor and acceptors that randomize by rotational diffusion prior to energy transfer, the magnitude of κ^2 is assumed to be $2/3$. $J(\lambda)$, the overlap integral, which expresses the degree of spectral overlap between the donor emission and the acceptor absorption, is given by,

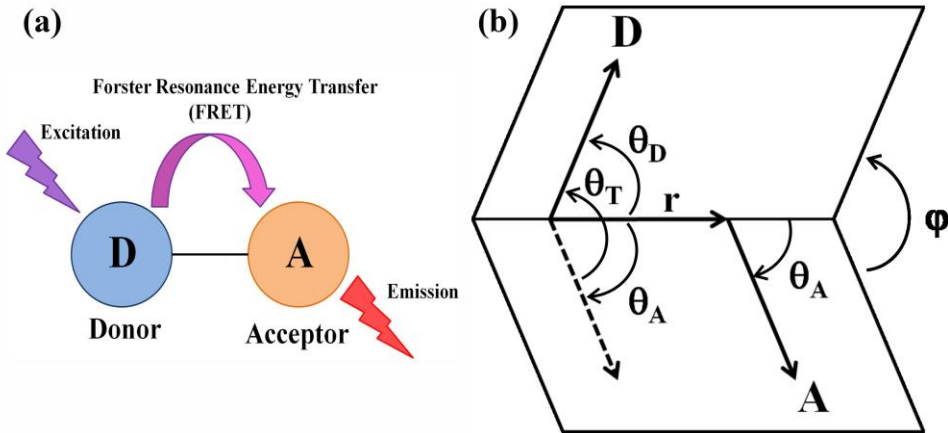


Figure 2.2. (a) Schematic illustration of the Förster Resonance Energy Transfer (FRET) process. (b) Dependence of the orientation factor κ^2 on the directions of the emission and absorption dipoles of the donor and acceptor, respectively.

$$J(\lambda) = \frac{\int_0^{\infty} F_D(\lambda) \varepsilon_A(\lambda) \lambda^4 d\lambda}{\int_0^{\infty} F_D(\lambda) d\lambda} \quad (2.26)$$

where $F_D(\lambda)$ is the fluorescence intensity of the donor in the wavelength range of λ to $\lambda+d\lambda$ and is dimensionless. $\varepsilon_A(\lambda)$ is the extinction coefficient (in $M^{-1}cm^{-1}$) of the acceptor at λ . If λ is in nm, then $J(\lambda)$ is in units of $M^{-1}cm^{-1}nm^4$.

Once the value of R_0 is known, the efficiency of energy transfer can be calculated. The efficiency of energy transfer (E) is the fraction of photons absorbed by the donor which are transferred to the acceptor and is defined as,

$$E = \frac{k_T(r)}{\tau_D^{-1} + k_T(r)} \quad (2.27)$$

$$\text{or} \quad E = \frac{R_0^6}{r^6 + R_0^6} \quad (2.28)$$

The transfer efficiency is measured using the relative fluorescence intensity of the donor, in absence (F_D) and presence (F_{DA}) of the acceptor as,

$$E = 1 - \frac{F_{DA}}{F_D} \quad (2.29a)$$

For D-A systems decaying with multiexponential lifetimes, E is calculated from the amplitude weighted lifetimes $\langle \tau \rangle = \sum_i \alpha_i \tau_i$ [1] of the donor in absence (τ_D) and presence (τ_{DA}) of the acceptor as,

$$E = 1 - \frac{\tau_{DA}}{\tau_D} \quad (2.29b)$$

The D-A distances can be measured using equations (2.28), (2.29a) and (2.29b). The distances measured using equations (2.29a) and (2.29b) are revealed as R^S (steady state measurement) and R^{TR} (time-resolved measurement), respectively. In one of recent studies from our group [6], we have reported the potential danger of using equation (2.29a) to conclude the nature of energy transfer as Förster type. The study shows that the energy transfer efficiency E, calculated from steady state experiment (equation 2.29a) might be due to re-absorption of donor emission, but not due to dipole-dipole interaction (FRET).

2.1.3. Dexter Energy Transfer: Unlike Förster, David L. Dexter provided another mechanism, say Dexter Energy Transfer that an excited donor group and an acceptor group might indeed exchange electrons to accomplish the non-radiative process [7]. Dexter transfer is identical to the Förster mechanism but does not require significant oscillator strength on the part of the acceptor. It requires direct donor–acceptor orbital overlap; and has an exponential-distance dependence with a range of ~ 1 nm. Hence, the exchange mechanism is also called the short-range energy transfer. The Dexter exchange energy transfer is generally associated with quenching. The term “quenching” means any physical process or molecular state that decreases the molecular fluorescence. Previously, the Dexter energy transfer was treated a fundamental phenomenon in photochemistry field. Recently, it is greatly applied to novel emitting materials, such as white organic light-emitting diodes and energy up-conversion systems (blue light emission; white light emission) and many others.

The energy transfer could take place via the interaction between an excited state donor, say D^* , and a ground-state acceptor, say A, without emitting a photon when transferring energy (Figure 2.3a & b).

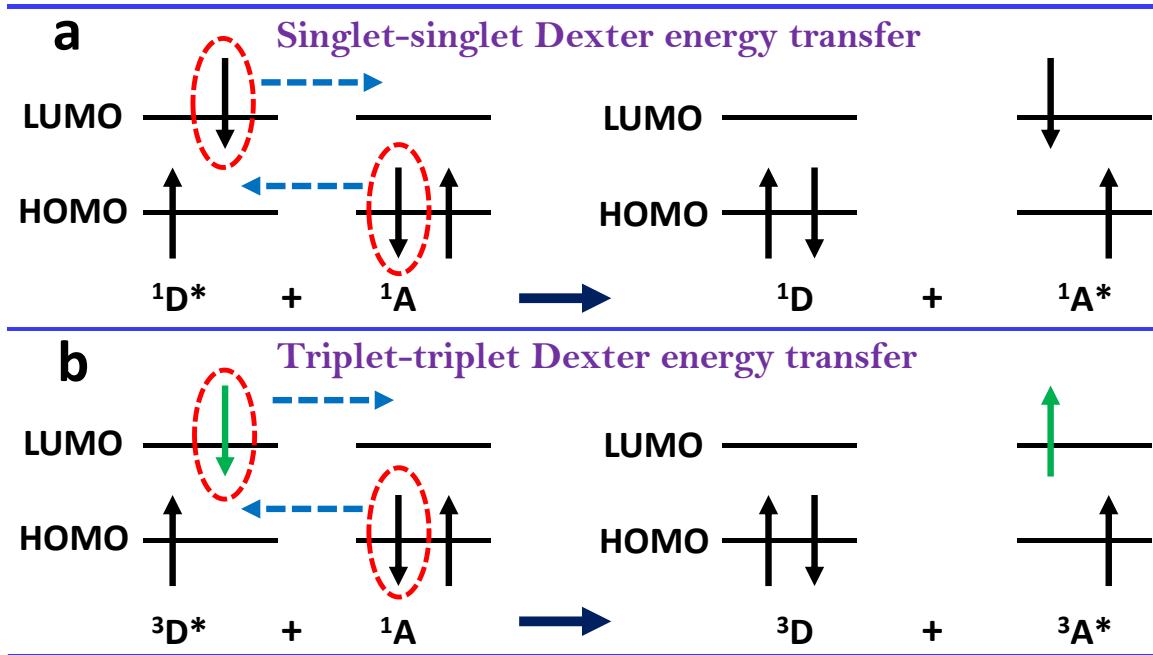


Figure 2.3. Schematic illustration of the (a) singlet-singlet and (b) triplet-triplet Dexter energy transfer process.

The exchange mechanism is based on the Wigner spin conservation rule [8]; thus, the spin-allow process could be:

Singlet-singlet energy transfer:



It could be understood by: a singlet group produces another singlet group.

Triplet-triplet energy transfer:



It could be understood by: a triplet group produces another triplet group.

The singlet-singlet energy transfer can happen when undergoing the Coulombic interaction. However, the Coulombic interaction will not involve the triplet-triplet energy transfer because that violates the Wigner spin conservation law [8]. In one of our studies [9], we have also estimated the rate of energy transfer (k_{ET}) and energy transfer efficiency (E) by using the following equations:

$$k_{\text{ET}} = 1/\tau_q - 1/\tau_u \quad (2.32)$$

$$E = 1 - \tau_q/\tau_u \quad (2.33)$$

where, τ_q is the “quenched” lifetime; and τ_u is the “unquenched” lifetime.

The Dexter energy transfer is a fundamental phenomenon in photochemistry. The difference between Förster and Dexter mechanism include (I) Dexter mechanism involves the overlap of wave functions so that electrons can occupy the other's molecular orbitals. (II) The reaction rate constant of Dexter energy transfer sharply decreases while the distance between D and A increase and the distance is generally smaller than 1 nm. (III) The Dexter mechanism can be applied to produce the triplet state of some molecules of interest. (IV) The special case of exchange-triplet-triplet annihilation-can “push” the electron to upper singlet states by exchanging the electrons of two triplet molecules.

2.1.4. Autocatalysis: A single chemical reaction is said to have undergone autocatalysis, or be autocatalytic, if the reaction product is itself the catalyst for that reaction. The rate equations for autocatalytic reactions are fundamentally nonlinear. This nonlinearity can lead to the spontaneous generation of order. For example, the reaction between potassium permanganate and oxalic acid [10]. When a few crystals of MnSO₄ are added to a mixture of permanganate and oxalic acid, the conversion to Mn(II) is sped up. If no MnSO₄ is added, then the reaction will gradually speed up of itself, because Mn(II) is gradually being created by the reaction, and this product autocatalyses the reaction itself. Autocatalysis in chemistry is usually considered to occur among relatively simple, fixed, and inflexible reactants. As such, it is commonly regarded as a subclass of general mechanisms.

Let us consider the following second order autocatalytic reaction catalysed by the product B:



The rate law for the autocatalytic reaction is defined as [11]:

$$v = \frac{d[B]}{dt} = k[A][B] \quad (2.35)$$

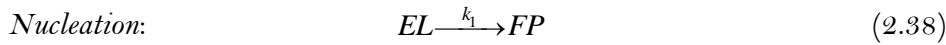
The concentrations of A and B vary in time according to the following equations [11]:

$$[A] = \frac{[A]_0 + [B]_0}{1 + \frac{[B]_0}{[A]_0} e^{([A]_0 + [B]_0)kt}} \quad (2.36)$$

$$\& \quad [B] = \frac{[A]_0 + [B]_0}{1 + \frac{[A]_0}{[B]_0} e^{([A]_0 + [B]_0)kt}} \quad (2.37)$$

The graph for these equations is a sigmoid curve, which is typical for autocatalytic reactions. These chemical reactions proceed slowly at the start because there is little catalyst present, the rate of reaction increases progressively as the reaction proceeds as the amount of catalyst increases and then it again slows down as the reactant concentration decreases. If the concentration of a reactant or product in an experiment follows a sigmoid curve, the reaction is likely to be autocatalytic.

In one of our studies, the modified protein-salt conjugate serves as a substrate in reactions. The general mechanism of the nanoparticle formation can be written as shown in the following equations:



where, L represents the salt i.e., AuCl_4^- , and E and F represent two different forms of protein where F-form is more perturbed than E-form, and k_1 and k_2 are the rate constants of the slow and fast step respectively. Here, EL denotes the protein-salt conjugate and FP denotes the protein nanoparticle conjugate. The corresponding rate equation (assuming first order reaction) of the first step can be written as,

$$[\text{FP}] = [\text{EL}]_0 (1 - \exp^{-k_1 t}) \quad (2.40)$$

where, $[\text{EL}]_0$ and $[\text{FP}]$ are the concentration of the E-form of the protein-salt conjugate at the initial time and the concentration of the protein nanoparticle conjugate at time = t respectively.

Equation 2.39 is the autocatalytic step [12]. For this autocatalytic reaction the concentration of the product can be written as,

$$[\text{FP}] = \frac{[\text{EL}]_0 + [\text{FP}]_0}{1 + \frac{[\text{EL}]_0}{[\text{FP}]_0} \exp^{-([EL]_0 + [FP]_0)k_2 t}} \quad (2.41)$$

So, the total concentration of the protein capped nanoparticles is obtained by the linear combination of equation (2.40) and equation (2.41) and thus it can be written as,

$$[\text{FP}] = m \times \left(\frac{[\text{EL}]_0 + [\text{FP}]_0}{1 + \frac{[\text{EL}]_0}{[\text{FP}]_0} \exp^{-([EL]_0 + [FP]_0)k_2 t}} \right) + n \times ([\text{EL}]_0 \times (1 - \exp^{-k_1 t})) \quad (2.42)$$

where, m and n denotes the contributions of the fast and slow step respectively.

2.1.5. Langmuir-Hinshelwood Mechanism: The term Langmuir-Hinshelwood (L-H) kinetics generally refers to heterogeneous catalytic reaction kinetics that can be described by a simple mechanistic model. In L-H model, both the reacting species are chemisorbed on the catalyst surface before the reaction takes place. The mechanism is described pictorially below:

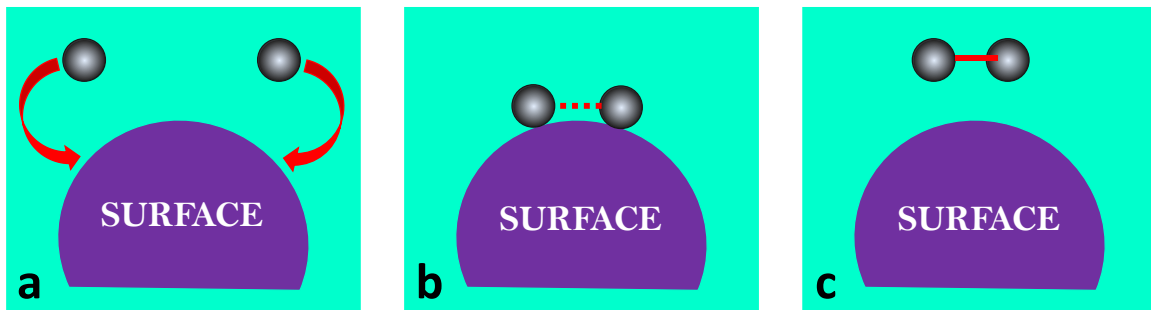


Figure 2.4. Schematic illustration of the L-H mechanism. (a) Two atoms adsorb onto the surface. (b) They diffuse across the surface and interact when they are close. (c) A molecule is formed which desorbs.

As the adsorbed molecules undergo a bimolecular reaction, we therefore expect the rate law to be second order in the extent of surface coverage (θ):



where, 'k' is the Langmuir–Hinshelwood rate constant, 'S' is the surface, and 'v' is the rate of reaction.

In this mechanism the adsorption of the reactants is modelled in terms of the Langmuir–Freundlich (L-F) isotherm [13]:

$$\theta_i = \frac{(k_i c_i)^{n_i}}{1 + \sum_{j=1}^N (k_j c_j)^{n_j}} \quad (2.44)$$

Here, ' θ_i ' is the surface coverage of compound i, ' k_i ' is the adsorption constant of the respective component, and ' c_i ' is the concentration in solution. The exponent n is related to the heterogeneity of the sorbent. For a homogeneous material, 'n' is equal to 1 whereas when 'n' is between 0 and 1 the material is heterogeneous. For homogeneous material ($n = 1$), the L-F isotherm reduces to the Langmuir isotherm.

Now, if in the above reaction both A and B follow Langmuir isotherms, and adsorb without dissociation, so that,

$$\theta_A = \frac{K_A C_A}{1 + K_A C_A + K_B C_B} \quad (2.45)$$

$$\& \quad \theta_B = \frac{K_B C_B}{1 + K_A C_A + K_B C_B} \quad (2.46)$$

Therefore the rate law can be written as,

$$v = \frac{k C_s^2 K_A K_B C_A C_B}{(1 + K_A C_A + K_B C_B)^2} \quad (2.47)$$

The rate law is complex and there is no clear order with respect to any of the reactants but we can consider different values of the constants, for which it is easy to measure integer orders:

- Both molecules have low adsorption

That means that $1 \gg K_A C_A, K_B C_B$ so, $v = k C_s^2 K_A K_B C_A C_B$

The order is one with respect to both the reactants.

- One molecule has very low adsorption

In this case, $K_A C_A, 1 \gg K_B C_B$ so, $v = k C_s^2 \frac{K_A K_B C_A C_B}{(1 + K_A C_A)^2}$

The reaction order is 1 respect to B. There are two extreme possibilities now:

1. At low concentrations of A, $v = k C_s^2 K_A K_B C_A C_B$; and the order is one respect to A.
2. At high concentrations of A, $v = k C_s^2 \frac{K_B C_B}{K_A C_A}$

The order is minus one respect to A. The higher the concentration of A, the slower the reaction goes, in this case we say that A inhibits the reaction.

- One molecule has very high adsorption

In this case, $K_A C_A, \gg 1, K_B C_B$ so, $v = k C_s^2 \frac{K_B C_B}{K_A C_A}$

The reaction order is 1 with respect to B and -1 with respect to A. Reactant A inhibits the reaction at all concentrations.

2.1.6. Tachiya Model: The excited state decay of the donor may be described by the following kinetic model assuming a competition of the energy transfer with unimolecular decay processes [14, 15]:



where P_n^* stands for excited state of the donor with n number of adjacent acceptor molecules, while P_n stands for ground state donor molecules. k_0 is the total decay constant of donor in excited state in absence of the acceptor molecules. k_q is the rate constant for energy transfer for one donor molecule. In this model, it is assumed that the distribution of the number of acceptor molecules in proximity with one donor follows a Poisson distribution [15], namely:

$$p(n) = (m^n / n!) \exp(-m) \quad (2.50)$$

where m is the mean number of acceptor molecules in close proximity to one donor molecule and

$$m = k_+ [A] / k_- \quad (2.51)$$

where k_+ is the rate constant for attachment of a acceptor to a donor molecule, while k_- is the rate constant for detachment of a acceptor from the donor. $[A]$ stands for the concentration of acceptor molecules in the aqueous phase. Based upon the above model, the equation for the total concentration $P^*(t)$ of excited state donor at time t is given by [15]:

$$P^*(t) = P^*(0) \exp\left[-(k_0 + \frac{k_0 k_+ [A]}{k_- + k_q}) t - \frac{k_q^2 k_+ [A]}{k_- (k_- + k_q)^2} \{1 - \exp[-(k_- + k_q)t]\}\right] \quad (2.52)$$

If ' k_- ' is much smaller than k_q , equation (2.52) reduces to:

$$P^*(t) = P^*(0) \exp\{-k_0 t - m \{1 - \exp(-k_q t)\}\} \quad (2.53)$$

In one of our study, we have used the Tachiya kinetic model where H258-DNA and MoS₂ nanocrystals have been used as donor and acceptor respectively. In our system, along with the acceptor MoS₂ NCs, there exist some unidentified traps that further cause quenching of the lifetime of excited probe, are also taken into account. If the distribution of the number of unidentified traps around the donor H258 follows a Poisson distribution with the average number (m), the decay curves of the excited state of H258 in the DNA in absence and presence of MoS₂ NCs are described by [16]:

$$P^*(t,0) = P^*(0) \exp\{-k_0 t - m_t \{1 - \exp(-k_{q_t} t)\}\} \quad (2.54)$$

$$\& \quad P^*(t,m) = P^*(0) \exp\{-k_0 t - m_t \{1 - \exp(-k_{q_t} t)\} - m \{1 - \exp(-k_q t)\}\} \quad (2.55)$$

where the quenching rate constant (k_{qt}) by unidentified traps may be different from that (k_q) by acceptor ($\text{MoS}_2@\text{DNA}$). We have determined the values of the parameters m_t , k_{qt} , k_0 , m , and k_q by fitting equation (2.54) and (2.55) to the decay curves in the absence and presence of acceptor.

2.1.7. Distance Distribution in Donor-Acceptor Systems: Distance distribution between donor and acceptor can be estimated according to the procedure described in the literature [1]. The fitting of the observed fluorescence transients of the donor molecules in absence of acceptor is implemented by using a nonlinear least-squares fitting procedure (software SCIENTIST) to the following function,

$$I_D(t) = \int_0^t E(t') P(t' - t) dt' \quad (2.56)$$

which comprises the convolution of the instrument response function (IRF) ($E(t)$) with exponential ($P(t) = \sum_i \alpha_{Di} \exp(-t/\tau_{Di})$). The convolution of the distance distribution function $P(r)$ in the fluorescence transients of donor in presence of acceptor in the system under studies is estimated using the same software (SCIENTIST) in the following way. The intensity decay of donor-acceptor pair, spaced at a distance 'r', is given by,

$$I_{DA}(r,t) = \sum_i \alpha_{Di} \exp\left[-\frac{t}{\tau_{Di}} - \frac{t}{\tau_{Di}} \left(\frac{R_0}{r}\right)^6\right] \quad (2.57)$$

and the intensuity decay of the sample considering $P(r)$ is given by,

$$I_{DA}(t) = \int_{r=0}^{\infty} P(r) I_{DA}(r,t) dr \quad (2.58)$$

Where $P(r)$ consist of the folowing terms:

$$P(r) = \frac{1}{\sigma \sqrt{2\pi}} \exp\left[-\frac{1}{2} \left(\frac{\bar{r}-r}{\sigma}\right)^2\right] \quad (2.59)$$

In this equation \bar{r} is the mean of the Gaussian with a standard deviation of σ . Usually distance distributions are described by the full width at half maxima. This half width is given by $hw = 2.354\sigma$.

2.2. Systems:

2.2.1. Molecular Probes:

In this section we will discuss about the different probe molecules that have been used in the course of study.

2.2.1.1. 2,5-Cyclohexadiene-1,4-Dione (*p*-Benzoquinone, BQ): BQ (Figure 2.5A) is a well-known probe for electron accepting and shuttling for any electron rich material/compound, which readily accepts electron and adapted to be resonance species hydroquinone [17]. Large doses could induce local irritation, clonic convulsions, decreased blood pressure and death due to paralysis of the medullary centres.

2.2.1.2. Crystal Violet (CV): CV has a positively charged ammonium ion and three aromatic rings (Figure 2.5G), used as a staining material. It can bind to the negatively charged phosphate backbone of DNA, negatively charged amino acids of proteins. It is highly soluble in water and other polar solvents. Its concentration is determined using extinction coefficient, $112,000 \text{ M}^{-1}\text{cm}^{-1}$ at 509 nm [18].

2.2.1.3. Ala-Ala-Phe-7-Amido-4-Methylcoumarin (AAF-AMC): Ala-Ala-Phe-7-amido-4-methylcoumarin (AAF-AMC) is a fluorescent aromatic tripeptide substrate (Figure 2.5) suitable for cleavage by serine protease. Its concentration is determined using extinction coefficient, $\epsilon = 16 \text{ mM}^{-1}\text{cm}^{-1}$ at 325 nm. The rate of catalytic activity is determined by monitoring absorbance of cleaved product (7-amido-4-methylcoumarin) having $\epsilon = 7.6 \text{ mM}^{-1}\text{cm}^{-1}$ at 370 nm in aqueous buffer solution [19].

2.2.1.4. N-CBZ-Gly-Gly-Leu *p*-Nitroanilide (CBZ-GGL-pNA): Catalytic activity measurements of SC has been made using the chromogenic synthetic substrates CBZ-GGL-pNA (Figure 2.5B) as per the conventional procedure. Its concentration in buffer pH = 7.0, is determined using extinction coefficient, $\epsilon = 14 \text{ mM}^{-1}\text{cm}^{-1}$ at 315 nm. The rate of catalytic activity is determined by monitoring absorbance of cleaved product having $\epsilon = 8.8 \text{ mM}^{-1}\text{cm}^{-1}$ at 410 nm in aqueous buffer solution [20].

2.2.1.5. 2'-(4-Hydroxyphenyl)-5-[5-(4-Methylpiperazine-1-yl)-Benzimidazo-2-yl-Benzimidazole, Hoechst 33258 (H258): The commercially available probe H258 (Figure 2.5E) is widely used as fluorescent cytological stain of DNA. Since it has affinity for the double stranded DNA, H258 can affect transcription/translation, and block topomerase/helicase activities. The dye is also used as a potential antihelminthic drug. X-

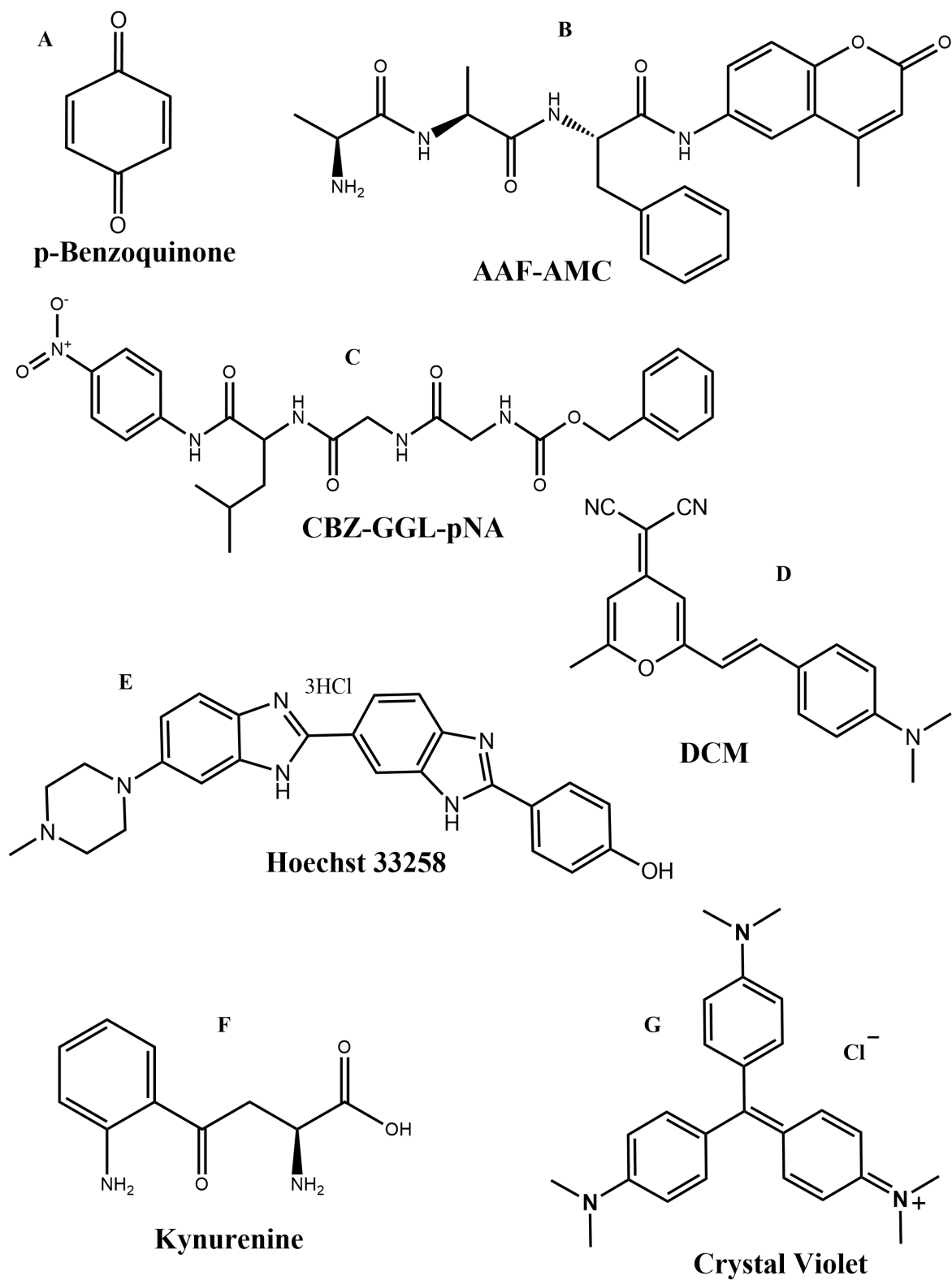


Figure 2.5. Molecular structures of the probes: Benzoquinone, AAF-AMC, CBZ-GGL-pNA, DCM, Hoechst 33258, Kynurenone, and Crystal violet.

ray crystallographic and NMR studies of the dye bound to a dodecamer DNA shows that the dye is bound to A-T rich sequence of the DNA minor groove. The binding constant of the dye [21] to double stranded DNA at low [dye]:[DNA] ratio is found to be 5×10^5 M⁻¹. The solvchromic properties of the dye can be used to report the hydration dynamics [22] as well as the dynamics of restricted systems [23].

2.2.1.6. Kynurenine (KN): It is one of the tryptophan metabolites (Figure 2.5F) and omnipresent in the lens of human eyes in order to protect retina from possible UV (300-400 nm) radiation damage [24]. KN is a central compound of tryptophan metabolism pathway since it can change to the neuroprotective agent kynurenic acid or to the neurotoxic agent quinolinic acid. It is a weak photosensitizer and redirect the absorbed light energy into benign channels. They are characterized by a low fluorescence quantum yield and short lifetime values [24]. In one of our study, we have reported an electron-transfer reaction in protein cavity which causes the tryptophan residue to undergo chemical modification to form KN [20].

2.2.1.7. 4-(Dicyanomethylene)-2-Methyl-6-(p-Dimethylamino-Styryl) 4H-Pyran (DCM): The laser dye DCM (Figure 2.5D), is completely insoluble in water, and has selective binding affinity to the micellar surface [25]. The dye is completely hydrophobic (nonpolar) in the ground state. However, UV excitation increases dipole moment of the probe making it polar and hence increases its hydrophilicity in the excited state. Thus the excited DCM diffuses from the micellar surface (relatively nonpolar) towards polar bulk water phase revealing a fluorescence emission signature (temporal line width) of the excursion through multiple environments in the excited state [26].

2.2.2. Proteins:

Four types of model proteins; Human Serum Albumin (HSA), Bovine Serum Albumin (BSA), α -Chymotrypsin (CHT) and Subtilisin *Carlsberg* (SC) have been used in our studies.

2.2.2.1. Human Serum Albumin (HSA): Serum albumins are multi-domain proteins forming the major soluble protein constituent (60% of the blood serum) of the circulatory system [27]. Human Serum Albumin (HSA) (molecular weight 66,479 Da) is a heart-shaped tridomain protein (Figure 2.6) with each domain comprising of two identical subdomains A and B with each domain depicting specific structural and functional

characteristics [28]. HSA having 585 amino acid residues assumes solid equilateral triangular shape with sides \sim 80 Å and depth \sim 30 Å [29]. Its amino acid sequence comprises of 17 disulfide bridges distributed over all domains, one free thiol (Cys34) in domain-I and a tryptophan residue (Trp214) in domain-IIA. About 67% of HSA is α -helical while the rest of the structure being turns and extended polypeptides [29]. Each domain contains 10 principle helices (h1-h10). Subdomains A and B share a common motif that includes h1, h2, h3 and h4 for subdomain-A, and h7, h8, h9, h10 for subdomain-B. The non-existence of disulfide linkage connecting h1 and h3 in subdomain-IA is an exception. HSA is engaged with various physiological functions involving maintenance of osmotic blood pressure, transportation of a wide variety of ligands in and out of the physiological system. The protein binds various kinds of ligands [30] including photosensitizing drugs [31]. The principal binding regions are located in subdomains IIA and IIIA of which IIIA binding cavity is the most active one [29] and binds digitoxin, ibuprofen and tryptophan. Warfarin, however, occupies a single site in domain-IIA. It is known that HSA undergoes reversible conformational transformation with change in pH of the protein solution [32, 33], which is very essential for picking up and releasing the drugs at sites of differing pH inside the physiological system. At normal

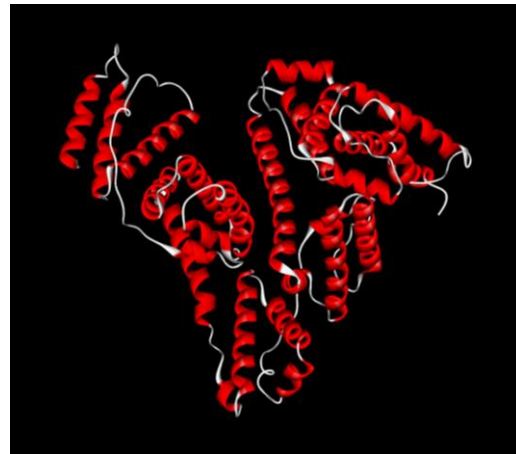


Figure 2.6. Schematic structure of Human Serum Albumin (HSA).

pH ($\text{pH} = 7$), HSA assumes the normal form (N) which abruptly changes to fast migrating form (F) at pH values less than 4.3, as this form moves “fast” upon gel electrophoresis [27]. Upon further reduction in pH to less than 2.7 the F-form changes

to the fully extended form (E). On the basic side of the normal pH (above pH = 8), the N-form changes to basic form (B) and above pH = 10, the structure changes to the aged form (A). Serum albumin undergoes an ageing process when stored at low ionic strength and alkaline pH. The ageing process is catalyzed by the free sulphydryl group and involves sulphydryl-disulfide interchange that results in the conservation of the sulphydryl at its original position.

2.2.2.2. Bovine Serum Albumin (BSA): BSA is the most abundant globular protein (~66,000 Da) in blood plasma and it serves as a vehicle for intracellular transportation [34]. It is the most studied protein, whose structure and property are not well-recognized as the crystal structure of BSA is still unknown. BSA is composed of 583 amino acid residues of which 35 are cysteine and 5 are methionine. The properties of BSA is almost similar to HSA, however differs from number of tryptophan residues. HSA contains single tryptophan residue, whereas BSA has two. It has long been used as a capping agent for making nanoparticles due to its strong affinity towards inorganic salts [35]. For example, it has been demonstrated that BSA can be used as the model protein for the synthesis and stabilization of Au nanoparticles [35, 36], Cu nanoclusters [37], Ag nanoclusters [38] and many others. Moreover, it is a low cost, commercially available protein, since large quantities of it can be readily purified from bovine blood, a byproduct of the cattle industry.

2.2.2.3. α -Chymotrypsin (CHT): α -Chymotrypsin (CHT) (Figure 2.7) isolated from bovine pancreas is a member of the family serine endopeptidase (molecular weight of 25,191 Da) [39] catalyzing the hydrolysis of proteins in the small intestine. The three dimensional structure of CHT was solved by David Blow [40]. The molecule is a three dimensional ellipsoid of dimensions 51 x 40 x 40 Å and comprises of 245 amino acid residues. CHT contains several antiparallel β -pleated sheet regions and little α -helix. All charged groups are on the surface of the molecule except the *catalytic triad* of His57, Asp102 and Ser195 which are essential for catalysis. The Ser195 residue is H-bonded to His57 residue, which in turn is H-bonded to β -carboxyl group of Asp102. An oxyanion

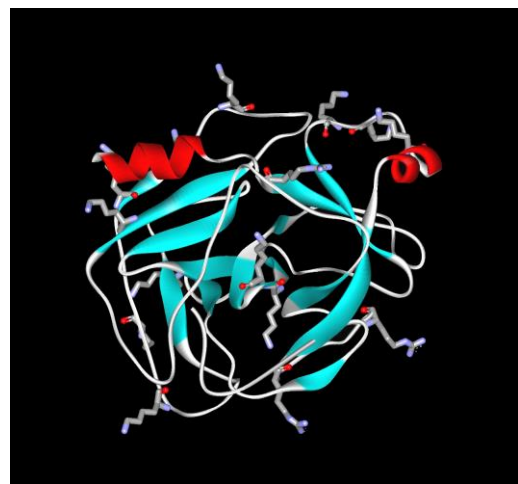


Figure 2.7. Schematic structure of α -Chymotrypsin (CHT).

hole is formed by amide nitrogens of Gly193 and Ser195. It is selective for hydrolyzing peptide bonds on the carboxyl side of the aromatic side chains of tyrosine, tryptophan, and phenylalanine and of large hydrophobic residues such as methionine. It also catalyzes the hydrolysis of ester bonds [41]. CHT enhances the rate of peptide hydrolysis by a factor of 10^9 . The reaction has two distinct phases—acylation and deacylation of the enzyme. Upon binding of the substrate, the hydroxyl group of the Ser195 attacks the carbonyl group of peptide bond, to generate a tetrahedral intermediate. In this transient structure, the oxygen atom of the substrate now occupies the oxyanion hole. The acyl-enzyme intermediate now forms, assisted by proton donation of His57. The N-terminal portion is now released and replaced by water. The acyl-enzyme intermediate subsequently undergoes hydrolysis and the enzyme is regenerated.

2.2.2.4. Subtilisin Carlsberg (SC): Subtilisin Carlsberg (SC) [EC: 3.4.21.62] extracted from *Bacillus licheniformis* having molecular weight of 27,600 Da [42] is another member of serine protease (Figure 2.8). It is also known as *Subtilisin A*, *Subtilopeptidase A* and *Alcalase Novo* and was discovered by Linderstrom-Lang and Ottensen [43] while they were studying the conversion of ovalbumin to plakalbumin. It contains a single polypeptide chain of 274 amino acid residues with two Ca^{2+} ion binding sites [44–46]. SC has 34 % α -helix content [47]. It was observed that 119 water molecules are bound to SC in aqueous solution [48].

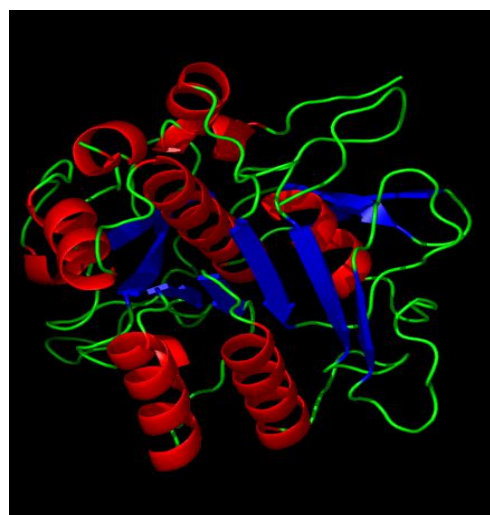


Figure 2.8. Schematic structure of *Subtilisin Carlsberg* (SC).

The amino acid sequence contains a single tryptophan (Trp113) and 13 tyrosine (Tyr) [42] with no cysteine residues. In this enzyme, Tyr fluorescence overwhelms the fluorescence of Trp which is not the case in other proteins due to energy transfer from Tyr to Trp residue. The *catalytic triad* of SC comprises of Asp32, His64 and Ser221 residues [49] and it catalyzes the hydrolysis of peptides and esters by the same acyl-enzyme mechanism as for CHT. It is important to note that *subtilisin* differs from the pancreatic enzymes by having a shallow binding groove on the surface, rather than the deep binding pocket of the pancreatic enzymes, to which it is related by convergent evolution [50]. Subtilisins are of considerable interest not only scientifically but also industrially, for they are used in such diverse applications as meat tenderizers, laundry detergents, and proteolytic medicines [51, 52]. Furthermore, their catalytic efficiency and specificity in organic media would enhance practical uses related to synthetic applications [53-56]. Subtilisins are covalently inactivated by standard serine protease inhibitors such as PMSF and DFP, and also by peptidyl-halomethanes [57, 58] and peptidyl-boronic acids [59].

2.2.3. Deoxyribonucleic Acid (DNA): Nucleic acids form the central molecules in transmission, expression and conservation of genetic information. DNA serves as carrier of genetic information [60, 61].

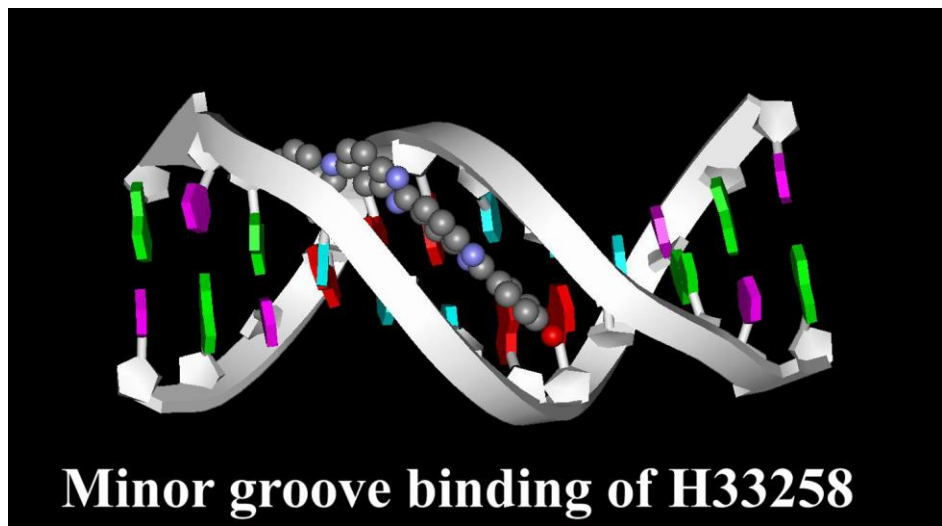


Figure 2.9. Schematic representation of minor groove binding and intercalation of H33258. The DNA structures are downloaded from the nucleic acid data bank and handled with the WEBLAB VIEWERLITE program.

The classic example of how biological function follows from biomolecular structure comes from the elucidation of double helical structure of DNA by Watson and Crick [62]. DNAs are polynucleotides with each nucleotide comprising of deoxyribose sugar, purine and pyrimidine bases and phosphate groups. The main bases whose intermolecular hydrogen bonding holds the DNA strands together are adenine, guanine, thymine and cytosine. There are generally three forms of DNA: the A, B and Z-form. Native DNA, however, exists in B-form. Native DNA is about a metre long and comprises of hundreds of base pairs. The distance between two base pairs in B-DNA is 3.4 Å [39]. In about 4 M NaCl, B-form is converted into Z-form. DNA structures consist of major and minor grooves and intercalation spaces through which DNA interacts with ligands. There are two modes of interaction of DNA with ligands: (i) intercalation, where the planar polycyclic heteroaromatic ligands occupy the space in between the base pairs of DNA and interact through $\pi-\pi$ interaction [63, 64], and (ii) groove binding where the ligands bind in the major and minor grooves of DNA (Figure 2.9) [65]. The water molecules at the surface of DNA are critical to the structure and to the recognition by other molecules, proteins and drugs. In our studies, genomic DNA from salmon sperm have been used. X-ray crystallographic studies have been reported which have confirmed the minor groove binding of Hoechst 33258 to DNA (Figure 2.9) [66]. The molecular weight of the salmon sperm DNA in the literature is reported to be 9.2×10^4 Da [67].

References

- [1] J.R. Lakowicz, Principles of Fluorescence Spectroscopy, 3rd ed., Springer, New York, 2006.
- [2] R.D. Spencer, G. Weber, Measurement of Subnanosecond Fluorescence Lifetimes with a Cross-Correlation Phase Fluorometer, *Ann. N. Y. Acad. Sci.* 158 (1969) 361.
- [3] D.V. O'Connor, D. Philips, Time-Correlated Single Photon Counting, Academic Press, London, 1984.
- [4] T. Förster, Intermolecular Energy Migration and Fluorescence. Translated by R. S. Knox, Department of Physics and Astronomy, University of Rochester, Rochester, NY 14627., *Ann. Phys.* 2 (1948) 55.
- [5] L. Stryer, Fluorescence Energy Transfer as a Spectroscopic Ruler, *Annu. Rev. Biochem.* 47 (1978) 819.
- [6] P. Majumder, R. Sarkar, A.K. Shaw, A. Chakraborty, S.K. Pal, Ultrafast Dynamics in a Nanocage of Enzymes: Solvation and Fluorescence Resonance Energy Transfer in Reverse Micelles, *J. Colloid Interf. Sci.* 290 (2005) 462.
- [7] D.L. Dexter, A Theory of Sensitized Luminescence in Solids *J. Chem. Phys.* 21 (1953) 836.
- [8] E. Wigner, The Transition State Method, *Trans. Faraday Soc.* 34 (1938) 29.
- [9] N. Goswami, A. Giri, S. Kar, M.S. Bootharaju, R. John, P.L. Xavier, T. Pradeep, S.K. Pal, Protein-Directed Synthesis of NIR-Emitting, Tunable HgS Quantum Dots and their Applications in Metal-Ion Sensing, *Small* 8 (2012) 3175.
- [10] S. Dash, S. Patel, B.K. Mishra, Oxidation by Permanganate: Synthetic and Mechanistic Aspects, *Tetrahedron* 65 (2009) 707.
- [11] P. Atkins, J. de Paula, Physical Chemistry, W. H. Freeman, 2006.
- [12] P.D. Drummond, T.G. Vaughan, A.J. Drummond, Extinction Times in Autocatalytic Systems, *J. Phys. Chem. A* 114 (2010) 10481.
- [13] R.J. Umpleby, S.C. Baxter, Y. Chen, R.N. Shah, K.D. Shimizu, Characterization of Molecularly Imprinted Polymers with the Langmuir Freundlich Isotherm, *Anal. Chem.* 73 (2001) 4584.
- [14] M. Tachiya, Application of a Generating Function to Reaction Kinetics in Micelles. Kinetics of Quenching of Luminescent Probes in Micelles, *Chem. Phys. Lett.* 33 (1975) 289.

- [15] M. Tachiya, Kinetics of Quenching of Luminescent Probes in Micellar Systems. II, *J. Chem. Phys.* 76 (1982) 340.
- [16] S. Sadhu, M. Tachiya, A. Patra, A Stochastic Model for Energy Transfer from CdS Quantum Dots/Rods (Donors) to Nile Red Dye (Acceptors), *J. Phys. Chem. C* 113 (2009) 19488.
- [17] C. Burda, T.C. Green, S. Link, M.A. El-Sayed, Electron Shuttling Across the Interface of CdSe Nanoparticles Monitored by Femtosecond Laser Spectroscopy, *J. Phys. Chem. B* 103 (1999) 1783.
- [18] H. Langhals, Color Chemistry. Synthesis, Properties and Applications of Organic Dyes and Pigments. 3rd revised edition. By Heinrich Zollinger, *Angew. Chem. Int. Ed.* 43 (2004) 5291.
- [19] J.K.A. Kamal, T. Xia, S.K. Pal, L. Zhao, A.H. Zewail, Enzyme Functionality and Solvation of Subtilisin Carlsberg: From Hours to Femtoseconds, *Chem. Phys. Lett.* 387 (2004) 209.
- [20] N. Goswami, A. Makhral, S.K. Pal, Toward an Alternative Intrinsic Probe for Spectroscopic Characterization of a Protein, *J. Phys. Chem. B* 114 (2010) 15236.
- [21] R. Jin, K.J. Breslauer, Characterization of the Minor Groove Environment in a Drug-DNA Complex: Bisbenzimide Bound to the Poly[d(AT)].Poly[d(AT)] Duplex, *Proc. Nat. Acad. Sci. USA* 85 (1988) 8939.
- [22] S.K. Pal, L.A. Zhao, A.H. Zewail, Water at DNA Surfaces: Ultrafast Dynamics in Minor Groove Recognition, *Proc. Nat. Acad. Sci. USA* 100 (2003) 8113.
- [23] D. Banerjee, S.K. Pal, Ultrafast Charge Transfer and Solvation of DNA Minor Groove Binder: Hoechst 33258 in Restricted Environments, *Chem. Phys. Lett.* 432 (2006) 257.
- [24] P.S. Sherin, J. Grilj, Y.P. Tsentalovich, E. Vauthey, Ultrafast Excited-State Dynamics of Kynurenone, a UV Filter of the Human Eye, *J. Phys. Chem. B* 113 (2009) 4953.
- [25] S.K. Pal, D. Sukul, D. Mandal, S. Sen, K. Bhattacharyya, Solvation Dynamics of DCM in Micelles, *Chem. Phys. Lett.* 327 (2000) 91.
- [26] R. Sarkar, A.K. Shaw, M. Ghosh, S.K. Pal, Ultrafast Photoinduced Deligation and Ligation Dynamics: DCM in Micelle and Micelle-Enzyme Complex, *J. Photochem. Photobiol. B: Biology* 83 (2006) 213.

- [27] J.F. Foster, Some Aspects of the Structure and Conformational Properties of Serum Albumin, Pergamon, Oxford, 1977.
- [28] M. Dockal, D.C. Carter, F. Ruker, The Three Recombinant Domains of Human Serum Albumin, *J. Biol. Chem.* 274 (1999) 29303.
- [29] X.M. He, D.C. Carter, Atomic Structure and Chemistry of Human Serum Albumin, *Nature* 358 (1992) 209.
- [30] J. Ghuman, P.A. Zunszain, I. Pettipas, A.A. Bhattacharya, M. Otagiri, S. Curry, Structural Basis of the Drug-binding Specificity of Human Serum Albumin, *J. Mol. Biol.* 353 (2005) 38.
- [31] M. Wardell, Z. Wang, J.X. Ho, J. Robert, F. Ruker, J. Ruble, D.C. Carter, The Atomic Structure of Human Methemalbumin at 1.9 Å, *Biochem. Biophys. Res. Comm.* 291 (2002) 813.
- [32] J.F. Foster, The Plasma Proteins, Academic Press, New York, 1960.
- [33] J.A. Luetscher, Serum Albumin. II. Identification of More than One Albumin in Horse and Human Serum by Electrophoretic Mobility in Acid Solution, *J. Am. Chem. Soc.* 61 (1939) 2888.
- [34] J.A. Ryan, K.W. Overton, M.E. Speight, C.N. Oldenburg, L. Loo, W. Robarge, S. Franzen, D.L. Feldheim, Cellular Uptake of Gold Nanoparticles Passivated with BSA-SV40 Large T Antigen Conjugates, *Anal. Chem.* 79 (2007) 9150.
- [35] A. Housni, M. Ahmed, S. Liu, R. Narain, Monodisperse Protein Stabilized Gold Nanoparticles via a Simple Photochemical Process, *J. Phys. Chem. C* 112 (2008) 12282.
- [36] J.P. Xie, Y.G. Zheng, J.Y. Ying, Protein-Directed Synthesis of Highly Fluorescent Gold Nanoclusters, *J. Am. Chem. Soc.* 131 (2009) 888.
- [37] N. Goswami, A. Giri, M.S. Bootharaju, P.L. Xavier, T. Pradeep, S.K. Pal, Copper Quantum Clusters in Protein Matrix: Potential Sensor of Pb²⁺ Ion, *Anal. Chem.* 83 (2011) 9676.
- [38] A. Mathew, P.R. Sajanlal, T. Pradeep, A Fifteen Atom Silver Cluster Confined in Bovine Serum Albumin, *J. Mater. Chem.* (2011) 11205.
- [39] D.L. Nelson, M.M. Cox, Lehninger Principles of Biochemistry, 3rd ed., W. H. Freeman & Co., New York, 2000.

- [40] J.J. Birktoft, D.M. Blow, The Structure of Crystalline Alpha-Chymotrypsin, V. The Atomic Structure of Tosyl-Alpha-Chymotrypsin at 2 Angstroms Resolution, *J. Mol. Biol.* 68 (1972) 187.
- [41] L. Stryer, Biochemistry, 4th ed., W. H. Freeman & Co., New York, 1995.
- [42] R.J. DeLange, E.L. Smith, Subtilisin Carlsberg I. Amino Acid Composition; Isolation and Composition of Peptides from the Tryptic Hydrolysate, *J. Biol. Chem.* 243 (1968) 2134.
- [43] K. Linderstrom-Lang, M. Ottensen, A New Protein from Ovalbumin, *Nature* 159 (1947) 807.
- [44] W. Bode, E. Papamokos, D. Musil, The High-Resolution X-ray Crystal Structure of the Complex Formed between Subtilisin Carlsberg and Eglin C, an Elastase Inhibitor from the Leech Hirudo Medicinalis, *Eur. J. Biochem.* 166 (1987) 673.
- [45] D.J. Neidhart, G.A. Petsko, The Refined Crystal Structure of Subtilisin Carlsberg at 2.5 Å Resolution, *Protein Eng.* 2 (1988) 271.
- [46] C.A. McPhalen, M.N.G. James, Structural Comparison of Two Serine Proteinase-Protein Inhibitor Complexes: Eglin-C-Subtilisin Carlsberg and CI-2-Subtilisin Nov, *Biochemistry* 27 (1988) 6582.
- [47] J.L. Schmitke, L.J. Stern, A.M. Klibanov, The Crystal Structure of Subtilisin Carlsberg in Anhydrous Dioxane and its Comparison with those in Water and Acetonitrile, *Proc. Natl. Acad. Sci. USA* 94 (1997) 4250.
- [48] P.A. Fitzpatrick, A.C.U. Steinmetz, D. Ringe, A.M. Klibanov, Enzyme Crystal Structure in a Neat Solvent, *Proc. Natl. Acad. Sci. USA* 90 (1993) 8653.
- [49] P. Castner, J.A. Wells, Dissecting the Catalytic Triad of Serine Protease, *Nature* 332 (1988) 564.
- [50] A. Fersht, Enzyme Structure and Mechanism in Protein Science: A Guide to Enzyme Catalysis and Protein Folding, Second ed., W. H. Freeman and company, New York, 1985.
- [51] N. Genov, B. Filippi, D. Dolashka, K.S. Wilson, C. Betzel, Stability of Subtilisins and Related Proteinases (Subtilases), *Int. J. Peptide Protein Res.* 45 (1995) 391.
- [52] P.A. Fitzpatrick, D. Ringe, A.M. Klibanov, X-Ray Crystal Structure of Cross-Linked Subtilisin Carlsberg in Water vs Acetonitrile, *Biochem. Biophys. Res. Commun.* 198 (1994) 675.

- [53] S. Chatterjee, A.J. Russell, Kinetic Analysis of the Mechanism for Subtilisin in Essentially Anhydrous Organic Solvents, *Enzyme Micro. Technol.* 15 (1993) 1022.
- [54] A.K. Chaudhary, S.V. Kamat, E.J. Beckman, D. Nurok, R.M. Kleyle, P. Hajdu, A.J. Russell, Control of Subtilisin Substrate Specificity by Solvent Engineering in Organic Solvents and Supercritical Fluoroform, *J. Am. Chem. Soc.* 118 (1996) 12891.
- [55] T. Kijima, S. Yamamoto, H. Kise, Fluorescence Spectroscopic Study of Subtilisins as Relevant to their Catalytic Activity in Aqueous-Organic Media, *Bull. Chem. Soc. Jpn.* 67 (1994) 2819.
- [56] J. Broos, A.J.W.G. Visser, J.F.J. Engbersen, W. Verboom, A. van Hoek, D.N. Reinhoudt, Flexibility of Enzymes Suspended in Organic Solvents Probed by Time-Resolved Fluorescence Anisotropy: Evidence that Enzyme Activity and Enantioselectivity are Directly Related to Enzyme Flexibility, *J. Am. Chem. Soc.* 117 (1995) 12657.
- [57] K. Morihara, T. Oka, Subtilisin BPN': Inactivation by Chloromethyl Ketone Derivatives of Peptide Substrates, *Arch. Biochem. Biophys.* 138 (1970) 526.
- [58] T.L. Poulos, R.A. Alden, S.T. Freer, J.J. Birktoft, J. Kraut, Polypeptide Halomethyl Ketones Bind to Serine Proteases as Analogs of Tetrahedral Intermediate, *J. Biol. Chem.* 251 (1976) 1097.
- [59] D.A. Matthews, R.A. Alden, J.J. Birktoft, S.T. Freer, J. Kraut, X-Ray Crystallographic Study of Boronic Acid Adducts with Subtilisin BPN' (Novo), *J. Biol. Chem.* 250 (1975) 7120.
- [60] A.D. Harshey, M. Chase, Independent Functions of Viral Protein and Nucleic Acid in Growth of Bacteria, *J. Gen. Physiol.* 36 (1952) 39.
- [61] O. Avery, C. Macleod, M. MacCarty, Studies on the Chemical Nature of the Substances Inducing Transformation of the Substances Inducing Transformation of Pneumococcal Types, *J. Expt. Med.* 7 (1944) 137.
- [62] J.D. Watson, F.H.C. Crick, Molecular Structure of Nucleic Acids. A Structure for Deoxyribose Nucleic Acid, *Nature* 171 (1953) 737.
- [63] L.S. Lerman, The Structure of the DNA-Acridine Complex, *Proc. Natl. Acad. Sci. USA* 49 (1963) 94.
- [64] M.B. Lyles, I.L. Cameron, Interactions of the DNA Intercalator Acridine Orange, with Itself, with Caffeine, and with Double Stranded DNA, *Biophys. Chem.* 96 (2002) 53.

- [65] P.B. Dervan, Molecular Recognition of DNA by Small Molecules, *Bioorg. Med. Chem.* 9 (2001) 2215.
- [66] P.E. Pjura, K. Grzeskowiak, R.E. Dickerson, Binding of Hoechst 33258 to the Minor Groove of B-DNA, *J. Mol. Biol.* 197 (1987) 257.
- [67] C.-J. Chang, J.D. Gomes, S.R. Byrn, Chemical Modification of Deoxyribonucleic Acids: A Direct Study by NMR Spectroscopy, *J. Am. Chem. Soc.* 103 (1981) 2892.

Chapter 3

Instrumentation and Sample Preparation

In this chapter we will describe the details of instrumental setup and sample preparation techniques used in our studies.

3.1. Instrumental Setup:

3.1.1. Steady-State Absorption and Fluorescence Spectroscopy: Steady-state UV-vis absorption and emission spectra of the probe molecules were measured with Shimadzu UV-2450 spectrophotometer and Jobin Yvon Fluoromax-3 fluorimeter, respectively. Schematic ray diagrams of these two instruments are shown in Figures 3.1 and 3.2.

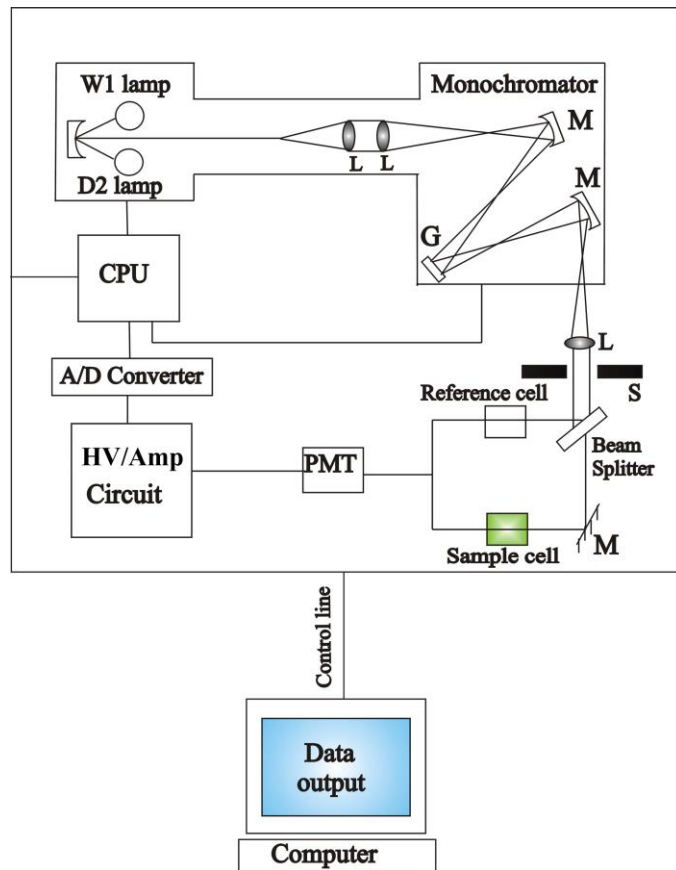


Figure 3.1. Schematic ray diagram of an absorption spectrophotometer. Tungsten halogen (W1) and Deuterium lamps (D2) are used as light sources in the visible and UV regions, respectively. M, G, L, S, PMT designate mirror, grating, lens, shutter and photomultiplier tube, respectively. CPU, A/D converter and HV/Amp indicate central processing unit, analog to digital converter and High-voltage/Amplifier circuit, respectively.

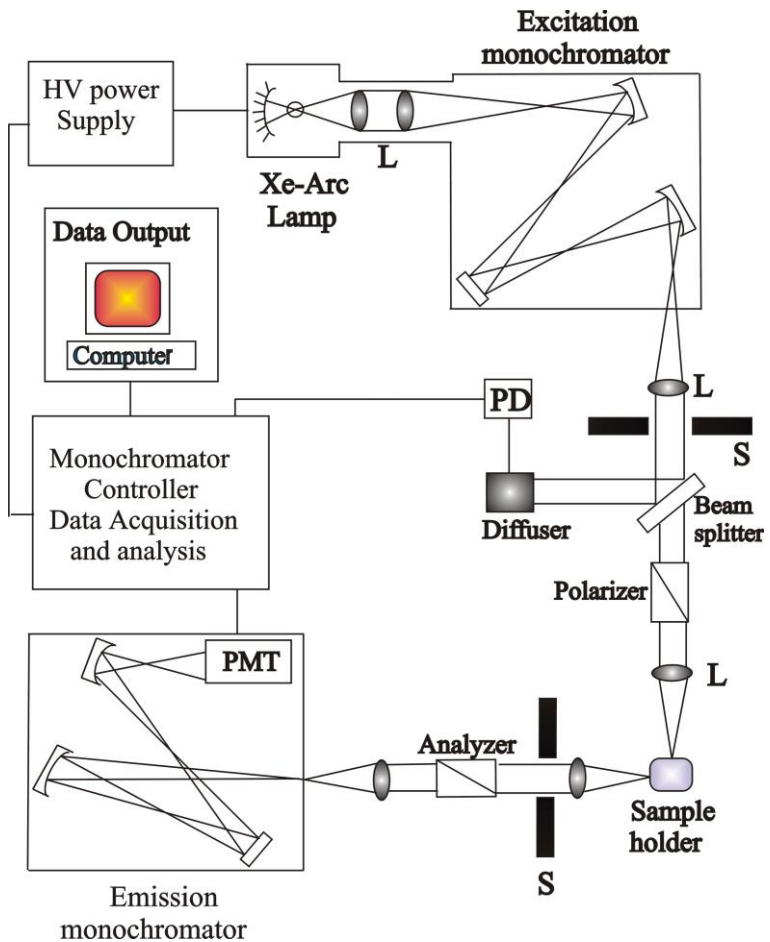


Figure 3.2. Schematic ray diagram of an emission spectrofluorimeter. M, G, L, S, PMT and PD represent mirror, grating, lens, shutter, photomultiplier tube and reference photodiode, respectively.

3.1.2. Circular Dichroism (CD) Spectroscopy: Circular Dichroism (CD) is a form of spectroscopy based on the differential absorption of left and right-handed circularly polarized light. It can be used to determine the structure of macromolecules (including the secondary structure of proteins and the handedness of DNA). The CD measurements were done in a JASCO spectropolarimeter with a temperature controller attachment (Peltier) (Figure 3.3). The CD spectra were acquired using a quartz cell of 1 cm path length. For proteins, the typical concentration used for CD measurements were within 10 μM while that for DNA were about 20 μM . The secondary structural data of the CD spectra were analyzed using CDNN deconvolution program.

The working principle of CD measurement is as follows: when a plane polarized light passes through an optically active substance, not only do the left (L) and right (R) circularly polarized light rays travel at different speeds, $c_L \neq c_R$, but these two rays are absorbed to a different extent, i.e. $A_L \neq A_R$. The difference in the absorbance of the left and right circularly polarized light, i.e., $\Delta A = A_L - A_R$, is defined as Circular Dichroism (CD). CD spectroscopy follows Beer-Lambert law. If I_0 is the intensity of light incident on the cell, and I , that of emergent light, then absorbance is given by,

$$A = \log_{10} \left(\frac{I_0}{I} \right) = \epsilon cl \quad (3.1)$$

i.e., A is proportional to concentration (c) of optically active substance and optical path length (l). If 'c' is in moles/litre and 'l' is in cm, then ϵ is called the molar absorptivity or molar extinction coefficient. In an optically active medium, two absorbances, A_L and A_R are considered, where $A_L = \log_{10}(I_0/I_L)$ and $A_R = \log_{10}(I_0/I_R)$. At the time of incidence on the sample, intensity of left and right circularly polarized light are same, i.e. $I_0 = I_L = I_R$. Any dicrograph passes periodically changing light through the medium, oscillating between left and right circular polarization, and the difference in absorbances are recorded directly.

$$\Delta A = A_L - A_R = \log_{10} \left(\frac{I_0}{I_L} \right) - \log_{10} \left(\frac{I_0}{I_R} \right) = \log_{10} \left(\frac{I_R}{I_L} \right) \quad (3.2)$$

$$\text{or} \quad \Delta A = (\Delta \epsilon) cl \quad (3.3)$$

As seen from equation 3.2, I_0 does not appear in this final equation, so there is no need for a reference beam. The instruments are, therefore, of single beam type. Most of the CD spectropolarimeters, although they measure differential absorption, produce a CD spectrum in units of ellipticity (θ) expressed in millidegrees versus λ , rather than ΔA versus λ . The relation between ellipticity and CD is given by,

$$\theta = \frac{2.303 \times 180 \times (A_L - A_R)}{4\pi} \text{ degrees} \quad (3.4)$$

To compare the results from different samples, optical activity is computed on a molar or residue basis. Molar ellipticity, $[\theta]$ is defined as,

$$[\theta] = \frac{\theta}{cl} \quad (3.5)$$

where ' Θ ' is in degrees, 'c' is in moles per litre and 'l' is in cm. The unit of molar ellipticity is deg M⁻¹ cm⁻¹.

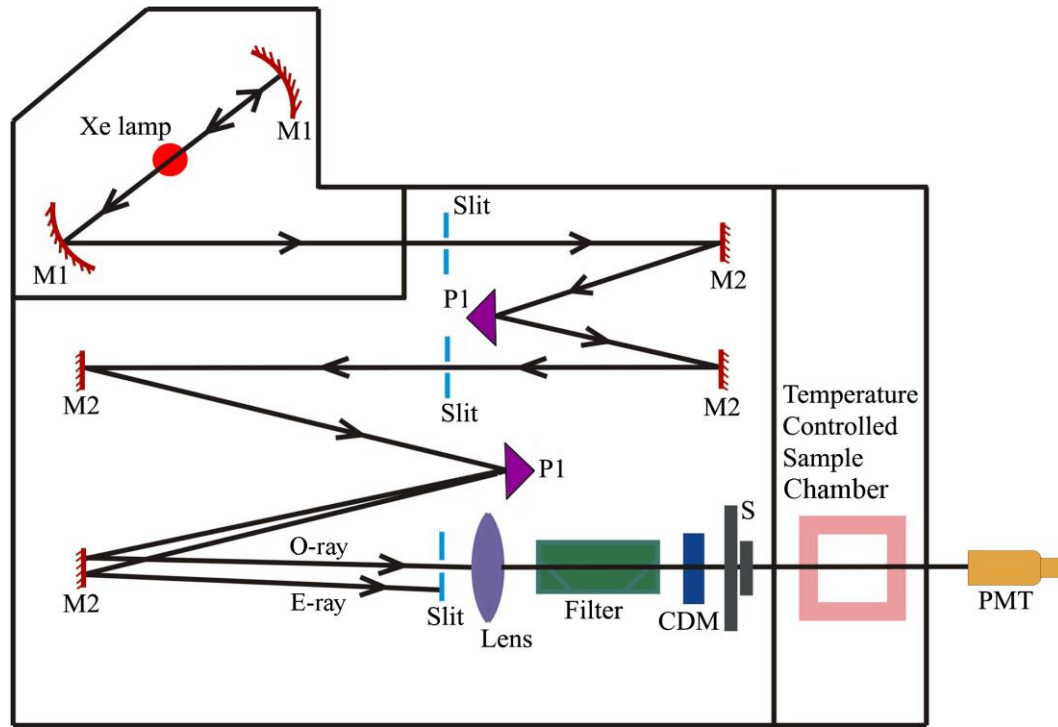


Figure 3.3. Schematic ray diagram of a circular dichroism (CD) spectropolarimeter. M1, M2, P1, S, PMT, CDM, O-ray and E-ray represent concave mirror, plain mirror, reflecting prism, shutter, photomultiplier tube, CD-modulator, ordinary ray and extraordinary ray, respectively.

3.1.3. Time Correlated Single Photon Counting (TCSPC): All the picosecond-resolved fluorescence transients were recorded using time correlated single photon counting (TCSPC) technique. The schematic block diagram of a TCSPC system is shown in Figure 3.4. TCSPC setup from Edinburgh instruments, U.K. was used during fluorescence decay acquisitions. The instrument response functions (IRFs) of the laser sources at different excitation wavelengths have been mentioned in our original published articles [1, 2]. The fluorescence from the sample was detected by a photomultiplier after dispersion through a grating monochromator. For all transients, the polarizer in the emission side was adjusted to be at 54.7° (magic angle) with respect to the polarization axis of excitation beam. In order to measure fluorescence anisotropy decay, the

fluorescence decays were taken with emission polarizer aligned in parallel and perpendicular directions with respect to vertical polarization of excitation light.

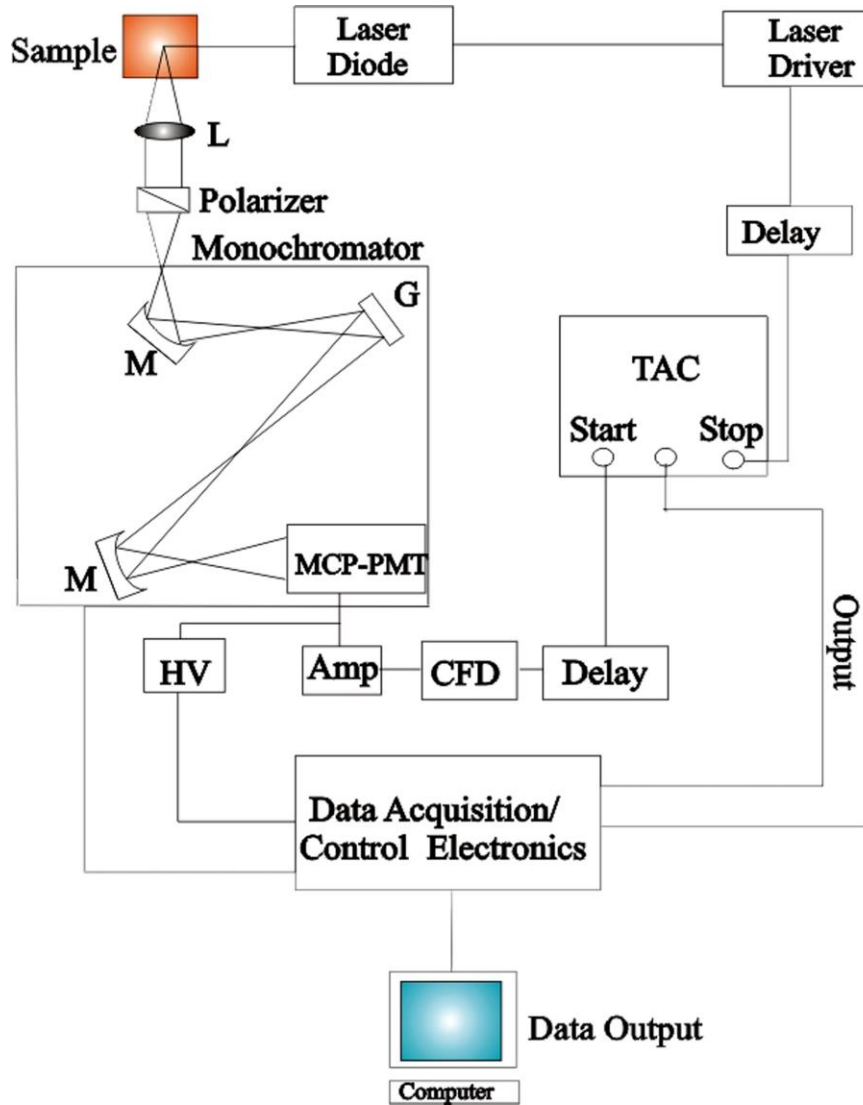


Figure 3.4. Schematic ray diagram of a time correlated single photon counting (TCSPC) spectrophotometer. A signal from microchannel plate photomultiplier tube (MCP-PMT) is amplified (Amp) and connected to start channel of time to amplitude converter (TAC) via constant fraction discriminator (CFD) and delay. The stop channel of the TAC is connected to the laser driver via a delay line. L, M, G and HV represent lens, mirror, grating and high voltage source, respectively.

3.1.4. Dynamic Light Scattering (DLS): Dynamic light scattering (DLS), also known as Photon Correlation Spectroscopy (PCS) or Quasi-Elastic Light Scattering (QELS), is one of the most popular techniques used to determine the hydrodynamic size of the particle. DLS measurements were performed on a Nano S Malvern instruments, U.K.

employing a 4 mW He-Ne laser ($\lambda = 632.8$ nm) and equipped with a thermostatted sample chamber. The instrument allows DLS measurements in which all the scattered photons are collected at 173° scattering angle (Figure 3.5). The instrument measures the time-dependent fluctuation in intensity of light scattered from the particles in solution at a fixed scattering angle.

It has been seen that particles in dispersion are in a constant, random Brownian motion and that this causes the intensity of scattered light to fluctuate as a function of time. The correlator used in a DLS instrument constructs the intensity autocorrelation function $G(\tau)$ of the scattered intensity,

$$G(\tau) = \langle I(t)I(t + \tau) \rangle \quad (3.6)$$

where τ is the time difference (the sample time) of the correlator. For a large number of monodisperse particles in Brownian motion, the correlation function (given the symbol G) is an exponential decaying function of the correlator time delay τ ,

$$G(\tau) = A[1 + B \exp(-2\Gamma\tau)] \quad (3.7)$$

where A is the baseline of the correlation function, B is the intercept of the correlation function. Γ is the first cumulant and is related to the translational diffusion coefficient as, $\Gamma = Dq^2$, where q is the scattering vector and its magnitude is defined as,

$$q = \left(\frac{4\pi n}{\lambda_0} \right) \sin\left(\frac{\theta}{2}\right) \quad (3.8)$$

where n is the refractive index of dispersant, λ_0 is the wavelength of the laser and θ , the scattering angle. For polydisperse samples, the equation can be written as,

$$G(\tau) = A \left[1 + B |g^{(1)}(\tau)|^2 \right] \quad (3.9)$$

where the correlation function $g^{(1)}(\tau)$ is no longer a single exponential decay and can be written as the Laplace transform of a continuous distribution $G(\Gamma)$ of decay times,

$$g^{(1)}(\tau) = \int_0^{\infty} G(\Gamma) \exp(-\Gamma\tau) d\Gamma \quad (3.10)$$

The scattering intensity data in DLS are processed using the instrumental software to obtain the hydrodynamic diameter (d_H) and the size distribution of the scatterer in each sample. In a typical size distribution graph from the DLS measurement, X-axis shows a distribution of size classes in nm, while the Y-axis shows the relative intensity of the

scattered light. The diffusion coefficient (D) can be calculated using the hydrodynamic diameter (d_H) of the particle by using the Stoke-Einstein relation,

$$D = \frac{k_B T}{3\pi\eta d_H} \quad (3.11)$$

where k_B , T , d_H , η are Boltzmann constant, temperature in Kelvin, hydrodynamic diameter and viscosity, respectively.

The ray diagram of the DLS setup is shown in Figure 3.5.

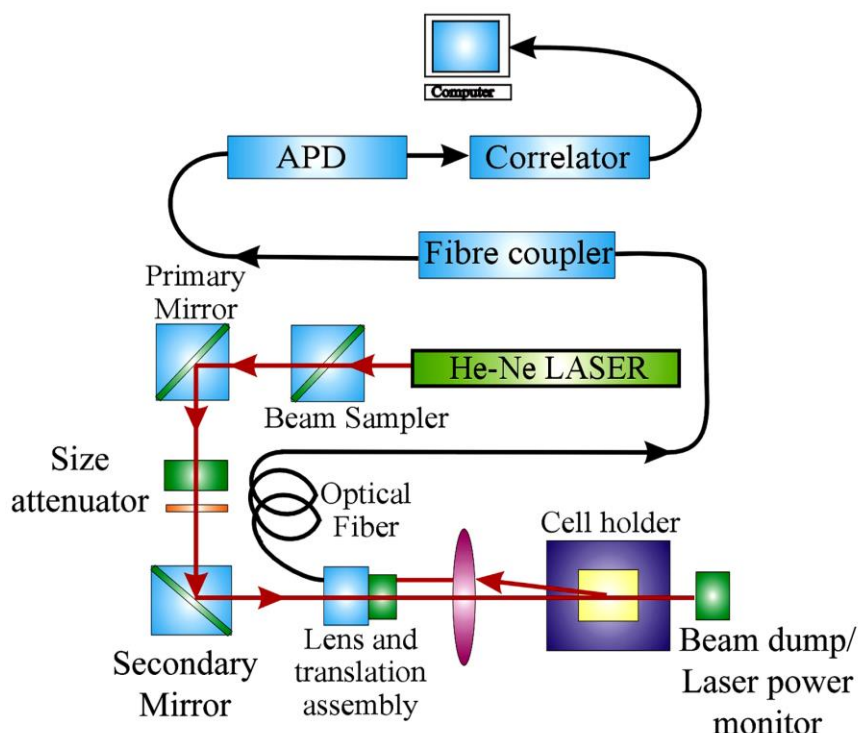


Figure 3.5. Schematic ray diagram of dynamic light scattering (DLS) instrument. The avalanche photo diode (APD) is connected to preamplifier/amplifier assembly and finally to correlator. It has to be noted that lens and translational assembly, laser power monitor, size attenuator, laser are controlled by the computer.

3.1.5. X-Ray Diffractometer (XRD): It is a popular and powerful technique for determining crystal structure of crystalline materials. By examining the diffraction pattern, one can identify the crystalline phase of the material. Small angle scattering is useful for evaluating the average inter particle distance while wide-angle diffraction is useful for refining the atomic structure of nanoclusters. The widths of the diffraction lines are closely related to strain and defect size and distribution in nanocrystals. As the size of

the nanocrystals decrease, the line width is broadened due to loss of long-range order relative to the bulk.

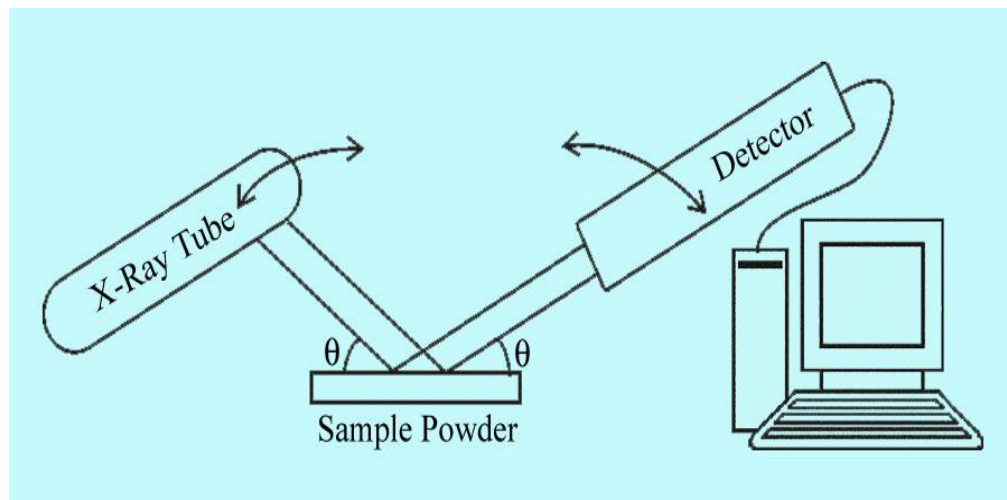


Figure 3.6. Schematic diagram of X-ray diffraction (XRD) instrument. By varying the angle θ , the Bragg's Law conditions, $n\lambda = 2d\sin\theta$ are satisfied by different d -spacings in polycrystalline materials. Plotting the angular positions and intensities of the resultant diffracted peaks of radiation produces a pattern, which is characteristic of the sample.

This XRD line width can be used to estimate the size of the particle by using the Debye-Scherrer formula,

$$D = \frac{0.9\lambda}{\beta \cos\theta} \quad (3.12)$$

where D is the nanocrystal diameter, λ is the wavelength of light, β is the full width half-maximum (fwhm) of the peak in radians, and θ is the Bragg angle. XRD measurements were performed on a PANalytical XPERT-PRO diffractometer (Figure 3.6) equipped with Cu K α radiation ($\lambda = 1.5418 \text{ \AA}$ at 40 mA, 40 kV). XRD patterns were obtained by employing a scanning rate of $0.02^\circ \text{ s}^{-1}$ in the 2θ range from 20° to 80° .

3.1.6. Fourier Transform Infrared (FTIR) Spectroscopy: It is a technique that can provide very useful information about functional groups in a sample. An infrared spectrum represents the fingerprint of a sample with absorption peaks which correspond to the frequencies of vibrations between the bonds of the atoms making up the material.

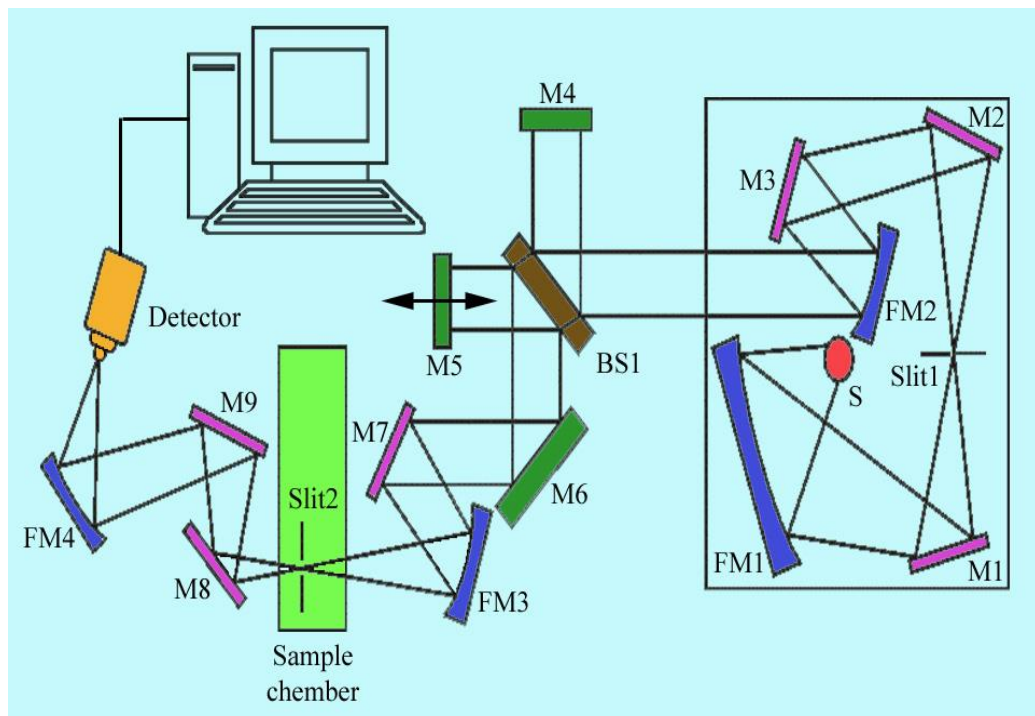


Figure 3.7. Schematic of Fourier transform infrared (FTIR) spectrometer. It is basically a Michelson interferometer in which one of the two fully-reflecting mirrors is movable, allowing a variable delay (in the travel-time of the light) to be included in one of the beams. M, FM and BS1 represent the mirror, focusing mirror and beam splitter, respectively. M5 is a moving mirror.

Because each different material is a unique combination of atoms, no two compounds produce the exact same infrared spectrum.

Therefore, infrared spectroscopy can result in a positive identification (qualitative analysis) of every different kind of material. In addition, the size of the peaks in the spectrum is a direct indication of the amount of material present. The two-beam Michelson interferometer is the heart of FTIR spectrometer. It consists of a fixed mirror (M4), a moving mirror (M5) and a beamsplitter (BS1), as illustrated in Figure 3.7. The beamsplitter is a laminate material that reflects and transmits light equally. The collimated IR beam from the source is partially transmitted to the moving mirror and partially reflected to the fixed mirror by the beamsplitter. The two IR beams are then reflected back to the beamsplitter by the mirrors. The detector then sees the transmitted beam from the fixed mirror and reflected beam from the moving mirror simultaneously. The two combined beams interfere constructively or destructively depending on the wavelength of the light (or frequency in wavenumbers) and the optical path difference

introduced by the moving mirror. The resulting signal is called an interferogram which has the unique property that every data point (a function of the moving mirror position) which makes up the signal has information about every infrared frequency which comes from the source. Because the analyst requires a frequency spectrum (a plot of the intensity at each individual frequency) in order to make identification, the measured interferogram signal cannot be interpreted directly. A means of “decoding” the individual frequencies is required. This can be accomplished via a well-known mathematical technique called the Fourier transformation. This transformation is performed by the computer which then presents the user with the desired spectral information for analysis. FTIR measurements were performed on a JASCO FTIR-6300 spectrometer (transmission mode). For the FTIR measurements, powdered samples were mixed with KBr powder and pelletized. The background correction was made using a reference blank of KBr pellet.

3.1.7. Matrix-Assisted Laser Desorption Ionization-Time of Flight (MALDI-TOF)

Mass Spectrometry: It is an analytical technique used for measuring the molecular mass of biomolecules (such as proteins, peptides, oligosaccharides and oligonucleotides) on the basis of the mass (m)-to-charge (z) ratio (m/z) of charged particles, which tend to be fragile and fragment when ionized by more conventional ionization methods. In MALDI-TOF mass spectrometry (Figure 3.8), the sample molecules are bombarded with a laser light to bring about sample ionization. The sample is pre-mixed with a highly absorbing matrix compound for the most consistent and reliable results and a low concentration of sample to matrix work best. The matrix transforms the laser energy into excitation energy for the sample, which leads to sputtering of analyte and matrix ions from the surface of the mixture. In this way energy transfer is efficient and also the analyte molecules are spared from excessive direct energy that may otherwise cause decomposition.

The ionized molecules are accelerated in an electric field and enter into a chamber under vacuum that contains no electric fields (analyzer). The time-of-flight analyzer separates ions according to their mass (m/z) ratios by measuring the time it takes for ions to travel through a field-free region. A detector is positioned at the end of the analyzer to measure the arrival time of ions. Ions of lesser m/z arrive first, followed by ions of

greater m/z. A plot of intensity or abundance versus time is made to show the arrival time distribution of the ions detected. The plot of intensity versus time is calibrated and replotted as intensity versus m/z. The method is used for detection and characterization of biomolecules with molecular masses between 400 and 350,000 Da. It is a very sensitive method, which allows the detection of low (10^{-15} to 10^{-18} mole) quantities of sample with an accuracy of 0.1–0.01%. MALDI MS studies were conducted using a Voyager-DE PRO Biospectrometry workstation from Applied Biosystems. A pulsed nitrogen laser of 337 nm was used for the MALDI MS studies. Mass spectra were collected in positive-ion mode and were averaged for 100 shots. Sinapinic acid was used as the matrix for MALDI-TOF MS.

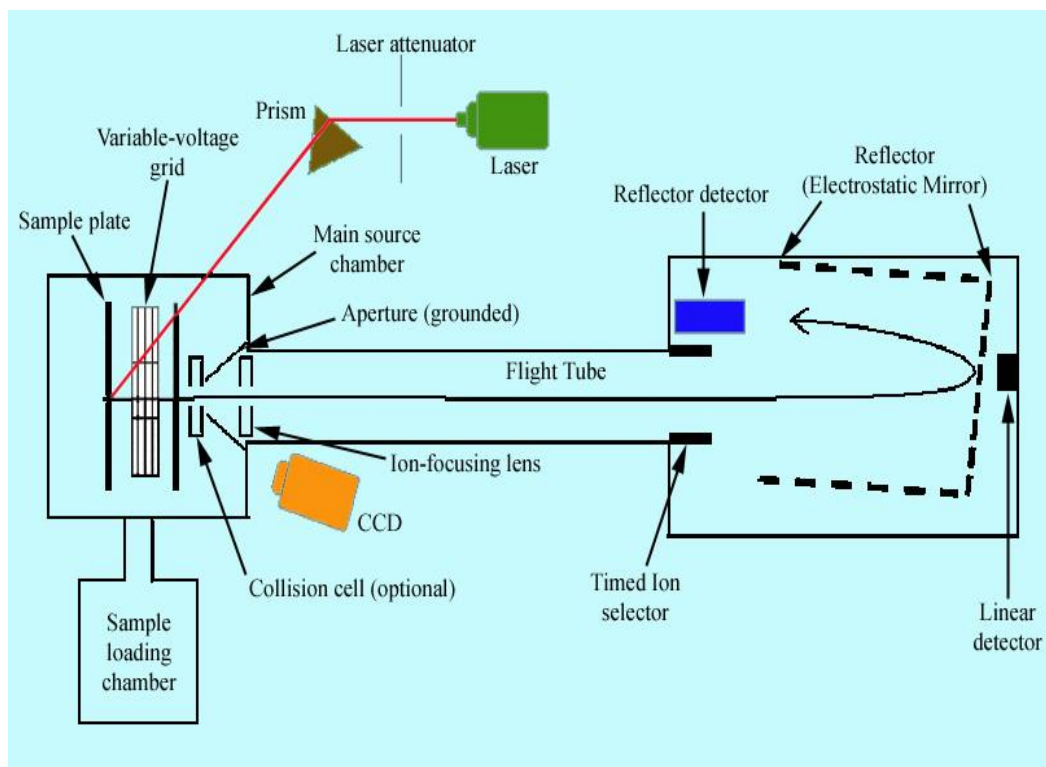


Figure 3.8. Schematic diagram of matrix-assisted laser desorption/ionization-time of flight mass spectrometry (MALDI-TOF) spectrometer. MALDI is a soft ionisation method and so results predominantly in the generation of singly charged molecular-related ions regardless of the molecular mass, hence the spectra are relatively easy to interpret. Fragmentation of the sample ions does not usually occur.

3.1.8. Transmission Electron Microscopy (HRTEM): An FEI TecnaiTF-20 field-emission high-resolution transmission electron microscope (HRTEM) (Figure 3.9)

equipped with an Energy Dispersive X-ray (EDAX) spectrometer was used to characterize the microscopic structures of samples and to analyze their elemental composition. The size of the nanoparticles was determined from the TEM images obtained at 200 kV. Samples for TEM were prepared by placing a drop of the colloidal solution on a carbon-coated copper grid and allowing the film to evaporate overnight at room temperature.

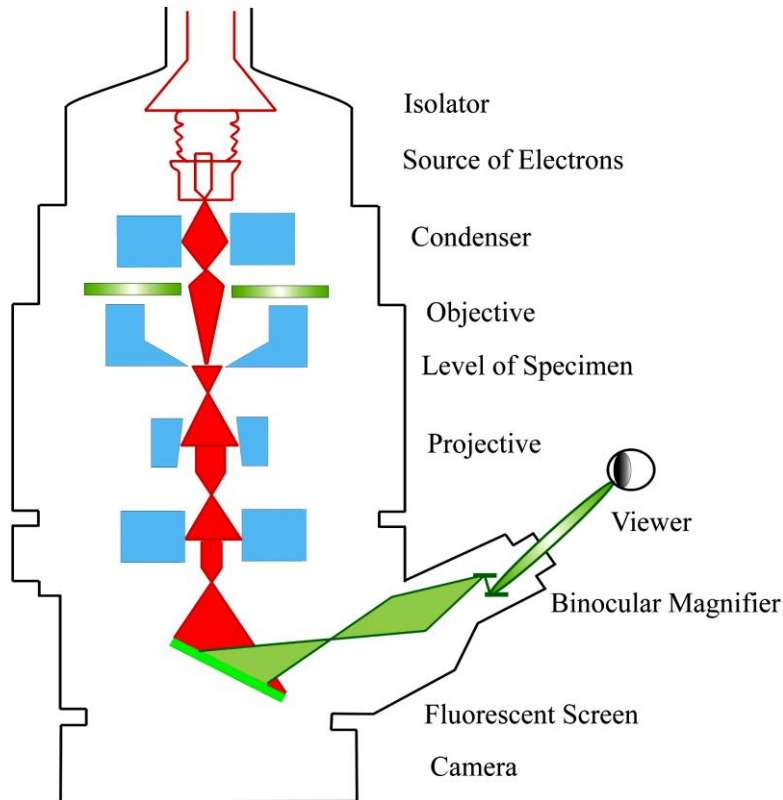


Figure 3.9. Schematic diagram of a typical transmission electron microscope (TEM). After the transmission of electron beam through a specimen, the magnified image is formed either in the fluorescent screen or can be detected by a CCD camera.

3.1.9. Scanning Electron Microscopy (SEM): Surface characteristics of Porous silicon samples were done by scanning electron microscope FE-SEM; JEOL. Ltd., JSM-6500F. A electron-gun is attached to SEM and the electrons from filament triggered by 0 KV to 30 KV voltages. These electrons go first through a condenser lens and then through a objective lens, then through a aperture and finally reach to the specimen. The high energy electrons go a bit in the sample and back again give secondary electrons. The

signal from secondary electrons are detected by detector and amplified. The ray diagram of the SEM setup is shown in Figure 3.10.

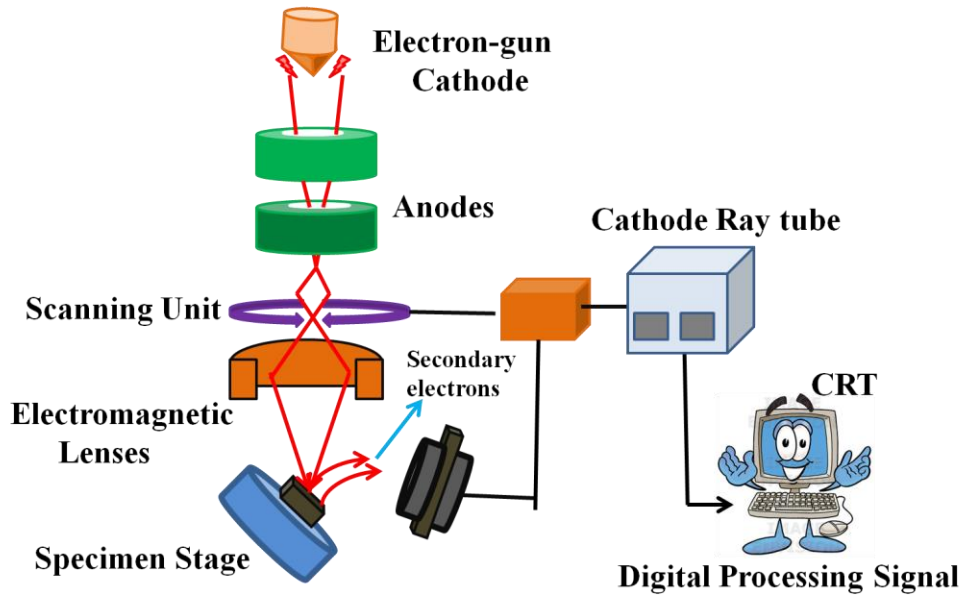


Figure 3.10. Schematic diagram of typical scanning electron microscope (SEM).

3.1.10. X-Ray Photoelectron Spectroscopy (XPS): XPS works on the principle of photoelectric effect discovered by Heinrich Hertz in 1887. When radiation of appropriate energy incident, electrons are emitted from the surface of the metal. The relation between the energy of the excitation radiation, work function of the metal and the maximum kinetic energy of the emitted electron as proposed by Einstein in 1905 is:

$$h\nu = \phi + KE_{\max} \quad (3.13)$$

' Φ ' is the work function of the metal, ' $h\nu$ ' is the energy of the radiation, ' KE_{\max} ' is the maximum kinetic energy of the emitted electron. For analysing the core electronic structure (0 – 1300 eV) of elements, radiation of high energy were used like X-rays, hence the corresponding spectroscopy is termed X-ray Photoelectron Spectroscopy (XPS) (Figure 3.11).

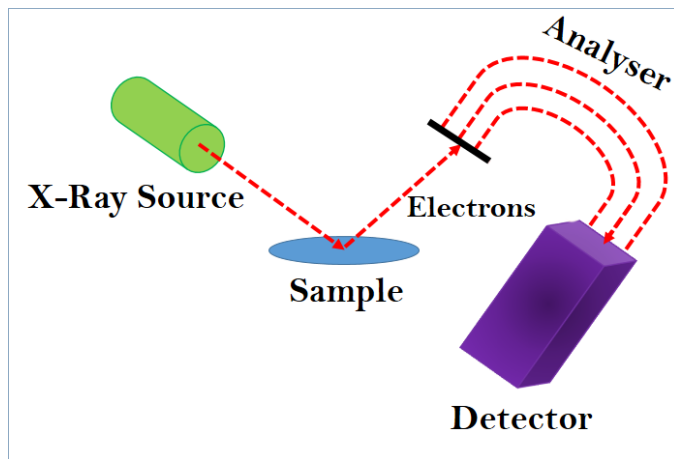


Figure 3.11. Schematic diagram of a typical X-ray photoelectron spectroscopy (XPS).

Surface analysis by XPS is accomplished by irradiating a sample with monoenergetic soft X-rays and analysing the energy of the detected electrons. Mg K α (1253.6 eV), Al K α (1486.6 eV), or monochromatic Al K α (1486.7 eV) X-rays are usually used. These photons have limited penetrating power in a solid of the order of 1 – 10 μm . They interact with atoms in the surface region, causing electrons to be emitted by the photoelectric effect. The emitted electrons have measured kinetic energies given by:

$$KE = h\nu - BE - \phi_S \quad (3.14)$$

where 'h ν ' is the energy of the photon, 'BE' is the binding energy of the atomic orbital from which electron originates, ' Φ_S ' is the work function of the spectrometer. The binding energy may be regarded as the energy difference between the initial and final states after the photoelectron has left the atom. Because there is a variety of possible final states of the ions from each type of atom, there is a corresponding variety of kinetic energies of the emitted electrons. Moreover there is a different probability or cross section for each final state.

Because each element has unique set of binding energies, XPS can be used to identify and determine the concentration of the elements in the surface. Variation in the elemental binding energies (the chemical shifts) arise from differences in the chemical potential and polarizability of compounds. These chemical shifts can be used to identify the chemical state of the material being analysed. In our studies, XPS were performed on

a Omicron ESCA probe spectrometer with polychromatic Mg K α X-rays ($h\nu = 1253.6$ eV).

3.1.11. Femtosecond Time-Resolved Fluorescence Up-Conversion: The femtosecond-resolved fluorescence spectroscopy was carried out using a femtosecond upconversion setup (FOG 100, CDP, Figure 3.12) in which the sample was excited at 364 nm, using the second harmonic of a mode-locked Ti-sapphire laser with 80 MHz repetition rate (Tsunami, Spectra Physics), pumped by 10 W Millennia (Spectra Physics). The fundamental beam was passed through a perisopic arrangement (P) (Figure 3.12) before getting frequency doubled in a nonlinear crystal, NC1 (1 mm BBO, $\theta = 25^\circ$, $\phi = 90^\circ$). This beam was then sent into a rotating circular cell of 1 mm thickness containing the sample via a dichroic mirror (DM), a polarizer and a mirror (M4). The resulting fluorescence emission was collected, refocused with a pair of lenses (L4 and L5) and

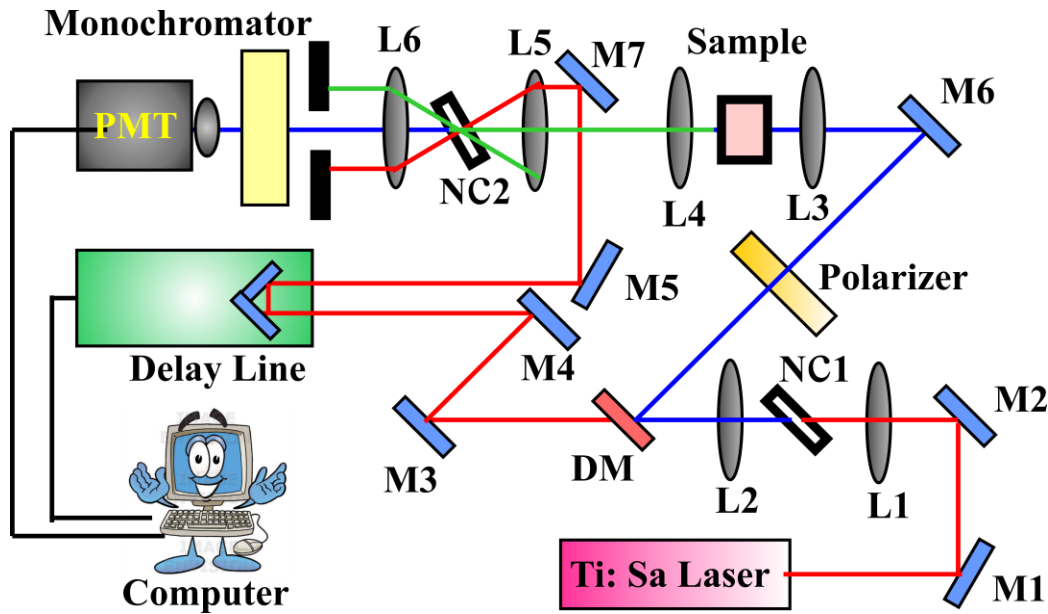


Figure 3.12. Schematic of the femtosecond fluorescence up-conversion experimental setup. BBO crystal (NC1) is used for second harmonic generation, which provides a pump beam in the UV region. Another BBO crystal (NC2) generates the up-conversion signal of pump and probe beams. L and M indicate lenses and mirrors, respectively. M1-M2 and M3, M4, M5, M7 are IR mirrors whereas M6 is a UV mirror. DM is dichroic mirror, and P is periscope.

mixed with the fundamental beam (728 nm) coming through a delay line to yield an upconverted photon signal in a nonlinear crystal, NC2 (0.5 mm BBO, $\theta = 10^\circ$, $\phi = 90^\circ$).

The upconverted light was dispersed in a double monochromator and detected using photon counting electronics. A cross-correlation function obtained using the Raman scattering from water displayed a full width at half maximum (FWHM) of 165 fs. The femtosecond fluorescence decays were fitted using a Gaussian shape for the exciting pulse.

3.1.12. Differential Scanning Calorimetry (DSC): It is a thermodynamical technique in which the difference in the amount of heat required to increase the temperature of a sample and reference is measured as a function of temperature. DSC is commonly used for the study of biochemical reactions, such as, single molecular transition of a molecule from one conformation to another [3]. Thermal transition temperatures (T ; melting points) of the samples are also determined in solution, solid, or mixed phases such as suspensions [4]. In a basic DSC experiment, energy is introduced simultaneously into a sample cell (which contains a solution with the molecule of interest) and a reference cell (containing only the solvent). Temperatures of both cells are raised identically over time. The difference in the input energy required to match the temperature of the sample to that of the reference would be the amount of excess heat absorbed or released by the molecule in the sample (during an endothermic or exothermic process, respectively). The schematic of the DSC setup is shown in Figure 3.13.

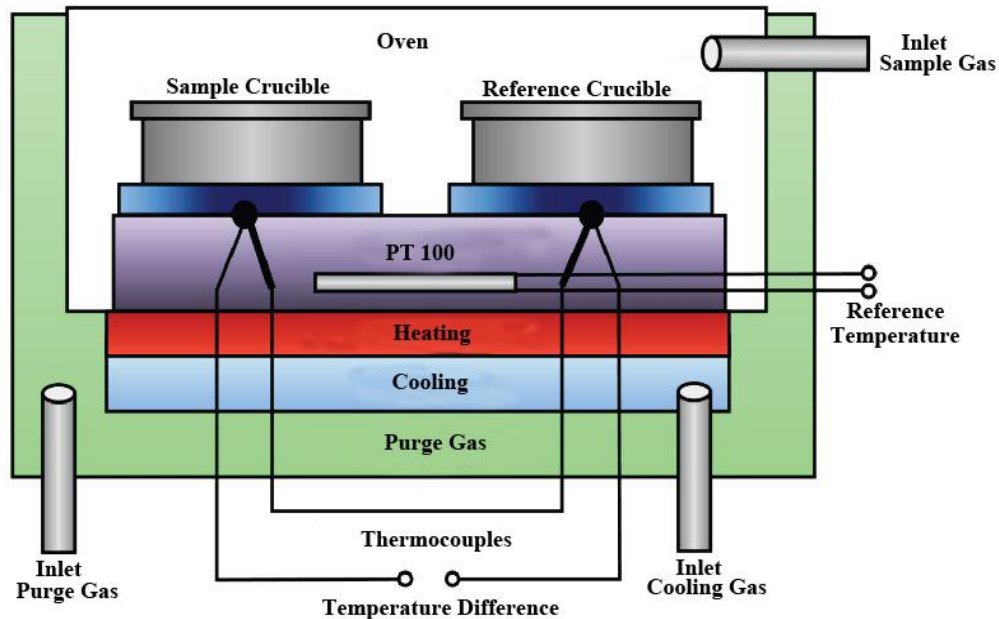


Figure 3.13. The schematic representation of differential scanning calorimetry (DSC) setup.

3.1.13. Refractive Indices Measurement: Refractive indices of the solutions were measured by using a Rudolph J357 automatic refractometer. The instrument measures the refractive indices using sodium D-line of wavelength 589.3 nm with accuracies ± 0.00004 . The measurement of the refractive index of the sample is based on the determination of the critical angle of total reflection. A light source, usually a long-life LED, is focused onto a prism surface via a lens system. Due to the focusing of light to a spot at the prism surface, a wide range of different angles is covered. As the measured sample is in direct contact with the measuring prism. Depending on its refractive index, the incoming light below the critical angle of total reflection is partly transmitted into the sample, whereas for higher angles of incidence the light is totally reflected. This dependence of the reflected light intensity from the incident angle is measured with a high-resolution sensor array. From the video signal taken with the CCD sensor the refractive index of the sample can be calculated.

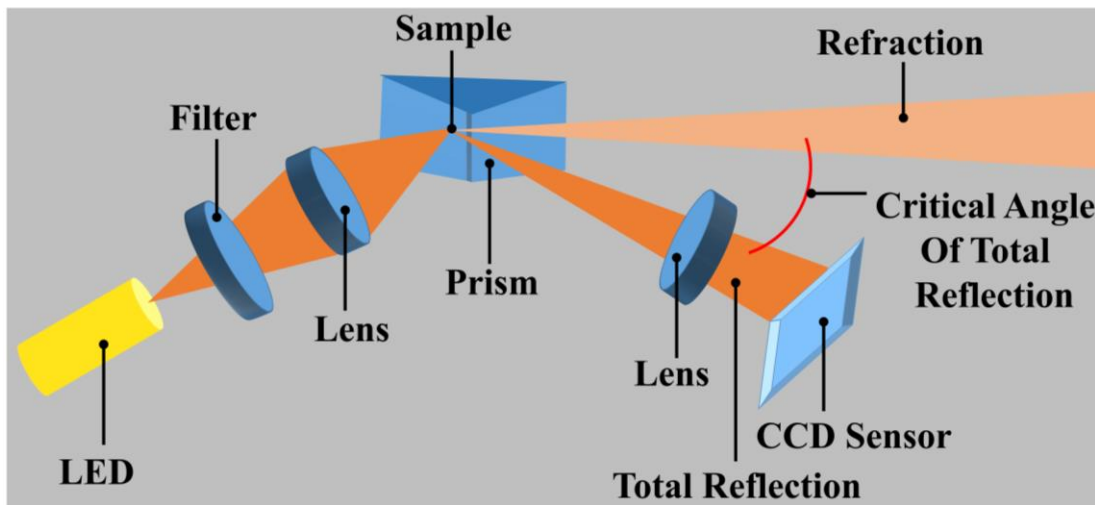


Figure 3.14. Schematic representation of the refractometer.

3.1.14. Thermogravimetric-Differential Thermal Analyzer (TG-DTA) Setup: The thermogravimetric (TG) analysis was carried out using Diamond thermogravimetric (TG)-differential thermal analyzer (DTA) from Perkin Elmer. The TG determines the weight change of a sample whereas the DTA measures the change in temperature between a sample and the reference as a function of temperature and/or time. The

schematic of the TG-DTA setup is shown in Figure 3.15. When a weight change occurs on the sample side, the beam holding the platinum pans is displaced. This movement is detected optically and the driving coil current is changed to return the displacement to zero. The detected driving coil current change is proportional to the sample weight change and the output is the TG signal. The DTA detects the temperature difference between the sample holder and the reference holder using the electromotive force of thermocouples, which are attached to the holders. This difference is measured as the DTA signal.

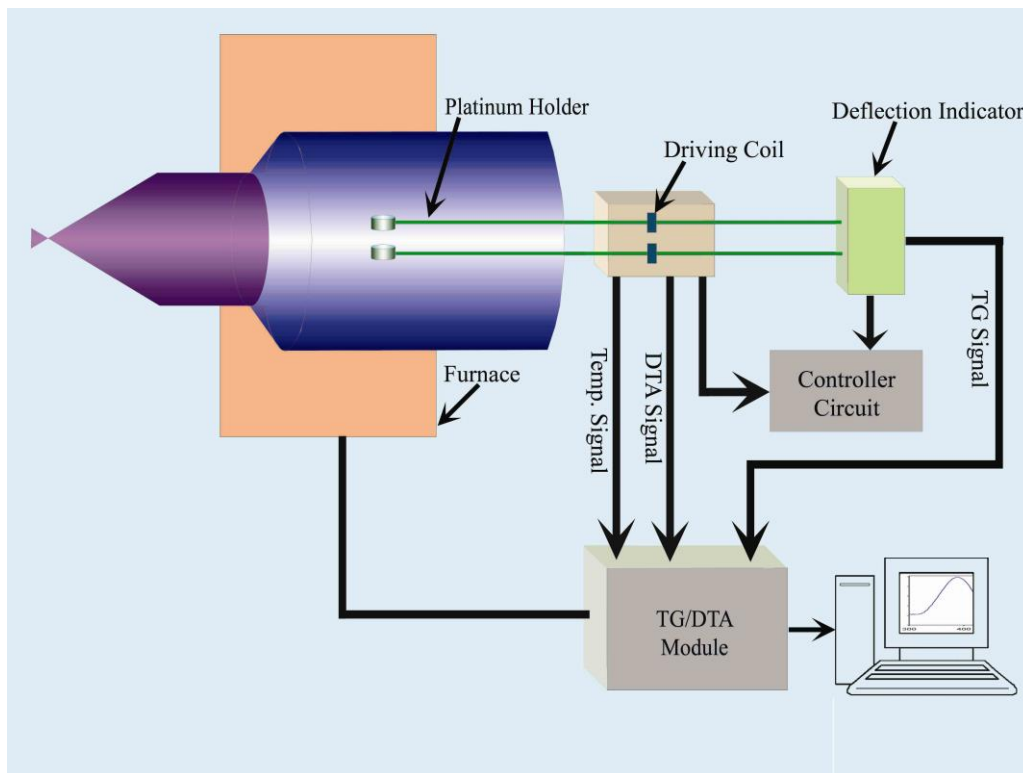


Figure 3.15. The schematic representation of thermogravimetric-differential thermal analyzer (TG-DTA) setup.

3.1.15. Laser Raman Spectroscopy: Raman spectroscopy is a useful technique for the identification of a wide range of substances: solids, liquids, and gases. It is a straightforward, non-destructive technique requiring no sample preparation. Raman spectroscopy involves illuminating a sample with monochromatic light and using a spectrometer to examine light scattered by the sample.

At the molecular level photons can interact with matter by absorption or scattering processes. Scattering may occur either elastically, or inelastically. The elastic process is termed Rayleigh scattering, whilst the inelastic process is termed Raman scattering. The electric field component of the scattering photon perturbs the electron cloud of the molecule and may be regarded as exciting the system to a ‘virtual’ state. Raman scattering occurs when the system exchanges energy with the photon, and the system subsequently decays to vibrational energy levels above or below that of the initial state. The frequency shift corresponding to the energy difference between the incident and scattered photon is termed the Raman shift. Depending on whether the system has lost or gained vibrational energy, the Raman shift occurs either as an up or down-shift of the scattered photon frequency relative to that of the incident photon. The down-shifted and up-shifted components are called, respectively, the Stokes and anti-Stokes lines. A plot of detected number of photons versus Raman shift from the incident laser energy gives a Raman spectrum. Different materials have different vibrational modes, and therefore characteristic Raman spectra. This makes Raman spectroscopy a useful technique for material identification. There is one important distinction to make between

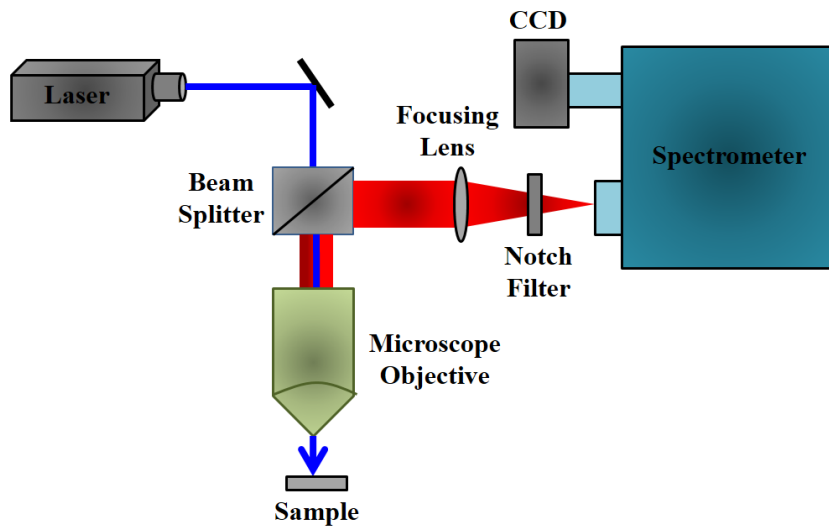


Figure 3.16. Schematic diagram of a Raman spectrometer is shown.

the Raman spectra of gases and liquids, and those taken from solids-in particular, crystals. For gases and liquids it is meaningful to speak of the vibrational energy levels of the individual molecules which make up the material. Crystals do not behave as if

composed of molecules with specific vibrational energy levels, instead the crystal lattice undergoes vibration. These macroscopic vibrational modes are called phonons.

In modern Raman spectrometers (LabRAM HR, Jobin Yvon), lasers are used as a photon source due to their highly monochromatic nature, and high beam fluxes (Figure 3.16). This is necessary as the Raman effect is weak, typically the Stokes lines are $\sim 10^5$ times weaker than the Rayleigh scattered component. In the visible spectral range, Raman spectrometers use notch filters to cut out the signal from a very narrow range centred on the frequency corresponding to the laser radiation. Most Raman spectrometers for material characterization use a microscope to focus the laser beam to a small spot ($<1\text{--}100 \mu\text{m}$ diameter). Light from the sample passes back through the microscope optics into the spectrometer. Raman shifted radiation is detected with a charge-coupled device (CCD) detector, and a computer is used for data acquisition and curve fitting. These factors have helped Raman spectroscopy to become a very sensitive and accurate technique.

3.2. Sample Preparation:

In this section the different sample preparation methods have been discussed. All the aqueous solutions were prepared using deionized water from Millipore system. Human serum albumin (HSA), bovine serum albumin (BSA), subtilisin *carlsberg* (SC), α -chymotrypsin (CHT), L-kynurenine, CV, acetonitrile (ACN), Ala-Ala-Phe 7-amido-4-methyl coumarin (AAF-AMC), N-CBZ-Gly-Gly-Leu *p*-nitroanilide (CBZGGL-pNA), phosphate buffer, 4-NPA, anhydrous Na₂S 9H₂O, Hg(NO₃)₂, HAuCl₄, CuSO₄ as well as all the nitrates and chlorides of various metal ions of highest commercially available grade were purchased from Sigma Chemicals. The electron-accepting BQ was obtained from Alfa-Aesar. Genomic DNA from Salmon testes was procured from Sigma chemicals. The proteins and DNA were of highest purity grade.

3.2.1. Measurement of Enzymatic Activity of α -Chymotrypsin (CHT) and Subtilisin *Carlsberg* (SC): Catalytic activity measurements of CHT and SC were made using the chromogenic synthetic substrates AAFAMC and CBZ-GGL-pNA as per the conventional procedure [5]. Catalytic activity measurements of CHT and SC were made using the chromogenic synthetic substrates AAFAMC and CBZ-GGL-pNA as per the conventional

procedure. Concentrations of the substrates were determined using $\epsilon_{325} = 16 \text{ mM}^{-1} \text{ cm}^{-1}$ for AAF-AMC in buffer pH = 7.0, and $\epsilon_{315} = 14 \text{ mM}^{-1} \text{ cm}^{-1}$ for CBZ-GGL-pNA in water. The extinction coefficients of the products formed are $7.6 \text{ mM}^{-1} \text{ cm}^{-1}$ (for AMC at 370 nm) and $8.8 \text{ mM}^{-1} \text{ cm}^{-1}$ (for pNA at 410 nm). For the enzymatic kinetics experiment, the enzyme concentration was maintained at $1 \mu\text{M}$ while that of substrate was maintained at 35 and $185 \mu\text{M}$ for AMC and pNA respectively. The rate of formation of product was monitored using the change in absorbance of the product with time.

3.2.2. Preparation of Genomic DNA Solutions: In order to reassociate the single strand DNA into self-complimentary double stranded DNA (ds DNA), thermal annealing was performed as per the methodology prescribed by the vendor. The aqueous solutions of ds DNA were then dialyzed exhaustively against Millipore water prior to further use. Aqueous sample solutions of genomic DNA were prepared in phosphate buffer (pH ~7). The procedure for making genomic DNA aqueous solution was similar to that of the references [6] and [7]. The nucleotide concentrations were determined by absorption spectroscopy using the average extinction coefficient per nucleotide of the DNA ($6,600 \text{ M}^{-1} \text{ cm}^{-1}$ at 260 nm) [6].

3.2.3. Preparation of CV–HSA Complex: HSA was labelled with CV as follows [5]: about 1 mg of CV was dissolved in 2 mL of double-distilled water and from there $20 \mu\text{L}$ of concentrate CV solution was injected to 2 mL of phosphate buffer containing $20 \mu\text{M}$ modified HSA. In order to ensure better energy transfer, the mixture was allowed to stir for 1 h.

3.2.4. Synthesis of Au@Protein Nanobioconjugates: The Au@protein nanobioconjugates were prepared by the following procedure [8]: 3 ml $20 \mu\text{M}$ protein solutions were prepared in 20 mM phosphate buffer solution. Then $60 \mu\text{l}$ 100 mM HAuCl₄ solution was added so that protein-HAuCl₄ ratio was maintained at 1:100. A detailed temperature dependent study was performed starting from 30°C for each mixture and it has been found that when the mixtures were heated at 76°C, 75°C and 60°C for HSA, BSA and SC respectively then the colours of the solutions were changed from light

yellow to reddish brown. Such colour transition is indicative of the formation of Au nanoparticles (NPs).

3.2.5. Extraction of Protein Mixture from E. Coli: Protein Mixture from E. Coli was extracted by the following procedure [8]: single Colony of E. Coli was inoculated in 100 ml Luria Broth (LB) and then incubated overnight at 37°C with shaking. The obtained cells from 100 ml culture were harvested by centrifugation (6,000 rpm) for 5 minute, washed twice with 0.1 M Tris-Cl (pH = 8.2) and re-centrifuged. The cells were then suspended in 2 ml lysis buffer and incubated for 20 minutes. Next, it was allowed to freeze thaw for 3 times giving 1 minute incubation at ice. Finally, the cell suspension was sonicated (80 amplitude. & 0.6 cps) for 10 minute and the supernatant collected by centrifugation (10,000 rpm) for 15 minute at 4°C was the protein.

3.2.6. Synthesis of Au@E. Coli Protein Extracts Nanobioconjugates: The Au@E. Coli extract protein conjugates were prepared by the following method [8]: 1 ml protein extract solution was diluted with 1 ml lysis buffer and then 60 µl 100 mM HAuCl₄ solution was added. The whole mixture was heated at 70°C so that all the proteins present in the mixture were denatured. After 10 minute the colours of the solutions were changed from light yellow to deep brown indicating the formation of Au NPs.

3.2.7. Synthesis of Protein Stabilized HgS Quantum Dots (QDs): It involves two steps. In the first step, the non-luminescent HgO nanoparticles were prepared in a vial by dissolving 5 mL 5 mM HgNO₃, H₂O and 5 mL BSA (15 mg/mL) solution in MQ water under vigorous stirring with final pH value of ~9 (adjusted by 1 M NaOH solution carefully). Then, the solution was allowed to stir for 8-12 hr. The final colour of the solution was pale yellow indicative to the formation of HgO@BSA nanobioconjugates [9]. In the second step, 4 mL of 20 mM Na₂S was added to 10 mL of as-synthesised HgO@BSA nanobioconjugates and the solution was stirred for 15 min. Completion of the reaction was observed visibly by colour changes from pale yellow to light brown. Such colour transition is indicative to the formation of HgS QDs.

3.2.8. Synthesis of Bulk HgO: Bulk HgO samples were prepared in a vial by dissolving 5 mL 50 mM HgNO₃, H₂O and 1 mL 2.5 M NaOH solution. Then, the solution was allowed to stir for 15 min to get the yellow precipitate of HgO [9]. Subsequently, the precipitate was centrifuged and washed with additional MQ water several times for measurements.

3.2.9. Synthesis of Bulk HgS: About 70 mg of HgNO₃, H₂O and 70 mg Na₂S powder were dissolved in 5 mL MQ water under vigorous stirring. The reaction mixture was stirred for 30 min. The resulting precipitate was collected and repeatedly washed with MQ water by centrifugal precipitation. Finally, the bulk HgS precipitate was dried in incubator at to get a dark brown powder [9].

3.2.10. Synthesis of MoS₂ Nanocrystals: It involves two steps. In the first step, an aqueous solution (5 mL) of DNA-Na⁺ from salmon testes (65 mg) and 5 mL of 100 mM MoCl₅, H₂O were mixed at room temperature under vigorous stirring with final pH value of ~ 9 (adjusted by 1 M NaOH solution carefully). Then, the solution was allowed to stir for 6-8 hr so that the solution becomes colourless. In the second step, 5 mL of 200 mM Na₂S was added to 10 mL of as-synthesised Mo-DNA complexes with final pH value of ~ 6 (adjusted by HCl carefully) and the solution was stirred for 15 min. Completion of the reaction was observed visibly by colour changes from colourless to yellow. Such colour transition is indicative to the formation of MoS₂ NCs [10].

3.2.11. Preparation of MoS₂@DNA-CTAC Thin Film: An aqueous solution (5 mL) of as-prepared MoS₂@DNA (final DNA concentration was 6.5 mg/mL) was added to 5 mL of aqueous solution of CTAC (6.5 mg/mL). A 1:1 stoichiometric combination led to the spontaneous formation of the MoS₂@DNA-CTAC complex precipitate. The precipitate was collected by filtration, washed with distilled water, and then lyophilized for 48 hrs. Finally, a yellowish powder was obtained when dried in a vacuum at 37°C. The powder was then dissolved in n-butanol and the solution was cast on a Teflon plate, and the solvent was evaporated slowly under the saturated vapour at room temperature. Finally, a yellowish, water insoluble thin film was formed which was used for spectroscopic characterization.

3.2.12. Preparation of Hoechst 33258 (H258)-DNA Complex: The H258-DNA solution was prepared by adding a requisite amount of the probe in DNA solution and stirring for 1 h. The final concentration ratio of [DNA]:[H258] was 10:1.

3.2.13. Synthesis of Cu_{QC}@BSA: Cu QCs were prepared by the following procedure [11]: First, aqueous CuSO₄ solution (1 mL, 20 mM) was added to BSA solution (5 mL, 15 mg/mL). The solution was stirred at room temperature for 2-3 min and then NaOH solution was introduced so that pH 12 is achieved. The colour of the solution changed from blue to violet within 2-5 min. Finally, the mixture was allowed to stir for 6 to 8 h at 55°C and the colour changes to light brown. It has to be noted that formation of the Cu QCs at room temperature is possible; however, need more time (48 h) compared to that at 55°C (6-8 h).

3.2.14. Quantum Yield Calculation: The quantum yield was calculated according to the equation [12]:

$$Q = Q_R \left(\frac{I}{I_R} \right) \left(\frac{OD_R}{OD} \right) \left(\frac{n^2}{n_R^2} \right) \quad (3.15)$$

where Q and Q_R are the quantum yield of the protein and reference, I and I_R are the integrated fluorescence intensities of the protein and reference, OD and OD_R are the optical densities of the protein and reference at the excitation wavelength, and n and n_R are the refractive indices of the protein and reference solutions.

References

- [1] R.K. Mitra, S.S. Sinha, S.K. Pal, Temperature-Dependent Solvation Dynamics of Water in Sodium Bis(2-ethylhexyl) Sulfosuccinate/Isooctane Reverse Micelles, *Langmuir* 24 (2008) 49.
- [2] R. Sarkar, S.S. Narayanan, L.-O. Palsson, F. Dias, A. Monkman, S.K. Pal, Direct Conjugation of Semiconductor Nanocrystals to a Globular Protein to Study Protein-Folding Intermediates, *J. Phys. Chem. B* 111 (2007) 12294.
- [3] K.E.V. Holde, W.C. Johnson, P.S. Ho, Principles of Physical Biochemistry, Pearson Prentice Hall, New Jersey, 2006.
- [4] A. Cooper, M.A. Nutley, A. Walood, Protein-Ligand Interactions: Hydrodynamics and Calorimetry, Oxford University Press, Oxford, 2000.
- [5] N. Goswami, A. Makhral, S.K. Pal, Toward an Alternative Intrinsic Probe for Spectroscopic Characterization of a Protein, *J. Phys. Chem. B* 114 (2010) 15236.
- [6] G. Cosa, K.-S. Focsaneanu, R.N. McLean, J.P. McNamee, J.C. Scaiano, Photophysical Properties of Fluorescent DNA-Dyes Bound to Single and Double Stranded DNA in Aqueous Buffered Solution, *Photochem. Photobiol.* 73 (2001) 585.
- [7] S.R. Gallagher, F.M. Ausubel, R. Brent, K.E. Kingston, D.D. Moore, J.G. Seidman, J.A. Smith, K. Struhl (Eds.) Current Protocols in Molecular Biology, Greene and Wiley-Interscience, New York, 1994.
- [8] N. Goswami, R. Saha, S.K. Pal, Protein-Assisted Synthesis Route of Metal Nanoparticles: Exploration of Key Chemistry of the Biomolecule, *J. Nanopart. Res.* 13 (2011) 1.
- [9] N. Goswami, A. Giri, S. Kar, M.S. Bootharaju, R. John, P.L. Xavier, T. Pradeep, S.K. Pal, Protein-Directed Synthesis of NIR-Emitting, Tunable HgS Quantum Dots and their Applications in Metal-Ion Sensing, *Small* 8 (2012) 3175.
- [10] N. Goswami, A. Giri, S.K. Pal, MoS₂ Nanocrystals Confined in a DNA Matrix Exhibiting Energy Transfer, *Langmuir* 29 (2013) 11471.
- [11] N. Goswami, A. Giri, M.S. Bootharaju, P.L. Xavier, T. Pradeep, S.K. Pal, Copper Quantum Clusters in Protein Matrix: Potential Sensor of Pb²⁺ ion, *Anal. Chem.* 83 (2011) 9676.

[12] J. Chen, S.L. Flaugh, P.R. Callis, J. King, Mechanism of the Highly Efficient Quenching of Tryptophan Fluorescence in Human gD-Crystallin, *Biochemistry* 45 (2006) 11552.

Chapter 4

Exploration of Key Pathways in the Biomolecule-assisted Metal Ion Reduction for Nanoparticle Synthesis

4.1. Introduction

Inorganic nanoparticles of controlled size have been of great interest recently for a number of possible applications in electronic or optical materials, as well as in catalysis [1-6]. For example, Au nanoparticles have attracted much attention in chemistry and material science because of their good biocompatibility, facile synthesis [7], and conjugation to a variety of bimolecular ligands, antibodies, and other targeting moieties [8], which make them suitable for the use in biochemical sensing and detection [9-11]. Biocompatibility of the inorganic nanoparticles often relies on two synthetic strategies; one uses nanocages of biological macromolecules (e.g., ferritin [12, 13], apoferritin [14] heat-shock protein [15] etc.) and the other method is involved with the self-assembling property of the biological macromolecules (e.g., protein [16], peptides [17], DNA [18, 19] etc.). The first synthetic strategy is quite straightforward as the size and its interaction with the nanocages dictate the quality of the synthesized nanoparticles [13, 14]. On the other hand the second route essentially depends on the primary condition for the nucleation and capping by the biomolecules, which is relatively less explored. One of the recent studies uses small peptides to prepare the nanoparticles [20]. It has been demonstrated that the reduction capability and the net charge of a peptide play the key role on the nucleation and growth of the Au nanoparticles. However, a detailed study highlighting every step involved in the formation of nanoparticles using large protein molecules is absent in the literature and is the motive of the present study.

In this chapter, we report the facile preparation of “green” Au nanoparticles (NPs) in a number of protein solutions starting from globular proteins to enzyme and finally protein mixture extract from Escherichia Coli, a gram negative bacterium, without the addition of any reducing agent. The nucleation of NPs in the protein environments, which is the consequence of electron transfer from protein to the metal ions, is observed to be dependent on the melting temperature of the host protein. However, time required

to start the nucleation (induction time) is also found to be protein-specific. Here, we have attempted to rationalize the protein-assisted formation of NPs in a simple analytical model of autocatalysis. This model is evolving under the impudence of two distinct reactions. The first of these is the thermal denaturation of the protein structure under thermal condition and the second one is reversible autocatalytic process in which Au NP is the autocatalytic species (both the product and catalyst for the reaction). The obtained nanoparticles are characterized by ultraviolet-visible (UV-vis) absorption spectroscopy, high resolution transmission electron microscopy (HRTEM). The change in the protein structure at various temperatures has been followed by circular dichroism (CD) spectroscopy. In this work, we have also demonstrated that the protein capped NPs can be utilized as an efficient catalyst for the degradation of 4-nitrophenylacetate (4-NPA) using NaBH₄ as the hydrogen donor. The reduction of 4-NPA to 4-aminophenol is of industrial importance as 4-aminophenol is a commercially important intermediate for the manufacture of analgesic and antipyretic drugs. Although a number of researchers have extensively studied the catalytic reduction of 4-nitrophenol (4-NP) by NaBH₄ using polymer/resin bead-supported metal NPs, [21-24] the synthesis of protein capped Au NPs and the use of these NPs without any support for this catalytic purpose has not been attempted earlier. The kinetics of the catalysis is observed to follow Langmuir-Hinshelwood model of surface mediated catalysis reaction.

4.2. Results and Discussion

4.2.1. Protein-assisted Synthesis Route of Metal Nanoparticles: Exploration of Key Chemistry of the Biomolecule [25]:

Figure 4.1a presents the TEM image of Au@HSA nanobioconjugates. The image reveals that the nanobioconjugates are almost spherical in shape and follow a uniform narrow size distribution. Particle sizes have been estimated by fitting our experimental TEM data to be 3.1 nm (inset in Figure 4.1a (right)). The corresponding HRTEM image of the particles is shown in Figure 4.1b. The interplanar distance of the fringes is measured to be about 0.24 nm, consistent with the distance between the (111) planes of the gold crystal lattice. The image in the inset of Figure 4.1b represents the corresponding selected area electron diffraction (SAED) pattern which confirms the

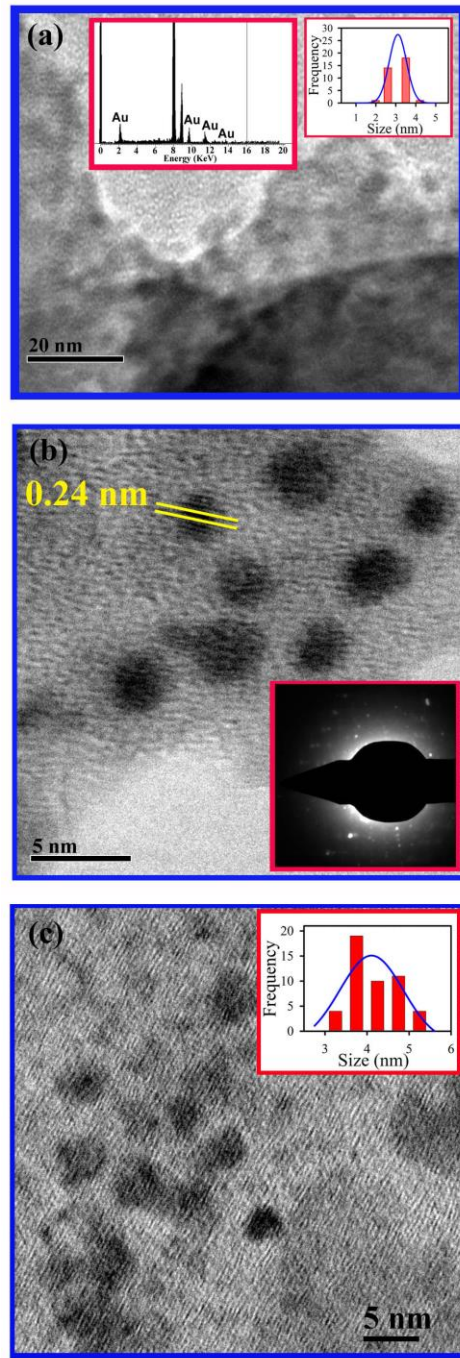


Figure 4.1. (a) HRTEM of Au@HSA nanobioconjugates. The EDAX pattern (left) and the size distribution (right) of the sample are shown in the insets. (b) HRTEM image and SAED showing the crystalline structure of Au@HSA NPs. (c) HRTEM of Au@BSA nanobioconjugates. The size distribution of the sample is shown in the inset.

crystallinity of those particles. It has to be noted that the average size of 3.1 nm Au NPs obtained in the Au@HSA nanobioconjugates, is also confirmed from TEM and absorption studies (see later in the text). Thus in our experimental conditions, the possibility of formation of free larger Au NPs of micrometre size (due to uncontrolled growth) is negligibly small as they are not revealed in the TEM images of the sample. A typical energy-dispersive X-ray (EDAX) spectrum of Au@HSA sample is shown in the inset of Figure 4.1a (left) revealing the presence of Au NPs. Figure 4.1c presents the HRTEM image of Au@BSA nanobioconjugates and the size distribution is shown as an inset of Figure 4.1c.

It is well-known that the Au NPs of less than 10 nm exhibit a surface plasmon (SP) band in the visible region (~ 530 nm) [26]. A change in absorbance or wavelength of the SP band [27-29] provides a measure of particle size, shape, concentration, and dielectric medium properties. Figure 4.2a shows the UV-vis spectra of the Au NPs conjugated with HSA, BSA, SC and E. coli extract protein revealing surface plasmon bands at 530 nm, 531 nm, 540 nm and 600 nm respectively. On the basis of Mie theory [30] and its expanded versions [31, 32], information concerning nanoparticle sizes can be derived from the analysis of this absorption band. The average radius of Au NPs (spherical as revealed from HRTEM), can be approximately estimated from the resonance optical absorption spectrum as per the Mie scattering formula [30]:

$$r_{metal} = \frac{v_F}{\Delta\omega_{1/2}} = \frac{v_F}{2\pi c_0 \left(\frac{\Delta\lambda}{\lambda_p^2} \right)} \quad (4.1)$$

where v_F = Fermi velocity (1.39×10^6 m/s for Au) [33] and $\Delta\omega_{1/2}$ is the full width at half-maximum (FWHM) of the SPR absorption when plotted as a function of angular frequency ω , c_0 is the speed of light in vacuum, λ_p is the wavelength where absorption peak appears, and $\Delta\lambda$ gives the FWHM of the band. The average diameters of the NPs calculated using equation (4.1) is found to be in the range of 3.4 nm, 3.5 nm and 3.7 nm for HSA, BSA and SC respectively, consistent with those observed in TEM studies. Relatively broad surface plasmon band of Au@E. Coli extract indicates the broad size distribution which is mainly due to the mixture of proteins present in the solution. Figure 4.2b shows the UV-vis absorption spectra obtained at different time intervals after

mixing with aqueous AuCl_4^- solution with HSA in phosphate buffer at 76°C temperature. Formation of Au nanoparticles in the colloidal solution was monitored from their absorption spectra as the small noble metal particles reveal absorption band in the UV-vis spectral region due to surface plasmon resonance (SPR) [34]. The sharp absorption band peaking at 530 nm indicates a relatively high monodispersity, both in size and shape of

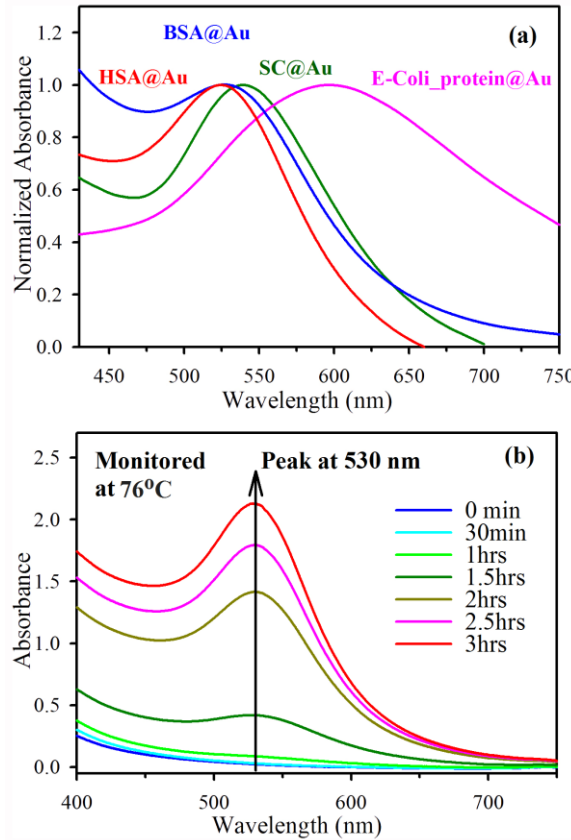


Figure 4.2. (a) UV-vis spectra of Au NPs conjugated with various proteins, HSA, BSA, SC and E. Coli extract respectively. (b) Time-resolved UV-vis spectra for one of the representative proteins (HSA) at 76°C .

the Au particles [35], consistent with the HRTEM images. Long-time stability of the Au NP in aqueous solutions (for several months) indicates that the HSA serves as capping agent. In the case of the other proteins, a similar trend was observed as that of the HSA.

The evolution of the optical density at 530 nm and 540 nm are presented for Au@HSA at 76°C and Au@SC at 60°C in Figure 4.3a and 4.3b respectively. It is apparent that for Au@HSA the optical density increases very slowly upto 120 min for HSA,

indicating an induction time (t_0), then sharply increases and finally saturates at a constant value which corresponds to a complete reduction stage. The induction time became shorter when the concentration of protein is increased. The most interesting information is the variation in induction period (shown in Figure 4.3d) for protein to protein with same concentration. We assume that the size as well as the melting temperature are the

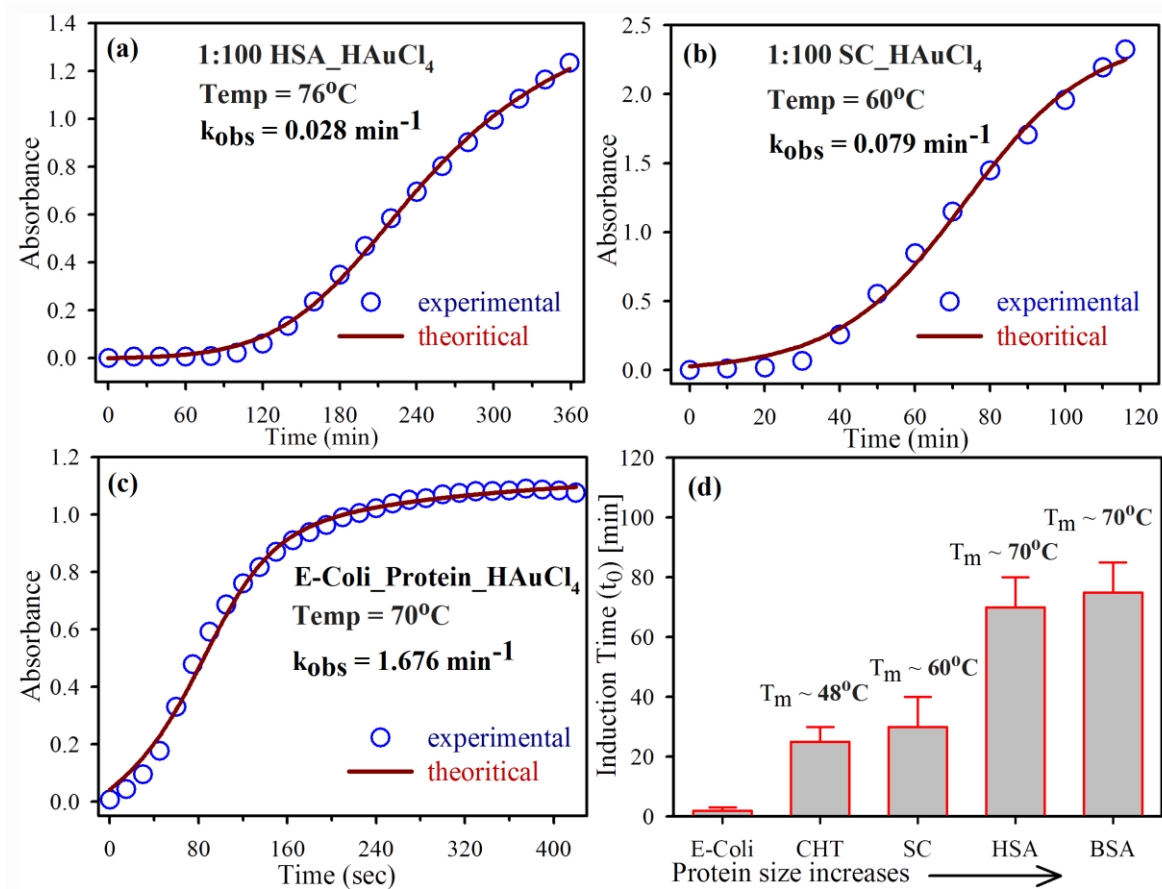


Figure 4.3. (a) Time course of absorbance at 530 nm during the formation of Au NPs particles by HSA protein in phosphate buffer solution. (b) Similar curve at 540 nm by using SC in phosphate buffer solution. The red lines are the theoretical curves generated by using equation (2.42). Blue circles are the experimental data for HSA and SC respectively. (c) Absorbance kinetics of the Au NPs formation at 580 nm using E. Coli extract as reducing agent. (d) Plot of induction time for different proteins. In all the cases (except E. Coli) the protein salt ratio has maintained to 1:100 where the protein concentration is fixed at 20 μM .

predominant factor for the induction period. The denaturation of protein plays an important role in activating the reaction. From Figure 4.3d, it is clear that proteins

having low melting temperature have small induction time and vice versa. Second, based on the experimental results, we have proposed an analytical model for the kinetics of the Au@protein system (Scheme 4.1) which suggests that autocatalysis is involved for the synthesis process. This model suggests that during the induction period, nucleations of the NPs are slowly formed and can be considered as seeds. The formation of these nucleations, or seeds, catalyses the reduction processes and thus in the next stage (2nd step of Scheme 4.1), seed-mediated nucleation and growth occur simultaneously, and the number of particles rapidly increases as the reaction progresses. Here, the strong capping property of the proteins inhibits the nanoparticle growth, thus generating high monodispersity. The solid lines in Figure 4.3 refer to the fit of the experimental data with equation (2.42), while Table 4.1 shows the fitting parameters. This model gives a quantitative explanation of the kinetic data shown in Figure 4.3 for all the proteins. In particular, it explains the dependence of induction time on the k_1 i.e., higher the value of rate constant (k_1), smaller the induction time and vice versa. The autocatalytic rate constant (k_2) as revealed from Table 4.1, demonstrates that larger proteins (i.e., HSA or BSA) are less active than smaller proteins (i.e., SC, CHT or E. Coli extract) for the growth of NPs. The overwhelming contribution of growth step compared to that of the nucleation is clear from Table 4.1. In simple autocatalytic reaction[36] the overall rate is obtained by plotting $\ln[a/(1-a)]$ vs time (data not shown) where $a = (O.D(t)/O.D(\infty))$ and $O.D(t)$ and $O.D(\infty)$ are the optical densities at times t and ∞ , respectively. The rate constant (k_{obs}) is obtained from the slopes of these plots. In case of Au@HSA the value of k_{obs} is found to be 0.028 min^{-1} .

Table 4.1. List of the parameters obtained from the analytical model of nanoparticle formation.

| Protein | $k_1 (\text{min}^{-1})$ | $k_2 (\text{M}^{-1}\text{min}^{-1})$ | m (%) | n (%) |
|----------------|-------------------------|--------------------------------------|-----------|-----------|
| HSA | 1.245×10^{-4} | 0.015 | 0.91(91%) | 0.09(9%) |
| SC | 4.677×10^{-4} | 0.020 | 0.79(79%) | 0.21(21%) |
| E-Coli Extract | 3.178×10^{-1} | 3.488 | 0.72(72%) | 0.28(28%) |

It is well known that conformational changes occur when proteins adsorb onto nanoparticles [37]. It has been demonstrated that in the presence of gold nanoparticles, BSA shows a decrease in α -helical structure, as detected by circular dichroism (CD), and a significant increase in sheet and turn structures, as detected by Fourier transform infrared (FTIR) spectroscopy [38]. In our study, although proteins are denatured at the particle formation temperature yet more conformational changes occur with time due to the intrinsic properties of the protein combined with features of the nanoparticles, such as surface chemistry and surface curvature. Figure 4.4 shows the decrease of molar ellipticity with time which describes more structural perturbation. The rate constant of

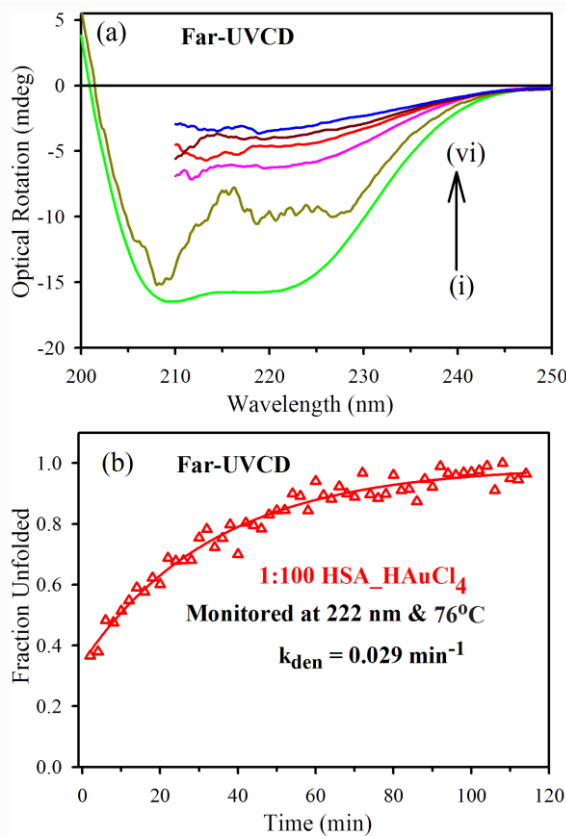
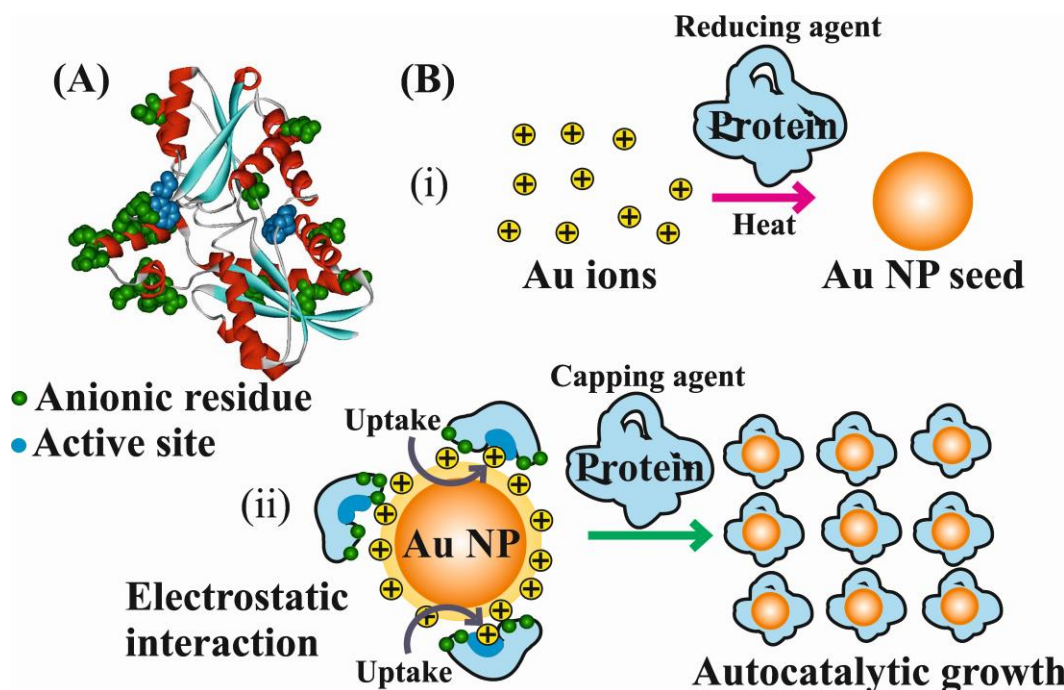


Figure 4.4. (a) Far-UV CD spectra of (i) $1\text{ }\mu\text{M}$ HSA and 1:100 HSA-HAuCl₄ at (ii) initially at room temperature (iii) after 30 min (iv) after 60 min (v) after 90 min (vi) after 180 min. (iii) to (vi) are at 76°C temperature. (b) Far-UV CD spectrum of 1:100 HSA-HAuCl₄ system monitored at 222 nm and 76°C temperature.

protein conformational change (k_{den}) is obtained by fitting the experimental data with first order exponential equation. It has been found that in case of Au@HSA system the

value of k_{den} (0.029 min^{-1}) is very much comparable to the value of k_{obs} (0.028 min^{-1}) which reveals more conformational change during the autocatalytic process. Figure 4.3c represents the evolution of the SPR peak at 580 nm with time for a mixture of proteins obtained from E. Coli extract. Here, the shorter induction time is probably due to the mixture of protein present in the extract. At higher temperature relatively smaller proteins are denatured very quickly resulting very fast reduction of Au ions. The role of DNA in the E. Coli extract in the formation of Au NPs has been ruled out as a control study on DNA-Au (III) ion mixture at 75°C fails to reveal any Au NPs even after 2 hours. Generalized two-step mechanism for autocatalytic growth is shown in Scheme 4.1 where the first step is the slow nucleation step and the second step indicates the seed mediated autocatalytic growth.

In the present study, the catalytic function of Au@protein nanobioconjugates is substantiated by carrying out the reduction of aqueous 4-NPA, which has a peak at 276 nm in the UV-visible spectrum (Figure 4.5a curve I). Addition of sodium borohydride to 4-NPA immediately results in a shift in the peak to 400 nm with intensification of yellow



Scheme 4.1. (a) (A) Molecular structure of Subtilisin *Carlsberg*. (B) Generalized two-step mechanism for solution-phase Au nanoparticle synthesis.

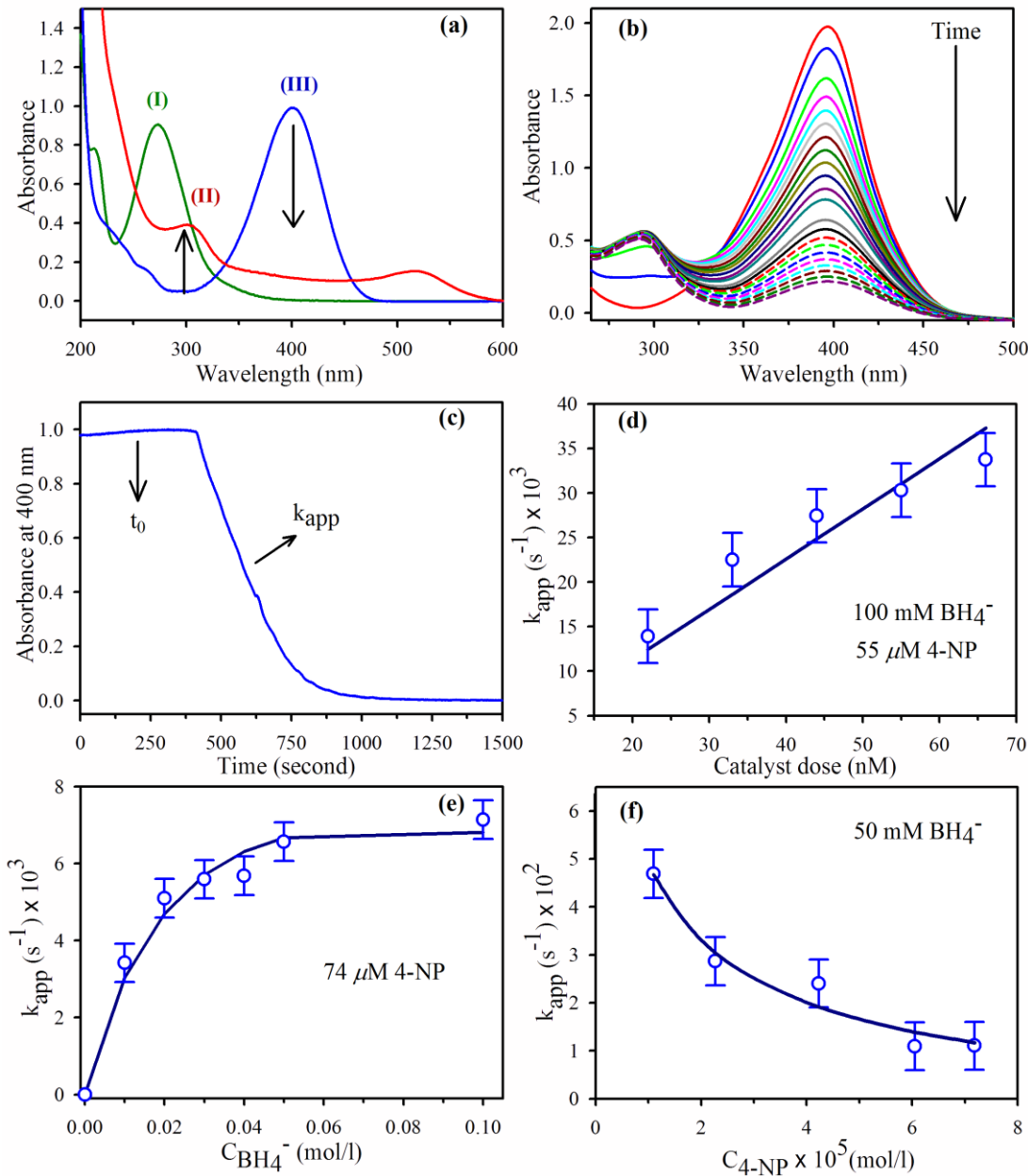


Figure 4.5. (a) Absorption spectra of 4-NPA (I) in absence of NaBH₄, (II) in presence of NaBH₄ at 0 min and (III) in presence of Au@protein nanobioconjugates. Conditions: [4-NP] = 5.5×10^{-5} M; [Au NPs] = 2.2×10^{-7} M; [NaBH₄] = 0.1 M. (b) Concentration versus time plot (monitored at 400 nm) for 4-NPA reduction by NaBH₄. Conditions: [4-NP] = 5.5×10^{-5} M; [NaBH₄] = 0.1 M. (c) Typical time dependence of the absorption of 4-NPA at 400 nm. (d) Plot of apparent rate constant (k_{app}) versus catalyst dose for 4-NPA reduction by NaBH₄ in the presence of Au@protein solution as catalyst. Conditions: [4-NP] = 5.5×10^{-5} M; [NaBH₄] = 0.1 M. (e) and (f) Dependence of the apparent rate constant k_{app} on the concentration of BH₄⁻¹ (e) and 4-NP (f). The blue solid lines are the fit of the Langmuir Hinshelwood model. The surface area of Au nanoparticles is $0.0106 \text{ m}^2 \text{L}^{-1}$ in both cases.

colour of the solution (Figure 4.5a curve III) due to nitrophenolate ion formation. In the absence of any catalyst, the peak at 400 nm remained unaltered even for two days. Addition of Au@protein nanobioconjugates to the yellow colour of the nitrophenolate ion solution immediately results the diminution of 400 nm peak with intensification of a new peak at \sim 297 nm (Figure 4.5a curve II) because of the reduction of 4-nitrophenolate species to 4-aminophenol (4-AP). A control experiment with denatured proteins devoid of gold nanoparticles did not provide any signature of 4-AP under the same experimental condition. The generation of 4-AP confirms the catalytic activity of the Au nanoparticles for the reduction of 4-nitrophenolate in aqueous solution. Figure 4.5b shows that after the addition of Au nanoparticles the absorption peak at 400 nm gradually drops with time. Figure 4.5c shows the time dependence results obtained from the reaction conducted at room temperature. This observation indicates that upon the addition of Au@protein nanobioconjugates, a certain period of time was required for the 4-nitrophenolate to adsorb onto the catalyst's surface before the reaction could be initiated. Here we define this period of time as the adsorption time or t_{ads} . After the adsorption time, the reaction becomes stationary and follows first order rate law. The apparent rate constant (k_{app}) is calculated from the linear slope of the curve and in the following we shall discuss it in terms of L-H model.

The mutual dependence of k_{app} on the catalytic dose as well as concentration of borohydride and 4-NP has shown in Figure 4.5 (d, e, and f) where the solid lines refer to the fits of the experimental data with use of equation (2.47) while the best fitting results are obtained with $k = 4.4 \pm 1.0 \times 10^{-4} \text{ mol/m}^2 \text{ s}$, $k_{4\text{-NP}} = 14000 \pm 200 \text{ lit/mol}$, $k_{\text{BH}_4} = 22 \pm 2 \text{ lit/mol}$, $m = 0.9 \pm 0.1$ and $n = 0.6 \pm 0.1$. The orders of the kinetic parameters so determined are quite close to those obtained by Wunder et al [39]. The k_{app} obtained from the linear slope of the kinetic curves has been linearly related to the catalyst dose (shown in Figure 4.5d) i.e., the surface area available for catalysis, keeping other parameters such as initial 4-NPA concentration and borohydride concentration the same, which could be rationalized by considering the fact that the catalysis usually takes place on the surface of the Au nanoparticles [40]. The nonlinear relationship of k_{app} versus c_{BH_4} i.e., conc. of borohydride and the saturation at high concentrations, shown in Figure 4.5e, clearly demonstrates the diffusion of the borohydride to the nanoparticles. The effect of 4-NPA concentration on the reduction rate was studied keeping other parameters such as

catalyst dose and borohydride concentration unchanged. As depicted in Figure 4.5f, in the case of 4-NP reduction using Au NPs as catalyst, it was found that in the very low concentration range of 4-NP, k_{app} decreased with the increase of 4-NP concentration, and in the high concentration range k_{app} remained constant. This is due to high concentration of 4-NP leads to almost full coverage of the surface of the nanoparticles. This slows down the reaction with the borohydride ions on the surface of the Au NPs. Figure 4.5e and 4.5f, clarifies the mutual relationship of k_{app} with c_{BH_4} and c_{4-NP} which demonstrates that there must be a competition between the reactants on the catalyst's surface. Moreover, the fitted data in Figure 4.5d, e and f clearly demonstrate that the reduction of 4-NP can be described by the L-H model with good accuracy.

4.3. Conclusion

In conclusion, detail understanding of the associated biochemistry of the proteins during the formation of inorganic nanoparticles has been successfully demonstrated. A number of proteins have been investigated to show the possible effects and it has been found that induction time may increase as the melting temperature of a protein is increased. This suggests that low melting temperatures may be important for the nucleation and growth of nanoparticle. An autocatalytic model has been proposed that fits well with the experimental data and suggest that some nucleations are slowly formed during the induction period that boosts the growth of the nanoparticles. Finally, we have demonstrated that the catalytic reduction of 4-NPA by borohydride in the presence of Au NPs can be modelled in terms of the Langmuir Hinshelwood model. All the parameters related to this model have been described here in a very efficient way. We hope that with the continuing efforts toward understanding the mechanism of protein-nanoparticle growth relationship is likely to find use in protein biochemistry, thereby making these studies much more widely accessible in nanobiotechnology.

References

- [1] Y. Sun, Y. Xia, Shape-Controlled Synthesis of Gold and Silver Nanoparticles, *Science* 298 (2002) 2176.
- [2] N. Tian, Z.Y. Zhou, S.-G. Sun, Y. Ding, Z.L. Wang, Synthesis of Tetrahedahedral Platinum Nanocrystals with High-Index Facets and High Electro-Oxidation Activity *Science* 316 (2007) 732.
- [3] R.C. Jin, Photoinduced Conversion of Silver Nanospheres to Nanoprisms, *Science* 294 (2001) 1901.
- [4] R. Narayanan, M.A. El-Sayed, Changing Catalytic Activity during Colloidal Platinum Nanocatalysis Due to Shape Changes: Electron-Transfer Reaction, *J. Am. Chem. Soc* 126 (2004) 7194.
- [5] S. Vajda, J.M. Pellin, P.J. Greeley, L.C. Marshall, A.L. Curtiss, A.G. Ballentine, W.J. Elam, S. Catillon-Mucherrie, C.P. Redfern, F. Mehmood, P. Zapol, Subnanometre Platinum Clusters as Highly Active and Selective Catalysts for the Oxidative Dehydrogenation of Propane, *Nat. Mater.* 8 (2009) 213.
- [6] S.K. Ghosh, T. Pal, Interparticle Coupling Effect on the Surface Plasmon Resonance of Gold Nanoparticles: From Theory to Applications, *Chem. Rev.* 107 (2007) 4797.
- [7] C. Burda, X. Chen, R. Narayanan, M.A. El-Sayed, Chemistry and Properties of Nanocrystals of Different Shapes, *Chem. Rev.* 105 (2005) 1025.
- [8] E. Katz, I. Willner, Integrated Nanoparticle-Biomolecule Hybrid Systems: Synthesis, Properties, and Applications, *Agnew. Chem. Int. Ed.* 43 (2004) 6042.
- [9] J.C. Riboh, A.J. Haes, A.D. McFarland, C. Ranjit, R.P. Van Duyne, A Nanoscale Optical Biosensor: Real-Time Immunoassay in Physiological Buffer Enabled by Improved Nanoparticle Adhesion, *J. Phys. Chem. B* 107 (2003) 1772.
- [10] K.E. Shafer-Peltier, C.L. Haynes, M.R. Glucksberg, R.P. Van Duyne, Toward a Glucose Biosensor Based on Surface-Enhanced Raman Scattering, *J. Am. Chem. Soc.* 125 (2003) 588.
- [11] J.J. Storhoff, R. Elghanian, R.C. Mucic, C.A. Mirkin, R.L. Letsinger, One-Pot Colorimetric Differentiation of Polynucleotides with Single Base Imperfections Using Gold Nanoparticle Probes, *J. Am. Chem. Soc.* 120 (1998) 1959.

- [12] R.M. Kramer, C. Li, D.C. Carter, M.O. Stone, R.R. Naik, Engineered Protein Cages for Nanomaterial Synthesis, *J. Am. Chem. Soc.* 126 (2004) 13282.
- [13] M.L. Flenniken, M. Uchida, L.O. Liepold, S. Kang, M.J. Young, T. Douglas, A Library of Protein Cage Architectures as Nanomaterials, *Curr. Top. Microbiol. Immunol.* 327 (2009) 71.
- [14] H. Kim, E. Pippel, U. Gosele, M. Knez, Titania Nanostructures Fabricated by Atomic Layer Deposition Using Spherical Protein Cages, *Langmuir* 25 (2009) 13284.
- [15] M.T. Klem, D. Willits, D.J. Solis, A.M. Belcher, M. Young, T. Douglas, Bio-Inspired Synthesis of Protein-Encapsulated CoPt Nanoparticles, *Adv. Funct. Mat.* 15 (2005) 1489.
- [16] J.P. Xie, Y.G. Zheng, J.Y. Ying, Protein-Directed Synthesis of Highly Fluorescent Gold Nanoclusters, *J. Am. Chem. Soc.* 131 (2009) 888.
- [17] E. Dinda, M.H. Rashid, T.K. Mandal, Amino Acid-Based Redox Active Amphiphiles to In Situ Synthesize Gold Nanostructures: From Sphere to Multipod, *Cryst. Growth Des.* 10 (2010) 2421.
- [18] C.A. Mirkin, R.L. Letsinger, R.C. Mucic, J.J. Storhoff, A DNA-Based Method for Rationally Assembling Nanoparticles into Macroscopic Materials, *Nature* 382 (1996) 607.
- [19] C.J. Loweth, W.B. Caldwell, X.G. Peng, A.P. Alivisatos, P.G. Schultz, DNA-Based Assembly of Gold Nanocrystals, *Agnew. Chem. Int. Ed.* 38 (1999) 1808.
- [20] Y.N. Tan, J.Y. Lee, D.I.C. Wang, Uncovering the Design Rules for Peptide Synthesis of Metal Nanoparticles, *J. Am. Chem. Soc.* 132 (2010) 5677.
- [21] K. Esumi, R. Isono, T. Yoshimura, Preparation of PAMAM- and PPI-Metal (Silver, Platinum, and Palladium) Nanocomposites and Their Catalytic Activities for Reduction of 4-Nitrophenol, *Langmuir* 20 (2004) 237.
- [22] S. Praharaj, S. Nath, S.K. Ghosh, S. Kundu, T. Pal, Immobilization and Recovery of Au Nanoparticles from Anion Exchange Resin: Resin-Bound Nanoparticle Matrix as a Catalyst for the Reduction of 4-Nitrophenol, *Langmuir* 20 (2004) 9889.
- [23] S. Saha, A. Pal, S. Kundu, S. Basu, T. Pal, Photochemical Green Synthesis of Calcium-Alginate-Stabilized Ag and Au Nanoparticles and Their Catalytic Application to 4-Nitrophenol Reduction, *Langmuir* 26 (2010) 2885.
- [24] H. Zhang, X. Li, G. Chen, Ionic Liquid-Facilitated Synthesis and Catalytic Activity of Highly Dispersed Ag Nanoclusters Supported on TiO₂, *J. Mater. Chem.* 19 (2009) 8223.

- [25] N. Goswami, R. Saha, S. Pal, Protein-Assisted Synthesis Route of Metal Nanoparticles: Exploration of Key Chemistry of the Biomolecule, *J. Nanopart. Res.* 13 (2011) 5485.
- [26] T.A. El-Brolossy, T. Abdallah, M.B. Mohamed, S. Abdallah, K. Easawi, S. Negm, H. Talaat, Shape and Size Dependence of the Surface Plasmon Resonance of Gold Nanoparticles Studied by Photoacoustic Technique, *Euro. Phys. J.* 153 (2008) 361.
- [27] J. Luo, M.M. Maye, L. Han, N.N. Kariuki, V.W. Jones, Y. Lin, M.H. Engelhard, C.J. Zhong, Spectroscopic Characterizations of Molecularly Linked Gold Nanoparticle Assemblies upon Thermal Treatment, *Langmuir* 20 (2004) 4254.
- [28] S. Link, M.A. El-Sayed, Shape and Size Dependence of Radiative, Non-radiative and Photothermal Properties of Gold Nanocrystals, *Int. Rev. Phys. Chem.* 19 (2000) 409.
- [29] T. Ung, L. Liz-Marzan, P. Mulvaney, Optical Properties of Thin Films of Au@SiO₂ Particles, *J. Phys. Chem. B* 105 (2001) 3441.
- [30] G. Mie, Contributions to the Optics of Turbid Media, Particularly of Colloidal Metal Solutions, *Ann. Phys.* 25 (1908) 377.
- [31] W.T. Doyle, Absorption of Light by Colloids in Alkali Halide Crystals, *Phys. Rev.* 111 (1958) 1067.
- [32] E.J. Zeman, G.C. Schatz, An Accurate Electromagnetic Theory Study of Surface Enhancement Factors for Silver, Gold, Copper, Lithium, Sodium, Aluminum, Gallium, Indium, Zinc, and Cadmium, *J. Phys. Chem.* 91 (1987) 634.
- [33] A. Dhawan, J.F. Muth, Plasmon Resonances of Gold Nanoparticles Incorporated Inside an Optical Fibre Matrix, *Nanotechnology* 17 (2006) 2504.
- [34] C.F. Bohren, D.R. Huffman, Absorption and Scattering of Light by Small Particles, in, John Wiley: New York, 1998.
- [35] N. Malikova, I. Pastoriza-Santos, M. Schierhorn, N.A. Kotov, L.M. Liz-Marzan, Layer-by-Layer Assembled Mixed Spherical and Planar Gold Nanoparticles: Control of Interparticle Interactions, *Langmuir* 18 (2002) 3694.
- [36] Z.Y. Huang, G. Mills, B. Hajek, Spontaneous Formation of Silver Particles in Basic 2-Propanol, *J. Phys. Chem.* 97 (1993) 11542.
- [37] L. Fei, S. Perrett, Effect of Nanoparticles on Protein Folding and Fibrillogenesis, *Int. J. Mol. Sci.* 10 (2009) 646.

- [38] L. Shang, Y. Wang, J. Jiang, S. Dong, pH-Dependent Protein Conformational Changes in Albumin: Gold Nanoparticle Bioconjugates: A Spectroscopic Study, *Langmuir* 23 (2007) 2714.
- [39] S. Wunder, F. Polzer, Y. Lu, Y. Mei, M. Ballauff, Kinetic Analysis of Catalytic Reduction of 4-Nitrophenol by Metallic Nanoparticles Immobilized in Spherical Polyelectrolyte Brushes, *J. Phys. Chem. C* 114 (2010) 8814.
- [40] A. Murugadoss, A. Chattopadhyay, Surface Area Controlled Differential Catalytic Activities of One-Dimensional Chain-like Arrays of Gold Nanoparticles, *J. Phys. Chem. C* 112 (2008) 11265.

Chapter 5

Studies on the Oxidation of Host Biological Macromolecules Relevant to Biomolecule-assisted Metal Ion Reduction

5.1. Introduction

Proteins represent essential building blocks behind cell structure and the engines supporting every metabolic reaction. Fluorescence spectroscopy is a powerful technique for studying various aspects of protein biophysics, such as protein folding, protein-protein interactions, and protein dynamics [1, 2]. Tagging a protein with extrinsic fluorophore is an important and valuable tool for studying structure and microenvironment. Extrinsic fluorescent probes, such as dansyl or related amino acid derivatives, can also be incorporated into proteins via modification of reactive residues, such as lysine and cysteine, or via chemical synthesis [3, 4]. In addition, quantum dots are also useful to know the energy transfer efficiency in protein [5]. However, one of the major disadvantages is the possibility of perturbation of structural integrity of the protein upon incorporation of the extrinsic probe. Moreover bulky nature of the external probe is not suitable for the spectroscopic characterization of a protein such as protein folding, energy transfer etc. An alternative choice for the spectroscopic studies of the proteins is intrinsic fluoroprobes. Most proteins contain amino acid residues that are intrinsically fluorescent: tryptophan, tyrosine, and phenylalanine. Among those tryptophan is the most attractive fluorophore in protein [6]. However, critical wavelength of excitation (295 nm -300 nm) in order to avoid interference of the other fluorescent amino acids (tyrosine and phenyl alanine) and the complicity in data interpretation due to ultrafast internal conversion [7, 8], make spectroscopic studies involving tryptophan as probe to be a bit difficult. Relatively inexpensive laser sources in the desired excitation wavelength (295 nm) are also a problem for such investigations.

Protein consists of several amino acids like tryptophan, tyrosine, arginine, lysine etc., which has the capability of reducing several metal ions. The reduction process involves electron transfer from the amino acid to the metal ion and as a consequence the corresponding amino acid becomes oxidized. It has been reported that the oxidation of

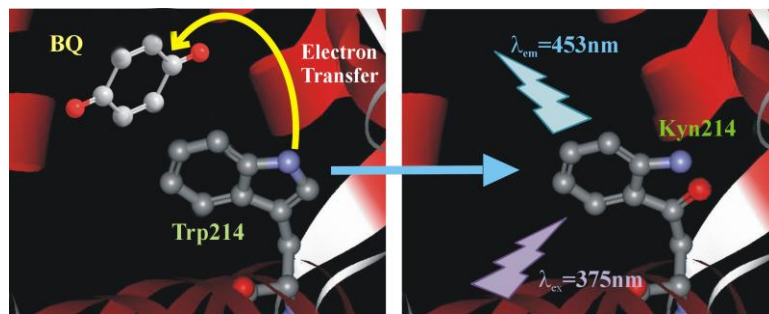
tryptophan in bulk solution results in the formation of a number of byproducts, such as ditryptophan, kynurenone, 3-hydroxy-kynurenone, N-formyl-kynurenone, and some cross-linked products, formed by reaction with these byproducts [9-15]. Each of these byproducts has a specific absorption and shows strong emission, which provides the basis for identifying a particular species. However, oxidation of tryptophan in protein environment is not well studied. In this regard we have modified Trp214 of a model single tryptophan protein human serum albumin (HSA) to kynurenone (Kyn214) by electron transfer reaction. Kynurenone is one of the tryptophan metabolites and omnipresent in the lens of human eyes in order to protect retina from possible UV (300-400 nm) radiation damage [16]. Structural integrity of the protein upon the modification is confirmed by circular dichroism (CD) spectroscopy. Similar unfolding pathways are confirmed by dynamic light scattering (DLS), near and far-UV CD. In order to compare the efficacy of the Kyn214 for the spectroscopic studies of the protein we have also excited Trp214 of the native protein. In this chapter, we have demonstrated that Kyn214 is equally capable compared to Trp214 in order to unravel various folded states of the protein. The femtosecond-resolved dynamics of hydration as revealed by Trp214 in the domain II can also be monitored by Kyn214. Finally, we have shown that the probe can be used for the dipolar interaction with other acceptor protein-bound dyes in order to study FRET [17, 18].

5.2. Results and Discussion

5.2.1. Toward an Alternative Intrinsic Probe for Spectroscopic Characterization of a Protein [19]:

It has been reported that amino acids such that tryptophan, have strong electron-donating properties [20], and the *p*-benzoquinone (BQ), which is hydrophobic in nature, is a strong electron acceptor [21]. Herein, we have utilized this property of BQ, which enters to the hydrophobic cavity of the protein and oxidized the tryptophan (Trp214) to kynurenone (Kyn214) as shown in Scheme 5.1. It can be seen from Figure 5.1a that a new absorption band at 353 nm with relatively broad bandwidth appears in the protein solution after the addition of ethanolic BQ. Although weak as compared to the 280 nm protein peak, the absorption band at 353 nm indicates the formation of Kyn214 in the model protein [22]. The newly generated fluorescence probe with excitation and

emission maxima at 350 and 450 nm, respectively, is clearly observed from modified protein solution (inset of Figure 5.1a). The peak (353 nm) and the bandwidth of the excitation spectrum are identical to the modified protein absorption band in Figure 5.1a. Consistency of the excitation spectrum with that of the absorption and the invariance of the emission spectra with the excitation wavelength confirm the presence of single emissive species i.e Kyn214. The evolutions of the emission spectrum at the various levels of modifications are shown in Figure 5.1b. Initially, no fluorescence (except Trp214 emission at 350 nm, excitation at 299 nm) is observed from protein solutions, but



Scheme 5.1. The modification of Trp214 of a model globular protein (HSA) as a result of electron transfer reaction with benzoquinone (BQ) in the protein cavity is shown (left). The product of the electron transfer reaction kynurenine (Kyn214) in the protein cavity is represented (right). A typical excitation wavelength (375 nm) used in our experiment and emission peak of the modified probe Kyn214 at 453 nm are also shown in the schematic.

modification is clearly demonstrated by the emission spectrum of the protein solution with increasing the concentration of BQ. Creation of an ultrafast component i.e., 290 ps (18%) (inset of Figure 5.1b) is the indication of newly generated fluorophore. The fluorescence decay transient of the modified protein solution (Figure 5.1c) shows three lifetime components: 160 ps (56%), 1240 ps (30%) and 4520 ps (15%) with an average lifetime of 1130 ps. The anisotropy decay reveals a long component of ~50 ns, consistent with the hydrodynamic rotational relaxation time of the protein [23] (inset of Figure 5.1c) in the solution.

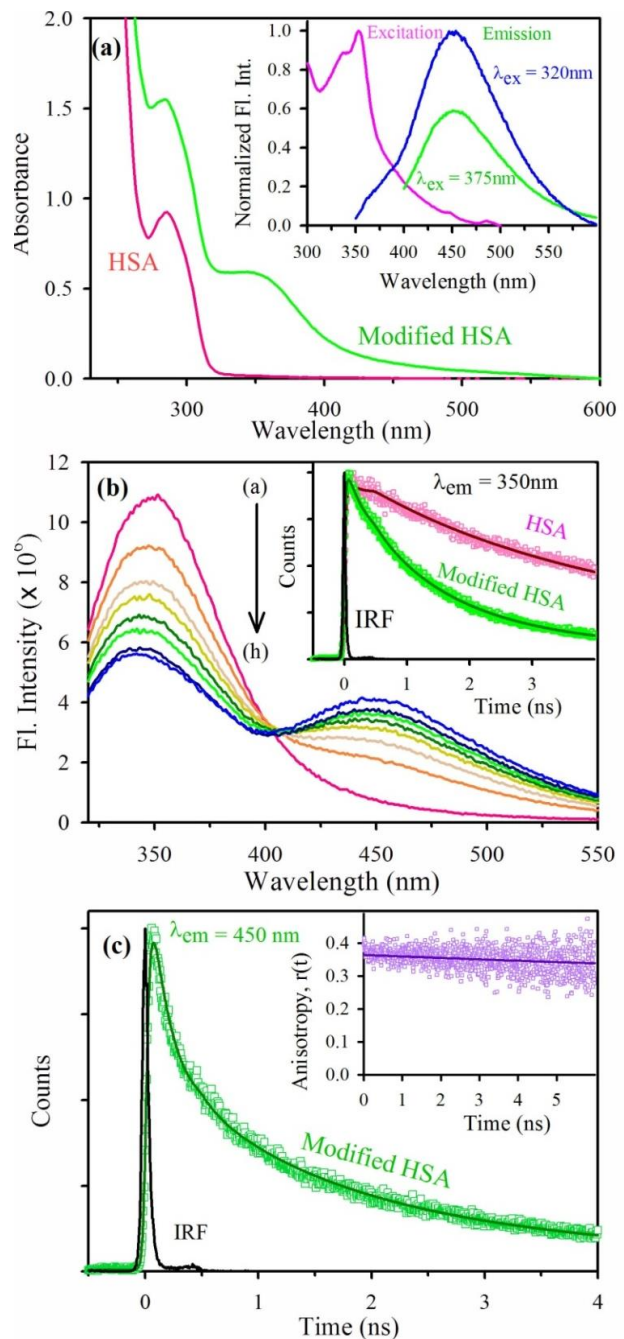


Figure 5.1. (a) Absorption spectrum of HSA and modified HSA. The spectra are recorded at room temperature with a concentration of $20\text{ }\mu\text{M}$ for both modified and non-modified HSA in sodium phosphate buffer ($\text{pH } 7.4, 20\text{ mM}$). Inset shows the excitation and emission spectra of modified HSA. (b) The steady state fluorescence spectrum of HSA in phosphate buffer solution using different BQ concentrations (a-h; $0\text{-}14\text{ }\mu\text{M}$). Inset shows the picosecond resolved fluorescence transients of protein before and after modification (excitation wavelength = 299 nm). (c) The picosecond resolved fluorescence transients of modified HSA collected at 450 nm (excitation wavelength = 375 nm). The fluorescence anisotropy of Kyn214 residue in HSA at 20°C is presented in the inset.

Structural study on the protein is thus of interest, because modification may perturb the native structure and changes in its native conformation could be translated into a loss of its biological function. Persistence of the structural integrity of the protein upon modification is confirmed by dynamic light scattering (DLS), near and far circular dichroism (CD) spectroscopy. The hydrodynamic diameter (d_H) of the modified protein (Figure 5.2a) as revealed from the DLS studies is consistent with that of its unmodified version [23]. The temperature dependent change of the d_H revealing the melting of the overall globular structure of the protein. The invariance of the thermal stability of the modified protein compared that of the native one, is further confirmed by near-UV CD studies [24] as shown in Figure 5.2b. From the Figure 5.2b it is evident that the CD signal at 268 nm indicative of the globular tertiary structure of the protein and the

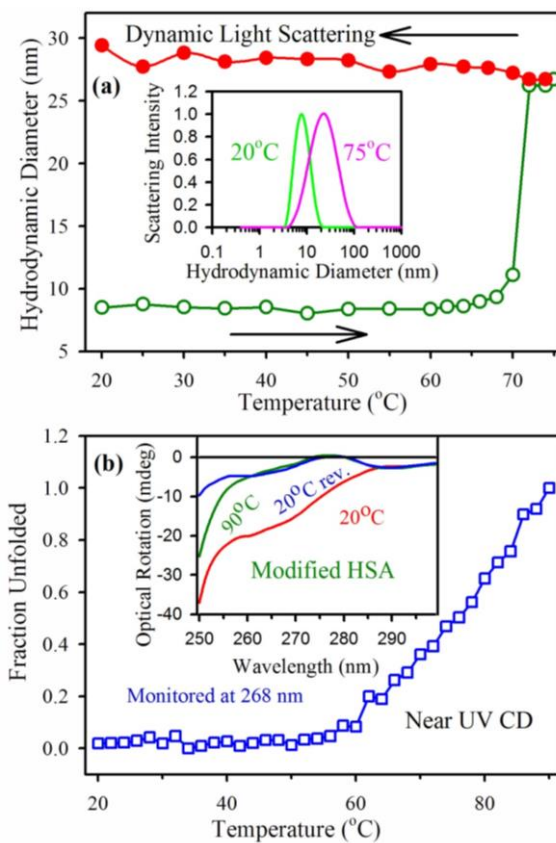


Figure 5.2. (a) Effect of temperature on the size of modified HSA in 20 mM phosphate buffer. Open symbols represent forward (unfolding) process, and closed symbols represent backward (refolding) process. DLS signals of modified HSA at 25°C and 75°C have been presented in the inset. (b) Thermal denaturation plots at 268nm obtained by near-UV CD, from 20 to 90°C. Inset shows the temperature dependence of the near-UV CD spectrum.

melting characteristics of the protein is consistent with that of the unmodified protein. From the DLS and near-UV CD studies it is also evident that the thermal unfolding above the melting temperature (70°C) is irreversible analogous to the thermal denaturation property of the native protein.

The effect of thermal denaturation on the secondary structure (far-UV CD) of the modified and unmodified protein is shown in Figure 5.3. From the Figure 5.3a-b, it is evident that the temperature induced evolution of the far-UV CD spectra of the protein reveals a decrease in the overall ellipticity and the presence of an isodichroic point at 202 nm indicative of a cooperative loss of the α -helix structure of the modified and unmodified proteins in a two-state-type transition [24]. Persistence of the structural integrity of the protein upon modification is further confirmed by monitoring ellipticity at 222 nm (far-UV CD). Both the proteins exhibit comparable sigmoidal transition indicating the similar unfolding pathways [24, 25] revealing melting temperature (T_m) to be 70°C . The observation is consistent with DLS and near-UV CD studies (Figure 5.2).

The efficacy of the probe Kyn214 for the exploration of dynamical information of the protein within its structural integrity as confirmed by CD studies is now point to be discussed. We have compared the efficacy of the Kyn214 to report the dynamics of solvent molecules in the protein cavity. By using femtosecond resolved fluorescence studies the dynamical time constants of the solvent molecules in the protein cavity has been explored to be ultrafast and multi-exponential [26, 27]. It has also been demonstrated that the chemical denaturation of the protein allows more bulk type water in the protein cavity revealing faster time constants in the solvation dynamics [26, 27]. A systematic study on the spectroscopy and dynamics of kynurenone in different solvents has been presented by Vauthay et al. [16]. The usefulness of the probe (Kynurenone) as a solvation reporter has also been established [16]. The main excited state deactivation channel of the probe depends on the interaction of the solvent molecules through hydrogen bonding ability. However, it has to be noted that reorganization of hydrogen bond forming solvents with respect to the probe solute is extremely important for the formation of solute solvent hydrogen bond formation [28]. The rate of reorganization of the water molecules around the solute probe (here kynurenone) is limited by the dynamics of solvation. Thus the two dynamical time scales in a system should be intimately related. The femtosecond fluorescence studies on the probe in various bulk solvents demonstrate

that the excited state lifetime of the probe in water (0.9 ps) significantly increases (more than 1 ns) in DMSO, where the probe-solvent hydrogen bonding interaction is absent. Herein, the femtosecond resolved time constants of the fluorescence transient of the

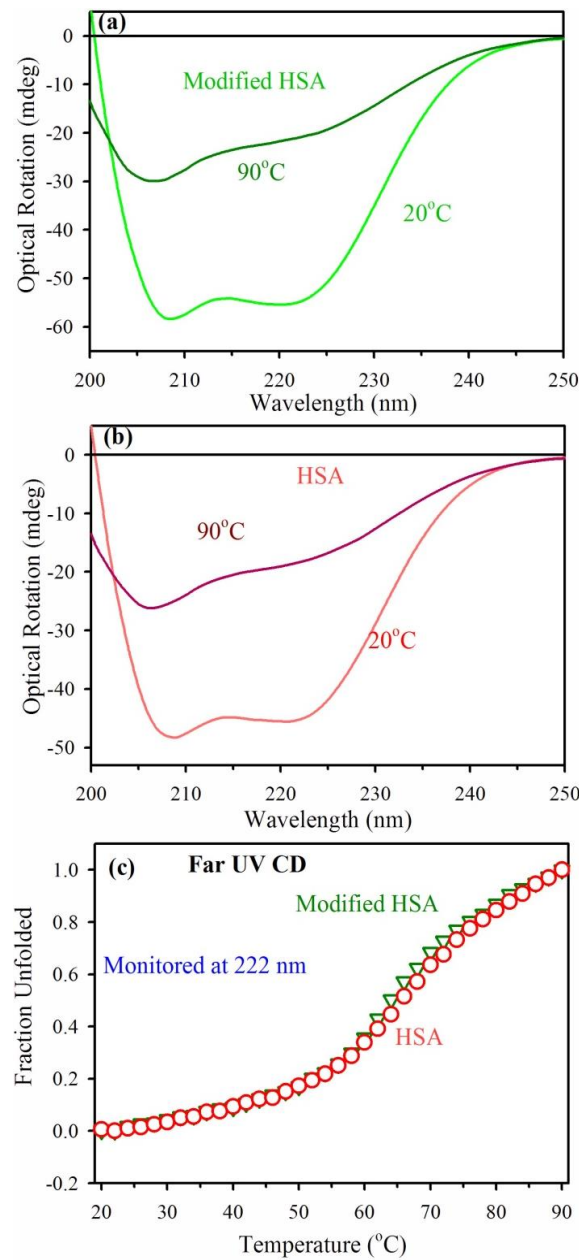


Figure 5.3. Far-UV CD spectrum of (a) modified HSA in sodium phosphate buffer (pH 7.4, 20 mM). (b) HSA in sodium phosphate buffer (pH 7.4, 20 mM). In both cases the spectrums are recorded at 20°C and 90°C. (c) Thermal denaturation plots at 222 nm obtained by far-UV CD, from 20 to 90°C. Transition temperature (T_m , the midpoint of unfolding transition) is 70°C for both (HSA and modified HSA) in phosphate buffer.

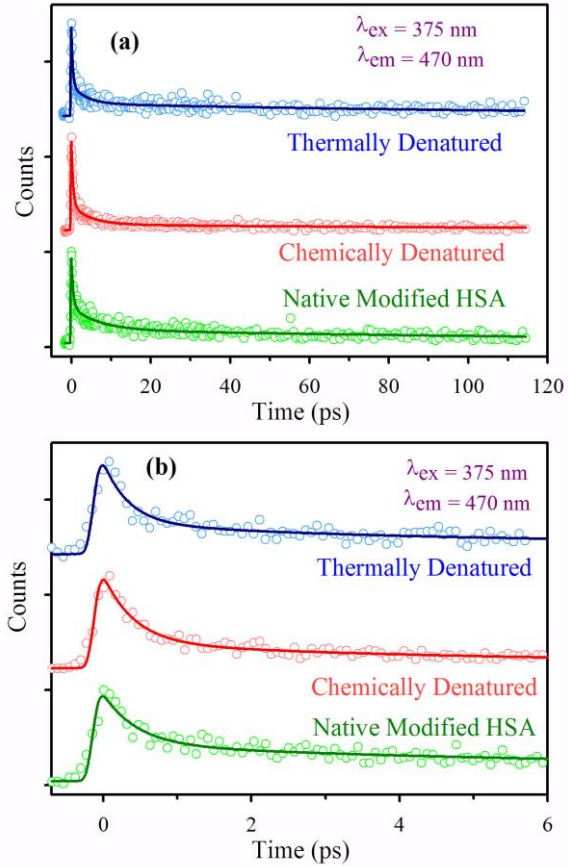


Figure 5.4. (a) Femtosecond time-resolved fluorescence transients of modified HSA in native, chemically and thermally denatured form. The protein is excited at 375 nm, and the transients were collected at 470 nm. (b) Early dynamics at the same wavelengths.

Kyn214 in the native protein (Figure 5.4) are 0.46 ps (65%), 6.80 ps (22%) and 157 ps (13%) revealing the interaction of the probe with water molecules in the cavity. The times constants 0.34 ps (73%), 3.70 ps (17%), 128 ps (10%) at 75°C and 0.42 ps (78%), 4.70 ps (18%), 128 ps (4%) at pH=12 in the denatured states distinctly reveal more water accessibility of the probe Kyn214 compared to that in native conformation consistent with the previous results [26, 27]. Recently Vauthey et al. [29] have explored the photophysics and photochemistry of the kynurenone covalently attached to amino acids and to a model protein. It has been demonstrated that increase of photoactivity of the kynurenone covalently attached to amino acids and protein is due to the decrease of the rate of solvent-assisted internal conversion.

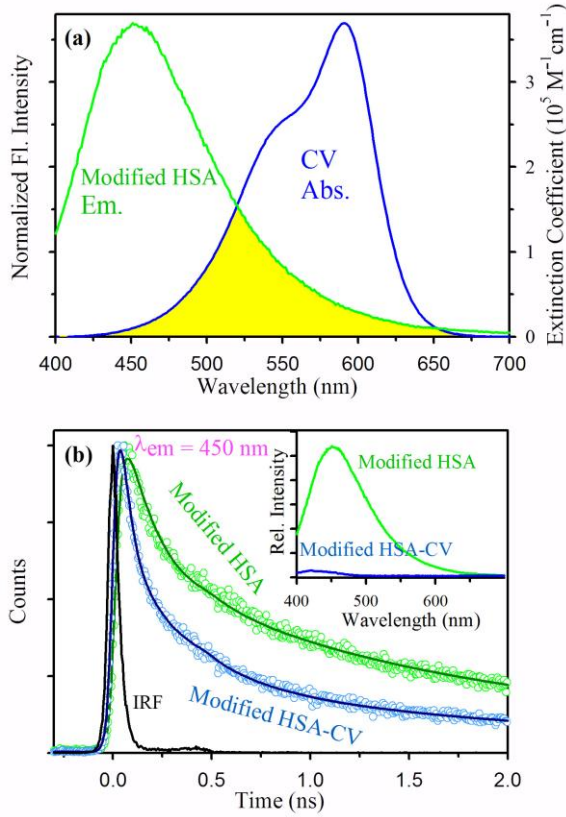


Figure 5.5. (a) Steady state absorption spectra of CV (blue) and emission spectra of Modified HSA (green) are shown. An overlapping zone between emission of Modified HSA and absorption of acceptor CV is indicated as a yellow shaded zone. (b) The picosecond resolved fluorescence transients of Modified HSA, in absence (green) and in presence of acceptor CV (blue) (excitation at 375 nm) collected at 450 nm, are shown. Inset of the Figure 5.5b shows the steady state emission spectrum of modified HSA in presence (blue) and absence (green) of CV.

In order to establish more general use of the modified probe Kyn214, we have described dipolar interaction of the probe with a surface bound organic dye, crystal violet (CV) [30]. From Figure 5.5a, a significant spectral overlap of the Kyn214 emission with the absorption spectrum of CV is evident. The significant quenching in the steady-state emission and picosecond resolved fluorescence transient (at 450 nm) as a consequence of the donor-acceptor dipolar interaction is clearly evident from Figure 5.5b. From this, we have estimated a Förster resonance energy transfer (FRET) efficiency to be 73% and the characteristic distance, R_0 of the FRET pair is 2.72 nm. FRET from Kyn214 (donor) in the native protein to a well-known surface bound organic dye CV is successfully demonstrated and donor acceptor distance of 2.29 nm is found to be consistent with that

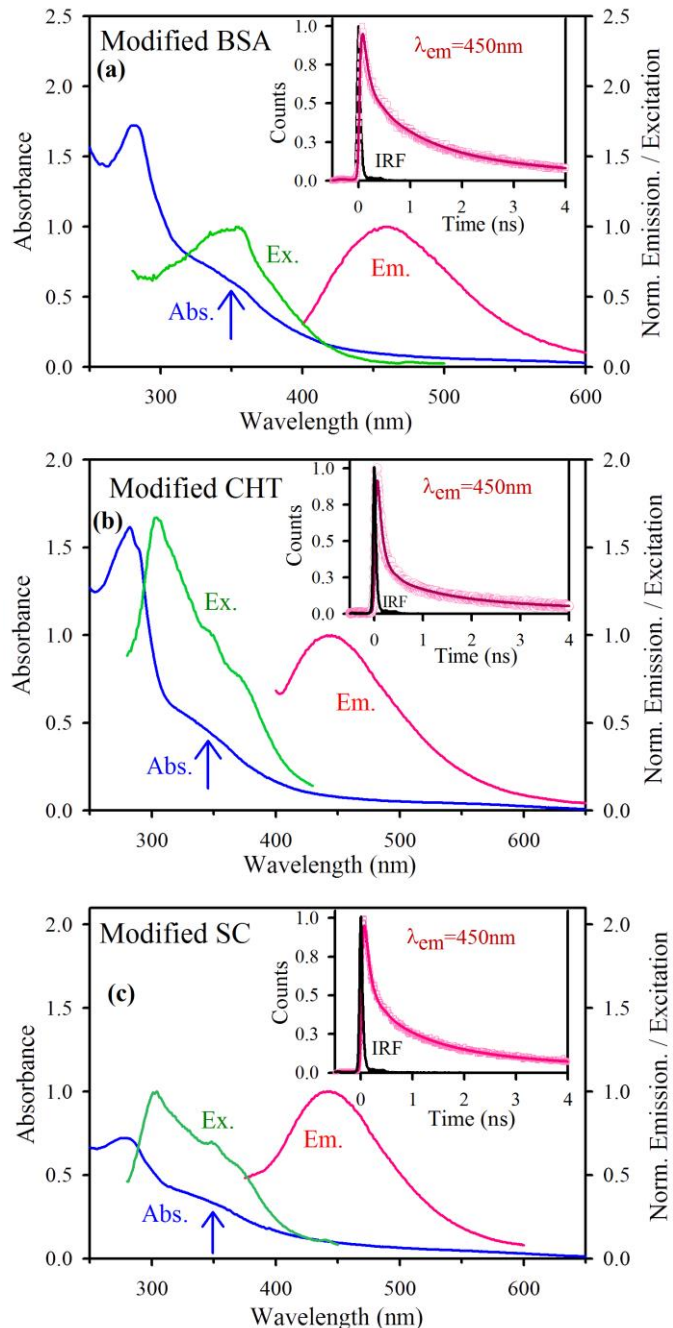


Figure 5.6. (a), (b) and (c) Absorption, excitation and emission spectra of modified bovine serum albumin (BSA), modified α -chymotrypsin (CHT) and modified subtilisin *Carlsberg* (SC) respectively. Insets show their picosecond-resolved fluorescence transients.

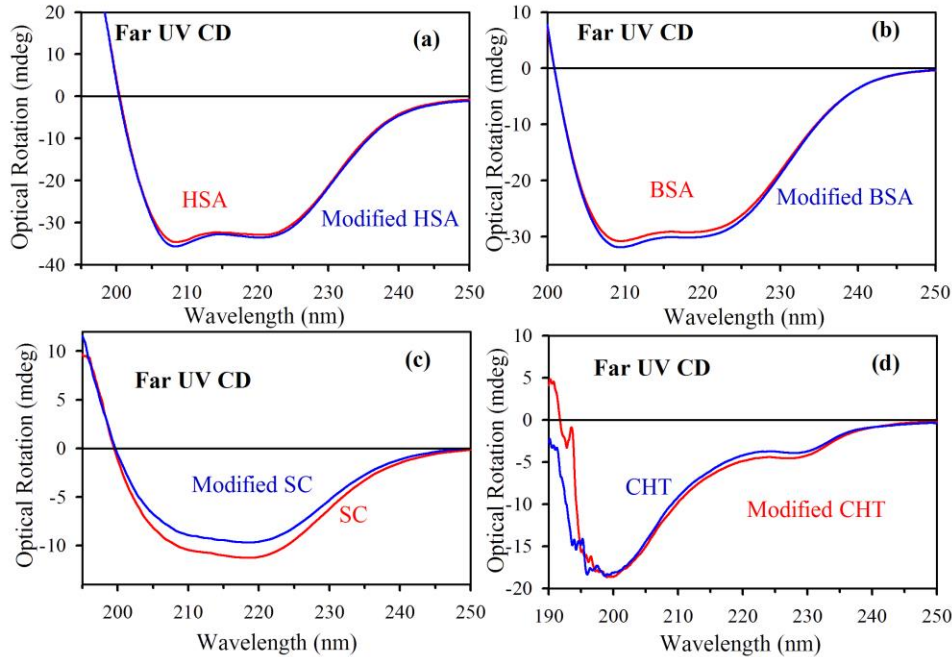


Figure 5.7. (a), (b), (c) and (d) Far-UV CD spectrum of human serum albumin (HSA), bovine serum albumin (BSA), subtilisin *Carlsberg* (SC) and α -chymotrypsin (CHT) respectively before and after modification. Here each protein and its modified form has the same concentration.

of the estimated value (1.84 nm) from X-ray crystallographic structure of the protein [31, 32].

In order to establish the generality of this electron transfer mechanism, we have performed similar experiment on a number of proteins and found that BQ is able to oxidize the Trp residues in any kind of protein. Figure 5.6a, b and c describes the absorption, excitation and emission spectra of modified bovine serum albumin (BSA), modified α -chymotrypsin (CHT) and modified subtilisin *Carlsberg* (SC) respectively. The numbers of tryptophan residues in the proteins are two, seven and one respectively.

Table 5.1. Multi-exponential fitting parameters of the picosecond resolved fluorescence transients of various proteins.

| Protein | τ_1 [ns] | τ_2 [ns] | τ_3 [ns] | τ_{av} [ns] |
|--------------|----------------|----------------|----------------|------------------|
| modified-BSA | 0.110 ns (59%) | 1.006 ns (28%) | 3.892 ns (13%) | 0.852ns |
| modified-CHT | 0.091 ns (82%) | 1.045ns (12%) | 5.112 ns (6%) | 0.506ns |
| modified-SC | 0.102 ns (68%) | 0.941 ns (22%) | 4.273 ns (10%) | 0.703ns |

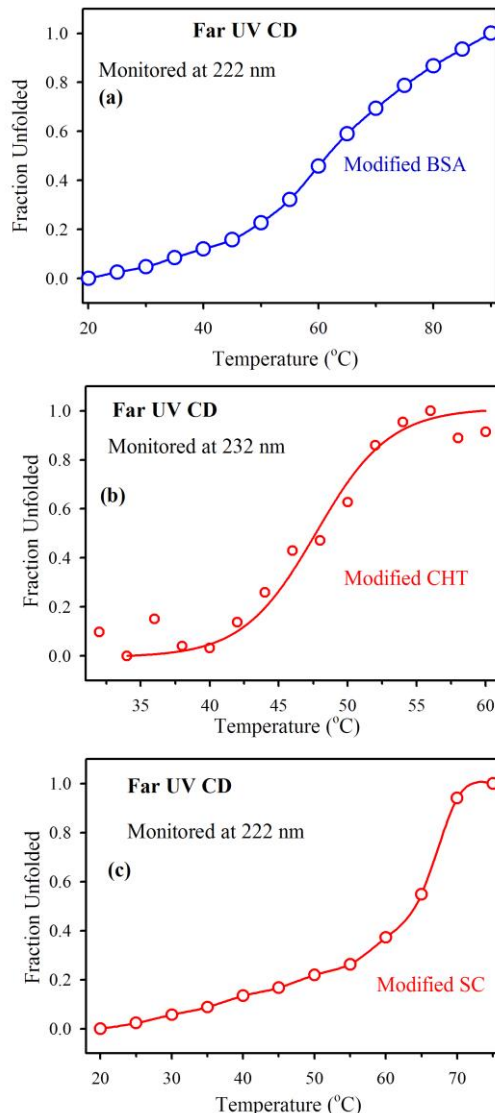


Figure 5.8. (a), (b) and (c) Temperature dependence of the far-UV CD spectrum of the modified bovine serum albumin (BSA), modified α -chymotrypsin (CHT) and modified subtilisin Carlsberg (SC) respectively in phosphate buffer (pH 7.4, 20 mM). Transition temperatures (T_m , the midpoint of unfolding transition) are $\sim 70^\circ\text{C}$, $\sim 50^\circ\text{C}$ and $\sim 62^\circ\text{C}$ respectively, which are consistent with those of the native proteins.

While BSA and CHT contain buried tryptophan residues, the protein SC is containing water-exposed single tryptophan residue. As evident from Figure 5.6, like HSA, all the proteins contain a broad absorption spectra peaking at 350 nm which indicates the formation of kynurenine. The excitation and emission spectra are also clear indications of the formation of newly generated fluoroprobe, kynurenine. Insets of Figure 5.6 show the picoseconds resolved multiexponential (shown in Table 5.1) fluorescence transients of modified BSA, modified CHT and modified SC respectively.

Persistence of the structural integrity of the proteins upon modification is confirmed by far UV-CD experiment. Figure 5.7 indicates that there is insignificant loss of overall ellipticity upon modification of HSA, BSA, SC and CHT proteins which indicates that BQ is good to oxidize Trp of any kind of proteins within structural integrity. Again when the ellipticity was monitored at 222 nm (for BSA and SC) and at 232 nm (for CHT) the thermal denaturation of the modified proteins exhibits a cooperative sigmoidal behavior with transition temperature (T_m) similar to those of the unmodified ones [25] (shown in Figure 5.8). Our observations indicate that unfolding pathways are not perturbed upon modification with ethanolic BQ.

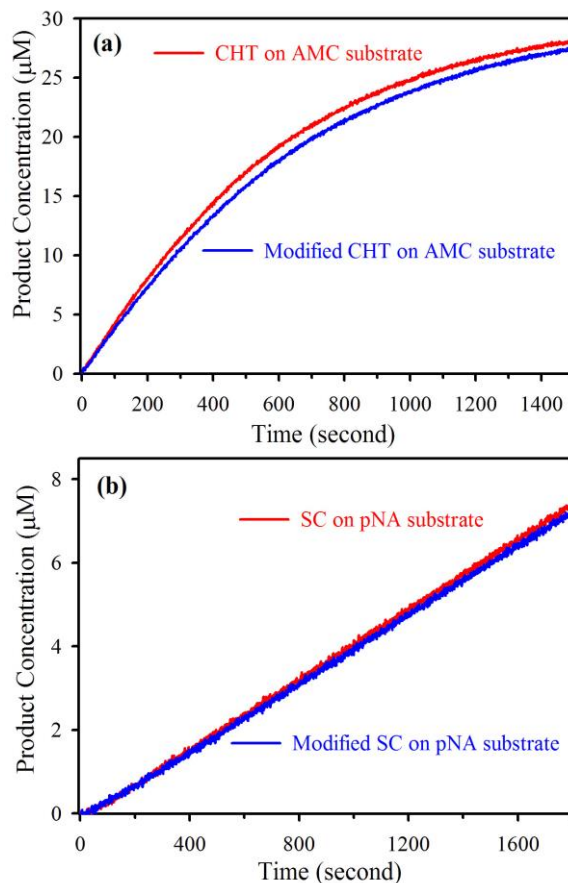


Figure 5.9. (a) The concentrations of the product as a function of time. Concentrations of CHT and AAF-AMC were 1 and 35 μM , respectively. (b) The concentrations of the product as a function of time. Concentrations of SC and Suc-AAPF-pNA were 1 and 185 μM , respectively.

Figure 5.9a shows the rate of formation of AMC-product upon enzymatic activity of CHT and modified CHT on AAF-AMC in phosphate buffer. Figure 5.9b shows time dependent product concentration as a result of enzymatic activity of SC and modified SC

on Suc-AAPF-pNA in phosphate buffer. Table 5.2 lists the specific activity (in units/mg) of CHT, modified CHT, SC and modified SC respectively. From Table 5.2, we find that the specific activity of the CHT and SC are close to the modified CHT and modified SC respectively which depicts that oxidation of Trp has minimal effect on the biological function of the protein.

Table 5.2. Comparison of specific activity in units/mg of CHT^a, modified CHT, SC^b and modified SC.

| System | Specific activity (units/mg) |
|--------------|------------------------------|
| CHT | 22.89 |
| Modified CHT | 22.41 |
| SC | 4.41 |
| Modified SC | 4.38 |

^a One unit of CHT will hydrolyze 1.0 µmol of AAF-AMC per minute at pH 7.0 at 25°C.

^b One unit of SC will hydrolyze 1.0 µmol of Suc-AAPF-pNA per minute at pH 7.0 at 25°C

5.3. Conclusion

In conclusion, an efficient intrinsic fluorescence probe i.e., Kyn214 have been successfully modified from Trp214 in a model protein cavity through an electron transfer reaction. It has to be noted that we have studied on a number of proteins and found that BQ is good to oxidize Trp in any proteins. Dynamics of hydration in the protein cavity as revealed by Kyn214 is also demonstrated by femtosecond studies and found to be consistent with other studies. Practical applications of protein bound kynurenone as an energy transfer probe is also established here. Our study further demonstrates that oxidation of tryptophan does not affects the biological functionality of the protein. With simple modification, such intrinsic fluorophore is likely to find use as spectroscopic studies of protein, thereby making these studies much more widely accessible. The intense emission and the excitation wavelength at near visible wavelength (~375 nm) and eligibility for the spectroscopic studies of a protein within structural integrity make it attractive fluorophore as an alternative of tryptophan. The study would find out the relevance in the protein-assisted metal ion reduction for the spectroscopic investigation of the protein molecule.

References

- [1] J.R. Lakowicz, Principles of Fluorescence Spectroscopy, Kluwer Academic/Plenum Publishers: New York, 2006.
- [2] J.M. Beechem, L. Brand, Time-Resolved Fluorescence of Proteins, *Annu. Rev. Biochem.* 54 (1985) 43.
- [3] B.E. Cohen, M.T. McAnaney, E.S. Park, Y.N. Jan, S.G. Boxer, L.Y. Jan, Probing Protein Electrostatics with a Synthetic Fluorescent Amino Acid, *Science* 296 (2002) 1700.
- [4] L.M. Mannuzzu, M.M. Moronne, E.Y. Isacoff, Direct Physical Measure of Conformational Rearrangement Underlying Potassium Channel Gating, *Science* 271 (1996) 213.
- [5] L. Shi, V.D. Paoli, N. Rosenzweig, Z. Rosenzweig, Synthesis and Application of Quantum Dots FRET-Based Protease Sensors, *J. Am. Chem. Soc.* 128 (2006) 10378.
- [6] A.C. Royer, Probing Protein Folding and Conformational Transitions with Fluorescence, *Chem. Rev.* 106 (2006) 1769.
- [7] X. Shen, J.R. Knutson, Subpicosecond Fluorescence Spectra of Tryptophan in Water, *J. Phys. Chem. B* 105 (2001) 6260.
- [8] D. Zhong, S.K. Pal, D. Zhang, S.I. Chan, A.H. Zewail, Femtosecond Dynamics of Rubredoxin: Tryptophan Solvation and Resonance Energy Transfer in the Protein, *Proc. Natl. Acad. Sci. USA* 99 (2002) 13.
- [9] S.J. Stachel, R.L. Habeeb, D.L. Van Vranken, Formation of Constrained, Fluorescent Peptides via Tryptophan Dimerization and Oxidation, *J. Am. Chem. Soc.* 118 (1996) 1225.
- [10] J.A. Aquilina, J.A. Carver, R.J.W. Truscott, Elucidation of a Novel Polypeptide Cross-Link Involving 3-Hydroxykynurenone, *Biochemistry* 38 (1999) 11455.
- [11] J.A. Aquilina, J.A. Carver, R.J.W. Truscott, Polypeptide Modification and Cross-Linking by Oxidized 3-Hydroxykynurenone, *Biochemistry* 39 (2000) 16176.
- [12] D.W. Cleveland, J.D. Rothstein, From Charcot to Lou Gehrig: Deciphering Selective Motor Neuron Death in ALS, *Nat. Rev. Neurosci.* 2 (2001) 806.
- [13] S. Vazquez, J.A. Aquilina, J.F. Jamie, M.M. Sheil, R.J. Truscott, Novel Protein Modification by Kynurenone in Human Lenses, *J. Biol. Chem.* 277 (2002) 4867.

- [14] L.B. Anderson, M. Maderia, A.J. Ouellette, C. Putnam-Evans, L. Higgins, T. Krick, M.J. MacCoss, H. Lim, J.R.r. Yates, B.A. Barry, Posttranslational modifications in the CP43 subunit of photosystem II., *Proc. Natl. Acad. Sci. USA* 99 (2002) 14676.
- [15] H. Zhang, C. Andreopoulos, J. Joseph, K. Chandran, H. Karoui, J.P. Crow, B. Kalyanaraman, Bicarbonate-dependent peroxidase activity of human Cu,Zn-superoxide dismutase induces covalent aggregation of protein: intermediacy of tryptophan-derived oxidation products, *J. Biol. Chem.* 278 (2003) 24078.
- [16] S.P. Sherin, J. Grilj, P.Y. Tsentalovich, E. Vauthey, Ultrafast Excited-State Dynamics of Kynurenine, a UV Filter of the Human Eye, *J. Phys. Chem. B* 113 (2009) 4953.
- [17] O.K. Abou-Zied, O.I.K. Al-Shihi, Characterization of Subdomain IIA Binding Site of Human Serum Albumin in its Native, Unfolded, and Refolded States Using Small Molecular Probes, *J. Am. Chem. Soc.* 130 (2008) 10793.
- [18] R. Sarkar, S.S. Narayanan, L. PaÈlsson, F. Dias, A. Monkman, S.K. Pal, Direct Conjugation of Semiconductor Nanocrystals to a Globular Protein to Study Protein-Folding Intermediates, *J. Phys. Chem. B* 111 (2007) 12294.
- [19] N. Goswami, A. Makhal, S.K. Pal, Toward an Alternative Intrinsic Probe for Spectroscopic Characterization of a Protein, *J. Phys. Chem. B* 114 (2010) 15236.
- [20] S. Si, T.K. Mandal, Tryptophan-Based Peptides to Synthesize Gold and Silver Nanoparticles: A Mechanistic and Kinetic Study, *Chem. Eur. J.* 13 (2007) 3160.
- [21] C. Burda, T.C. Green, S. Link, M.A. El-Sayed, Electron Shuttling Across the Interface of CdSe Nanoparticles Monitored by Femtosecond Laser Spectroscopy, *J. Phys. Chem. B* 103 (1999) 1783.
- [22] S. Yamashita, E. Nishimoto, A.G. Szabo, N. Yamasaki, Steady-State and Time-Resolved Fluorescence Studies on the Ligand-Induced Conformational Change in an Active Lysozyme Derivative, Kyn62-Lysozyme, *Biochemistry* 35 (1996) 531.
- [23] R.K. Mitra, S.S. Sinha, S.K. Pal, Hydration in Protein Folding: Thermal Unfolding/Refolding of Human Serum Albumin, *Langmuir* 23 (2007) 10224.
- [24] M. Balsera, M. Menéndez, J.L. Sáiz, J. de las Rivas, J.M. Andreu, J.B. Arellano, Structural Stability of the PsbQ Protein of Higher Plant Photosystem II., *Biochemistry* 43 (2004) 14171.

- [25] J.K.A. Kamal, T. Xia, S.K. Pal, L. Zhao, A.H. Zewail, Enzyme Functionality and Solvation of Subtilisin Carlsberg: from Hours to Femtoseconds, *Chem. Phys. Lett.* 387 (2004) 209.
- [26] W. Qiu, L. Zhang, O. Okobiah, Y. Yang, L. Wang, D. Zhong, A.H. Zewail, Ultrafast Solvation Dynamics of Human Serum Albumin: Correlations with Conformational Transitions and Site-Selected Recognition, *J. Phys. Chem. B* 110 (2006) 10540.
- [27] J.K.A. Kamal, L. Zhao, A.H. Zewail, Ultrafast Hydration Dynamics in Protein Unfolding: Human Serum Albumin, *Proc. Natl. Acad. Sci. USA* 101 (2004) 13411.
- [28] S. Chakraborty, S. Bandyopadhyay, Correlation between the Dynamics of Hydrogen Bonds and the Local Density Reorganization in the Protein Hydration Layer, *J. Phys. Chem. B* 111 (2007) 7626.
- [29] P.S. Sherin, J. Grilj, L.V. Kopylova, V.V. Yanshole, Y.P. Tsentalovich, E. Vauthey, Photophysics and Photochemistry of the UV Filter Kynurenone Covalently Attached to Amino Acids and to a Model Protein, *J. Phys. Chem. B* 114 (2010) 11909.
- [30] J. Santhanalakshmi, S. Balaji, Binding Studies of Crystal Violet on Proteins, *Colloids Surf. A* 186 (2001) 173.
- [31] M. Wardell, Z. Wang, J.X. Ho, J. Robert, F. Ruker, J. Ruble, D.C. Carter, The Atomic Structure of Human Methemalbumin at 1.9 Å, *Biochem. Biophys. Res. Commun.* 291 (2002) 813.
- [32] P.A. Zunszain, J. Ghuman, T. Komatsu, E. Tsuchida, S. Curry, Crystal Structural Analysis of Human Serum Albumin Complexed with Hemin and Fatty Acid, *BMC Struct. Biol.* 3 (2003) 6.

Chapter 6

Biomineralization and Sensing Mechanism of Toxic Metal Ion in Biological Matrix

6.1. Introduction

In the past decade, semiconductor quantum dots (QDs) have become well-established photo luminescent platforms for many scientific and industrial applications [1-3]. For example, QDs are highly sensitive to charge/energy transfer, which can alter their optical properties, thus generating interest in charge/energy-transfer-based bio-sensing [1, 4]. Among all the semiconducting QDs, mercury chalcogenide QDs are one of the least studied families because of the toxicity and volatility of corresponding organo-mercury compounds. Such materials are highly attractive for infrared sensing, optoelectronics as well as for more fundamental studies of their optical properties. Luminescence across the visible spectral region with mercury chalcogenide is extremely difficult, while it is common for zinc and cadmium based chalcogenides. Despite the potential toxicity of mercury and the restricted application in biology, it would be of great interest to develop mercury chalcogenide QDs with tunable luminescence as there is immense potentiality in their application in chemical sensing, infrared detection as well as development of electrical device etc. [2, 5, 6].

Of all the mercury chalcogenides, HgTe is widely studied having various synthetic routes leading to high quality materials based on both aqueous and organic based chemistries. Recently, Keuleyan et al. [7] prepared colloidal HgTe QDs having narrow photo luminescence tunable across the near and mid-IR regions. In contrast, there have been very few detailed studies on HgS QDs. Wichiansee et al. [8] have successfully prepared HgS QDs based on an organic route, using trioctylphosphine oxide (TOPO) as the capping agent. Higginson et al. [9] have synthesized HgS QDs exhibiting narrow, size-dependent transitions between 500 and 800 nm for sizes ranging from 1 to 5 nm in diameter. Typically, in most cases, HgS QDs were synthesized via thermal decomposition of organo-metallic precursors in organic solvents and/or in the presence of surfactants [8, 10, 11]. However, unlike them, the use of a biomolecule as template or scaffold for the synthesis possesses many advantages due to their inherent

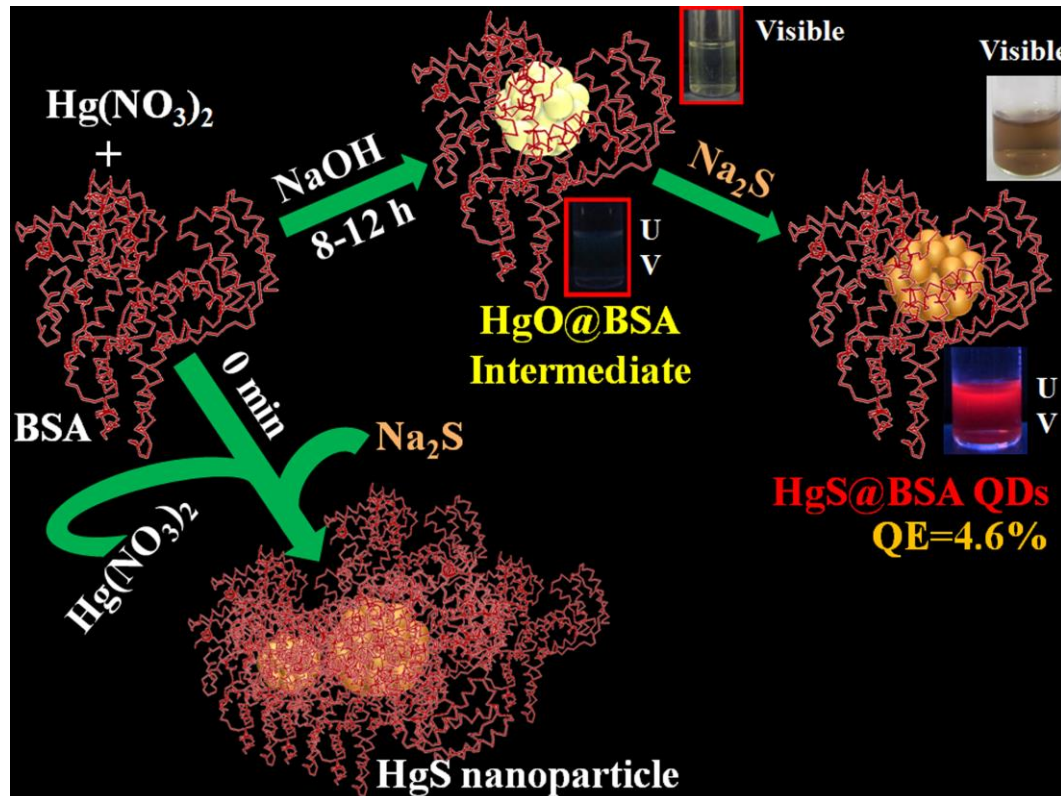
biocompatibility and ease of functionalization. Thus, novel synthetic strategies for the preparation of HgS QDs using biomolecules that yield extremely stable, water soluble QDs with tunable luminescence in the visible and near IR region would be highly desirable.

Among many biological systems that could participate in biominerization and be incorporated into bionanomaterials, proteins have been the subject of particular attention due to their nanoscale dimensions, distinctive molecular structures and functionalities, and their capability to control the size of inorganic crystals during nucleation and growth to a remarkable degree due to their bulky nature. For example, bovine serum albumin (BSA) and several other proteins have been used to synthesize sub-nanometer sized luminescent metal clusters [12-18]. Recently, aqueous, protein-driven synthesis of transition metal-doped ZnS QDs has also been reported by Zhou et al [19]. Akin to the biominerization process, herein, we have developed a facile approach to prepare water-soluble, highly stable NIR-luminescent HgS QDs, which are protected and stabilized by the protein matrix. We have also used the HgS QDs formed as a fluorometric sensor for the detection of Hg(II) and Cu(II) ions. Uses of the QDs in metal ion sensing by exploiting their luminescence properties is not new and have been reported before [20, 21]. The mechanisms of luminescence quenching involving inner-filter effects, nonradiative recombination pathways and electron transfer processes have also been reported. However, the quenching mechanisms addressing the specific interaction of detected ions with the sensor QDs are sparse in the existing literature. The reason for quenching relies on the metallophilic interaction between Hg(II)/Cu(II) and Hg(II) ions present on the surface of the HgS QDs. We have used time-resolved luminescence methods to study the mechanism of excited-state reactivity which reveals that both Hg(II) and Cu(II) ions can reduce the lifetime of the HgS QDs. After considering all kinds of excited state deactivation mechanisms, we have found that Dexter energy transfer is the reason in case of Hg(II)-induced quenching whereas photoinduced electron transfer dominates in case of Cu(II)-induced quenching. In several control experiments, we have also ruled out other possibilities of the quenching mechanisms including aggregation, Förster resonance energy transfer (FRET), etc.

6.2. Results and Discussion

6.2.1. Protein Directed Synthesis of NIR-Emitting, Tunable HgS Quantum Dots and their Applications in Metal Ion Sensing [22]:

The process for synthesizing the HgS QDs is simple and involves two steps (see section 3.2.7. for details). The various stages of synthesis are shown in Scheme 6.1. In the first step, addition of mercury nitrate solution to aqueous BSA causes the mercury ions to be coordinated with the various functional groups of BSA such as -SH, -NH, etc. The pH of the solution was adjusted to ~9 by the addition of NaOH followed by vigorous stirring at room temperature. After 8-12 hrs the colour of the solution changes from colourless to pale yellow intermediate which we have analyzed by Raman spectroscopy (see later in the text) and found it to be HgO@BSA. Photographs of the intermediate under UV and visible light are shown in Scheme 6.1. In the last step, Na₂S is added and the color changes from pale yellow to light brown (Scheme 6.1) which indicates the formation of HgS QDs.



Scheme 6.1. Schematic illustration of the synthesis of HgS QDs through biomineratization process mediated by the BSA protein.

Figure 6.1A illustrates the UV-vis absorption spectra of HgS@BSA QDs. In particular, Figure 6.1A gives the plot of the natural logarithm of the Jacobian factor versus wavelength of the QDs, to show the features more clearly. Well-defined absorption features are marked with arrows. Three distinct excitonic absorption shoulders of the HgS QDs are found at 473 (2.62), 546 (2.27) and 594 nm (2.09 eV), respectively which indicate the presence of different size QDs. The band gaps calculated for UV features at 2.62, 2.27, and 2.09 eV are 2.02, 1.94 and 1.90 eV, respectively, which are very much blue shifted from the average band gap of bulk β -HgS (-0.2 to 0.5 eV)[8] due to high quantum confinement effect. Figure 6.1B shows the luminescence profile of the as-prepared QDs. A clear excitation maximum at 550 nm and luminescence peak at around 730 nm is evident from Figure 6.1B. Photographs of QDs under UV and visible radiations are shown in Scheme 6.1. As a control study, we have performed the reaction in the absence of Na₂S; however, no such luminescent material is obtained even after 48 hrs. This result reveals that external sulphur is required for the growth of QDs. It has to be noted that direct addition of mercury nitrate and Na₂S with protein solution leads to the formation of non-luminescent HgS nanomaterial which provide evidence that yellow colour intermediate formation is necessary to get the luminescent QDs. The photoluminescence quantum yield of the HgS@BSA is ~4.6%, estimated using 4-(dicyanomethylene)-2-methyl-6-(p-dimethylaminostyryl)-4H-pyran (DCM) as a reference with a 450 nm excitation wavelength. The obtained HgS QDs are found to be very stable, showing the same luminescence spectra after almost seven days of being stored at room temperature (Figure 6.2). The luminescence is maximum at neutral pH, however, relatively less stable in acidic and basic pH as shown in Figure 6.3. In order to investigate the thermal stability of the QDs, temperature dependent luminescence of HgS@BSA has been monitored. It can be seen from Figure 6.4 that luminescence of the HgS@BSA in the aqueous solution decreased significantly upon increase in temperature. The reason may be the increase in hydrophilicity around the HgS QDs as protein is perturbed at higher temperature.

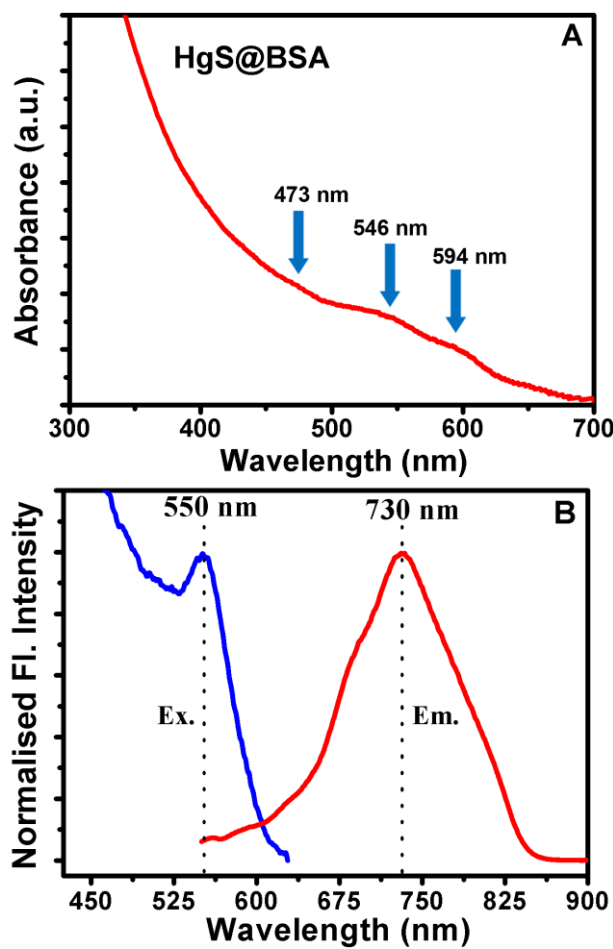


Figure 6.1. A. UV-vis absorbance spectrum of HgS@BSA. B. Excitation and emission spectrum of HgS@BSA. Excitation spectrum is taken by monitoring at 730 nm. Luminescence spectrum is collected with 450 nm excitation.

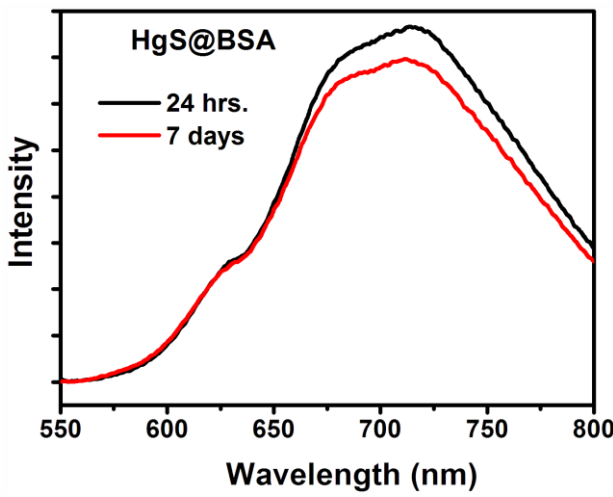


Figure 6.2. Luminescence spectra ($\lambda_{\text{ex}} = 550 \text{ nm}$) of HgS@BSA at different time indicating the high stability of QDs.

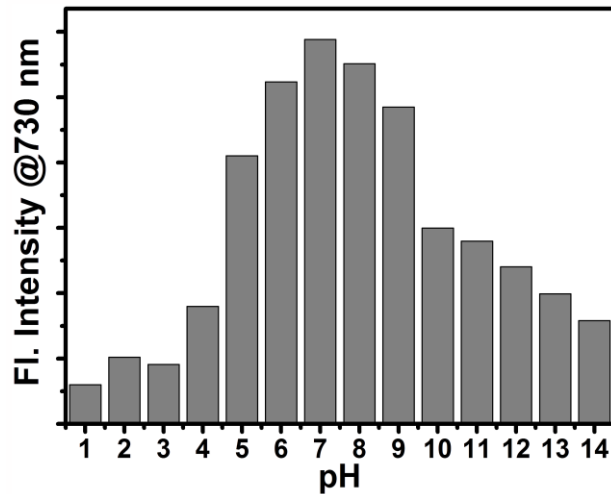


Figure 6.3. Luminescence spectra ($\lambda_{\text{ex}} = 550 \text{ nm}$) of HgS@BSA at different pHs showing the maximum stability of the QDs at pH=7.

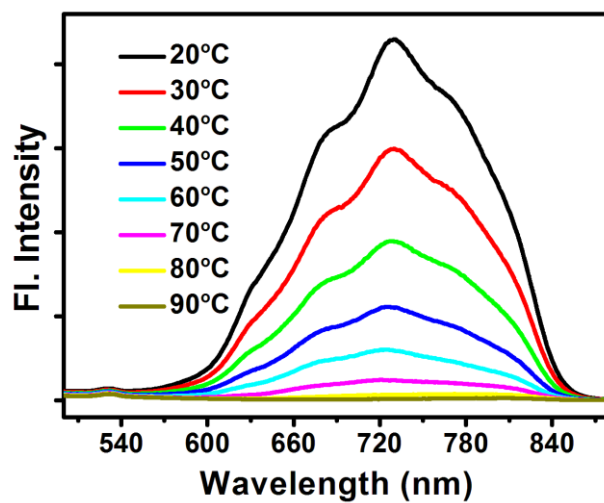


Figure 6.4. Steady-state luminescence spectra of HgS@BSA measured at different temperatures.

By varying the experimental conditions, e.g., Hg/S ratio we have achieved the variation of QDs diameter, resulting the tunability of their luminescence (Figure 6.5A). As shown in Figure 6.5B, a variation of excitation peak maxima is clearly observed, pointing to the presence of QDs having different sizes. In photoluminescence spectra the peak maxima varied from 680-800 nm which corresponds to a QD diameter from 4-10 nm according to our DLS results (Figure 6.5C).

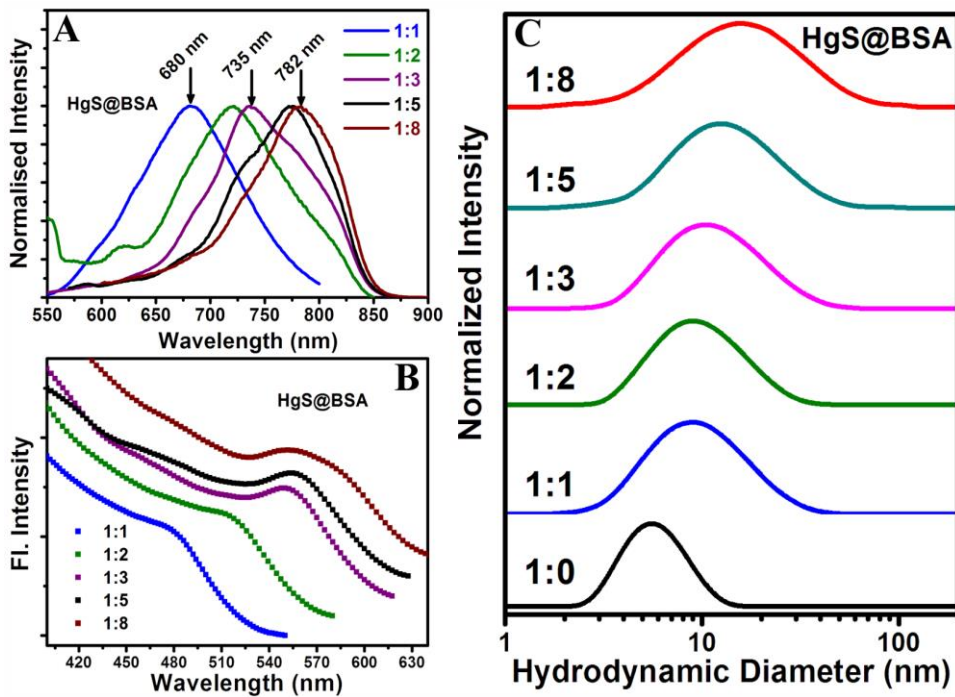


Figure 6.5. Normalized spectra. (A). luminescence, (B) excitation and (C) dynamic light scattering spectra for HgS@BSA QDs with different Hg/S molar ratio.

HR-TEM image confirmed the presence of nearly spherical nanocrystals having a size of 3.8 ± 0.2 nm (Figure 6.6A). As shown in Figure 6.6B, characteristic hydrodynamic diameter of BSA is shifted from $5.6 (\pm 0.6)$ nm to $9.3 (\pm 0.6)$ nm in DLS after the formation of HgS QDs. This observation is consistent with the fact that QDs are formed within the protein matrix. Again, the size obtained from the TEM study is roughly comparable to the swelling of the protein size ($\sim 4.4 \pm 0.6$ nm), as revealed from our DLS measurements. HR-TEM image of the HgS QDs is shown in Figure 6.6C. The distance between two adjacent planes is 0.256 nm, corresponding to the (200) lattice plane of cubic β -HgS (ICDD, Reference no: 00-002-0453). The distinct fringe spacing and the corresponding selected area electron diffraction (SAED) pattern (inset of Figure 6.6C) reveal the reasonably good crystallinity of the as-prepared HgS QDs. Energy dispersive X-ray analysis (EDAX) spectrum and elemental mapping of the scanning electron microscopy (SEM) image. Figure 6.6D demonstrates the EDAX spectrum of the HgS@BSA. SEM image of the HgS@BSA and EDAX maps using C K, O K, S K, Hg L and Na K are shown in the inset of Figure 6.6D.

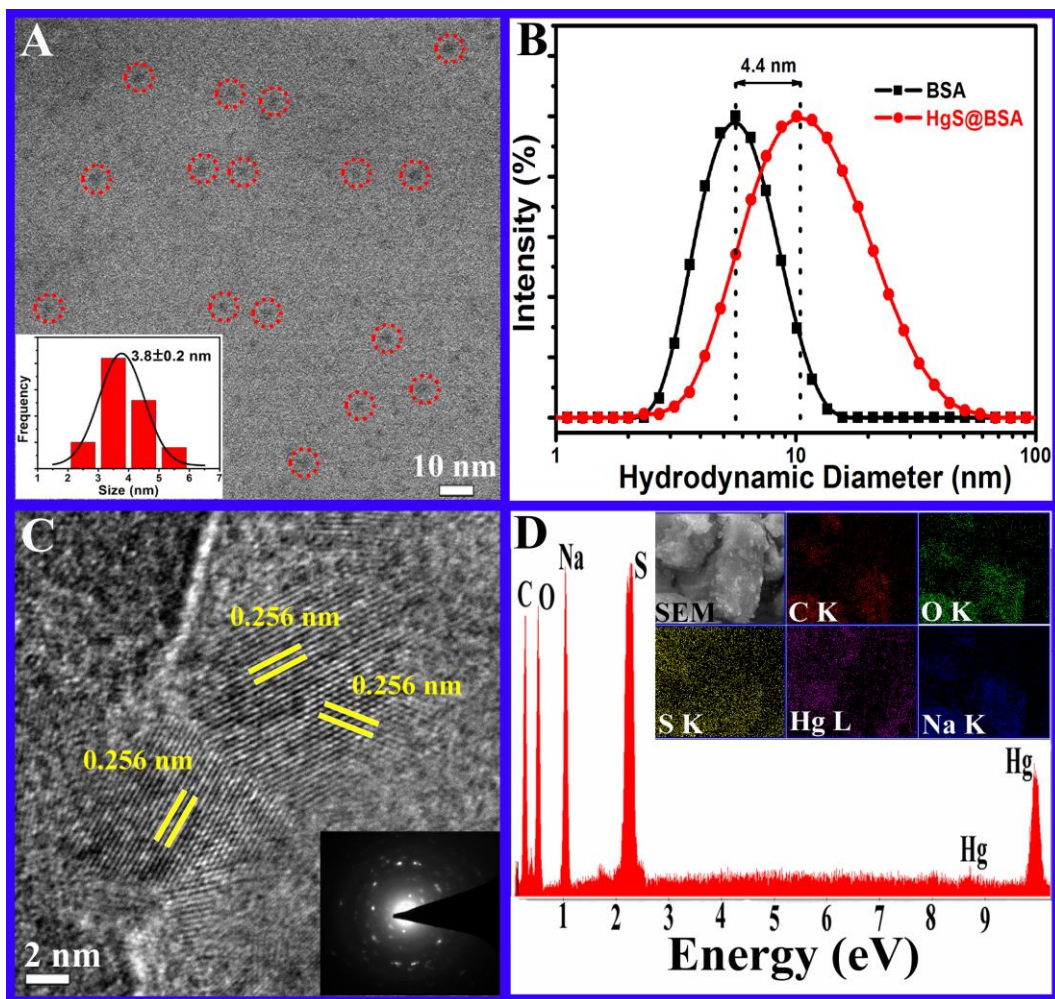


Figure 6.6. A. Typical TEM images of HgS QDs. The size distribution of HgS@BSA is shown in the inset. B. Dynamic light scattering spectra of BSA (black) and HgS@BSA in aqueous solution at pH~9. The swelling of the protein size by 4.4 nm has also been assigned. C. High-resolution TEM micrograph of HgS QDs. SAED pattern in an area including HgS QDs is shown in the inset. D. EDAX spectrum collected from HgS@BSA. Inset showing the SEM image of the HgS@BSA sample from which the EDAX spectrum was taken. EDAX maps using C K, O K, S K, Hg L and Na K are also shown in the inset.

X-ray photoelectron spectroscopy (XPS) of the intermediate, HgO@BSA and the final product, HgS@BSA were carried out to verify the oxidation state of Hg and elemental composition. Survey spectra of HgO@BSA and HgS@BSA show the expected elements, C, N, O, S (from protein and QDs) and Hg (from QDs) (Figure 6.7). The Hg 4f regions of the above samples are compared with the synthesized bulk HgO and HgS in Figure 6.8. The Hg 4f_{7/2} peaks of bulk HgO and HgS appeared at 100.6 and 100.1 eV, respectively whereas in HgO@BSA and, HgS@BSA, they are at 101.4 and 100.6 eV,

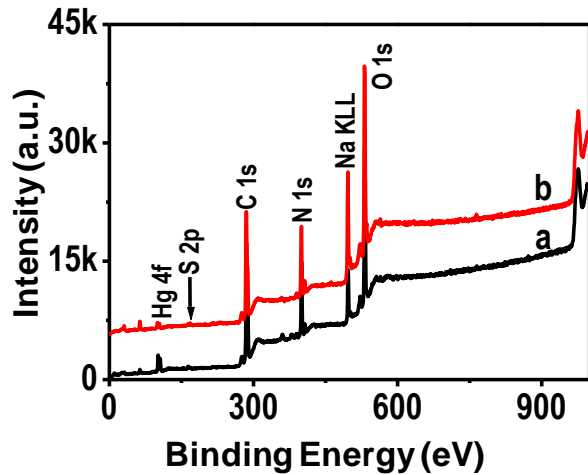


Figure 6.7. XPS survey spectra of (a) $\text{HgO}@\text{BSA}$ and (b) $\text{HgS}@\text{BSA}$ which show the expected elements.

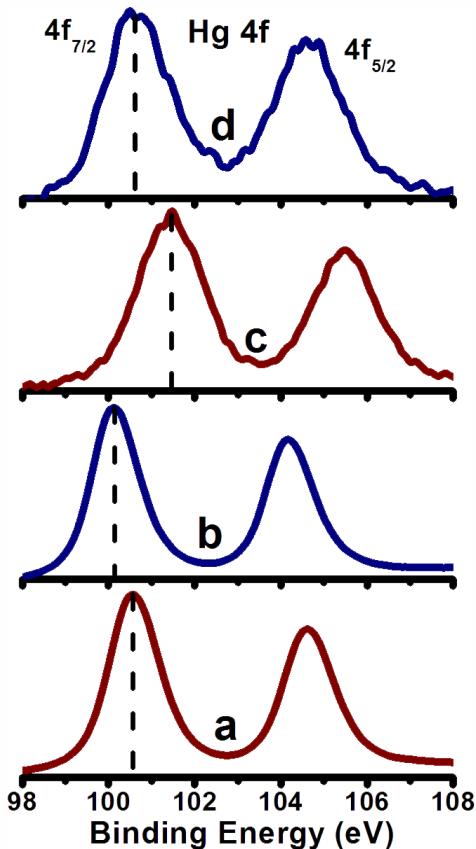


Figure 6.8. XPS spectra in the $\text{Hg } 4\text{f}$ region of (a) bulk HgO , (b) bulk HgS , (c) $\text{HgO}@\text{BSA}$ and (d) $\text{HgS}@\text{BSA}$. The vertical dotted lines represent the $\text{Hg } 4\text{f}_{7/2}$ binding energies.

respectively. This expected increase in the nanoparticles confirms the presence of mercury in +2 state in all the samples. The shift of $\text{Hg } 4\text{f}_{7/2}$ peak to higher binding energy region in both $\text{HgO}@\text{BSA}$, and $\text{HgS}@\text{BSA}$ samples indicate the functionalization

of HgO, HgS by protein and the difference from the corresponding bulk systems. Presence of S 2p_{3/2} in bulk HgS at 161.2 and 168.0 eV is due to sulphide and partially oxidized species like sulphate, respectively (Figure 6.9A). Formation of HgS in protein sample was confirmed by the presence of S 2p_{3/2} around 161.2 eV (Figure 6.9B, trace b). Presence of other sulphur species like disulphides and sulphates (due to X-ray induced damage which is expected in protein samples) [16] are observed in HgO@BSA and HgS@BSA samples (S 2p_{3/2} peaks at 163.3 and 167.8 eV).

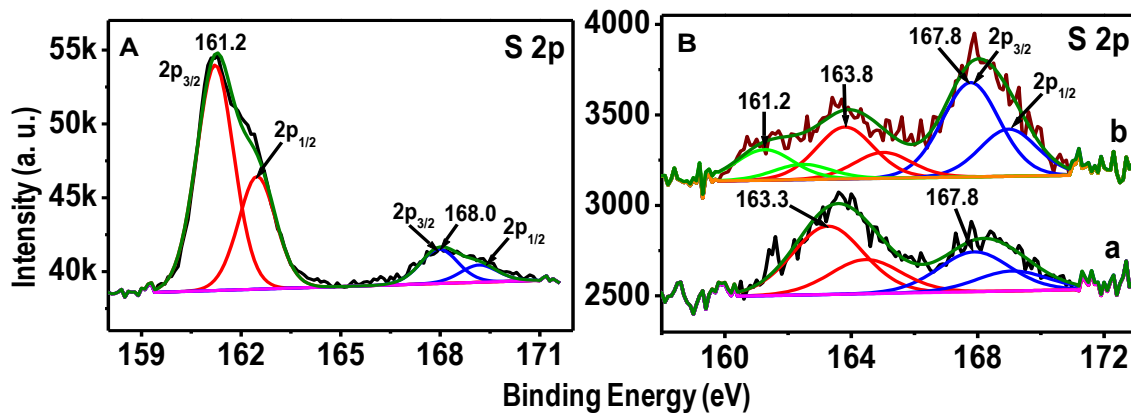


Figure 6.9. XPS spectra. A) S2p region of bulk HgS B) S2p region of (a)HgO@BSA and (b)HgS@BSA shows the presence of feature which is present in bulk HgS.

Raman spectroscopic measurements were performed on the HgS QDs formed and the reaction intermediate to elucidate the reaction mechanism. The spectra of bulk HgO, bulk HgS, HgO@BSA, HgS@BSA and BSA are compared in Figure 6.10A. Bulk HgO has a main band centred at 334 cm⁻¹ whereas the intermediate has a red shifted feature at 330 cm⁻¹; which originates from the oxygen inter-chain mode of the HgO with A_g symmetry [23]. These features are highlighted using a dotted circle in Figure 6.10A. Raman spectrum of the HgS QDs shows a slightly blue shifted peak around 262 cm⁻¹, in comparison to bulk HgS which has a feature at 254 cm⁻¹ (dashed circle) originating from a mode of A₁ symmetry [24]. BSA shows several Raman features corresponding to the detailed structure of the protein including the amide signatures [25]. It should be noted that several of these features are retained in the Raman spectra of the reaction intermediate and the QDs confirming the formation of HgO and HgS, respectively in the protein. In the case of HgO@BSA, the amide regions of the protein are more distorted (or several features could be merged) than in the case of HgS@BSA.

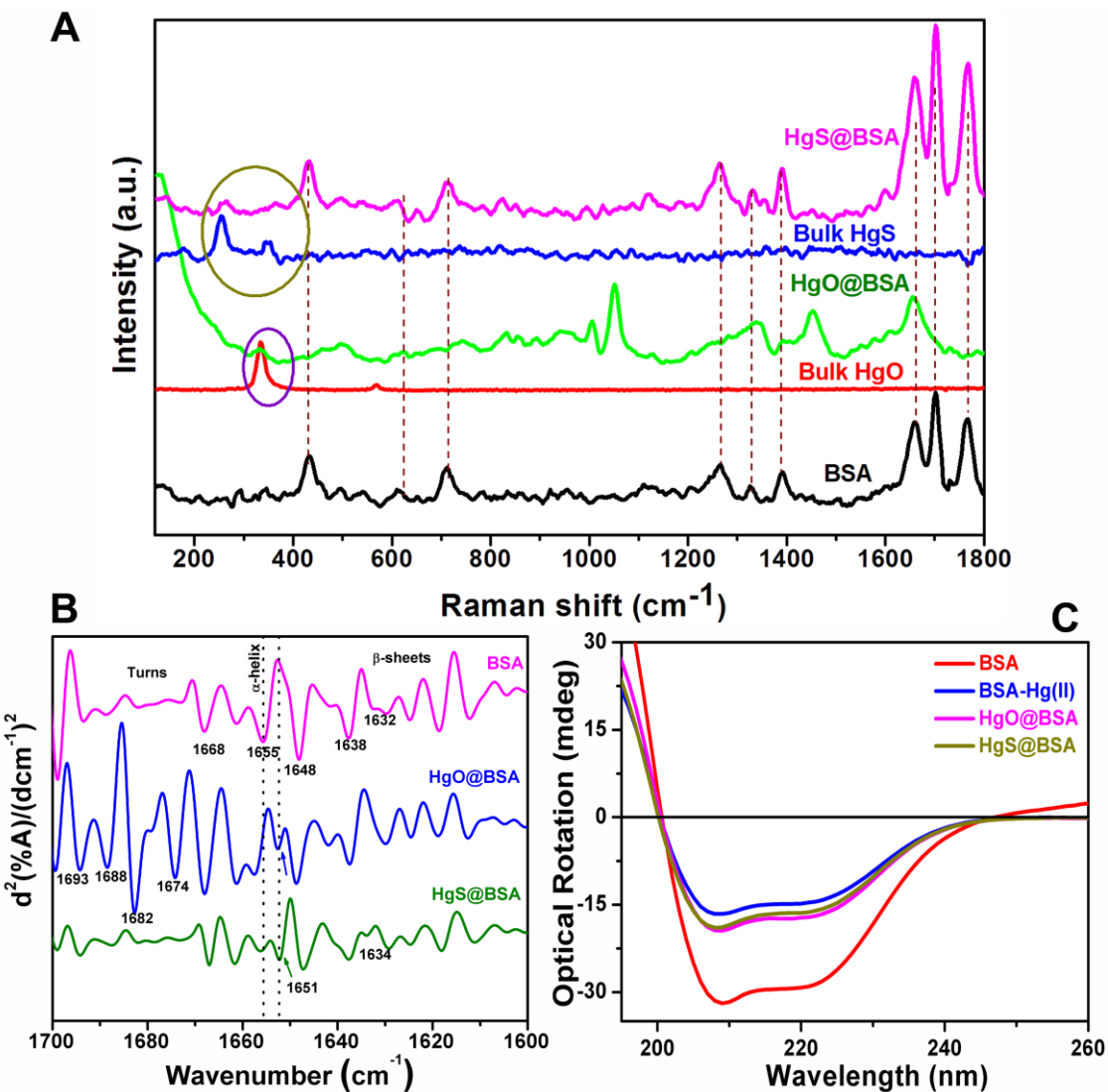


Figure 6.10. A. Raman spectra of BSA, bulk HgO, HgO@BSA, bulk HgS and HgS@BSA in solid state collected using 633 HeNe laser. The violet marking highlights the presence of features due A_g oxygen inter-chain mode in HgO and HgO@BSA as well. The dark yellow marking highlights the presence of HgS vibrations (A_1 mode of the sulfur atom in HgS) in the NIR emitting HgQD confirming the product to be HgS@BSA. B. Second derivative spectra of amide I region of BSA, HgO@BSA and HgS@BSA. C. Circular dichroism spectra of BSA (red), BSA-Hg(II) complex (blue), HgO@BSA (pink) and HgS@BSA (yellow).

FTIR has been one of the most common methods to investigate the structure of proteins by probing their functional group signatures. Amide I, II and III bands provide the information about secondary structural changes in proteins [26-28]. Solid state IR analysis results suggested, in general, that the bands were broadened and shifted to a higher frequency, suggesting perturbation of the secondary structure. Spectral regions

between 1600–1690, 1480–1575, 1229–1301 and 3300 cm⁻¹ have been assigned as amide I, amide II, amide III and amide A, respectively (Figure 6.10B). Increase in the intensity and decrease in the peak width is seen around 1399 cm⁻¹ which is attributed to the C=O stretching of COO⁻ suggests that the COO⁻ groups are more influenced by the formation of HgO and HgS or could be associated with Hg in the protein matrix. Regions between 1651–1658, 1618–1642 cm⁻¹, 1666–1688 cm⁻¹, and 1650±1 cm⁻¹ have been assigned as α -helix, β sheets, turns and unordered structures, respectively [28]. The band appearing around 700 cm⁻¹ can be assigned to –NH₂ and –NH wagging and the band around 2960 cm⁻¹ can be attributed to C–H vibrations. Band near 1400 cm⁻¹ is due to C=O stretching of COO⁻, and that at 1468 cm⁻¹ can be assigned as C–H deformation of >CH₂, and the band at 3500 cm⁻¹ is due to O–H stretching [26, 28]. In the second derivative spectra, compared to native BSA, in HgO@BSA and HgS@BSA, the alpha helix content decreased significantly as the prominent band at 1655 cm⁻¹ disappeared and increase in β -turns in the 1662–1688 cm⁻¹ region was also observed. In case of HgO@BSA, comparatively the β -turn content was higher than native BSA and HgS@BSA, suggesting more perturbation in the intermediate form. A new band around 1651 cm⁻¹ may be attributed to the increased in random coil structures. This observation is corroborated by observation made in Raman measurements.

Circular dichroism (CD) has been employed to study the conformational behaviour of BSA before and after the formation of the HgS QDs. Native BSA displays CD features with minima at 208 and 222 nm, corresponding to the secondary structure of the protein (Figure 6.10C). Figure 6.10C shows the decrease of molar ellipticity in presence of Hg(II), which describes more structural perturbation. From Figure 6.10C, it is also reflected that there is an insignificant perturbation of the secondary structure of the protein after the addition of Na₂S. The observation clearly signifies that addition of Na₂S has minimal effect on the secondary structure of the protein.

The optical responses of HgS QDs towards metal ions such as Hg(II), Ca(II), Cu(II), Co(II), Zn(II), Ni(II), Cd(II), Mg(II), Na(I), and K(I) have been investigated. Among these ions, only Cu(II) and Hg(II) can quench the luminescence of the as-prepared HgS QDs. Figure 6.11 demonstrates the high optical selectivity and sensitivity towards Cu(II) and Hg(II) over the other biologically relevant metal ions and could be seen with naked eye (Figure 6.11, lower panel). The mechanism to be proposed below is due to the

following reasons: A number of sulphur and Hg(II) (having $5d^{10}6s^0$ electronic configuration) are present on the surface of the HgS QDs. Addition of metal ion to the HgS QD solution therefore generates two possibilities: either it will interact with sulphur or mercury. Moreover, sulphur has an affinity towards other metal ions including Hg(II), Cu(II), Zn(II) and Cd(II). Thus, if quenching of the luminescence of QDs occurs through the interaction with sulphur, then all the above mentioned metal ions are expected to reduce the luminescence of HgS@BSA. However, almost insignificant change in the QDs luminescence spectrum with Zn(II) and Cd(II) as revealed from Figure 6.11, clearly rules out the possibility of luminescence quenching through the interaction with sulphur. Recent theoretical studies suggest that metal centres with a d^{10} electronic configuration have a strong affinity towards other closed shell metal ions with similar electronic configuration[29]. In particular, this phenomenon associated with strong d^{10} - d^{10} interaction is known as metallophilic interaction[30]. This interaction originates due to

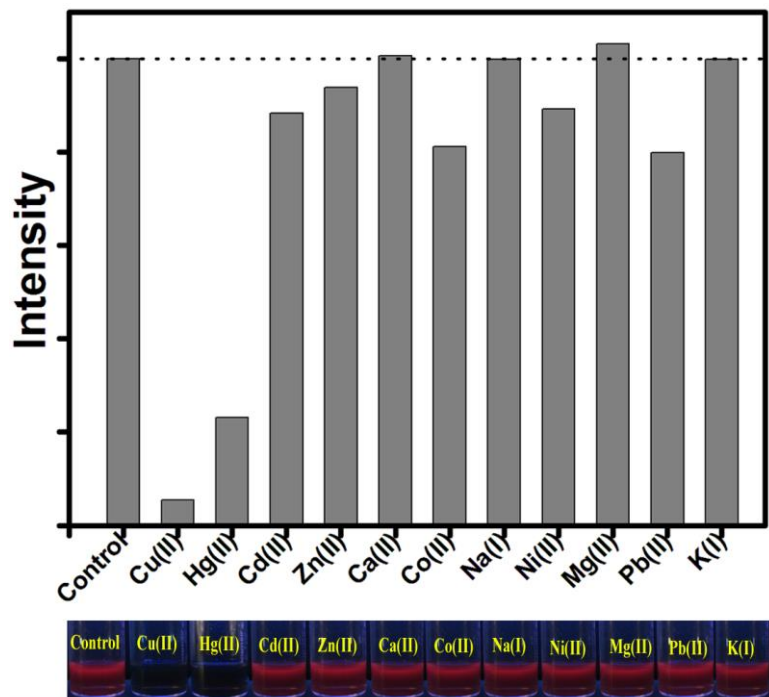


Figure 6.11. Upper panel. Selectivity of the HgS@BSA to different metal ions. The luminescence intensities are recorded at 730 nm. For all cases, the final metal ion concentrations are 50 ppm. Dotted line refers to see the change of luminescence with respect to the control one. Lower panel. Photographs of the HgS@BSA solution under UV light after addition of 50 ppm of various metal ions.

dispersive forces which are further augmented by relativistic effects[30]. In the case of mercury ion ($5d^{10}6s^0$), a number of examples of such interactions are present in the literature, even in absence of protecting ligands [13, 14, 31]. Our study suggests that luminescence quenching of HgS QDs in presence of Hg(II) is due to the same $5d^{10}$ - $5d^{10}$ metallophilic interaction (Scheme 6.2). In case of Cu(II), luminescence quenching could occur through $5d^{10}$ - $3d^{10}$ metallophilic interaction as in the protein environment Cu(II) is reduced to Cu(I) (Scheme 6.2) [32]. In order to unravel the consequence of the metallophilic interaction, a series of systematic picosecond resolved photoluminescence studies have been performed. The faster excited state lifetime of the HgS/Hg(II) and HgS/Cu(II) with respect to that of the free HgS QDs are clearly noticeable from Figure 6.11. Details of the fitting parameters of the time-resolved decays are tabulated in Table 6.1. As evidenced from our study, the nature of the quenching of QDs lifetime by metal ion is dynamic.

Table 6.1. Picosecond resolved luminescence transients of HgS@BSA in absence and presence of Hg(II) and Cu(II). Lifetime values of the HgS@BSA system in presence of well-known electron accepting agent, benzoquinone has also been shown. The luminescence of HgS QDs ($\lambda_{max} = 730$ nm) has been detected with 409 nm excitation laser. Numbers in the parentheses indicate relative weightage.

| System | τ_1 (ps) | τ_2 (ps) | τ_3 (ns) | τ_4 (ns) | τ_{av} (ns) |
|----------------|---------------|---------------|---------------|---------------|------------------|
| HgS@BSA | - | 120(0.23) | 1.8(0.40) | 12.5(0.36) | 5.2 |
| HgS@BSA_Hg(II) | - | 105(0.43) | 1.2(0.42) | 6.5(0.15) | 1.5 |
| HgS@BSA_Cu(II) | 30(0.82) | 430(0.07) | 2.5(0.07) | 17.0(0.04) | 1.0 |
| HgS@BSA_BQ | 55(0.86) | 320(0.12) | 1.2(0.02) | - | 0.1 |

There are two possible types of dynamic quenching mechanism through which a metal ion centre can induce the non-radiative deactivation of QDs luminescence: electron transfer or energy transfer. As far as the electron-transfer mechanism is concerned, it can occur between species in intimate contact. Energy transfer, which involves deactivation of an electronic excited state of the donor and concomitant formation of an excited state of the acceptor, can occur via through-space (Förster) or through-bond (Dexter) mechanisms [33]. The Förster mechanism[34] requires direct donor–acceptor spectral overlap and arises from the Coulombic interaction between the donor and acceptor electric fields. However, in case of HgS-Cu(II)/HgS-Hg(II), the probability of such energy transfer is usually negligible due to the lack of absorption of the unsupported metal ions (Cu and Hg). Dexter transfer [35] is identical to the Förster mechanism but

does not require significant oscillator strength on the part of the acceptor. It requires direct donor–acceptor orbital overlap; and has exponential distance dependence with a range of ~ 1 nm.

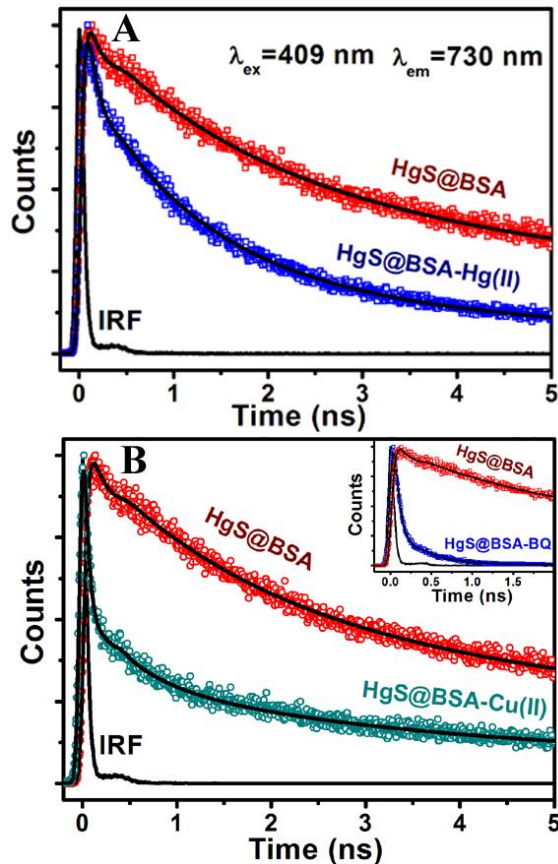
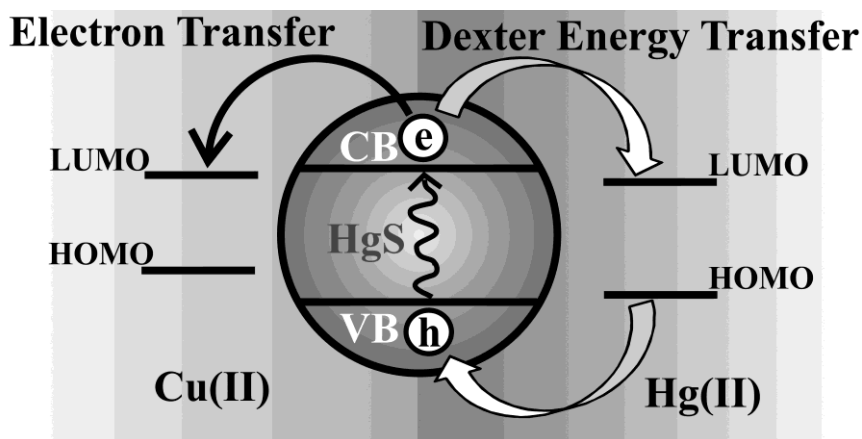


Figure 6.11. A. The picosecond-resolved fluorescence transients of HgS QDs, in the absence (red) and in the presence of acceptor Hg(II) (blue). B. The picosecond-resolved fluorescence transients of HgS QDs, in the absence (red) and in the presence of acceptor Cu(II) (cyan). Inset showing the same of HgS QDs, in the absence (red) and in the presence of benzoquinone (blue).

In the present study, both the possibilities i.e., electron transfer or Dexter energy transfer are open to Hg(II) and Cu(II) that can induce the lifetime quenching of the HgS QDs. To investigate the electron transfer dynamics from the HgS QDs upon excitation, we have studied the complexation of the HgS QDs with an organic molecule, benzoquinone (BQ), which is well-known as an electron acceptor [36] and efficiently accepts excited electrons from the surface of the semiconductor quantum dots [37]. As revealed from the inset of Figure 6.11B, in the presence of BQ a very sharp decay (monitored at 730 nm) is observed, which is associated with the transfer of excited

electrons from the conduction band of the HgS QDs into the LUMO of BQ molecules. It can be seen from Table 6.1 that HgS/BQ system exhibits an ultrafast time component of 55 ps with a majority (86%) of the excited electrons following this path. The similar faster decay component i.e., 30 ps (82%) in the presence of Cu(II) as compared to HgS/BQ system at the same excitation of 409 nm may be indicative of favourable electron transfer from the HgS QDs to the Cu(II) rather than Dexter energy transfer. However, the possibility of such kind of energy transfer can-not be completely ruled out.



Scheme 6.2. The Schematic representation of the excited-state quenching mechanism for the Cu(II) and Hg(II) ion. HOMO and VB represents highest occupied molecular orbital and valence band, respectively.

After the addition of Hg(II) solution to the HgS@BSA, although the decay is faster compared to the HgS@BSA, no such ultrafast time constant with majority like HgS/BQ system has been found, which reveals the electron transfer is not associated with this process. Assuming the formation of Hg(II)-Hg(II) metallophilic bond, the filled $5d_{z^2}$ and empty 6s orbital of each Hg(II) would overlap with each other [38], which then give rise to a bonding and anti-bonding orbitals [39]. Reorganization of these orbitals would therefore lead to a new energy-accepting levels on the Hg(II), which provides the basis of double electron exchange process (Dexter). We have also estimated the rate of energy transfer (k_{ET}) and energy transfer efficiency (E) by using the following equations:

$$k_{ET} = 1/\tau_q - 1/\tau_u \quad (6.1)$$

$$E = 1 - \tau_q / \tau_u \quad (6.2)$$

where, τ_q is the “quenched” lifetime, here 1.5 ns; and τ_u is the “unquenched” lifetime, here 5 ns. From our time resolved study, the rate of energy transfer (k_{ET}) and energy transfer efficiency (E) are found to be $4.7 \times 10^8 \text{ s}^{-1}$ and 72%, respectively.

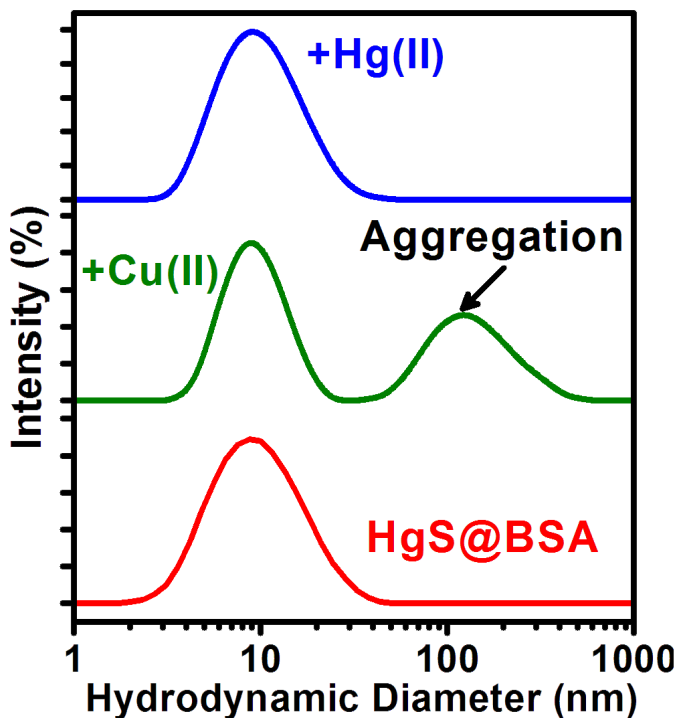


Figure 6.12. Dynamic light scattering spectra of HgS@BSA solution alone (red) upon addition of Cu(II) (green) and Hg(II) (blue).

Additionally, we have performed DLS study to know the effect of aggregation on the luminescence of as-prepared HgS@BSA. As shown in Figure 6.12, the addition of Hg(II) to HgS@BSA solution has insignificant effect on the size of HgS QDs, which rules out the possibility of luminescence quenching due to QDs aggregation [16]. In case of HgS@BSA solution containing Cu(II), the DLS peak at ~9 nm remains unaltered, however, a new peak around 150 nm appeared which is consistent with the aggregation of the free protein in solution [16]. To further confirm the aggregation effect by Cu(II) and Hg(II), a control experiment has been carried out with ethylenediaminetetraacetate (EDTA). EDTA can chelate both the metal ions in a 1:1 ratio and Cu(II) has more affinity towards EDTA than BSA [40]. If the metal ion induces the aggregation of the HgS@BSA, then, in the presence of EDTA, the metal ion would be chelated and should result in the recovery of its luminescence. However, no such recovery effect has been

observed even in 1:2 (metal ion:EDTA) ratio (data not shown) which further corroborates the direct interaction between the QDs with Cu(II) and Hg(II) ions. Attempt has also been made to separate the metal ions from the protein capped QDs by extensive dialysis against MQ water. However, no evidence of the dissociation of the metal ions resulting the recovery of the QD luminescence has been observed.

6.3. Conclusion

We have developed a simple straightforward biomineralization process for the synthesis of HgS QDs using a model protein, BSA. These QDs are extremely stable, tunable luminescence from 685-800 nm and highly quantum efficient. The luminescence of as-prepared QDs can be used as highly sensitive and selective sensing system for the detection of Hg(II) and Cu(II). The sensing mechanism is demonstrated to be based on the formation of metallophilic bond between Hg(II)/Cu(II) and Hg(II) present onto the surface of the HgS QDs. In the excited state, the metallophilic bond facilitates the Dexter energy transfer to the Hg(II) and electron transfer to the Cu(II) over the other processes associated with the dynamic quenching. The synthetic approach and the metal ion sensing with proper mechanism described herein may be extended to other types of protein-semiconductor conjugates with tailored properties for diverse applications.

References

- [1] I.L. Medintz, M.H. Stewart, S.A. Trammell, K. Susumu, J.B. Delehanty, B.C. Mei, J.S. Melinger, J.B. Blanco-Canosa, P.E. Dawson, H. Mattoussi, Quantum-Dot/Dopamine Bioconjugates Function as Redox Coupled Assemblies for In Vitro and Intracellular pH Sensing, *Nat. Mater.* 9 (2010) 676.
- [2] L. Wu, B. Quan, Y. Liu, R. Song, Z. Tang, One-Pot Synthesis of Liquid Hg/Solid β -HgS Metal–Semiconductor Heterostructures with Unique Electrical Properties, *ACS Nano* 5 (2011) 2224.
- [3] M.K. So, C.J. Xu, A.M. Loening, S.S. Gambhir, J.H. Rao, Self-Illuminating Quantum Dot Conjugates for In Vivo Imaging, *Nat. Biotechnol.* 24 (2006) 339.
- [4] P. Yang, Y. Zhao, Y. Lu, Q.Z. Xu, X.W. Xu, L. Dong, S.H. Yu, Phenol Formaldehyde Resin Nanoparticles Loaded with CdTe Quantum Dots: A Fluorescence Resonance Energy Transfer Probe for Optical Visual Detection of Copper(II) Ions, *ACS Nano* 5 (2011) 2147.
- [5] M.F. Frasco, N. Chaniotakis, Semiconductor Quantum Dots in Chemical Sensors and Biosensors, *Sensors* 9 (2009) 7266.
- [6] M. Razeghi, Y. Wei, A. Gin, G.J. Brown, Quantum Dots of InAs/GaSb Type II Superlattice for Infrared Sensing, *Mater. Res. Soc. Symp. Proc.* 692 (2002) 99.
- [7] S. Keuleyan, E. Lhuillier, P. Guyot-Sionnest, Synthesis of Colloidal HgTe Quantum Dots for Narrow Mid-IR Emission and Detection, *J. Am. Chem. Soc.* 133 (2011) 16422.
- [8] W. Wichiansee, M.N. Nordin, M. Green, R.J. Curry, Synthesis and Optical Characterization of Infra-Red Emitting Mercury Sulfide (HgS) Quantum Dots, *J. Mater. Chem.* 21 (2011) 7331.
- [9] K.A. Higginson, M. Kuno, J. Bonevich, S.B. Qadri, M. Yousuf, H. Mattoussi, Synthesis and Characterization of Colloidal b-HgS Quantum Dots, *J. Phys. Chem. B* 106 (2002) 9982.
- [10] Y.G. Yang, H.G. Liu, L.J. Chen, K.C. Chen, H.P. Ding, J. Hao, One-Step Synthesis and Assembly of Two-Dimensional Arrays of Mercury Sulfide Nanocrystal Aggregates at the Air/Water Interface, *Langmuir* 26 (2010) 14879.

- [11] T. Ren, S. Xu, W.B. Zhao, J.J. Zhu, A Surfactant-Assisted Photochemical Route to Single Crystalline HgS Nanotubes, *J. Photochem. Photobiol. A* 173 (2005) 93.
- [12] A. Mathew, P.R. Sajanlal, T. Pradeep, A Fifteen Atom Silver Cluster Confined in Bovine Serum Albumin, *J. Mater. Chem.* (2011) 11205.
- [13] J.P. Xie, Y.G. Zheng, J.Y. Ying, Highly Selective and Ultrasensitive Detection of Hg(2+) Based on Fluorescence Quenching of Au Nanoclusters by Hg(2+)-Au(+) Interactions, *Chem. Commun.* 46 (2010) 961.
- [14] C.L. Guo, J. Irudayaraj, Fluorescent Ag Clusters via a Protein-Directed Approach as a Hg(II) Ion Sensor, *Anal. Chem.* 83 (2011) 2883.
- [15] S.S. Narayanan, S.K. Pal, Structural and Functional Characterization of Luminescent Silver-Protein Nanobioconjugates, *J. Phys. Chem. C* 112 (2008) 4874.
- [16] N. Goswami, A. Giri, M.S. Bootharaju, P.L. Xavier, T. Pradeep, S.K. Pal, Copper Quantum Clusters in Protein Matrix: Potential Sensor of Pb²⁺ Ion, *Anal. Chem.* 83 (2011) 9676.
- [17] A.V. Singh, B.M. Bandgar, M. Kasture, B.L.V. Prasad, M. Sastry, Synthesis of Gold, Silver and Their Alloy Nanoparticles Using Bovine Serum Albumin as Foaming and Stabilizing Agent, *J. Mater. Chem.* 15 (2005) 5115.
- [18] P.L. Xavier, K. Chaudhari, A. Bakshi, T. Pradeep, Protein-Protected Luminescent Noble Metal Quantum Clusters: An Emerging Trend in Atomic Cluster Nanoscience, *Nano Rev.* 3 (2012) 14767.
- [19] W. Zhou, F. Baneyx, Aqueous, Protein-Driven Synthesis of Transition Metal-Doped ZnS Immuno-Quantum Dots, *ACS Nano* 5 (2011) 8013.
- [20] Y. Long, D. Jiang, X. Zhu, J. Wang, F. Zhou, Trace Hg²⁺ Analysis via Quenching of the Fluorescence of a CdS-Encapsulated DNA Nanocomposite, *Anal. Chem.* 81 (2009) 2652.
- [21] B.B. Campos, M. Algarra, B. Alonso, C.M. Casado, J.C.G. Esteves da Silva, Mercury(II) Sensing Based on the Quenching of Fluorescence of CdS-Dendrimer Nanocomposites, *Analyst* 134 (2009) 2447.
- [22] N. Goswami, A. Giri, S. Kar, M.S. Bootharaju, R. John, P.L. Xavier, T. Pradeep, S.K. Pal, Protein-Directed Synthesis of NIR-Emitting, Tunable HgS Quantum Dots and their Applications in Metal-Ion Sensing, *Small* 8 (2012) 3175.

- [23] T. Zhou, U. Schwarz, M. Hanfland, Z.X. Liu, K. Syassen, M. Cardona, Structural and Optical Properties of HgO at High Pressure, *Phys. Stat. Sol. B* 198 (1996) 411.
- [24] S.V. Gotoshia, L.V. Gotoshia, Laser Raman and Resonance Raman Spectroscopies of Natural Semiconductor Mineral Cinnabar, α -HgS, from Various Mines, *J. Phys. D: Appl. Phys.* 41 (2008) 115406.
- [25] B.A. Bolton, J.R. Scherer, Raman-Spectra and Water-Absorption of Bovine Serum-Albumin, *J. Phys. Chem.* 93 (1989) 7635.
- [26] A. Dong, P. Huang, W.S. Caughey, Protein Secondary Structures in Water from Second-Derivative Amide-I Infrared Spectra, *Biochemistry* 29 (1990) 3303.
- [27] P.L. Xavier, K. Chaudhari, P.K. Verma, S.K. Pal, T. Pradeep, Luminescent Quantum Clusters of Gold in Transferrin Family Protein, Lactoferrin Exhibiting FRET, *Nanoscale* 2 (2010) 2769.
- [28] L. Shang, Y. Wang, J. Jiang, S. Dong, pH-Dependent Protein Conformational Changes in Albumin:Gold Nanoparticle Bioconjugates: A Spectroscopic Study, *Langmuir* 23 (2007) 2714.
- [29] P. Pyykko, Theoretical Chemistry of Gold, *Angew. Chem. Int. Ed.* 43 (2004) 4412.
- [30] S. Sculfort, P. Braunstein, Intramolecular d10-d10 Interactions in Heterometallic Clusters of the Transition Metals, *Chem. Soc. Rev.* 40 (2011) 2741.
- [31] M. Kim, T.J. Taylor, F.P. Gabbai, Hg(II)…Pd(II) Metallophilic Interactions, *J. Am. Chem. Soc.* 130 (2008) 6332.
- [32] K.J. Wiechelman, R.D. Braun, J.D. Fitzpatrick, Investigation of the Bicinchoninic Acid Protein Assay - Identification of the Groups Responsible for Color Formation, *Anal. Biochem.* 175 (1988) 231.
- [33] G.D. Scholes, K.P. Ghiggino, A.M. Oliver, M.N. Paddonrow, Through-Space and Through-Bond Effects on Exciton Interactions in Rigidly Linked Dinaphthyl Molecules, *J. Am. Chem. Soc.* 115 (1993) 4345.
- [34] T. Forster, Transfer Mechanisms of Electronic Excitation Energy, *Discuss. Faraday Soc.* 27 (1959) 7.
- [35] D.L. Dexter, A Theory of Sensitized Luminescence in Solids *J. Chem. Phys.* 21 (1953) 836.
- [36] N. Goswami, A. Makhal, S.K. Pal, Toward an Alternative Intrinsic Probe for Spectroscopic Characterization of a Protein, *J. Phys. Chem. B* 114 (2010) 15236.

- [37] C. Burda, T.C. Green, S. Link, M.A. El-Sayed, Electron Shuttling Across the Interface of CdSe Nanoparticles Monitored by Femtosecond Laser Spectroscopy, *J. Phys. Chem. B* 103 (1999) 1783.
- [38] A. Gorling, N. Rosch, D.E. Ellis, H. Schmidbaur, Electronic-Structure of Main-Group-Element-Centered Octahedral Gold Clusters, *Inorg. Chem.* 30 (1991) 3986.
- [39] C.-K. Li, X.-X. Lu, K.M.-C. Wong, C.-L. Chan, N. Zhu, V.W.-W. Yam, Molecular Design of Luminescence Ion Probes for Various Cations Based on Weak Gold(I)…Gold(I) Interactions in Dinuclear Gold(I) Complexes, *Inorg. Chem.* 43 (2004) 7421.
- [40] M.A.H. Muhammed, P.K. Verma, S.K. Pal, A. Retnakumari, M. Koyakutty, S. Nair, T. Pradeep, Luminescent Quantum Clusters of Gold in Bulk by Albumin-Induced Core Etching of Nanoparticles: Metal Ion Sensing, Metal-Enhanced Luminescence, and Biolabeling, *Chem. Eur. J.* 16 (2010) 10103.

Chapter 7

Synthesis and Promising Application of a Potential Nanobiocomposite

7.1. Introduction

Transition metal chalcogenide semiconductors display interesting properties that are important for sensing, catalysis, photovoltaic, and even biology [1-8]. In particular, Molybdenum disulphide (MoS_2) is a prototypical transition metal dichalcogenide material which consists of covalently bonded Mo and S atoms. It is an indirect band gap semiconductor in its bulk form with a band gap of 1.29 eV [9]. These nano-materials have been known in the form of layered 2D sheet, nested fullerene-like nanodots, inorganic nanotubes or even as nanocrystals [10-14]. Although graphene is the best among all the known 2D materials, MoS_2 nanosheets have proved to be certainly promising as it exhibit robust mechanical properties and superior electrical performance [15, 16]. MoS_2 is also an effective lubricant because of its layered structure. Ultrathin layers of MoS_2 display strong photoluminescence that increases when the material is thinned from multilayer to monolayer because of the indirect-to-direct transition, arising from quantum confinement effects [17]. Nano structured MoS_2 has been demonstrated to be an efficient catalyst for hydrogen evolution reaction (HER) and hydro desulfurization (HDS) [18]. That all these intense properties are combined in one material implies that MoS_2 could also be one of the most valuable materials in nanotechnology.

MoS_2 nanosheets, nanofibers and nanorods have been prepared by a number of techniques-such as liquid exfoliation [19], vapour deposition [20], hydrothermal [21], electro-spinning [22], wet chemical methods [23] etc. At the same time, the colloidal synthesis of MoS_2 nanocrystals (NCs) is quite delicate, and as a result, there is less development compared to other synthetic routes. MoS_2 nanoparticles having size between 10 and 40 nm have been synthesised by metal-organic chemical vapour deposition method [24, 25]. Other approaches like sonochemical [26], solvothermal [27] or thermal decomposition methods [28] do exist, however, lack of size and shape control, and produce poorly crystalline or totally amorphous products with little solvent dispersity. Yu et al. have reported less than 5 nm MoS_2 NCs, unfortunately dispersible only in organic solvents[13]. All these methods involved complex or high temperature

reaction, and the morphology cannot be easily controlled. So, it is still a challenge to develop a facile, room temperature method to synthesize MoS₂ NCs.

The importance of finding a proper synthetic route for MoS₂ nanocrystals has been a driving force for the present work. The use of biomolecules would be an interesting template for the synthesis of MoS₂ nanocrystals as they are known to be nontoxic, viable and excellent protecting agents. Quantum dots of ZnS, CdS, HgS and PbS have been synthesised using various biomolecules [2, 29-32]. Among many biological systems that could participate in biomineralization and be indeed used as a biotemplate, DNA have been the subject of particular attention due to its excellent and predictable self-assembly properties, high rigidity of their double helices on the nanoscale, their stabilizing property and most importantly high affinity towards the metal cations. For example, self-assembled functionalization properties of DNA have enabled researchers to generate well-defined nanoparticles, quantum dots or even various superlattices [31, 33, 34]. Herein, we report a facile wet chemical synthesis of MoS₂ NCs using DNA macromolecules. To the best of our knowledge this is the first time DNA has been used to synthesise and anchor MoS₂ NCs. High resolution transmission electron microscopic (HRTEM) study reveals that nanoparticles are highly crystalline in nature with average diameter of ~5 nm. UV-vis absorption study and the corresponding band gap calculation demonstrate that as-synthesised NCs are in quantum confinement compare to the bulk MoS₂. Moreover, our Raman spectroscopic studies indicate that the optically attractive MoS₂ NCs could be Raman active in strong resonance condition. The presence of strong Raman peak at 447 cm⁻¹ along with 2nd and 3rd order Raman line in case of MoS₂ thin film further reinforce our justification on resonance Raman effect. In the present study, we also establish that akin to the other nanomaterials, MoS₂ NCs could be an efficient fluorescence quencher. For that, we have chosen Hoechst33258 (referred as H258 henceforth), which is well-known as a potential DNA minor groove binders. It could be a Förster resonance energy transfer (FRET) donor when confined in DNA. Afterwards, we show efficient energy transfer between H258, and proximal MoS₂ NCs confined in DNA by using steady-state and time resolved spectroscopy. We first demonstrate a FRET based model, which follows 1/r⁶ distance dependence, to calculate the donor-acceptor distance (r). We then explore the probability of donor-acceptor distance distribution by using a simple mathematical model. Finally, employing the

kinetic model developed by Tachiya (for the quenching of luminescent probes) [35, 36], we analyze the picosecond-resolved fluorescence results to understand the kinetics of energy transfer.

7.2. Results and Discussion

7.2.1. MoS₂ Nanocrystals Confined in DNA Matrix Exhibiting Energy Transfer [37]:

The process for synthesizing the MoS₂ nanocrystals (NCs) is simple and involves two steps. First, addition of molybdenum chloride to the DNA solution followed by the increase of pH to 9 (by the addition of NaOH) under vigorous stirring renders the molybdenum ion to be coordinated with the DNA. After 6-8 hrs the solution becomes colourless. Finally, sodium sulphide (Na₂S) is added and pH of the solution has been adjusted to 6 by adding hydrochloric acid (HCl). The colourless solution turns into yellow indicating the formation of MoS₂ NCs. We have analyzed the as-synthesised NCs by various microscopic and spectroscopic techniques. A typical transmission electron microscopic (TEM) image of the MoS₂ NCs is shown in Figure 7.1a. The NCs appear to be spherical in shape and fairly uniform in size. The particle sizes are estimated by fitting our experimental TEM data over 45 particles which provides the mean diameter of ~5 nm (Figure 7.1b). High-resolution (HR) images of single particle are shown in Figure 7.1c & d. The HRTEM images shown in Figure 7.1f & g, as well as the selected area electron diffraction (SAED), demonstrate the crystalline nature of the as-synthesised particles. The distance between two adjacent planes is 0.25 nm, corresponding to the (102) lattice plane of hexagonal MoS₂ [38] (International Centre for Diffraction Data (ICDD), Reference no: 00-006-0097). Further confirmation regarding the composition of as-prepared NCs is also evident from Energy-dispersive X-ray spectroscopy (EDAX).

Figure 7.2a illustrates the UV-vis absorption spectra of DNA and MoS₂@DNA in water. Well-defined absorption bands featuring at 384 nm and 468 nm appear for the final MoS₂@DNA solution. Chikan et al have reported size dependent spectroscopic study of MoS₂ nanoclusters [28]. They have established that MoS₂ nanoclusters having size in between 3-8 nm have absorption maxima around 362-470 nm. Since the two absorption peaks are present in MoS₂@DNA absorption spectrum, we associate the peaks

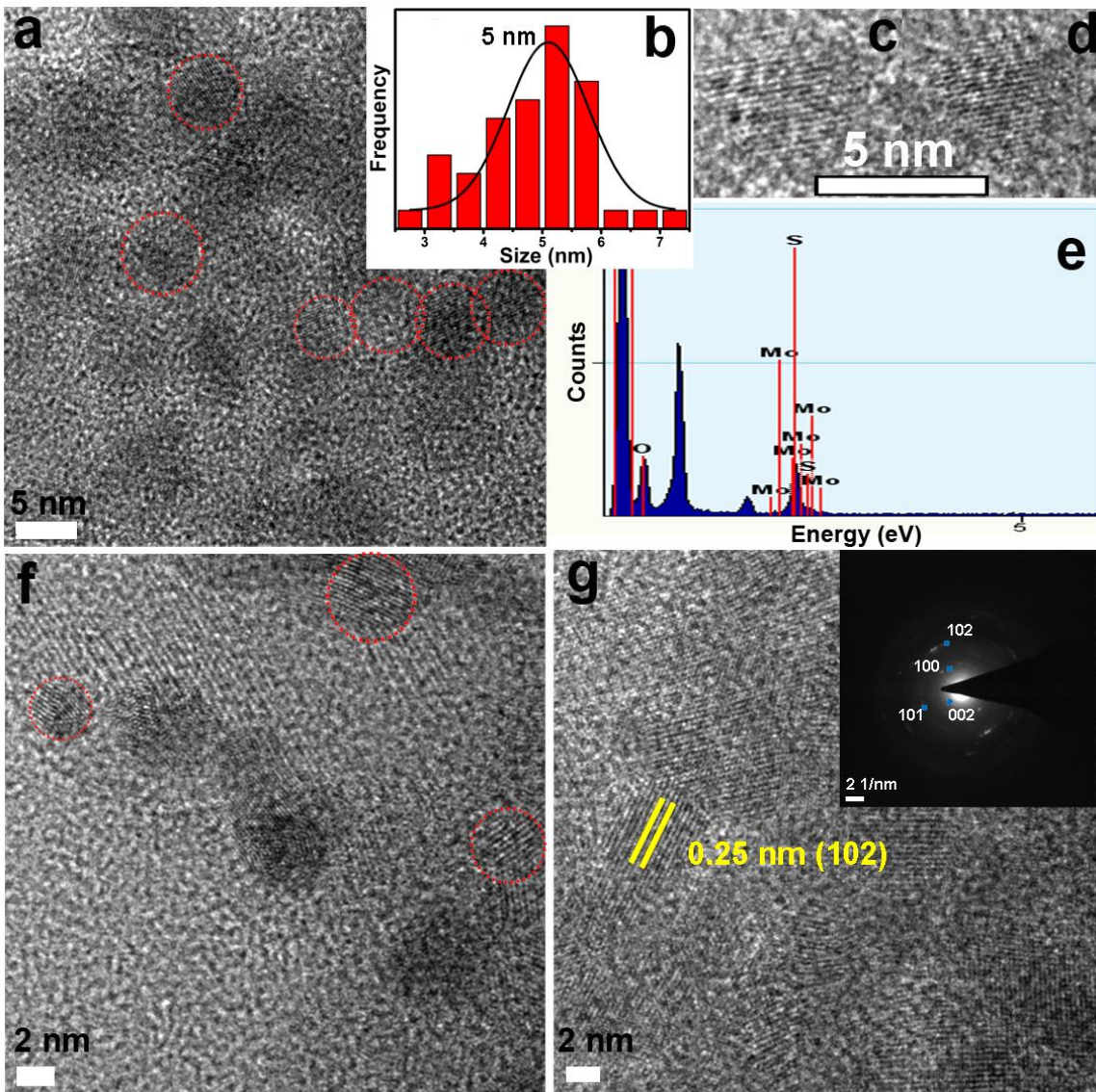


Figure 7.1. a & f. TEM image of the MoS_2 NCs. b. size distribution curve. c & d. HRTEM images of single MoS_2 NC. e. EDAX spectrum collected for $\text{MoS}_2@\text{DNA}$. g. HRTEM image and selected area electron diffraction (SAED) pattern (inset).

with different size of MoS_2 NCs rather 1st and 2nd order quantum confined state of the same NCs. This observation is also consistent with the broad size distribution obtained from our TEM studies. The optical band gaps of MoS_2 NCs, measured from the onset of the absorption peaks, are ~ 2.30 eV and 2.51 eV respectively (Figure 7.2b). Taking into account the band gap of bulk MoS_2 , i.e., 1.29 eV, one might expect photoluminescence from the as prepared NCs due to large quantum confinement effect. However, no such

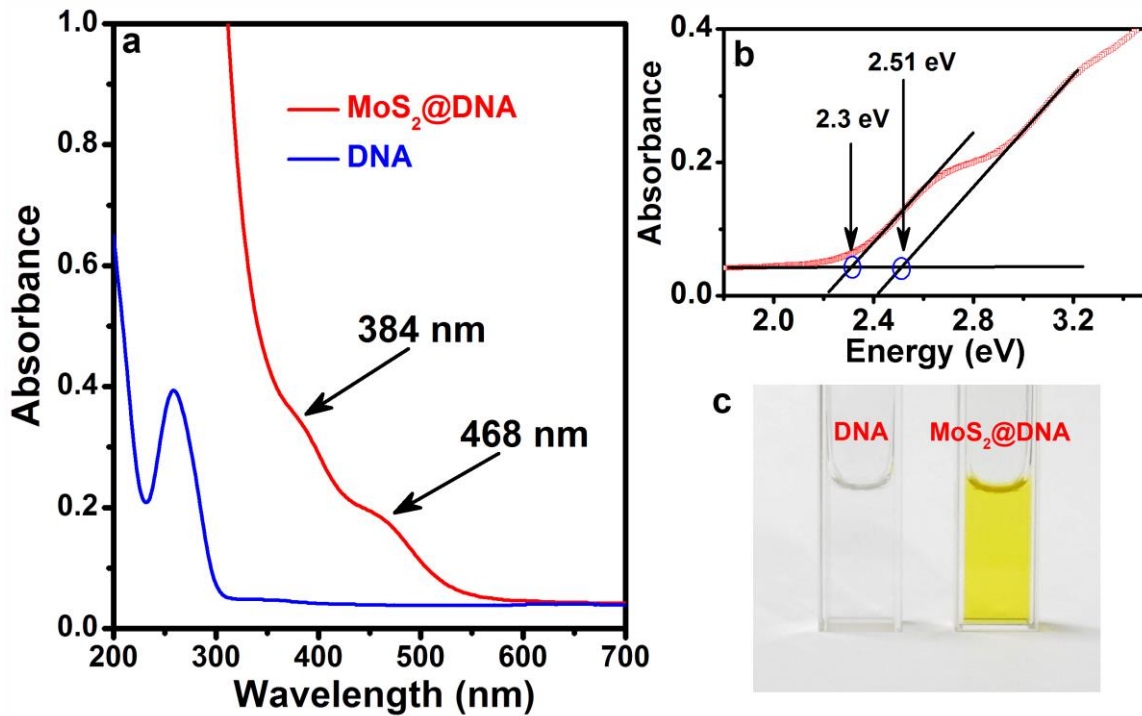


Figure 7.2. a. UV-vis absorption spectra of DNA and MoS₂@DNA in water. Well defined absorption bands of the NCs are marked with arrows. b. Band gaps from the onset of the absorption bands of the MoS₂ NCs. c. Photographs of DNA and MoS₂@DNA solution under visible light.

photoluminescence has been observed from our as prepared NCs (data not shown), which reveals that evolution of photoluminescence due to quantum confinement effect may not be applicable for our NCs; rather it is more relevant for MoS₂ nanosheets [17]. Photographs of the DNA and MoS₂@DNA solutions under visible light are shown in Figure 7.2c.

It is important to know the role of various parameters during the synthesis as it would be beneficial for scalable synthesis. We propose that sodium hydroxide has a role for the binding of molybdenum ion to the DNA, whereas, acidic medium assists the formation of hydrogen sulphide (H₂S) from Na₂S, which then react with Mo-DNA complex. Direct addition of Na₂S to the molybdenum chloride solution at acidic pH leads to the formation of bulk MoO₃ precipitate as reflected from the Raman spectrum (Figure 7.3) [39]. To investigate MoS₂ binding sites of DNA, we have performed FTIR studies. Figure 7.4 compares the FTIR of DNA and MoS₂@DNA. Absorptions in the 1500~1250 cm⁻¹ region are caused by base-sugar vibrations. Sugar-phosphate vibrations appear

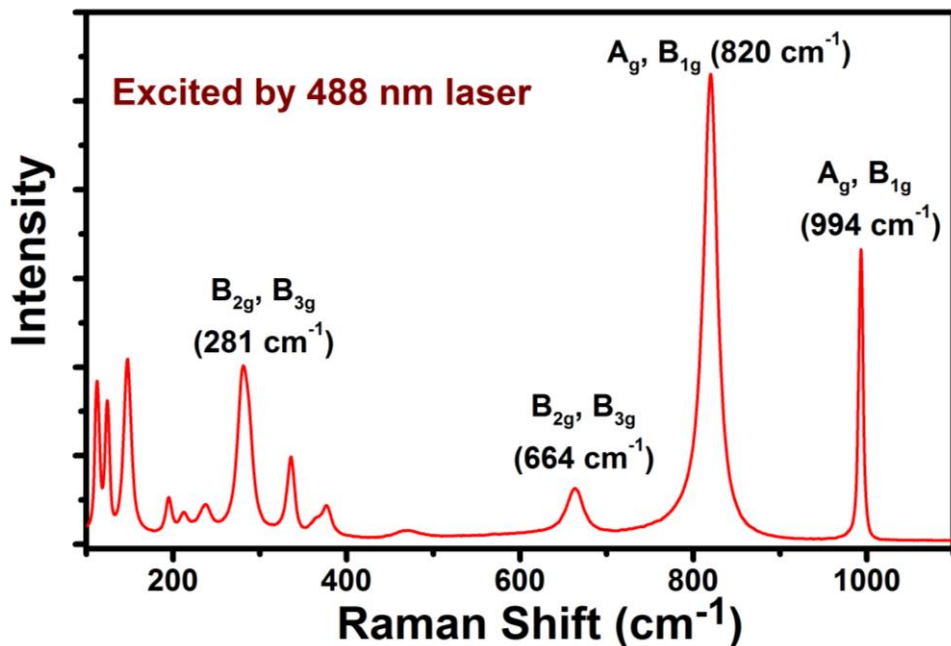


Figure 7.3. Raman spectrum (488 nm excitation) of the precipitate obtained from the mixture of MoCl_5 and Na_2S at acidic pH. The entire region of the spectrum matches with bulk MoO_3 powder indicates that presence of DNA is essential for the synthesis of MoS_2 NCs.

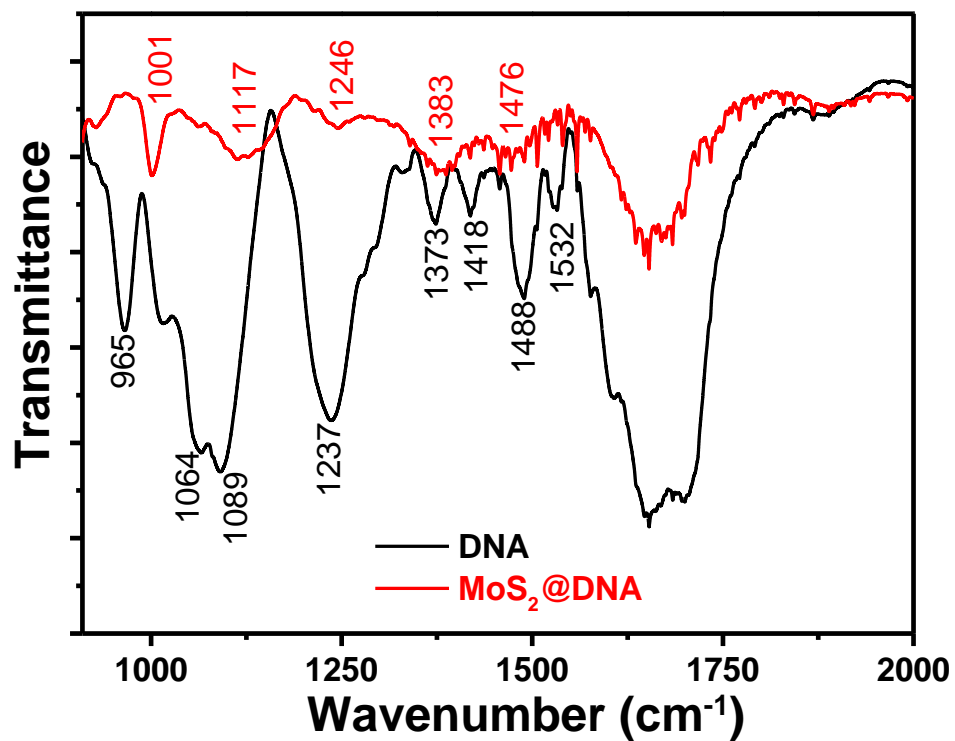


Figure 7.4. FTIR spectra of DNA (black colour) and $\text{MoS}_2@\text{DNA}$ (red colour).

in the $1250\sim1000\text{ cm}^{-1}$ region. From the spectra, we can observe that both the spectral regions have perturbed significantly which indicates that there is a significant interaction of the MoS_2 with the DNA and that the samples are not merely mixtures of DNA and MoS_2 .

Raman spectra have been recorded at ambient temperatures using different excitation wavelengths. Figure 7.5 displays the Raman spectra of $\text{MoS}_2@\text{DNA}$ excited by 488 nm and 785 nm lines, respectively. It is clearly observed that there is a variation of peak intensity corresponding to the change in the excitation line. As depicted in Figure 7.5, the Raman spectra obtained upon excitation with 488 nm line have peaks at 450 and 901 cm^{-1} , respectively, whereas a broad peak around 450 cm^{-1} has been observed for the 785 nm excitation line. The evident peak broadening could be caused by the low spectral

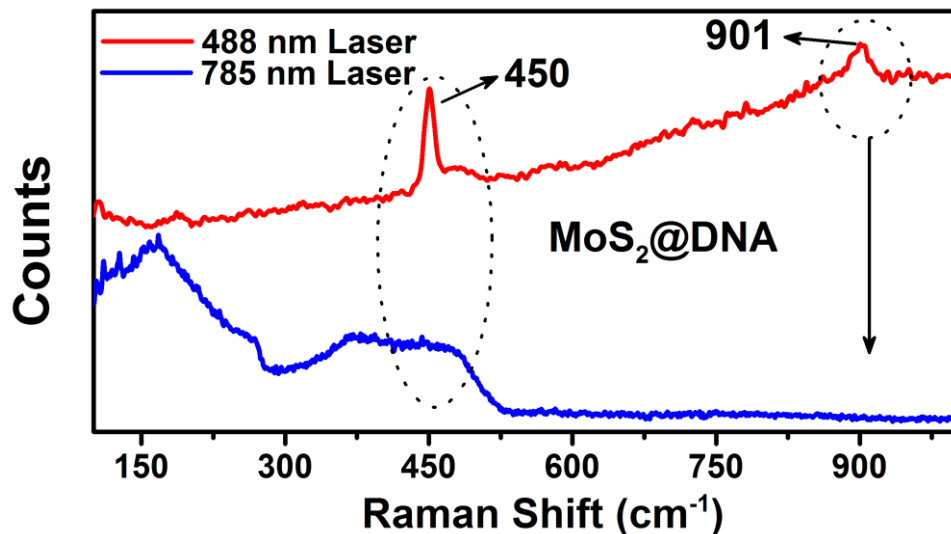


Figure 7.5. Raman characterization of $\text{MoS}_2@\text{DNA}$ in solid state using 488 nm (red) and 785 nm (blue) excitation line.

resolution of the Raman spectroscopy with 785 nm laser or due to the small size of the NCs integrated in large macromolecules. In contrast, in case of 488 nm excitation the Raman spectrum shows strong peaks owing to the resonance Raman (RR) scattering, because the 488 nm line is in resonance with the band gap of the MoS_2 NCs (2.3 eV). Furthermore, second order Raman peak at 901 cm^{-1} also provides evidence about the RR effect.

Frey et al. disputed that the broad asymmetric peak around $450\text{-}460\text{ cm}^{-1}$ for bulk MoS₂ consists of two peaks, i.e., a 2nd order zone-edge phonon peak 2LA(M) at 454 cm^{-1} and a 1st order optical phonon peak A_{2u} at 465 cm^{-1} .^[40] Li et al. ascribed that the asymmetric feature splits into three peaks around 440, 450, and 459 cm^{-1} where the 440 cm^{-1} peak has been assigned to Mo-S vibrations for oxy-sulphide species and the later provided the supportive evidence for Frey et al.'s argument.^[41] Most recently, Rao et al. have reported resonant Raman studies of few layers of MoS₂, where they have found that $450\text{-}460\text{ cm}^{-1}$ region become intense in resonance condition.^[42] Taking into account the high resonance conditions, we anticipate that 450 cm^{-1} peak observed for MoS₂ NCs excited by 488 nm line is due to the strong electron-phonon coupling as expected in RR scattering.

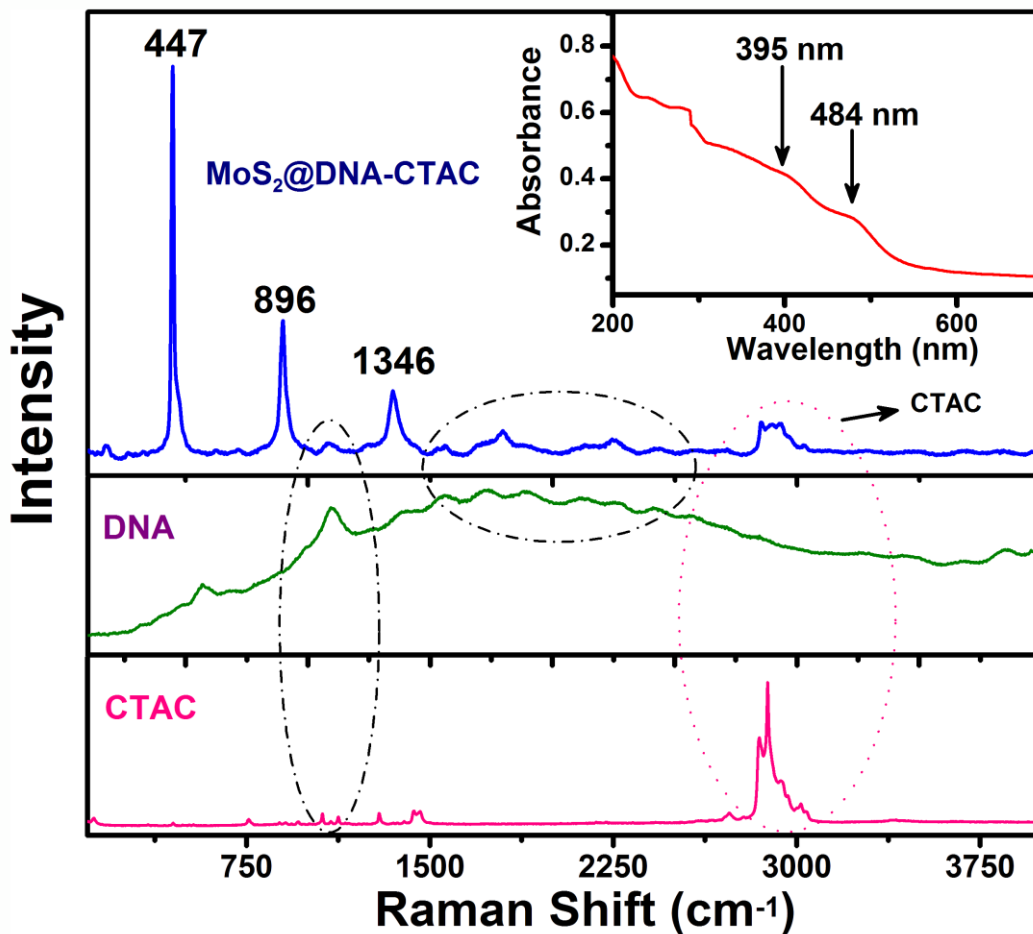


Figure 7.6. Raman Raman spectra of CTAC (pink), DNA (green) and MoS₂@DNA-CTAC film (blue). 488 nm excitation line has been used for the Raman studies. Inset shows the absorption spectrum of the MoS₂@DNA-CTAC thin film.

As 2D MoS₂ has huge application in mechanics and field-effect transistors (FETs) at the nanoscale [43-45], we choose to prepare thin film of MoS₂ NCs. The procedure for the synthesis of MoS₂@DNA-CTAC thin film has been mentioned in the experimental section. The UV-vis absorption spectrum of the film has been shown in the inset of Figure 7.6. As both CTAC and DNA have no UV-vis absorption after 300 nm, implying that 395 nm and 484 nm peaks are solely due to the MoS₂ NCs. Note that, the absorption peaks have been red shifted in the thin film, and the effect of which is later reflected in the Raman spectrum of the MoS₂@DNA-CTAC thin film. In comparison with solid MoS₂@DNA, MoS₂@DNA-CTAC thin film has more intense Raman peaks (excited by 488 nm line), as depicted in Figure 7.6. Raman spectra of DNA and CTAC alone have also been shown in the Figure 7.6. While most of the Raman peaks of DNA and CTAC remain unaltered, a strong peak at 447 cm⁻¹ along with two other peaks at 896 cm⁻¹ and 1346 cm⁻¹ are clearly evident in the MoS₂@DNA-CTAC thin film. The fact that Raman peaks originated for the MoS₂ thin film are much stronger as well as blue shifted about 3-4 cm⁻¹ compare to MoS₂@DNA in the solid state. In obvious contrast, the strong resonance condition arises in the MoS₂ thin film, as the laser excitation energy coincides more with the electronic absorption band of the MoS₂ thin film compare to MoS₂@DNA, causing an enhancement in the total scattering cross section.

To investigate any conformational and structural changes in DNA, due to the formation of MoS₂ NCs, circular dichroism (CD) spectroscopy has been carried out. Figure 7.7 represents the CD spectra of DNA, in absence and presence of MoS₂ NCs. As evidenced from the Figure, a negative band at 246 nm and a positive band at 280 nm point towards the B-form of DNA, consisting with the existing literature [46]. Insignificant broadening with a slight red shift of the 280 nm band in the CD spectrum of MoS₂@DNA indicates a little perturbation of the DNA structure. Decrease of molar ellipticity of the 248 nm band as well as slight increase of 280 nm band intensity in the presence of MoS₂ NCs indicate the perturbation of overall secondary structure of the DNA. The study of DNA-nanoparticle (NP) interaction by Narayanan et al. and many others have also reported this kind of perturbation and argued that the perturbation may be associated with the condensation of the DNA in presence of NPs as it could easily wrap around the NPs due to its flexible nature [47-49]. Our study also provides a supportive evidence for their argument.

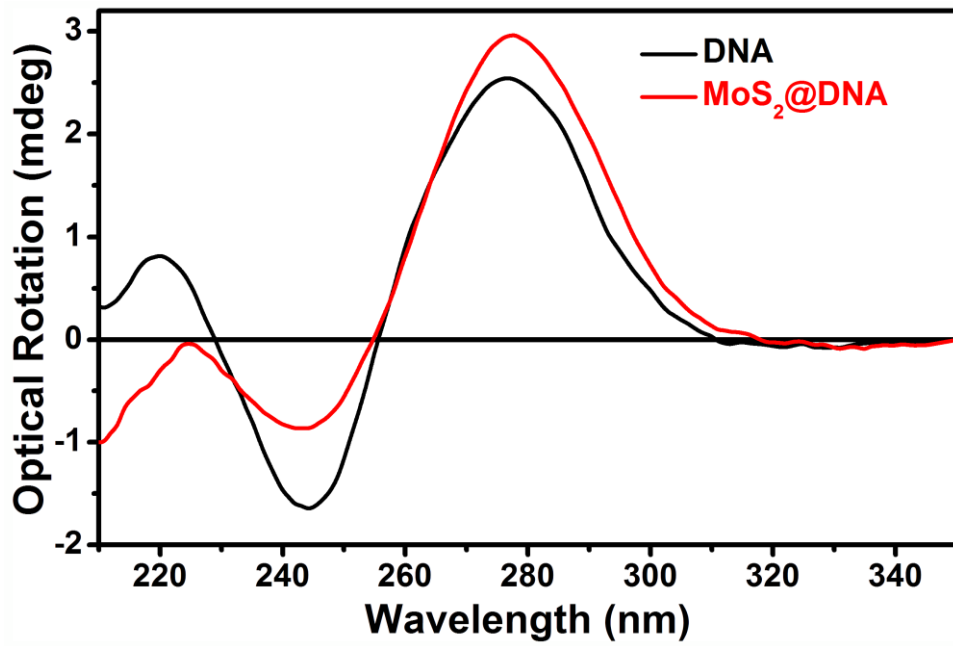


Figure 7.7. Circular dichroism spectra of DNA and MoS₂@DNA in water.

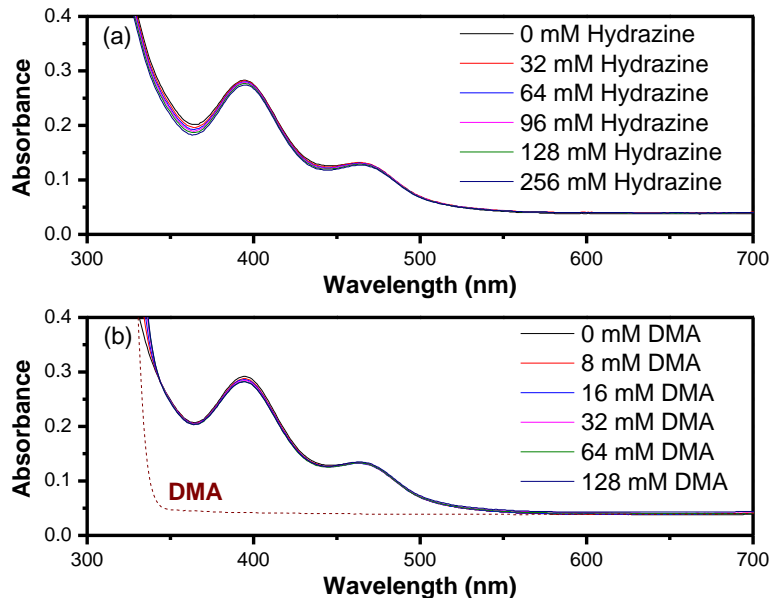


Figure 7.8. UV-vis absorption spectra of MoS₂@DNA before and after interaction with different concentrations of hydrazine (a) and DMA (b). Spectrum of DMA is also shown in dotted line.

A very recent studies by Rao et al. demonstrated that MoS₂ could be a p-type conductor, so it would prefer to interact with electron donor molecules [50]. They have shown the charge-transfer interaction of MoS₂ with an electron donor molecule like tetrathiafulvalene (TTF) by monitoring the absorption band of TTF as well as MoS₂. We

have also monitored the UV-vis spectrum of the MoS₂ NCs with various concentration of a well-known electron donor, however, the absorption bands of MoS₂ NCs remain unaltered indicating that MoS₂@DNA could not accept electron in the ground state (Figure 7.8). It is widely accepted that nanomaterial confined in biomolecule involves in the energy transfer process and several studies have been performed on this direction [49, 51, 52]. Now, the question is, could MoS₂ NCs adequately quench the fluorescence of the dye/donor molecules so that it can replace some of the currently used nanomaterials? In the present study, we have taken H258 as donor, which is a well-known dye that interacts with the minor grooves of the DNA molecule. Steady-state fluorescence measurements have been carried out on both the H258-DNA and MoS₂@H258-DNA solutions. It has been found that fluorescence of H258 underwent drastic quenching in presence of MoS₂ NCs. Figure 7.9b depicts the fluorescence spectra of H258 without and with the presence of MoS₂ NCs. As evidenced from the Figure, an unprecedented fluorescence quenching of 94% has been observed. The drastic quenching in the steady-state obviously proves the efficacy of the MoS₂ NCs as a fluorescence quencher, however, does not provide any information about the nature of the quenching, i.e., whether it is static or dynamic. Picosecond-resolved fluorescence spectroscopy is a useful technique which provides information about the excited state dynamics. Figure 7.9c shows the decay profiles of the H258-DNA and MoS₂@H258-DNA monitored at the fluorescence maxima of the donor i.e., at 470 nm ($\lambda_{ex} = 375$ nm). The decay transient of the donor (H258) has been fitted with two components with an average lifetime of 2.6 ns. The fluorescence decay trace of the donor-acceptor (MoS₂@H258-DNA) could be fitted with a fast component, apparently corresponding to some nonradiative channel, along with two other components. The average lifetime of the donor-acceptor pair has been calculated to be 0.28 ns, which is much shorter than the donor's average lifetime. Details of the fitting parameters of the time-resolved decays are tabulated in Table 7.1. Energy transfer, which involves deactivation of an electronic excited state of the donor and requires direct donor-acceptor spectral overlap, arises from the Columbic interaction between the donor and acceptor electric fields. Our study indeed demonstrates the incidence of huge spectral overlap between the fluorescence of the H258 (donor) and the absorbance of the MoS₂ NCs (acceptor). The quenching of fluorescence decay transients

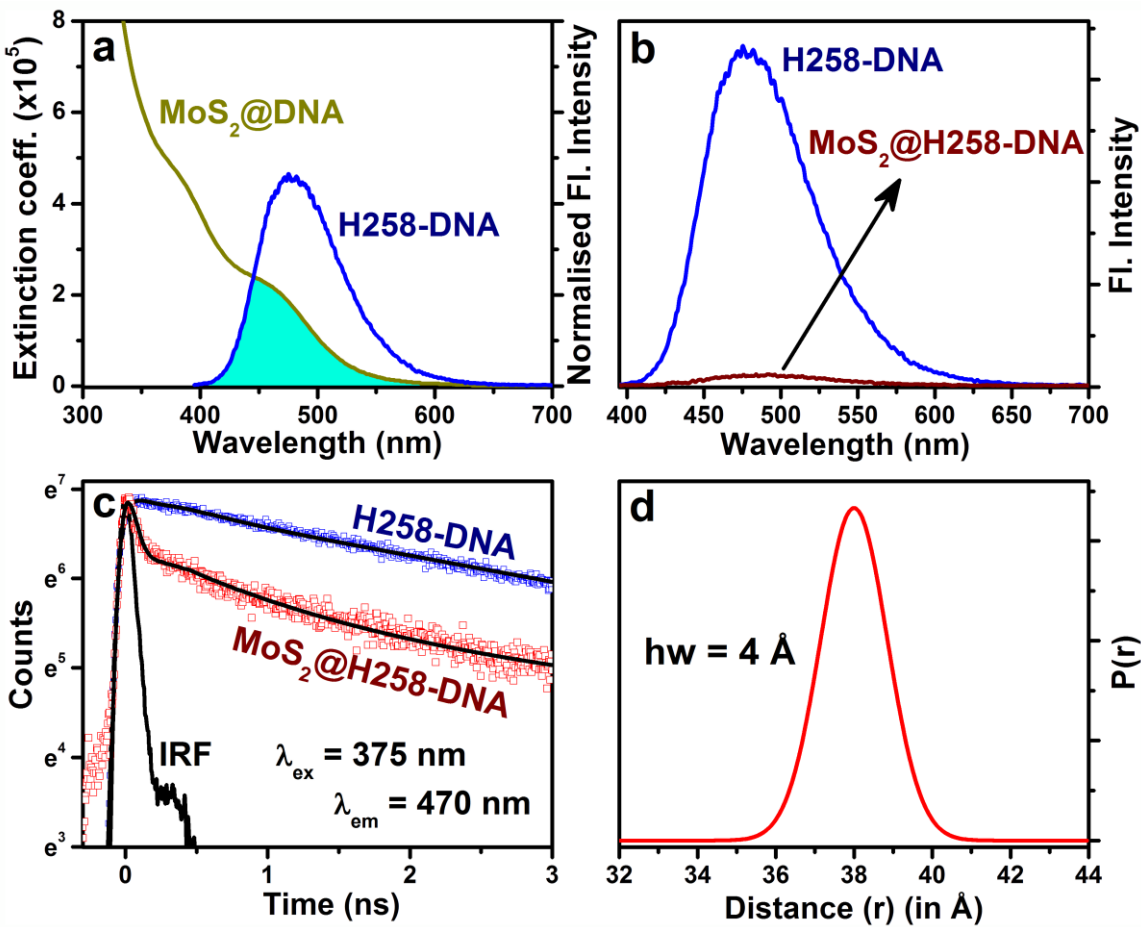


Figure 7.9. a. Spectral overlap between fluorescence spectrum of H258-DNA and the absorption spectrum of $\text{MoS}_2@\text{DNA}$ (the extinction coefficient value is for the acceptor, $\text{MoS}_2@\text{DNA}$). b. Steady-state fluorescence quenching of H258 in presence of the acceptor $\text{MoS}_2@\text{DNA}$. c. Picosecond-resolved fluorescence transients of H258-DNA and $\text{MoS}_2@\text{H258-DNA}$ monitored at 470 nm ($\lambda_{\text{ex}} = 375 \text{ nm}$). d. Probability of distance distribution ($P(r)$) with respect to mean donor-acceptor distance.

Table 7.1. Fitted decay time constants of H258-DNA and $\text{MoS}_2@\text{H258-DNA}$ from picosecond time resolved experiments. Values in parentheses represent the relative weight percentage of the time components. Standard error is $\sim 5\%$.

| System | $\tau_1(\%)$ | $\tau_2(\%)$ | $\tau_3(\%)$ | τ_{av} |
|--------------------------------|---------------|---------------|--------------|--------------------|
| H258-DNA | 0.30 ns (25%) | 3.40 ns (75%) | 0.00 ns | 2.60 ns |
| $\text{MoS}_2@\text{H258-DNA}$ | 0.02 ns (90%) | 0.92 ns (6%) | 6.1 ns (4%) | 0.28 ns |

as well as the spectral overlap therefore leads to the association of energy transfer process.

The fitting result obtained from the decay transients is typical of a FRET (Förster resonance energy transfer) donor decay transient, where rapid nonradiative transfer of energy from an excited donor to a ground-state acceptor manifests in a rapid drop off of the donor signal with time. We have estimated the energy transfer efficiency from the lifetime of the donor and donor-acceptor pair to be 89%. The energy transfer efficiency obtained from the lifetime measurements are different from the steady-state measurements, however, more reliable as former is more sensitive than the later because of the lamp fluctuation as well as many other process. It is noteworthy to mention that we have calculated the donor-acceptor distance by using FRET method. Details of the FRET have been described in the experimental section (see Chapter 2, Section 2.1.2). We have estimated the overlap integral $J(\lambda)$ to be $6.86 \times 10^{15} \text{ M}^{-1}\text{cm}^{-1}\text{nm}^4$ according to the equation 2.26 (see Chapter 2, Section 2.1.7). The characteristic Förster distance (R_0) is calculated to be 55 Å. Using the efficiency of FRET, we have calculated the donor-acceptor distance (r) to be 38 Å. Taking into account that the average radii of the MoS₂ NC is 2.5 nm (25 Å) (from the TEM measurements), the calculated donor-acceptor distance indicates that the residing probability of the donor H258 is very close to the surface of the NCs. In order to get idea of the probability distribution of donor-acceptor distance, we have analyzed the time resolved decay transients of H258 in presence and absence of MoS₂ NCs to construct the distance distribution function, $P(r)$ (see Chapter 2, Section 2.1.7). As evident in Figure 7.9d, the half width (hw) of the distance distribution is found to be 4 Å. This corresponds to a very high efficiency of energy transfer.

For better understanding of the energy transfer between the excited state of H258 with MoS₂ NCs, it is essential to know the distribution of acceptor (MoS₂ NCs) around the H258 molecules (bonded to the minor grove of DNA), because this is a governing factor that can influence the efficient energy transfer as observed from the time resolved fluorescence studies (Figure 7.9c). In this regard, we have applied a kinetic model developed by Tachiya for the quenching of fluorescent probes [35, 36]. Figure 7.10 demonstrates the time resolved fluorescence transients of H258 in absence and presence of MoS₂ NCs and black curves correspond to the fitting of the decay transients with

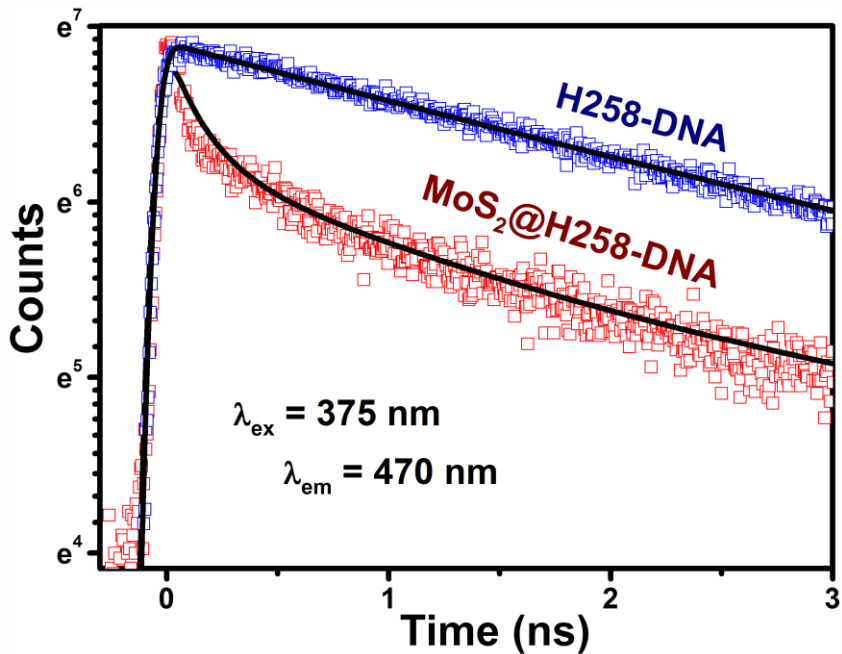


Figure 7.10. Picosecond-resolved fluorescence transients of H258-DNA (blue) and MoS₂@H258-DNA (red), fitted with Tachiya's kinetic model. The fitted curves are shown in black.

Table 7.2. Fitted Overview of the value of quenching parameters using kinetic model developed by Tachiya.

| System | k_o [ns ⁻¹] | m_t | k_{qt} [ns ⁻¹] | m | k_q [ns ⁻¹] |
|----------------------------|---------------------------|-------|------------------------------|------|---------------------------|
| H258-DNA | 0.01 | 8.47 | 0.03 | - | - |
| MoS ₂ @H258-DNA | 0.01 | 8.47 | 0.03 | 1.08 | 6 |

equation 2.54 and 2.55 (see Chapter 2, Section 2.1.6 for details). The observed fluorescence transients were fitted using a nonlinear least squares fitting procedure (software SCIENTIST™) to a function ($X(t) = \int_0^t E(t')P(t-t')dt'$) comprising of the convolution of the instrument response function (IRF) ($E(t)$) with exponential ($P(t,m) = P(0)\exp\{-k_0t - m_t[1 - \exp(-k_{qt}t)] - m[1 - \exp(-k_qt)]\}$). The purpose of this fitting is to obtain the decays in an analytic form suitable for further data analysis. Reasonably good fitting has been observed from the model. The quenching parameters are summarized in Table 7.2. The quenching rate constant (k_{qt}), which corresponds to unidentified traps, are same even after addition of acceptor (MoS₂ NCs), and this indicates the average number

of unidentified trap states to be the same. However, it is observed from Table 7.2 that the average number of unidentified traps state (m) increases with addition of acceptor molecules. Since, there are still many unknown parameters in the excitation dynamics of H₂₅₈, for an accurate interpretation of this observation a more complex model is required. One important finding is the mean number of acceptor (MoS₂ NCs) associated with each donor is 1.08 and the estimated rate constant for energy transfer (k_q) per acceptor molecules is 6 ns⁻¹. The energy transfer rate calculated from conventional FRET model has been found to be comparable (3.57 ns⁻¹) from the value obtained using Tachiya's model (6 ns⁻¹).

7.3. Conclusion

In conclusion, well crystallized ~ 5 nm MoS₂ NCs have been synthesised in DNA matrix. The calculated band gaps from the optical absorption of MoS₂ NCs confirm the quantum confinement of the NCs conjugated with DNA matrix. Strong electron-phonon resonance condition makes MoS₂ NCs to be Raman active. Compare to MoS₂ NCs, MoS₂ thin film has more intense Raman peaks as the laser excitation energy coincides more with the electronic absorption band of the MoS₂@DNA-CTAC thin film compare to MoS₂@DNA. Moreover, present study also reveals that similar to the other various nanomaterials, MoS₂ NCs would have profound impact as an efficient fluorescence quencher. Analysis suggests that the fluorescence quenching of donor in presence of MoS₂ NCs is mainly due to nonradiative decay channel which confirms the energy transfer process. Donor-acceptor distance of 38 Å has been estimated using the efficiency of FRET model. Further analysis of the probability of donor-acceptor distance distribution suggests that the donor molecules are very close proximity to the surface of the NCs. We have employed a kinetic model developed by Tachiya for understanding the kinetics of energy transfer from H₂₅₈ to MoS₂ NCs, assuming the Poisson distribution of the quencher molecules around H₂₅₈ bound to the DNA minor grooves, which closely resembles the FRET data. Such a synthetic route of MoS₂ NCs as well as thin film based on the DNA template may be extended to the other transition metal chalcogenide materials and we believe that MoS₂ NCs-based energy transfer is expected to grow in near future.

References

- [1] I.L. Medintz, M.H. Stewart, S.A. Trammell, K. Susumu, J.B. Delehanty, B.C. Mei, J.S. Melinger, J.B. Blanco-Canosa, P.E. Dawson, H. MattoSSI, Quantum-Dot/Dopamine Bioconjugates Function as Redox Coupled Assemblies for In Vitro and Intracellular pH Sensing, *Nat. Mater.* 9 (2010) 676.
- [2] N. Goswami, A. Giri, S. Kar, M.S. Bootharaju, R. John, P.L. Xavier, T. Pradeep, S.K. Pal, Protein-Directed Synthesis of NIR-Emitting, Tunable HgS Quantum Dots and their Applications in Metal-Ion Sensing, *Small* 8 (2012) 3175.
- [3] Q.H. Wang, K. Kalantar-Zadeh, A. Kis, J.N. Coleman, M.S. Strano, Electronics and Optoelectronics of Two-Dimensional Transition Metal Dichalcogenides, *Nat. Nanotechnol.* 7 (2012) 699.
- [4] Q. Xiang, J. Yu, M. Jaroniec, Synergetic Effect of MoS₂ and Graphene as Cocatalysts for Enhanced Photocatalytic H₂ Production Activity of TiO₂ Nanoparticles, *J. Am. Chem. Soc.* 134 (2012) 6575.
- [5] W. Ho, J.C. Yu, J. Lin, J. Yu, P. Li, Preparation and Photocatalytic Behavior of MoS₂ and WS₂ Nanocluster Sensitized TiO₂, *Langmuir* 20 (2004) 5865.
- [6] B. Radisavljevic, A. Radenovic, J. Brivio, V. Giacometti, A. Kis, Single-Layer MoS₂ Transistors, *Nat. Nanotechnol.* 6 (2011) 147.
- [7] R. Shen, X. Shen, Z. Zhang, Y. Li, S. Liu, H. Liu, Multifunctional Conjugates to Prepare Nucleolar-Targeting CdS Quantum Dots, *J. Am. Chem. Soc.* 132 (2010) 8627.
- [8] X. Michalet, F.F. Pinaud, L.A. Bentolila, J.M. Tsay, S. Doose, J.J. Li, G. Sundaresan, A.M. Wu, S.S. Gambhir, W. S., Quantum Dots for Live Cells, in Vivo Imaging, and Diagnostics *Science* 307 (2005) 538.
- [9] K.F. Mak, C. Lee, J. Hone, J. Shan, T.F. Heinz, Atomically Thin MoS₂: A New Direct-Gap Semiconductor, *Phys. Rev. Lett.* 105 (2010) 136805.
- [10] K.-K. Liu, W. Zhang, Y.-H. Lee, Y.-C. Lin, M.-T. Chang, C.-Y. Su, C.-S. Chang, H. Li, Y. Shi, H. Zhang, C.-S. Lai, L.-J. Li, Growth of Large-Area and Highly Crystalline MoS₂ Thin Layers on Insulating Substrates, *Nano Lett.* 12 (2012) 1538.
- [11] L. Chang, H. Yang, W. Fu, J. Zhang, Q. Yu, H. Zhu, J. Chen, R. Wei, Y. Sui, X. Pang, G. Zou, Simple Synthesis of MoS₂ Inorganic Fullerene-Like Nanomaterials from MoS₂ Amorphous Nanoparticles, *Mater. Res. Bull.* 43 (2008) 2427.

- [12] M. Nath, A. Govindaraj, C.N.R. Rao, Simple Synthesis of MoS₂ and WS₂ Nanotubes, *Adv. Mater.* 13 (2001) 283.
- [13] H. Yu, Y. Liu, S.L. Brock, Synthesis of Discrete and Dispersible MoS₂ Nanocrystals, *Inorg. Chem.* 47 (2008) 1428.
- [14] H. Liao, Y. Wang, S. Zhang, Y. Qian, A Solution Low-Temperature Route to MoS₂ Fiber, *Chem. Mat.* 13 (2000) 6.
- [15] C. Ataca, H. Sahin, E. Aktürk, S. Ciraci, Mechanical and Electronic Properties of MoS₂ Nanoribbons and Their Defects, *J. Phys. Chem. C* 115 (2011) 3934.
- [16] D.J. Late, B. Liu, H.S.S.R. Matte, V.P. Dravid, C.N.R. Rao, Hysteresis in Single-Layer MoS₂ Field Effect Transistors, *ACS Nano* 6 (2012) 5635.
- [17] A. Splendiani, L. Sun, Y. Zhang, T. Li, J. Kim, C.-Y. Chim, G. Galli, F. Wang, Emerging Photoluminescence in Monolayer MoS₂, *Nano Lett.* 10 (2010) 1271.
- [18] P. Afanasiev, C. Geantet, I. Llorens, O. Proux, Biotemplated Synthesis of Highly Divided MoS₂ Catalysts, *J. Mater. Chem.* 22 (2012) 9731.
- [19] A. O'Neill, U. Khan, J.N. Coleman, Preparation of High Concentration Dispersions of Exfoliated MoS₂ with Increased Flake Size, *Chem. Mat.* 24 (2012) 2414.
- [20] Y.-H. Lee, X.-Q. Zhang, W. Zhang, M.-T. Chang, C.-T. Lin, K.-D. Chang, Y.-C. Yu, J.T.-W. Wang, C.-S. Chang, L.-J. Li, T.-W. Lin, Synthesis of Large-Area MoS₂ Atomic Layers with Chemical Vapor Deposition, *Adv. Mater.* 24 (2012) 2320.
- [21] G. Nagaraju, C.N. Tharamani, G.T. Chandrappa, J. Livage, Hydrothermal Synthesis of Amorphous MoS₂ Nanofiber Bundles via Acidification of Ammonium Heptamolybdate Tetrahydrate, *Nanoscale Res. Lett.* 2 (2007) 461.
- [22] S. Liu, X. Zhang, H. Shao, J. Xu, F. Chen, Y. Feng, Preparation of MoS₂ Nanofibers by Electrospinning, *Mater. Lett.* 73 (2012) 223.
- [23] H.S.S. Ramakrishna Matte, A. Gomathi, A.K. Manna, D.J. Late, R. Datta, S.K. Pati, C.N.R. Rao, MoS₂ and WS₂ Analogues of Graphene, *Angew. Chem. Int. Ed.* 49 (2010) 4059.
- [24] J. Etzkorn, H.A. Therese, F. Rocker, N. Zink, U. Kolb, W. Tremel, Metal–Organic Chemical Vapor Deposition Synthesis of Hollow Inorganic–Fullerene–Type MoS₂ and MoSe₂ Nanoparticles, *Adv. Mater.* 17 (2005) 2372.

- [25] X.-L. Li, J.-P. Ge, Y.-D. Li, Atmospheric Pressure Chemical Vapor Deposition: An Alternative Route to Large-Scale MoS₂ and WS₂ Inorganic Fullerene-like Nanostructures and Nanoflowers, *Chem. Eur. J.* 10 (2004) 6163.
- [26] I. Uzcanga, I. Bezverkhyy, P. Afanasiev, C. Scott, M. Vrinat, Sonochemical Preparation of MoS₂ in Aqueous Solution: Replication of the Cavitation Bubbles in an Inorganic Material Morphology, *Chem. Mat.* 17 (2005) 3575.
- [27] Y. Peng, Z. Meng, C. Zhong, J. Lu, W. Yu, Z. Yang, Y. Qian, Hydrothermal Synthesis of MoS₂ and Its Pressure-Related Crystallization, *J. Solid. State. Chem.* 159 (2001) 170.
- [28] V. Chikan, D.F. Kelley, Size-Dependent Spectroscopy of MoS₂ Nanoclusters, *J. Phys. Chem. B* 106 (2002) 3794.
- [29] W. Zhou, F. Baneyx, Aqueous, Protein-Driven Synthesis of Transition Metal-Doped ZnS Immuno-Quantum Dots, *ACS Nano* 5 (2011) 8013.
- [30] I.L. Medintz, H.T. Uyeda, E.R. Goldman, H. Mattoussi, Quantum Dot Bioconjugates for Imaging, Labelling and Sensing, *Nat. Mater.* 4 (2005) 435.
- [31] L. Levina, V. Sukhovatkin, S. Musikhin, S. Cauchi, R. Nisman, D.P. Bazett-Jones, E.H. Sargent, Efficient Infrared-Emitting PbS Quantum Dots Grown on DNA and Stable in Aqueous Solution and Blood Plasma, *Adv. Mater.* 17 (2005) 1854.
- [32] S.S. Narayanan, R. Sarkar, S.K. Pal, Structural and Functional Characterization of Enzyme-Quantum Dot Conjugates: Covalent Attachment of CdS Nanocrystal to α -Chymotrypsin, *J. Phys. Chem. C* 111 (2007) 11539.
- [33] M.R. Jones, R.J. Macfarlane, B. Lee, J. Zhang, K.L. Young, A.J. Senesi, C.A. Mirkin, DNA-Nanoparticle Superlattices Formed from Anisotropic Building Blocks, *Nat. Mater.* 9 (2010) 913.
- [34] F.A. Aldaye, H.F. Sleiman, Dynamic DNA Templates for Discrete Gold Nanoparticle Assemblies: Control of Geometry, Modularity, Write/Erase and Structural Switching, *J. Am. Chem. Soc.* 129 (2007) 4130.
- [35] M. Tachiya, Application of a Generating Function to Reaction Kinetics in Micelles. Kinetics of Quenching of Luminescent Probes in Micelles, *Chem. Phys. Lett.* 33 (1975) 289.
- [36] M. Tachiya, Kinetics of Quenching of Luminescent Probes in Micellar Systems. II, *J. Chem. Phys.* 76 (1982) 340.

- [37] N. Goswami, A. Giri, S.K. Pal, MoS₂ Nanocrystals Confined in a DNA Matrix Exhibiting Energy Transfer, *Langmuir* 29 (2013) 11471.
- [38] M.A. Albiter, R. Huirache-Acuna, F. Paraguay-Delgado, J.L. Rico, G. Alonso-Nunez, Synthesis of MoS₂ Nanorods and Their Catalytic Test in the HDS of Dibenzothiophene, *Nanotechnology* 17 (2006) 3473.
- [39] B. Windom, W.G. Sawyer, D. Hahn, A Raman Spectroscopic Study of MoS₂ and MoO₃: Applications to Tribological Systems, *Tribol. Lett.* 42 (2011) 301.
- [40] G.L. Frey, R. Tenne, M.J. Matthews, M.S. Dresselhaus, G. Dresselhaus, Raman and Resonance Raman Investigation of MoS₂ Nanoparticles, *Phys. Rev. B* 60 (1999) 2883.
- [41] H. Li, Q. Zhang, C.C.R. Yap, B.K. Tay, T.H.T. Edwin, A. Olivier, D. Baillargeat, From Bulk to Monolayer MoS₂: Evolution of Raman Scattering, *Adv. Funct. Mat.* 22 (2012) 1385.
- [42] B. Chakraborty, H.S.S.R. Matte, A.K. Sood, C.N.R. Rao, Layer-Dependent Resonant Raman Scattering of a Few Layer MoS₂, *J. Raman Spectrosc.* 44 (2013) 92.
- [43] W.S. Hwang, M. Remskar, R.S. Yan, T. Kosel, J.K. Park, B.J. Cho, W. Haensch, H.L. Xing, A. Seabaugh, D. Jena, Comparative Study of Chemically Synthesized and Exfoliated Multilayer MoS₂ Field-Effect Transistors, *Appl. Phys. Lett.* 102 (2013).
- [44] S.-W. Min, H.S. Lee, H.J. Choi, M.K. Park, T. Nam, H. Kim, S. Ryu, S. Im, Nanosheet Thickness-Modulated MoS₂ Dielectric Property Evidenced by Field-Effect Transistor Performance, *Nanoscale* 5 (2013) 548.
- [45] A. Castellanos-Gomez, M. Poot, G.A. Steele, H.S.J. van der Zant, N. Aggraït, G. Rubio-Bollinger, Elastic Properties of Freely Suspended MoS₂ Nanosheets, *Adv. Mater.* 24 (2012) 772.
- [46] R. Sarkar, S.K. Pal, Ligand–DNA Interaction in a Nanocage of Reverse Micelle, *Biopolymers* 83 (2006) 675.
- [47] S. Shankara Narayanan, S.S. Sinha, P.K. Verma, S.K. Pal, Ultrafast Energy Transfer from 3-Mercaptopropionic Acid-Capped CdSe/ZnS QDs to Dye-Labelled DNA, *Chem. Phys. Lett.* 463 (2008) 160.
- [48] R. Jin, G. Wu, Z. Li, C.A. Mirkin, G.C. Schatz, What Controls the Melting Properties of DNA-Linked Gold Nanoparticle Assemblies?, *J. Am. Chem. Soc.* 125 (2003) 1643.

- [49] A. Giri, N. Goswami, P. Lemmens, S.K. Pal, Preparation of Water Soluble L-Arginine Capped CdSe/ZnS QDs and Their Interaction with Synthetic DNA: Picosecond-Resolved FRET Study, *Mater. Res. Bull.* 47 (2012) 1912.
- [50] S. Dey, H.S.S.R. Matte, S.N. Shirodkar, U.V. Waghmare, C.N.R. Rao, Charge-Transfer Interaction between Few-Layer MoS₂ and Tetrathiafulvalene, *Chem. Asian J.* 8 (2013) 1780.
- [51] T. Sen, A. Patra, Recent Advances in Energy Transfer Processes in Gold-Nanoparticle-Based Assemblies, *J. Phys. Chem. C* 116 (2012) 17307.
- [52] I.L. Medintz, T. Pons, K. Susumu, K. Boeneman, A.M. Dennis, D. Farrell, J.R. Deschamps, J.S. Melinger, G. Bao, H. Matoussi, Resonance Energy Transfer Between Luminescent Quantum Dots and Diverse Fluorescent Protein Acceptors, *J. Phys. Chem. C* 113 (2009) 18552.

Chapter 8

Reduction of a Trace Element in Biological Matrix and its Potential Application in Toxic Metal Ion Sensing

8.1. Introduction

The drive towards optoelectronic nanodevices [1], bio-sensors [2], bio-imaging [3], nanoelectronics [4] and novel catalysts [5] has generated a need to synthesize new metal clusters. Compared to bulk materials, clusters are of fundamental interest due to their own intrinsic properties but also because of their intermediate position between molecular and materials science. Owing to their ultra-small size, biocompatibility, and highly luminescent properties, applications of these luminescent quantum clusters would be an attractive field to study. In the past few years, extensive studies have been performed on luminescent Au and Ag nanoclusters [6-10] using various templates such as peptides [11], DNA [12], thiols [13], dendrimers [14], polymers [15] and proteins [6]. Among all of them, the use of a biomolecule as template or scaffold for synthesis possesses many advantages in biological applications. However, to date, only a few experimental studies have given direct insight into copper nanoclusters [16-18] primarily because of the difficulty in preparing highly stable and extremely tiny Cu particles. Additionally, sub-nanometer sized Cu intrinsically suffers from unstable colloidal dispersion of its particles and easy surface oxidation on exposure to air. Therefore, it would be of great interest to develop very stable, highly luminescent, biocompatible copper quantum-clusters (Cu QC)s with emission in the visible range.

In this chapter, we report the synthesis of Cu QC's by a simple one-pot chemical reduction method by using a commercially available protein, bovine serum albumin (BSA). It has been demonstrated that BSA can be used as the model protein for the synthesis and stabilization of gold nanoclusters [6]. The resulting Cu QC's were highly resistant to oxidation and exhibits photoluminescence and highly stable properties in a colloidal dispersion. The as prepared blue emitting clusters were assigned a molecular formula based on MALDI-MS. The as synthesised quantum clusters were characterized thoroughly using various spectroscopic and microscopic techniques (UV-vis, luminescence, TEM, DLS, XPS, MALDI-TOF, TGA, and DSC). The effect of oxidizing agent on the luminescence property of the cluster solution was probed. The luminescence

of the QCs was exploited as a selective sensor for the detection of the toxic Pb²⁺ ion. The reason of quenching was found to be aggregation manifested as revealed from our DLS study. To the best of our knowledge this is the first time protein protected Cu QCs have been synthesised in a protein matrix and used as toxic metal ion sensor at ppm level even in the presence of other interfering ions.

8.2. Results and Discussion

8.2.1. Copper Quantum Clusters in Protein Matrix: Potential Sensor of Pb²⁺ Ion [19]:

Although weak as compared to the 280 nm peak of pure BSA, a clear absorption spectrum at 325 nm appears in the final solution (Figure 8.1A). In order to realize the origin of 325 nm peak, we have taken into account any kind of oxidation product of the amino acids in protein. However, it is well known that, all the aromatic amino acids have a characteristic absorption peak \leq 280 nm and a few tryptophan metabolites like kynurenone, 3-hydroxykynurenone, N-formylkynurenone have an absorption peak above 300 nm. Our earlier extensive studies confirmed that kynurenone [20] and its derivatives [21] in proteins have a distinct UV-Vis peak at above 350 nm. The observed 325 nm absorption peak as well as the emission maxima (see below) revealed in the present study clearly rules out the possibility of any tryptophan metabolites rather the formation of a new type of material in the protein environment. The high-resolution transmission electron microscopy (HRTEM) images (Inset of Figure 8.1A) showed that the average size is 2.8 ± 0.5 nm where the crystal lattice fringes are 2.02 Å apart which indicates the (111) planes of the metallic Cu. This is not surprising because clusters may fuse to form crystals in presence of strong electron beam irradiation [22]. Swelling of the protein size as revealed from dynamic light scattering (DLS) measurement indicates the formation of new species inside the protein having size about ~ 3 nm. Protein fragmentation as well as enhancement of aggregation is also shown in Figure 8.1B. Recently, it has been reported that fragmentation of protein can occur when pH of the environment changes drastically [23]. It is also well established that protein coordinates with copper ion to form aggregates [24].

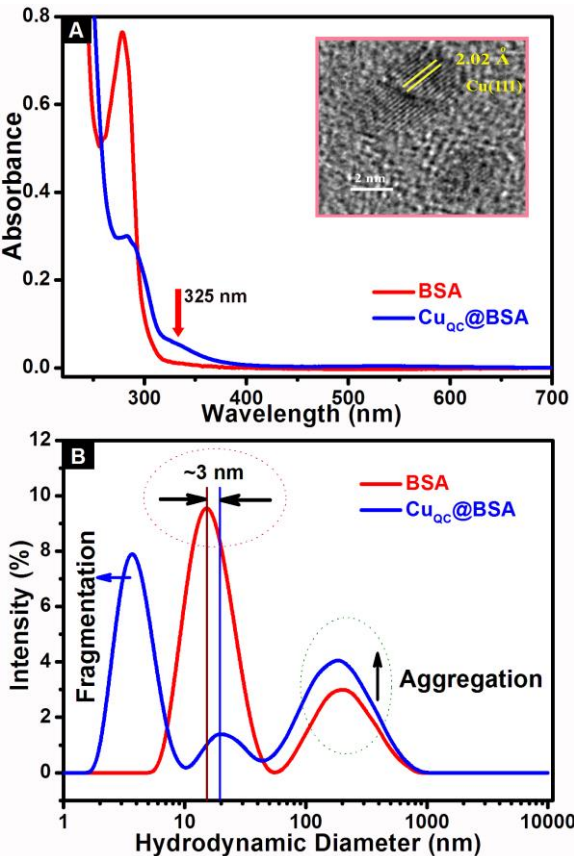


Figure 8.1. (A) UV-vis absorption spectra of BSA (red line) and Cu_{QC}@BSA solution (blue line). Inset: HRTEM of Cu QCs after being exposed to the electron beam. (B) DLS spectra of BSA (red) and Cu_{QC}@BSA (blue). All the parameters are same in both cases.

XPS analysis is carried out to determine the oxidation state of copper in the samples. Two intense peaks are observed at 932.3 and 952.0 eV (Figure 8.2B), which are assigned to $2p_{3/2}$ and $2p_{1/2}$ features of Cu (0). Although the lack of a satellite feature is assured in the Figure 8.2B, a shakeup can be observed at 942 eV, suggesting very minimal presence of Cu (II) in the system. It is also worth mentioning that the $2p_{3/2}$ binding energy of Cu (0) is only ~ 0.1 eV different from Cu (I). Therefore, the valence state of the Cu in protein matrix most likely lies between 0 and +1. Previous studies confirmed that in gold clusters, atoms can have different oxidation states depending on their position inside the clusters [25, 26]. All other expected elements are seen in the survey spectrum (Figure 8.2A).

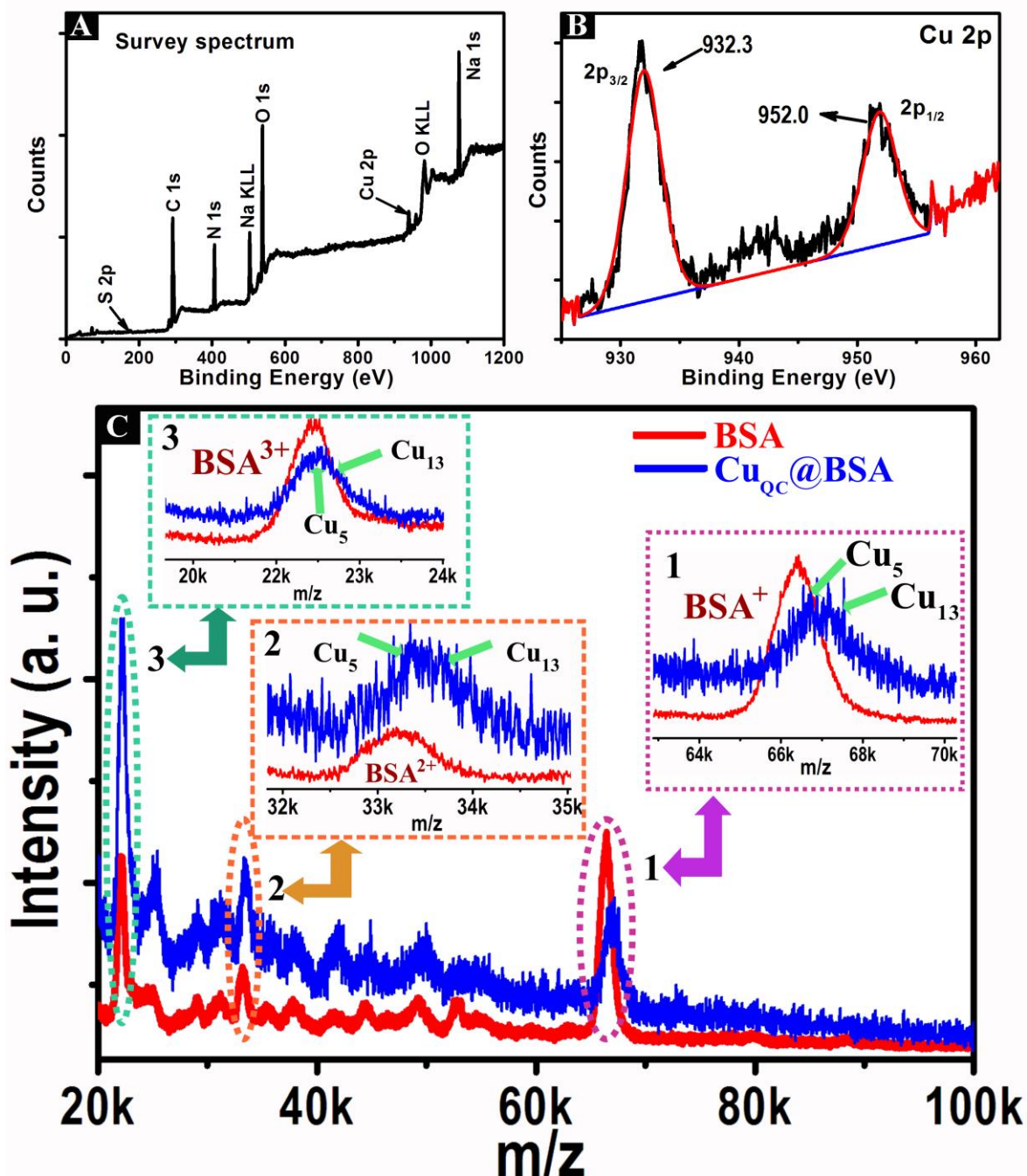


Figure 8.2. (A) XPS survey spectrum of CuQC@BSA (black). (B) XPS spectrum in the Cu 2p region of CuQC@BSA. (C) MALDI-TOF mass spectra of BSA (red) and CuQC@BSA (blue). The peaks due to singly, doubly, and triply charged ions of CuQC@BSA are expanded in the inset.

As-synthesized material has been studied using matrix-assisted laser desorption/ionization time of flight (MALDI-TOF) mass spectrometry to understand the number of copper atoms in the cluster core. The mass spectrum of BSA showed a major peak at around 66.4 kDa due to the mono-cation, which agrees with previous results on

Ag_{15} clusters [27] (Figure 8.2C, Inset 1). Cu cluster containing BSA showed two distinct, but low intensity peaks at m/z 66 723 and 67 228 Da besides the parent protein peak. The difference between the above peaks with the host protein spectrum measured at pH 12 may be attributed to the 5 and 13 copper atoms respectively; we assign the clusters to be Cu_5 and Cu_{13} . The presence of doubly as well as triply charged clusters along with the corresponding peaks of the protein observed in the MALDI MS data clearly indicates that the Cu cluster is associated with a single protein molecule (see Figure 8.2C, Inset 2-3). From all the data presented so far, we conclude that the copper quantum clusters (Cu QCs) are formed within BSA and would be referred as $\text{Cu}_{\text{QC}}@\text{BSA}$ henceforth

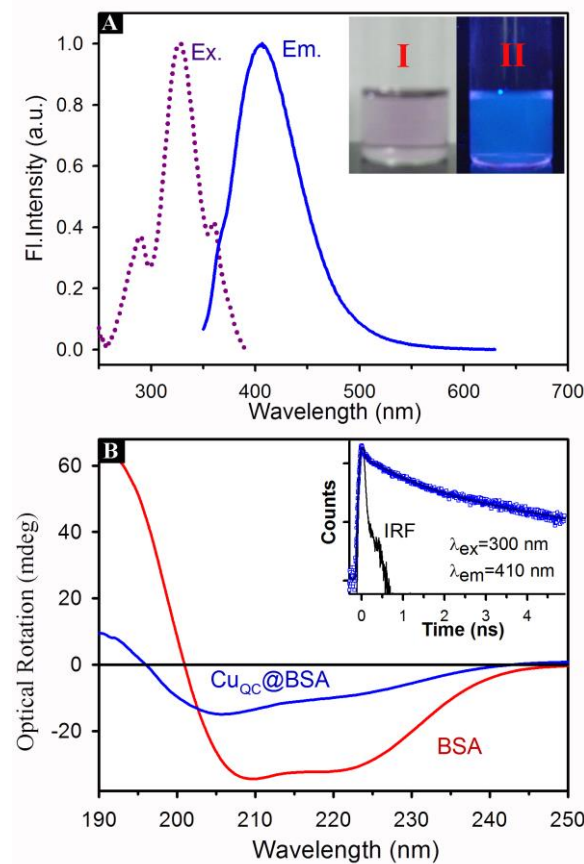


Figure 8.3. (A) Excitation and emission spectra of $\text{Cu}_{\text{QC}}@\text{BSA}$ at room temperature (pink and blue line). The inset contains the photographs of the $\text{Cu}_{\text{QC}}@\text{BSA}$ under visible light (I) and under UV light (II). (B) Far-UV CD spectra of BSA (red) and $\text{Cu}_{\text{QC}}@\text{BSA}$ (blue). Inset: photoluminescence decay of $\text{Cu}_{\text{QC}}@\text{BSA}$ with instrument response function (IRF) ~ 60 ps. Standard errors of decay time component are $\sim 5\%$.

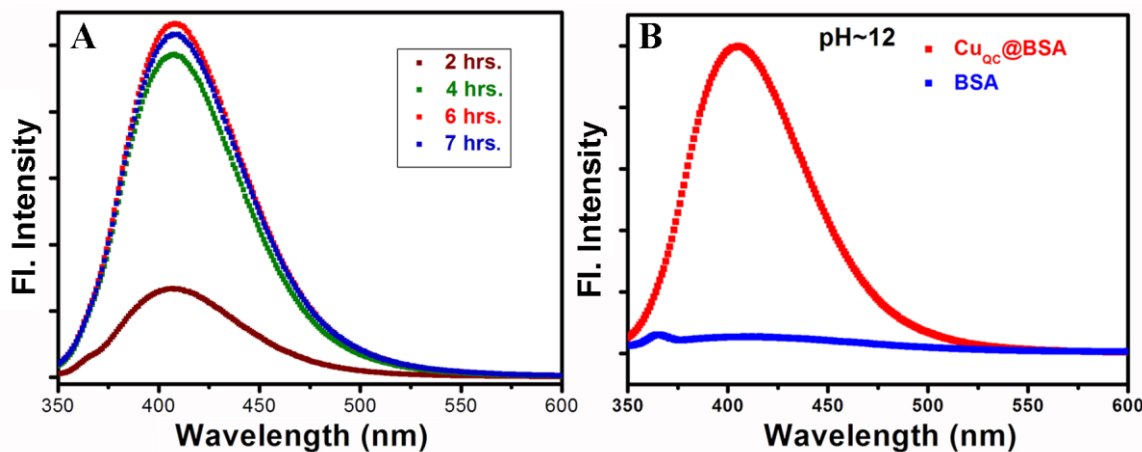


Figure 8.4. A. Time evolution of the photoluminescence spectrum ($\lambda_{\text{ex}} = 325 \text{ nm}$) for Cu_{Qc}@BSA during the synthesis of cluster. B. Photoluminescence spectrum ($\lambda_{\text{ex}} = 325 \text{ nm}$) of Cu_{Qc}@BSA (red) and BSA (blue) at pH~12 while all the parameters are same in both cases.

The luminescence of Cu_{Qc}@BSA revealing distinct excitation and emission maxima at 325 and 410 nm, respectively is evident from Figure 8.3A. The peak position (325 nm) of the excitation spectrum is almost alike to the Cu QCs absorption band in Figure 8.1A. As the reaction progressed, a gradual increase in the luminescence from the solution has been observed (Figure 8.4A). After around 6–8 h of reaction, there is no further enhancement in the luminescence and the reaction is considered to be terminated. Moreover, for 325-nm excitation, integrated fluorescence quantum yield for Cu_{Qc}@BSA is 0.15 using kynurenone as the reference. Protein alone shows insignificant emission upon 325 nm excitation at pH 12 (Figure 8.4B) confirming the absence of emitting amino acid metabolites. At this juncture it is important to mention that we have checked the possibility of interfering luminescence from the protein matrix in a similar experimental condition. The yield is found to be 2×10^{-2} with no specific absorption and emission maxima. This observation clearly rules out the possible interference in the measured luminescence for the Cu_{Qc}@BSA complex. The luminescence decay of the Cu_{Qc}@BSA in water is measured by a picosecond-resolved time-correlated single-photon counting (TCSPC) technique (Inset of Figure 8.3B). The decay profile of the Cu_{Qc}@BSA is monitored at an excitation wavelength of 300 nm. The numerical fitting of the luminescence collected at 410 nm reveals time constants of 0.03 ns (78%), 0.71 ns (15%) and 3.50 ns (7%), which may be due to the electronic transitions between “sp” conduction band and filled “d¹⁰” band.

This Cu_{QC}@BSA has a photoluminescence peak at ~410 nm, indicating the presence of Cu₁₃ quantum clusters based on our estimation using the spherical Jellium model[28]: i.e., $E_g = E_{\text{fermi}}/N^{1/3}$, where E_{fermi} is the Fermi energy of bulk material and N is the number of atoms per cluster, which also supports our MALDI MS data. Theoretical calculations [28] and all the above mentioned observations from UV-vis, PL, lifetime, MALDI MS and XPS investigations indicate the formation of Cu QC_s. Nevertheless, in order to further confirm the formation of QC_s, as some aromatic amino acid metabolites are also known to emit in the blue region, we have performed the following experiments. In the presence of an oxidizing agent, Cu QC_s, if present, would be oxidized and should result quenching of its luminescence and optical absorption. However, if the blue luminescence originates from the oxidized product of protein then it would expect to increase. We have added H₂O₂ of different concentrations to the as-synthesized Cu QC_s and we notice concentration dependent quenching of luminescence which further corroborates the presence of Cu QC_s in the protein matrix (Figures 8.5A-B). From an application point of view, it can be used as H₂O₂ sensor in nanomolar level. In contrast, the control protein solution does not provide any luminescence enhancement upon addition of H₂O₂ which rules out the possibility of oxidized product of protein (Figure 8.6). Thermo-gravimetric analysis (TGA) and differential scanning calorimetric

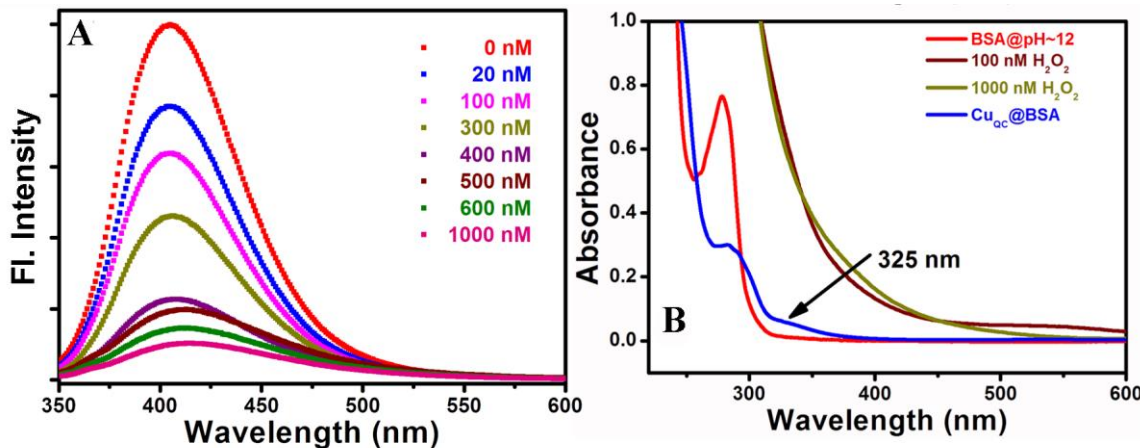


Figure 8.5. A. Photoluminescence spectrum ($\lambda_{\text{ex}} = 325 \text{ nm}$) of Cu_{QC}@BSA with the addition of H₂O₂ (0-1000 nM). B. Absorbance of Cu_{QC}@BSA after addition of H₂O₂. The result indicates that the prominent absorption shoulder at 325 nm in Cu_{QC}@BSA (blue). The spectrum of Cu_{QC}@BSA in presence of H₂O₂, does not show clear disappearance of the absorption shoulder at 325 nm because of the very large absorption at this wavelength-region after addition of H₂O₂.

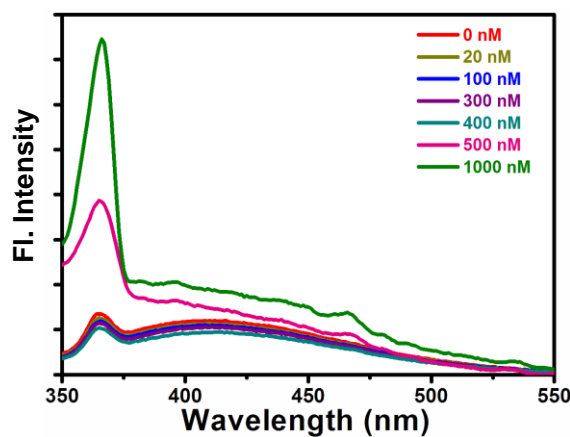


Figure 8.6. Photoluminescence spectrum ($\lambda_{\text{ex}} = 325 \text{ nm}$) of BSA with the addition of H₂O₂ (0-1000 nM).

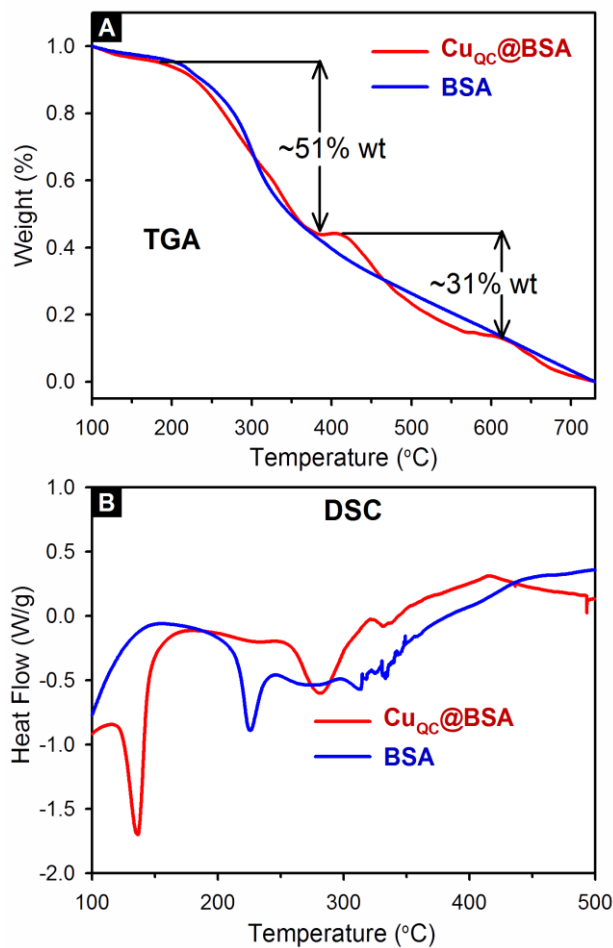


Figure 8.7. A. Thermo gravimetric (TG) analysis of Cu_{QC}@BSA (red) and BSA (blue) performed under N₂. Mass loss below 150°C is attributed to water. Protein mass loss is seen only above 200°C. B. This is also reflected in the DSC spectra.

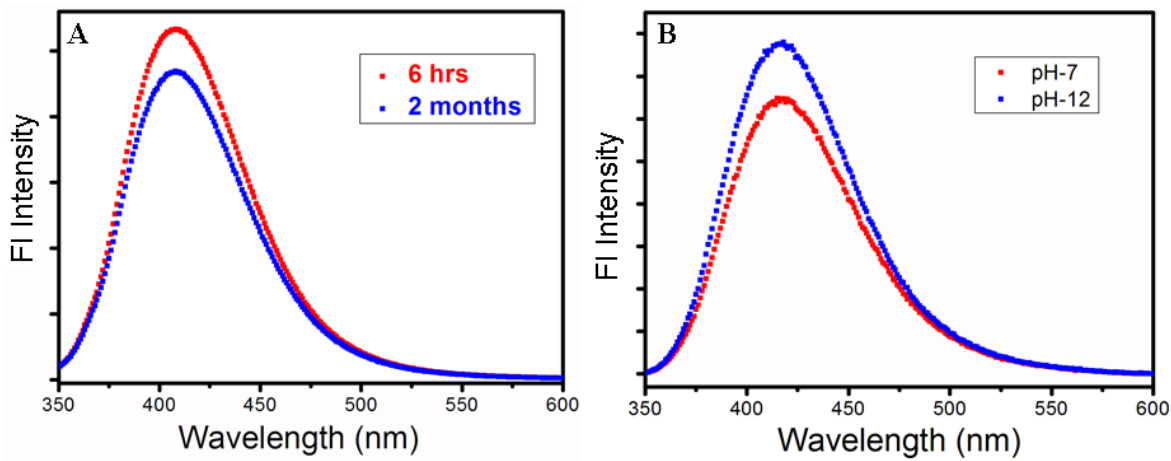


Figure 8.8. A. Photoluminescence spectra of CuQc@BSA at different time indicating the high stability of clusters. B. Photoluminescence spectra of CuQc@BSA at different pH indicate the high stability of the clusters.

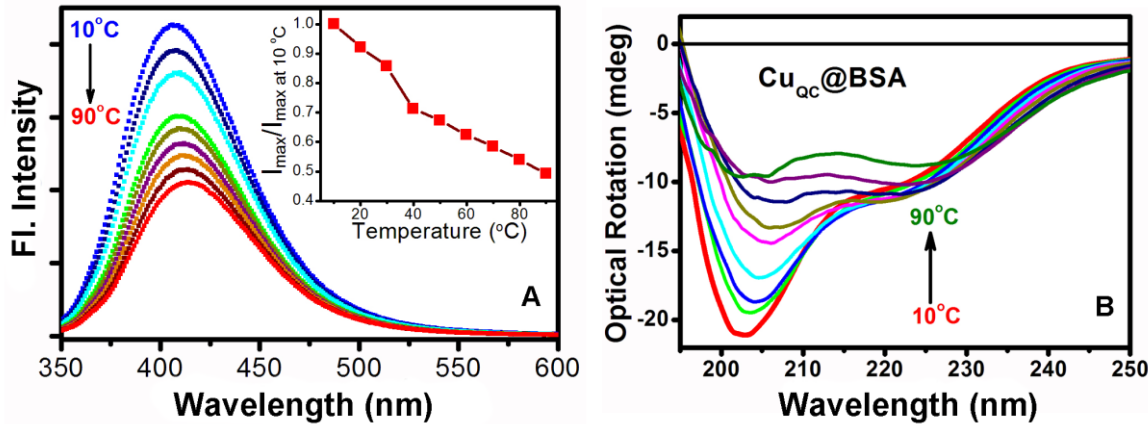


Figure 8.9. A. Steady-state photoluminescence spectra of CuQc@BSA recorded at different temperatures. Inset: Plot of temperature versus maximum fluorescence intensity of the cluster with respect to I_{\max} at 10°C . B. Circular dichroism spectra of CuQc@BSA recorded at different temperatures indicating the perturbation of the secondary structure of the protein.

(DSC) studies on other metal clusters are found to be very informative about the formation of cluster in protein and thiol matrices [6, 29]. Our TGA and DSC studies of BSA and CuQc@BSA also provided supporting evidence for the formation of the QCs (Figure 8.7).

The obtained Cu QCs are found to be very stable, showing the same emission spectra after almost 2 months of being stored at room temperature (Figure 8.8A). The emission peak remains unchanged at pH 7 to 12, as it can be seen in Figure 8.8B. In order to investigate the thermal stability of the QCs, temperature dependent luminescence of CuQc@BSA has been monitored. It can be seen from Figure 8.9A that emission of the CuQc@BSA in the aqueous solution decreased significantly upon increase in temperature.

The reason may be the increase in hydrophilicity around the Cu QCs as protein is perturbed at higher temperature (which is also reflected in circular dichroism (CD) measurements, see Figure 8.9B). The minor red shift of the position of luminescence maximum with temperature is due to the relative strengths of ground and excited-state solvent stabilization. We have employed circular dichroism (CD) method to study the conformational behavior of BSA before and after the formation of the Cu QCs. Native BSA displays CD features with minima at 208 and 222 nm, corresponding to the secondary structure of the protein (Figure 8.3B). However, after the formation of Cu QCs, the 208 nm peak is shifted to 204 nm indicating the loss of α - helix content and increase in β -sheet and random coil structures. The percentage of various conformations has been determined for both pure BSA and Cu_{QC}@BSA by using CDNN software which revealed 15% loss of α -helix structure.

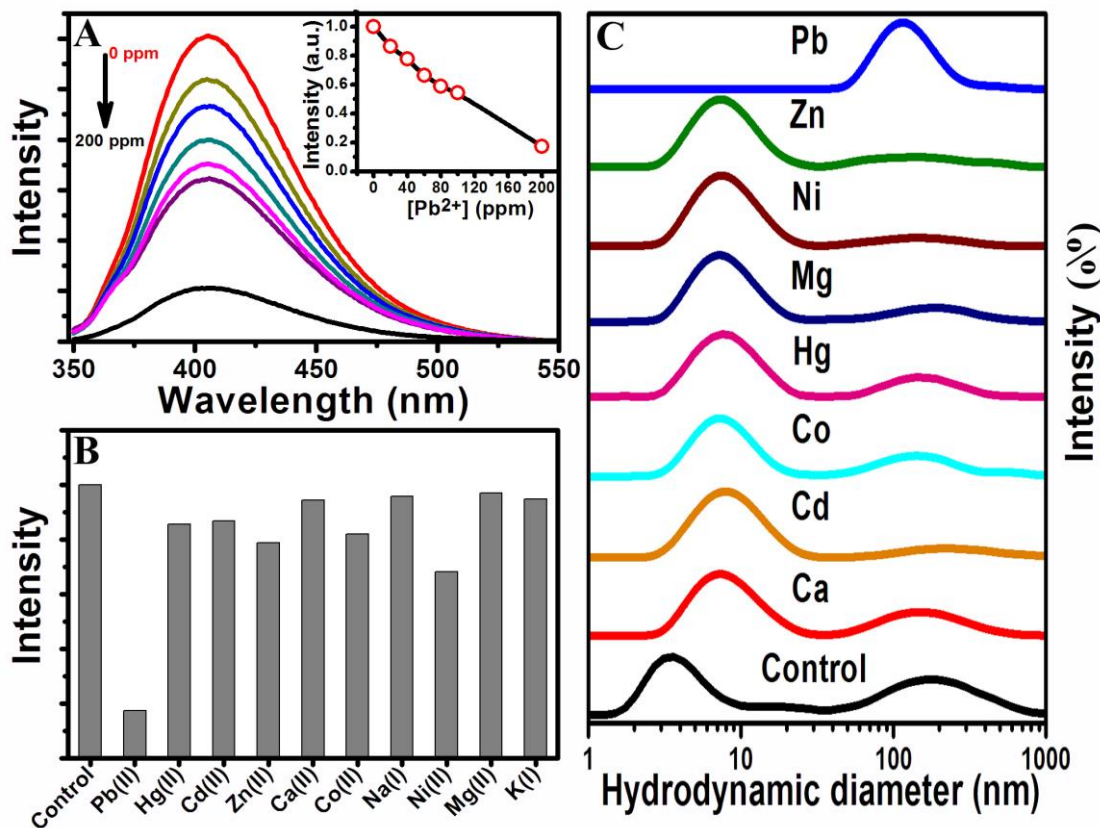


Figure 8.10. (A) Luminescence responses of Cu_{QC}@BSA after the addition of Pb²⁺ ion (0-200 ppm). Inset: Plot of the luminescence peak intensity versus the concentration of Pb²⁺ ion. (B) Selectivity of the Cu_{QC}@BSA to different metal ions. The luminescence intensities were recorded at 406 nm. For panel B, the final metal ion concentrations are 200 ppm. (C) DLS spectra of Cu_{QC}@BSA solution in absence (control) and presence of different metal ions.

The luminescence of the as-prepared CuQC@BSA can be used as a highly sensitive and selective luminescence “turn-off” sensor for the Pb²⁺ ion. We found that the luminescence of Cu QC_s is quenched in the presence of Pb²⁺ ion. It can be seen from the Figure 8.10A that more and more quenching occurs with an increase in Pb²⁺ ion. Herein, we have also carried out studies with other metal ions, such as Hg²⁺, Ca²⁺, Co²⁺, Zn²⁺, Ni²⁺, Cd²⁺, Mg²⁺, Na⁺, and K⁺ under exactly similar conditions that were used for the detection of Pb²⁺ ion. Chlorides and nitrates of the metals are used. Metal ions are added to aqueous solutions of the Cu QC_s such that the final concentration was 200 ppm and the luminescence of the Cu QC_s is measured immediately after the addition of ions. However, no such quenching effect like that of the Pb²⁺ ion is observed. The relative luminescence quenching of CuQC@BSA toward various common metal ions is presented in Figure 8.10B. This result suggests that our luminescent Cu QC_s are selective for Pb²⁺ detection. The luminescence quenching in the presence of Pb²⁺ can be attributed to the QC aggregation induced by the complexation between BSA and the Pb²⁺ ion. BSA contains a high-affinity site for Pb²⁺ ion; the binding involves carboxylate groups. To explore the quenching mechanism, we have performed DLS measurement. It can be seen from Figure 8.10C that only Pb²⁺ ion can induce the protein–protein interaction which leads to spherical aggregation of CuQC@BSA.

8.3. Conclusion

In summary, we have reported a method for preparing highly stable, blue luminescent and water-soluble Cu QC_s using a common protein, BSA. It can selectively and very sensitively detect highly toxic lead ions at ppm concentrations even in presence of other interfering ions. This study would be potentially extended to generate other quantum clusters and applied as a good candidate for biolabelling, biosensing, and applications in material and biomaterial sciences.

References

- [1] A.P. Alivisatos, Semiconductor Clusters, Nanocrystals, and Quantum Dots, *Science* 271 (1996) 933.
- [2] R. Elghanian, J.J. Storhoff, R.C. Mucic, R.L. Letsinger, C.A. Mirkin, Selective Colorimetric Detection of Polynucleotides Based on the Distance-Dependent Optical Properties of Gold Nanoparticles, *Science* 277 (1997) 1078.
- [3] L. Polavarapu, M. Manna, Q.H. Xu, Biocompatible Glutathione Capped Gold Clusters as One- and Two-Photon Excitation Fluorescence Contrast Agents for Live Cells Imaging, *Nanoscale* 3 (2011) 429.
- [4] G. Schmid, Nanoclusters - Building Blocks for Future Nanoelectronic Devices?, *Adv. Eng. Mater.* 3 (2001) 737.
- [5] Y. Zhu, H.F. Qian, R.C. Jin, An Atomic-Level Strategy for Unraveling Gold Nanocatalysis from the Perspective of Au-n(SR)(m) Nanoclusters, *Chem. Eur. J.* 16 (2010) 11455.
- [6] J.P. Xie, Y.G. Zheng, J.Y. Ying, Protein-Directed Synthesis of Highly Fluorescent Gold Nanoclusters, *J. Am. Chem. Soc.* 131 (2009) 888.
- [7] J. Zheng, P.R. Nicovich, R.M. Dickson, Highly Fluorescent Noble-Metal Quantum Dots, *Annu. Rev. Phys. Chem.* 58 (2007) 409.
- [8] G.Y. Lan, C.C. Huang, H.T. Chang, Silver Nanoclusters as Fluorescent Probes for Selective and Sensitive Detection of Copper Ions, *Chem. Comm.* 46 (2010) 1257.
- [9] T.U.B. Rao, B. Nataraju, T. Pradeep, Ag₉ Quantum Cluster through a Solid-State Route, *J. Am. Chem. Soc.* 132 (2010) 16304.
- [10] P.L. Xavier, K. Chaudhari, P.K. Verma, S.K. Pal, T. Pradeep, Luminescent Quantum Clusters of Gold in Transferrin Family Protein, Lactoferrin Exhibiting FRET, *Nanoscale* 2 (2010) 2769.
- [11] J.M. Slocik, D.W. Wright, Biomimetic Mineralization of Noble Metal Nanoclusters, *Biomacromolecules* 4 (2003) 1135.
- [12] J.T. Petty, J. Zheng, N.V. Hud, R.M. Dickson, DNA-Templated Ag Nanocluster Formation, *J. Am. Chem. Soc.* 126 (2004) 5207.
- [13] Z. Wu, E. Lanni, W. Chen, M.E. Bier, D. Ly, R. Jin, High Yield, Large Scale Synthesis of Thiolate-Protected Ag₇ Clusters, *J. Am. Chem. Soc.* 131 (2009) 16672.

- [14] S.-I. Tanaka, J. Miyazaki, D.K. Tiwari, T. Jin, Y. Inouye, Fluorescent Platinum Nanoclusters: Synthesis, Purification, Characterization, and Application to Bioimaging, *Angew. Chem. Int. Ed.* 50 (2011) 431.
- [15] J.M. Tam, J.O. Tam, A. Murthy, D.R. Ingram, L.L. Ma, K. Travis, K.P. Johnston, K.V. Sokolov, Controlled Assembly of Biodegradable Plasmonic Nanoclusters for Near-Infrared Imaging and Therapeutic Applications, *ACS Nano* 4 (2010) 2178.
- [16] W.T. Wei, Y.Z. Lu, W. Chen, S.W. Chen, One-Pot Synthesis, Photoluminescence, and Electrocatalytic Properties of Subnanometer-Sized Copper Clusters, *J. Am. Chem. Soc.* 133 (2011) 2060.
- [17] N. Vilar-Vidal, M.C. Blanco, M.A. Lopez-Quintela, J. Rivas, C. Serra, Electrochemical Synthesis of Very Stable Photoluminescent Copper Clusters, *J. Phys. Chem. C* 114 (2010) 15924.
- [18] H. Kawasaki, Y. Kosaka, Y. Myoujin, T. Narushima, T. Yonezawa, R. Arakawa, Microwave-Assisted Polyol Synthesis of Copper Nanocrystals without Using Additional Protective Agents, *Chem. Commun.* 47 (2011) 7740.
- [19] N. Goswami, A. Giri, M.S. Bootharaju, P.L. Xavier, T. Pradeep, S.K. Pal, Copper Quantum Clusters in Protein Matrix: Potential Sensor of Pb^{2+} ion, *Anal. Chem.* 83 (2011) 9676.
- [20] N. Goswami, A. Makhal, S.K. Pal, Toward an Alternative Intrinsic Probe for Spectroscopic Characterization of a Protein, *J. Phys. Chem. B* 114 (2010) 15236.
- [21] S. Si, T.K. Mandal, Tryptophan-Based Peptides to Synthesize Gold and Silver Nanoparticles: A Mechanistic and Kinetic Study, *Chem. Eur. J.* 13 (2007) 3160.
- [22] P. Ramasamy, S. Guha, E. Sidharth Shibu, T.S. Sreeprasad, S. Bag, A. Banerjee, T. Pradeep, Size Tuning of Au Nanoparticles Formed by Electron Beam Irradiation of Au₂₅ Quantum Clusters Anchored within and outside of Dipeptide Nanotubes, *J. Mater. Chem.* 19 (2009) 8456.
- [23] K. Chaudhari, P. Lourdu Xavier, T. Pradeep, Understanding the Evolution of Luminescent Gold Quantum Clusters in Protein Templates, *ACS Nano* (2011).
- [24] S.C. Drew, K.J. Barnham, The Heterogeneous Nature of Cu^{2+} Interactions with Alzheimer's Amyloid- β Peptide, *Acc. Chem. Res.* (2011).
- [25] R.L. Whetten, R.C. Price, Nano-Golden Order, *Science* 318 (2007) 407.

- [26] J. Akola, M. Walter, R.L. Whetten, H. Hakkinen, H. Gronbeck, On the Structure of Thiolate-Protected Au-25, *J. Am. Chem. Soc.* 130 (2008) 3756.
- [27] A. Mathew, P.R. Sajanlal, T. Pradeep, A Fifteen Atom Silver Cluster Confined in Bovine Serum Albumin, *J. Mater. Chem.* (2011) 11205.
- [28] J. Zheng, C.W. Zhang, R.M. Dickson, Highly Fluorescent, Water-Soluble, Size-Tunable Gold Quantum Dots, *Phys. Rev. Lett.* 93 (2004) 409.
- [29] M. Zhu, E. Lanni, N. Garg, M.E. Bier, R. Jin, Kinetically Controlled, High-Yield Synthesis of Au25 Clusters, *J. Am. Chem. Soc.* 130 (2008) 1138.

List of Publications

1. **N. Goswami**, A. Makhal and S.K. Pal
“Toward an Alternative Intrinsic Probe for Spectroscopic Characterization of a Protein”
J. Phys. Chem. B 114 (2010) 15236.
2. **N. Goswami**, R. Saha and S. K. Pal
“Protein-assisted Synthesis Route of Metal Nanoparticles: Exploration of Key Chemistry of the Biomolecule”
J. Nanopart. Res. 13 (2011) 5485.
3. **N. Goswami**, A. Giri, S. Kar, M. S. Bootharaju, R. John, P. L. Xavier, T. Pradeep and S. K. Pal
“Protein Directed Synthesis of NIR-Emitting, Tunable HgS Quantum Dots and Their Applications in Metal Ion Sensing”
Small 8 (2012) 3175.
4. **N. Goswami**, A. Giri and S. K. Pal
“MoS₂ Nanocrystals Confined in a DNA Matrix Exhibiting Energy Transfer”
Langmuir 29 (2013) 11471.
5. **N. Goswami**, A. Giri, M.S. Bootharaju, P.L. Xavier, T. Pradeep and S.K. Pal
“Copper Quantum Clusters in Protein Matrix: Potential Sensor of Pb²⁺ Ion”
Anal. Chem. 83 (2011) 9676.
- 6.* A. Giri, **N. Goswami**, M. S. Bootharaju, P. L. Xavier, R. John, N. T. K. Thanh, T. Pradeep, B. Ghosh, A. K. Raychaudhuri and S. K. Pal
“Emergence of Multicolor Photoluminescence in La_{0.67}Sr_{0.33}MnO₃ Nanoparticles”
J. Phys. Chem. C 116 (2012) 25623.

- 7.* A. Giri, N. Goswami, P. Lemmens and S. K. Pal
 “Preparation of Water Soluble L-Arginine Capped CdSe/Zns QDs and Their Interaction with Synthetic DNA: Picosecond-Resolved FRET Study”
Mater. Res. Bull. 47 (2012) 1912 (Cover Article).
- 8.* A. Giri, N. Goswami, M. Pal, M.T. Zar Myint, S. Al-Harthi, A. Singha, B. Ghosh, J. Dutta and S.K. Pal
 “Rational Surface Modification of Mn₃O₄ Nanoparticles to Induce Multiple Photoluminescence and Room Temperature Ferromagnetism”
J. Mater. Chem. C 1 (2013) 1885.
- 9.* A. Giri, N. Goswami, S. Sarkar and S. K. Pal
 “Bio-Nanomaterials: Understanding Key Biophysics and Their Applications”
 Book Chapter in “Biomaterials” Edited by J.N. Govil, STUDIUM PRESS LLC, USA, 2013.
- 10.* S. Rakshit, N. Goswami and S. K. Pal
 “Slow Solvent Relaxation Dynamics of Nanometer Sized Reverse Micellar Systems through Tryptophan Metabolite, Kynurenone”
Photochem. Photobiol. 88 (2012) 38.
- 11.* S. Banerjee, N. Goswami, and S. K. Pal
 “Vibronic Bands of a Potential Carcinogenic Pyrene Derivative under FRET to various Energy Acceptors in Nanoscopic Environments”
Chem. Phys. Chem. (2013) (DOI: 10.1002/cphc.201300568)
- 12.* T. Udayabhaskararao, Y. Sun, N. Goswami, S. K. Pal, K. Balasubramanian and T. Pradeep
 “Ag₇Au₆: A 13 Atom Alloy Quantum Cluster”
Angew. Chem. Int. Ed. 51 (2012) 2155.

- 13*. A. Baksi, P. L. Xavier, K. Chaudhari, N. Goswami, S. K. Pal and T. Pradeep
“Protein-Encapsulated Gold Cluster Aggregates: The Case of Lysozyme”
Nanoscale 5 (2013) 2009.
- 14*. J. S. Mohanty, P. L. Xavier, K. Chaudhari, M. S. Bootharaju, N. Goswami,
S. K. Pal and T. Pradeep
“Luminescent, Bimetallic AuAg Alloy Quantum Clusters in Protein
Templates”
Nanoscale 4 (2012) 4255.

* Not included in the thesis.